

**Dynamic compression and torsion behavior of C300 Maraging steels  
produced via powder bed fusion technique**

By

**Shirin Dehgahi**

**M.Sc. Materials Engineering, Shiraz University of Technology, Iran (2014)**

A Dissertation Submitted in Partial Fulfillment  
of the Requirements for the Degree of

**Doctor of Philosophy**

in the Graduate Academic Unit of Mechanical Engineering

**Supervisor:** Mohsen Mohammadi, Ph.D., Dept of Mechanical Engineering

**Examining Board:** Othman Nasir, Ph.D., Dept of Civil Engineering  
Andy Simoneau, Ph.D., Dept of Mechanical Engineering  
Clodualdo Aranas, Ph.D., Dept of Mechanical Engineering

**External Examiner:** Hamid Abdolvand, Ph.D., Dept of Mechanical Engineering,  
Western University

**This dissertation is accepted by the  
Dean of Graduate Studies**

**THE UNIVERSITY OF NEW BRUNSWICK**

March 2022

© Shirin Dehgahi, 2022

## Abstract

Maraging steel components are subjected to dynamic compression and torsion loadings in their applications. Their response in these loading directions is the focus of this study. In order to have a thorough overview of the dynamic torsion behavior of maraging steels, the quasi-static and dynamic compression behavior of maraging steel was evaluated first. Gas atomized C300 metal powders containing two different Ti contents (0.72 and 1.17 wt.%) were used to additively manufacture maraging steel samples via laser powder bed fusion (LPBF). A comprehensive study was conducted to investigate the effects of chemical composition, heat treatment, and building direction on the quasi-static mechanical and dynamic compression and torsion behavior of 18Ni-300 maraging steel parts produced using LPBF. Initially, the effect of Ti on the quasi-static and dynamic responses of additively manufactured maraging steel parts was investigated. A Split Hopkinson pressure bar apparatus (SHPB) was utilized for high strain rate compression tests. In the as-built condition, the results showed that the Ti-rich samples exhibited higher hardness and tensile strength. After heat-treating at 490 °C for 6 h, the Ti-rich maraging steels showed higher strength and ductility (2057.74 MPa and 4.05%). As-built and heat-treated maraging steel samples were subjected to dynamic compression tests and results showed that as-built samples were fractured in strain rate of 3500 s<sup>-1</sup>, while heat-treated samples began to fragment in strain rate of 1930 s<sup>-1</sup>. Texture development during high strain rate tests of as-built and heat-treated samples was also investigated and the results showed that crystallographic texture changed significantly in as-built samples. Vertically built samples fractured in strain rate of 1300 s<sup>-1</sup>, while for horizontally built samples, failure occurred in strain rate of 2200 s<sup>-1</sup>. The reason for different behavior is related to different

microstructures, where columnar and equiaxed microstructures were developed in the vertical and horizontal samples, respectively. High strain rate compressive results showed that until strain rate of  $5000 \text{ s}^{-1}$ , the fracture did not happen for Ti-rich samples due to higher fraction of austenite phase in Ti-rich samples. As Ti-rich maraging steel showed exceptional behavior on quasi-static and dynamic compressive loadings, the dynamic torsion behavior of these samples was also evaluated. Finally, a Split Hopkinson torsion bar (SHTB) apparatus was utilized for studying the dynamic torsion behavior of the Ti-rich maraging steel sample in which at an angle of twist of 12 degrees, the failure happened. The Chang-Asaro constitutive model was developed for describing the dynamic compressive behavior of as-built and heat-treated samples and an acceptable agreement between the experimental results and modeling practice was observed. In addition, Johnson-cook and Voyiadjis, and Abed models were employed to describe the dynamic behavior of horizontal and vertical heat-treated samples. Furthermore, Kobayashi-Odd and Nemat-Nasser models were employed for describing the torsion behavior of LPBF-maraging steel parts. Fair agreement between the model results and the experimental findings were observed.

## **Dedication**

To my family and my husband that it would be impossible for me to complete my study without their encouragement.

## **Acknowledgements**

First and foremost, I am extremely grateful to my supervisor, Dr. Mohsen Mohammadi for his invaluable advice, continuous support and patience during my PhD journey. His immense knowledge and plentiful experience have encouraged me all the time during my academic research and daily life. I would like to express gratitude to Dr. Zahra Khatami for her help and advice with this PhD as well.

I would like to thank all the members of my committee who kindly agreed to stand on my committee and for their encouragement, insightful comments, and good questions.

My appreciation goes to Mechanical Engineering Department staff for their help and support all through my studies. Special thanks go to Krista McCarthy for her help during my study. I would like to thank technicians who helped me during my PhD, Vince Boardman, Brian Guidry, Victoria Jarvis and Steven Cogswell. I am also grateful for the help and support of Dr. Amir Hadadzadeh from the University of Memphis, Dr. Babak Shalchi Amirkhiz and Dr. Mehdi Sanjari from the CanmetMATERIALS, Dr. Hadi Pirgazi and Dr. Leo Kestens from Ghent University and Dr. Akindele Odeshi from University of Saskatchewan.

I would like thank all of my friends in MAMCE group who helped me during my PhD and last but not least, I am extremely grateful of my brothers and my sister for supporting me spiritually throughout my life.

# Table of contents

Abstract .....	ii
List of tables.....	xi
List of figures.....	xiii
Nomenclature.....	xxi
Chapter 1: Introduction .....	1
1.1 Maraging steels .....	2
1.2 Literature review .....	3
1.2.1 Additive manufacturing .....	3
1.2.2 Different additive manufacturing techniques.....	4
1.2.3. Powder bed fusion.....	4
1.2.4. Laser powder bed fusion technique .....	5
1.2.5 LPBF-maraging steel .....	6
1.2.5.1 Microstructure of maraging steel .....	6
1.2.5.2. Process parameters.....	6
1.2.5.3. Heat treatment.....	7
1.2.6. Chemical composition of maraging steel.....	8
1.2.7. Dynamic behavior of maraging steel .....	9
1.2.8. Corrosion behavior of maraging steel.....	9
1.3. Gap of knowledge .....	10
1.4. Study outline .....	15
1.5. Hypothesis .....	16
1.6. References.....	17
Chapter 2: The Role of Titanium on the Microstructure and Mechanical Properties of Additively Manufactured C300 Maraging Steels .....	25
2.1. Introduction.....	25
2.2. Experimental Methodology .....	27
2.3. Results and Discussions .....	31
2.3.1. Phase Identification.....	31
2.3.2. Powders Shape and Size Distribution .....	34
2.3.3. As-built Microstructural Characteristics and Porosity Formation .....	40
2.3.5. Solute Clustering and Precipitates Formation.....	45
2.3.6. Mechanical Properties.....	51

2.4. Conclusions.....	56
2.5. References.....	58
Chapter 3: Concurrent improvement of strength and ductility in heat-treated C300 maraging steels produced by laser powder bed fusion technique .....	70
3.1. Introduction.....	70
3.2. Experiments .....	74
3.2.1 Sample preparation .....	74
3.2.2. Phase and microstructural analyses.....	76
3.2.3. Mechanical properties .....	77
3.3. Results.....	77
3.3.1. Mechanical properties of as-built and heat treated samples.....	77
3.3.2. Microstructure.....	80
3.3.3 Crystallographic orientation.....	82
3.3.4. Grain morphology .....	86
3.3.5. Phase identification of as-built and heat treated samples.....	86
3.3.6. TEM analysis in the heat treated samples .....	90
3.3.7. Texture evolution during the deformation .....	97
3.3.8. The effect of Ti content on recrystallization fraction.....	100
3.4. Discussion.....	104
3.4.1. The effect of Ti content on reverted austenite formation.....	104
3.4.2. The effect of reverted austenite on mechanical properties.....	106
3.4.3. The effect of microstructure characteristic on mechanical properties .....	108
3.4.4. The effect of precipitate formation on mechanical properties .....	109
3.4.5. The effect of preferred orientation on mechanical properties .....	112
3.5. Conclusion .....	113
3.5. References.....	115
Chapter 4: Microstructural evolution and high strain rate compressive behavior of as-built and heat-treated additively manufactured maraging steels.....	124
4.1. Introduction.....	124
4.2. Experimental procedure .....	127
4.2.1. Laser powder bed fusion (LPBF)process and maraging steel rods fabrication.....	127
4.2.2. Heat-treatment.....	129
4.2.3. Dynamic compression tests.....	129
4.2.4. Microscopy .....	132

4.3. Results.....	132
4.3.1. Dynamic compression behavior of LPBF-maraging steel .....	132
4.3.1.1. Dynamic flow curves .....	132
4.3.1.2. Microstructure features of as-built and dynamically deformed LPBF-maraging steel.....	139
4.3.1.3. Texture development in the as-built deformed alloy .....	143
4.3.2. Dynamic compression behavior of heat treated LPBF-maraging steel.....	148
4.3.2.1. Dynamic flow curves .....	148
4.3.2.2. Microstructure of heat treated deformed LPBF-maraging steel .....	155
4.3.3. Constitutive modeling of dynamic deformation behavior .....	158
4.3.3.1. Mathematical modeling development for as-built LPBF-maraging steel .....	158
4.3.3.2. Mathematical modeling development for heat treated LPBF-maraging steel.....	161
4.4. Conclusion .....	163
4.5. References.....	164
Chapter 5: Texture evolution during high strain-rate compressive loading of maraging steels	
produced by laser powder bed fusion .....	171
5.1. Introduction.....	171
5.2. Experimental procedure .....	173
5.2.1. Materials and the LPBF process .....	173
5.2.2. High strain rate test.....	174
5.2.3. Texture measurement.....	175
5.3. Results and discussion .....	176
5.3.1. Mechanical properties .....	176
5.3.2. Texture analysis .....	182
5.3.3. Grain analysis.....	198
5.4. Conclusion .....	203
5.5. References.....	203
Chapter 6: Effect of building direction on high strain rate compressive behavior of heat-treated	
LPBF-maraging steel using Split Hopkinson pressure bar apparatus .....	210
6.1. Introduction.....	210
6.2. Experimental procedure .....	213
6.2.1. LPBF process.....	213
6.2.2. Dynamic compression testing .....	214
6.2.3. Microstructural studies.....	216
6.3. Results and discussion .....	217

6.3.1. Dynamic compressive behavior of horizontal and vertically oriented maraging steel ....	217
6.3.2. Microstructural evolution during dynamic loading of horizontal and vertically printed maraging steel (TEM studies).....	229
6.3.3. Microstructural evolution during dynamic loading of horizontal and vertically printed maraging steel (SEM studies).....	232
6.3.4. Texture evolution during dynamic loading of horizontal and vertically printed maraging steel:.....	238
6.4. Mathematical modeling .....	245
6.4.1. Johnson-Cook model .....	246
6.4.2. Voyiadjis-Abed model .....	249
6.5. Conclusion .....	251
6.5. References.....	252
<b>Chapter 7: Influence of composition on mechanical and corrosion behavior of L-PBF maraging steel.....</b>	<b>258</b>
7.1. Introduction.....	258
7.2. Material and methods.....	261
7.2.1. Material and process parameters.....	261
7.2.2. Dynamic compression loading on Split Hopkinson pressure bar .....	262
7.2.3. Electrochemical measurements.....	263
7.2.4. Microstructure analysis.....	264
7.3. Results and discussion .....	264
7.3.1. Dynamic impact behavior of Low-Ti C300 maraging steel.....	264
7.3.2. Dynamic impact behavior of High-Ti C300 maraging steel.....	269
7.3.3. Comparison of dynamic behavior of Low and High-Ti tested samples.....	273
7.3.4. Microstructural studies after dynamic loading.....	275
7.3.5. Electrochemical tests .....	281
7.3.5.1. Potentiodynamic polarization measurement .....	282
7.3.5.2. Electrochemical impedance spectrum measurement .....	283
7.3.6. Surface observation after immersion .....	292
7.4. Conclusions.....	294
7.5. References.....	295
<b>Chapter 8: High strain rate torsional response of maraging steel parts produced by laser powder bed fusion techniques: deformation behavior and constitutive model.....</b>	<b>303</b>
8.1. Introduction.....	303

8.2. Materials and methods .....	305
8.2.1. Material and process parameters.....	305
8.2.2. High strain rate torsion test .....	306
8.2.3. Microstructural studies.....	310
8.3. Results and discussion .....	311
8.3.1. Dynamic torsion test of LPBF-maraging steel samples.....	311
8.3.2. Microstructural studies of twisted M.S samples .....	317
8.3.3. Texture evolution of LPBF-M.S during dynamic torsion.....	323
8.4. Mathematical modeling .....	330
8.4.1. Kobayashi-Odd model .....	331
8.4.2. Nemat Nasser-Isaacs model.....	332
8.5. Conclusion .....	336
8.6. References.....	337
Chapter 9: Discussion .....	342
Chapter 10: Conclusions and future works .....	346
10.1. Conclusions.....	346
10.2. Recommendations for future work .....	348
10.2.1. Tailored mechanical properties .....	348
10.2.2. Modeling and simulations.....	350
Appendix A.....	352
Curriculum Vitae	

## List of tables

Table 2. 1. Chemical composition of the standard C300 maraging steel and virgin powders used in this study.....	29
Table 2. 2. Volumetric percentage of phases presented in the C300 maraging powders and AM products.....	32
Table 2. 3. Thermal properties of the AM LowTi and HighTi samples. ....	39
Table 2. 4. Mechanical properties of the AM LowTi and HighTi tensile samples.....	54
Table 2. 5. Comparison between mechanical properties of the AM maraging steel at various Ti contents, reported in some studies. ....	55
Table 3. 1. Chemical composition of powders used in this study.....	74
Table 3. 2. Process parameters of the LPBF process.....	76
Table 3. 3. Area fraction of columnar and equiaxed grains in the as-built and heat-treat conditions.....	86
Table 3. 4. Volumetric percentage of phases in the as-built and heat-treat conditions.....	88
Table 3. 5. Chemical composition (wt. %) by EDS/TEM of heat-treated maraging 300 steel extracted from Fig13.....	94
Table 3. 6. Phase analysis before and after deformation in as-built condition. ....	100
Table 3. 7. Phase analysis before and after deformation in heat treat condition.....	100
Table 4. 1. Chemical composition of maraging steel 300 based on EOS datasheet. ....	128
Table 4. 2. Process parameter of the LPBF process.....	128
Table 4. 3. Dynamic mechanical properties of compressed LPBF-maraging steel. ....	138
Table 4. 4. Observations from the EBSD analysis of maraging steel original and post-impact samples.....	146
Table 4. 5. Dynamic mechanical properties of compressed heat-treated LPBF-maraging steel..	154
Table 5. 1. Dynamic mechanical properties of the compressed as-built LPBF-maraging steel samples.....	180
Table 5. 2. Dynamic mechanical properties of the compressed heat-treated LPBF-maraging steel samples.....	182
Table 5. 3. The volume fraction of fibres in different strain rates in as-built and heat treat maraging steel samples before and after deformation.....	193
Table.6. 1. Chemical composition of maraging steel 300 based on EOS datasheet [14].....	213
Table.6. 2. Process parameter of the LPBF process.....	214

Table.6. 3. Dynamic mechanical properties of the compressed vertical heat-treated maraging steel specimens.....	221
Table.6. 4. Dynamic mechanical properties of the compressed horizontal heat-treated maraging steel specimens .....	227
Table.6. 5. Chemical composition (wt. %) by EDS/TEM of vertical and horizontal samples. ...	231
Table.6. 6. Determined values of J-C model parameters. ....	248
Table.6. 7. Determined values of V-A model parameters.....	250
Table 7. 1. Chemical composition of two C300 powders used for this study.....	261
Table 7. 2. Process parameters of the L-PBF process.....	261
Table 7. 3. Observations from the dynamic impact responses of Low-Ti maraging steel specimens .....	268
Table 7. 4. Observations from the dynamic impact responses of High-Ti maraging steel specimens.....	272
Table 7. 5. Nomination of samples, titanium content, and prior mechanical treatments. ....	281
Table 7. 6. Open circuit potential and Tafel fitted parameters after potentiodynamic test. ....	283
Table 7. 7. Fitting parameters obtained from EIS spectra.....	288
Table 8. 1. Chemical composition of M.S based on EOS datasheet.....	305
Table 8. 2. Process framework of the LPBF process.....	306
Table 8. 3. Dynamic mechanical properties of the twisted M.S samples fabricated by LPBF. ....	317
Table 8. 4. Determined parameters values of Kobayashi-Odd model. ....	331
Table 8. 5. Determined parameters values of Nemat-Nasser model.....	334

## List of figures

Fig 1. 1 Generic illustration of BPF system [30]. .....	5
Fig 2. 1 The geometry of the AM tensile and cubic samples.....	31
Fig 2. 2 The XRD profiles of (a) C300 powders, and (b) as-built sample at different Ti contents. .....	32
Fig 2. 3 The SEM micrographs of the LowTi and HighTi powders at two magnifications (i) satellite-shape, and (ii) irregular powders.....	36
Fig 2. 4 Size distribution and cumulative frequency of (a) LowTi, and (b) HighTi alloy powders. .....	37
Fig 2. 5 The SEM micrographs of (a) LowTi, and (b) HighTi alloy powders (i: dendritic, ii: equiaxed, iii: columnar, and iv: equiaxed morphologies). .....	38
Fig 2. 6 The Fe-Ni isopleth of (a) LowTi, and (b) HighTi alloying systems indicating the liquidus and solidus temperatures of the studied materials. ....	39
Fig 2. 7 The OM micrographs of (a) LowTi, and (b) HighTi as-built structure revealing the presence of porosities (i: spherical gas porosity, ii: irregular shrinkage porosity). ....	40
Fig 2. 8 Microstructure of the as-built (a, c) LowTi, and (b, d) HighTi samples (i: columnar, ii: fine equiaxed, iii: coarse equiaxed morphologies).....	42
Fig 2. 9 The IPF-Z maps of the as-built (a) LowTi, and (b) HighTi structures along with the building direction (BD), followed by distribution maps of (c) columnar/equiaxed grains, and (d) grain area.....	44
Fig 2. 10{100} pole figures and the grain boundary map of the as-built (a, c) LowTi, and (b, d) HighTi samples (In subfigures c and d, red and black lines indicate the LAGBs and HAGBs, respectively).....	45
Fig 2. 11The STEM-BF image and its corresponding elemental distribution maps showing the existence of $\gamma$ phase between $\alpha'$ pockets in the as-built LowTi sample. ....	48
Fig 2. 12 The STEM-BF image and its corresponding elemental distribution maps showing the existence of ultra-fine CoNi precipitates in the as-built HighTi sample.....	49
Fig 2. 13 (a) Diffraction pattern of the HighTi sample and its corresponding Miller index (i: superlattice reflections showing the presence of CoNi clusters), (b, c) TEM-DF and TEM-BF images of the LowTi matrix (ii: $\gamma$ phase, iii: dislocations networks).....	51
Fig 2. 14 Stress-strain curves of the AM as-built samples.....	54

Fig 2. 15 The SEM fractographs of (a) LowTi-horizontal, (b) HighTi-horizontal, (c) LowTi-vertical, and (d) HighTi-vertical samples. ....	56
Fig 3. 1 Schematic of cube and rod fabricated samples in the LPBF process. ....	75
Fig 3. 2 Uniaxial tensile stress-strain curves in as-built and heat-treat conditions. ....	79
Fig 3. 3 SEM images of the microstructure of the as-built and heat-treated samples. (a) LowTi as-built, (b) HighTi as-built, (c) LowTi heat treated, (d) HighTi heat treated. ((i) Columnar structure at the bottom of the melt pools, (ii) Equiaxed structure at the top of the MP borders, (iii) Cellular structure inside the MP). ....	81
Fig 3. 4 EBSD results of the side of the samples at $\times 300$ magnification. IPF-Z map of the HighTi and LowTi samples in as-built and heat-treat conditions. Build direction (z-axis) is marked as BD in the IPF maps. (a) LowTi-as built, (b) HighTi- as built, (c) LowTi heat treat, (d) HighTi-heat treat. ....	83
Fig 3. 5 EBSD results of the side of the samples at $\times 300$ magnification. (100) and (111) Pole figure maps of HighTi and LowTi samples in as-built and heat-treat conditions. (a) LowTi-as built, (b) HighTi- as built, (c) LowTi heat treat, (d) HighTi-heat treat.....	84
Fig 3. 6 EBSD results of the side of the samples at $\times 300$ . ODF maps ( $\phi_2=45^\circ$ ) of the HighTi and LowTi samples in as-built and heat-treat conditions. (a) texture component key (b) LowTi-as built, (c) HighTi- as built, (d) LowTi heat treat, (e) HighTi-heat treat. ....	85
Fig 3. 7 XRD pattern of HighTi and LowTi LPBF-maraging steel samples in (a) as-built and (b) heat-treated conditions. ....	88
Fig 3. 8 EBSD results of the side of the samples at $\times 5000$ magnification. (a) IPF-Z map of heat-treated LowTi sample (b) Phase map of heat-treated LowTi sample. (c)IPF-Z map of heat-treated HighTi sample and (d) phase map of heat-treated HighTi sample. Yellow spots represent reverted austenite, and green spots represent $\text{Ni}_3\text{Ti}$ precipitates.....	90
Fig 3. 9 STEM image along with EDS mapping from LowTi heat-treated specimen along with a compositional map of Ni, Ti, Mo showing the distribution of alloying elements in austenite. ....	91
Fig 3. 10 TEM micrograph of LowTi heat-treated maraging steel showing (a) TEM-Bright field, (b) Corresponding SAAD pattern. (c) Dark filed A as matrix, (d) Dark field B as austenite.....	92
Fig 3. 11 STEM image along with EDS mapping from the HighTi specimen along with a compositional map of Ni, Mo, Ti, showing composition and morphology of precipitates after heat treatment. ....	93
Fig 3. 12 TEM micrograph of LowTi heat-treated maraging steel showing (a) TEM-Bright field of LowTi sample. (b) Corresponding SAAD pattern where the superlattice spots represent needle-shaped precipitates ( $\text{Ni}_3\text{Ti}$ ), (c) Dark field from reflection A (d) Dark filed from reflection B. ...	95

Fig 3. 13 TEM micrograph of HighTi heat-treated maraging steel showing (a) TEM-Bright field of HighTi sample. (b) Corresponding SAAD pattern where the superlattice spots represent spherical precipitates ( $\text{Ni}_3\text{Mo}$ ). (c), (d), (e) Dark filed from reflections A, B, C respectively. ....	96
Fig 3. 14 STEM image along with EDS mapping. a) LowTi, b) HighTi samples showing the difference in precipitate volume fraction. ....	97
Fig 3. 15 XRD pole figures of as-built samples before and after uniaxial tensile test. (a) LowTi-as-built - undeformed, b) HighTi- as-built - undeformed, c) LowTi- as-built - deformed, d) HighTi- as-built - deformed. ....	99
Fig 3. 16 XRD pole figures of heat-treated samples before and after uniaxial tensile test. (a) LowTi- heat treat- undeformed, b) HighTi- heat treat- undeformed, c) LowTi- heat treat- deformed, d) HighTi- heat treat- deformed. ....	99
Fig 3. 17 EBSD results of the side of the samples at $\times 300$ magnification. Recrystallization maps of the HighTi and LowTi samples in as-built and heat-treat conditions. (a) LowTi-as built, b) HighTi- as built, c) LowTi heat treat, d) HighTi-heat treat. (Red represent deformed grains, Blue represent recrystallized grains, and Yellow represent sub structured grains). ....	102
Fig 3. 18 EBSD results of the side of the samples at $\times 300$ magnification. KAM graphs for as-built and heat-treat samples. ....	103
Fig 4. 1 Schematic of an LPBF-Maraging steel rod fabricated in the horizontal direction. The schematic of samples cut for dynamic impact loading is illustrated. ....	128
Fig 4. 2 Schematic of a split-Hopkinson Pressure Bar (SHPB) apparatus. ....	131
Fig 4. 3 Pictures of deformed samples after dynamic compressive loading. a) as-built maraging steel samples. b) heat-treated maraging steel samples. ....	131
Fig 4. 4 Strain rate-strain curves of LPBF-maraging steel samples at different firing pressure bars, showing the strain rate variation during high strain rate compression loadings. ....	133
Fig 4. 5 True stress vs. true strain curves of LPBF-maraging steel dynamically compressed at the strain rates of $1500 \text{ s}^{-1}$ , $2000 \text{ s}^{-1}$ , $3200 \text{ s}^{-1}$ , $3500 \text{ s}^{-1}$ , and $4000 \text{ s}^{-1}$ . The specimens' flow curves deformed at the strain rate of $1500 \text{ s}^{-1}$ in the inset ensure repeatability. ....	137
Fig 4. 6 Strain hardening rate vs. strain curves of LPBF-maraging steel dynamically compressed at the strain rates of $1500 \text{ s}^{-1}$ , $2000 \text{ s}^{-1}$ , $3200 \text{ s}^{-1}$ , $3500 \text{ s}^{-1}$ , and $4000 \text{ s}^{-1}$ . ....	139
Fig 4. 7 Microstructures of the a) as-built sample, deformed specimens at strain rates of b) $1500 \text{ s}^{-1}$ , c) $2000 \text{ s}^{-1}$ , and d) $3200 \text{ s}^{-1}$ . (BD and LD represent building direction and loading direction, respectively). ....	142
Fig 4. 8 SEM fractography of the fracture surfaces of specimens deformed at the strain rates of a, b, c) $3500 \text{ s}^{-1}$ and d, e, f) $4000 \text{ s}^{-1}$ . ....	143

Fig 4. 9 EBSD pole figure and ODF maps of as-built and impacted maraging steel samples. (BD represents building direction and LD represents loading direction). .....	145
Fig 4. 10 EBSD analysis of impacted maraging steel sample at a strain rate of 3200 s <sup>-1</sup> a) band contrast map, b) IPF-Y map along the loading direction, c) grain boundary map, d) KAM map. ....	148
Fig 4. 11 Strain rate-strain curves of heat-treated LPBF-maraging steel samples at different firing pressure bars, showing the strain rate variation during high strain rate compression loadings. ...	149
Fig 4. 12 True stress vs. true strain curves of heat-treated LPBF-maraging steel dynamically compressed at the strain rates of 150 s <sup>-1</sup> , 400 s <sup>-1</sup> , 670 s <sup>-1</sup> , 890 s <sup>-1</sup> , and 1930 s <sup>-1</sup> . The specimens' flow curves deformed at the strain rate of 150 s <sup>-1</sup> in the inset to ensure repeatability. ....	152
Fig 4. 13 Strain hardening rate vs. strain curves of LPBF-maraging steel dynamically compressed at the strain rates of 150 s <sup>-1</sup> , 400 s <sup>-1</sup> , 670 s <sup>-1</sup> , 890 s <sup>-1</sup> , and 1930 s <sup>-1</sup> . ....	153
Fig 4. 14 Microstructures of the a) initial heat-treated maraging steel, b) deformed samples in strain rate of 150 s <sup>-1</sup> , c) deformed sample in strain rate of 400 s <sup>-1</sup> , d) deformed sample in strain rate of 670 s <sup>-1</sup> . ....	156
Fig 4. 15 Microstructures of the deformed specimens at strain rates of 890 s <sup>-1</sup> . (LD represent loading direction). ....	157
Fig 4. 16 SEM fractography of the fracture surfaces of the heat-treated specimen deformed at the strain rate of 1930 s <sup>-1</sup> . ....	158
Fig 4. 17 Comparison of the Chang-Asaro modeling with the experimental data for the LPBF-maraging steel samples at the strain rates of 1500 s <sup>-1</sup> , 2000 s <sup>-1</sup> , 3200 s <sup>-1</sup> , 3500 s <sup>-1</sup> , and 4000 s <sup>-1</sup> . ....	160
Fig 4. 18 Effect of strain rate on the (a) saturation stress and (b) initial hardening rate of dynamically deformed LPBF-maraging steel based on the Chang-Asaro model. ....	161
Fig 4. 19 Comparison of the Chang-Asaro modeling with the experimental data for the LPBF-maraging steel samples at the strain rates of 150 s <sup>-1</sup> , 400 s <sup>-1</sup> , 670 s <sup>-1</sup> , 890 s <sup>-1</sup> , and 1930 s <sup>-1</sup> . ....	162
Fig 4. 20 Effect of strain rate on the (a) saturation stress and (b) initial hardening rate of dynamically deformed heat-treated LPBF-maraging steel based on the Chang-Asaro model. ...	163
Fig 5. 1 Schematic of a Split-Hopkinson Pressure Bar (SHPB) apparatus. ....	175
Fig 5. 2 (a) True strain rate- true strain curves of maraging steel samples at different firing pressure bar. (b) Dynamic true stress- true strain curves of the as-built maraging steel samples deformed at the strain rates of 2000, 2300, and 3200 s <sup>-1</sup> . The specimens' flow curves deformed at the strain rate of 2000 s <sup>-1</sup> in the inset ensure repeatability. ....	179

Fig 5. 3 (a) Strain rates employed for dynamic loading on the heat-treated maraging steel samples. (b) True stress- true strain curves for dynamically deformed heat-treated maraging steel samples at the strain rates of 650, 680, 950 s <sup>-1</sup> . The specimens' flow curves deformed at the strain rate of 680 s <sup>-1</sup> in the inset ensure repeatability. ....	182
Fig 5. 4 The Y-IPF map of as-built maraging steel samples during high strain rate test (a) undeformed and deformed in strain rates of (b) 2000, (c) 2300, (d) 3200 s <sup>-1</sup> (LD represents the loading direction and BD represents building direction). The building direction is perpendicular to the loading direction. ....	186
Fig 5. 5 The (001) and (111) pole figures of as-built maraging steel samples during high strain rate test (a) undeformed and deformed in strain rates of (b) 2000, (c) 2300, and (d) 3200 s <sup>-1</sup> ....	187
Fig 5. 6 The Y-IPF map of heat-treated maraging steel samples during high strain rate test (a) undeformed and deformed in strain rates of (b) 650, (c) 680, (d) 950 s <sup>-1</sup> (LD represents the loading direction). The building direction is perpendicular to the loading direction. ....	188
Fig 5. 7 The (001) and (111) pole figures of heat-treated maraging steel samples during high strain rate test (a) undeformed and deformed in strain rates of (b) 650, (c) 680, (d) 950 s <sup>-1</sup> . ....	189
Fig 5. 8 The $\phi_2=0^\circ$ and 45 ° sections of the ODF of as-built maraging steel samples during high strain rate test in strain rates of (a) 2000, (b) 2300, (c) 3200 s <sup>-1</sup> . ....	191
Fig 5. 9. The $\phi_2=0^\circ$ and 45 ° sections of the ODF of heat-treated maraging steel samples during high strain rate test in strain rates of (a) 650, (b) 680, (c) 950 s <sup>-1</sup> . ....	192
Fig 5. 10 The (112) pole figure of as-built maraging steel samples during high strain rate test in strains of (a) 2300, (b) 3200 s <sup>-1</sup> . ....	195
Fig 5. 11 Microstructures of the a) as-built initial sample, b) deformed sample at the strain rate of 3200 s <sup>-1</sup> . ....	196
Fig 5. 12 The KAM distribution of as-built and heat treated maraging steel samples during high strain rate test in strain rates of (a) 2000, (b) 2300, (c) 3200 s <sup>-1</sup> for as-built samples (d) 650, (e) 680, (f) 950 s <sup>-1</sup> for heat treated samples. ....	200
Fig 5. 13 Grain size distribution, misorientation angle distribution of as-built maraging steel samples during high strain rate test in strain rates of (a) 2000, (b) 2300, (c) 3200 s <sup>-1</sup> . ....	202
Fig 6. 1 Schematic of specimen geometry used for Split Hopkinson pressure bar (SHPB) apparatus. ....	214
Fig 6. 2 Schematic of Split-Hopkinson pressure bar (SHPB) apparatus. ....	216
Fig 6. 3 True strain rate-strain curves of vertical heat-treated maraging steel samples in different firing pressure bars (KPa). ....	218

Fig 6. 4 Dynamic true stress-strain curves of vertical heat-treated maraging steel samples deformed at strain rates of 190 to 1300 s <sup>-1</sup> . The specimens' flow curves deformed at the strain rate of 1100 s <sup>-1</sup> in the inset show repeatability.....	220
Fig 6. 5 Strain hardening rate vs. strain curves of vertical heat-treated maraging steel dynamically compressed at the strain rates of 190 s <sup>-1</sup> , 460 s <sup>-1</sup> , 810 s <sup>-1</sup> , 1100 s <sup>-1</sup> , and 1300 s <sup>-1</sup> . ....	222
Fig 6. 6 True strain rate-strain curves of horizontal heat-treated maraging steel samples in different firing pressure bars (KPa). ....	223
Fig 6. 7 Dynamic true stress-strain curves of horizontal heat-treated maraging steel samples at strain rates of 120 to 2200 s <sup>-1</sup> . The specimens' flow curves deformed at the strain rate of 745 s <sup>-1</sup> in the inset ensure repeatability.....	226
Fig 6. 8 Strain hardening rate vs. strain curves of horizontal heat-treated maraging steel dynamically compressed at the strain rates of 120 s <sup>-1</sup> , 615 s <sup>-1</sup> , 745 s <sup>-1</sup> , 890 s <sup>-1</sup> , and 2200 s <sup>-1</sup> ....	229
Fig 6. 9 TEM bright-field images of (a) horizontally built maraging steel deformed at the strain rate of 890 s <sup>-1</sup> and (b) vertically built maraging steel deformed at the strain rate of 1100 s <sup>-1</sup> .....	231
Fig 6. 10 Microstructures of the vertical heat-treated specimens at strain rates of a) 190 of b) 460, c) 810, and d) 1100 s <sup>-1</sup> .....	234
Fig 6. 11 Microstructures of the horizontal heat-treated specimens at strain rates a) 120, b) 615, c) 745, and d) 890 s <sup>-1</sup> .....	235
Fig 6. 12 SEM fractography of the fracture surfaces of vertical heat-treated specimen deformed at the strain rates of 1300 s <sup>-1</sup> . ....	236
Fig 6. 13 SEM fractography of the fracture surfaces of horizontal heat-treated specimen deformed at the strain rates of 2200 s <sup>-1</sup> . ....	237
Fig 6. 14 IPF-Y map of vertical and horizontal samples after dynamic compressive loading at different strain rates (a) Vertical- 460 s <sup>-1</sup> , b) Vertical- 810 s <sup>-1</sup> , c) Vertical-1100 s <sup>-1</sup> , d) Horizontal- 615 s <sup>-1</sup> , e) Horizontal- 745 s <sup>-1</sup> , f) Horizontal- 890 s <sup>-1</sup> .....	240
Fig 6. 15 (001) and (111) pole figures of vertical samples after dynamic compressive loading. a) Vertical- 460 s <sup>-1</sup> , b) Vertical- 810 s <sup>-1</sup> , c) Vertical-1100 s <sup>-1</sup> .....	241
Fig 6. 16 (001) and (111) pole figures of horizontal samples after dynamic compressive loading. a) Horizontal- 615 s <sup>-1</sup> , b) Horizontal- 745 s <sup>-1</sup> , c) Horizontal- 890 s <sup>-1</sup> .....	241
Fig 6. 17 The $\phi_2=0^\circ$ and $45^\circ$ sections of the ODF maps of vertical samples after dynamic compressive loading. (a) Vertical- 460 s <sup>-1</sup> , b) Vertical- 810 s <sup>-1</sup> , c) Vertical-1100 s <sup>-1</sup> . ....	243
Fig 6. 18 The $\phi_2=0^\circ$ and $45^\circ$ sections of the ODF maps of horizontal samples after dynamic compressive loading. a) Horizontal-615 s <sup>-1</sup> , b) Horizontal- 745 s <sup>-1</sup> , c) Horizontal- 890 s <sup>-1</sup> . ....	243

Fig 6. 19 KAM values of vertical and horizontal samples after dynamic compressive loading in different strain rates (a) Vertical- 460 s <sup>-1</sup> , b) Vertical- 810 s <sup>-1</sup> , c) Vertical-1100 s <sup>-1</sup> , d) Horizontal- 615 s <sup>-1</sup> , e) Horizontal- 745 s <sup>-1</sup> , f) Horizontal- 890 s <sup>-1</sup> .....	245
Fig 6. 20 Comparison between the tested flow stress curves and the J-C model description for (a) Vertical-1100 s <sup>-1</sup> , (b) Vertical-1300 s <sup>-1</sup> , (c) Horizontal-890 s <sup>-1</sup> , (d) Horizontal-2200 s <sup>-1</sup> .....	248
Fig 6. 21 Comparison between the tested flow stress curves and the V-A model description for (a) Vertical-1100 s <sup>-1</sup> , (b) Vertical-1300 s <sup>-1</sup> , (c) Horizontal-890 s <sup>-1</sup> , (d) Horizontal-2200 s <sup>-1</sup> .....	250
Fig 7. 1 Schematic of compression samples used for SEM studies.....	264
Fig 7. 2 Strain rate-strain curves of Low-Ti- maraging steel samples deformed using different firing pressures (kPa).....	267
Fig 7. 3 Dynamic stress-strain curves of Low-Ti maraging steel samples in strain rates of 1500 to 3670 s <sup>-1</sup> .....	267
Fig 7. 4 Strain hardening rate vs. strain curves of Low-Ti maraging steel dynamically compressed at the strain rates of 1500 s <sup>-1</sup> , 1950 s <sup>-1</sup> , 2770 s <sup>-1</sup> , 3150 s <sup>-1</sup> , and 3670 s <sup>-1</sup> .....	269
Fig 7. 5 Strain rate-strain curves of High-Ti maraging steel samples deformed using different firing pressures (kPa).....	271
Fig 7. 6 Dynamic stress-strain curves of High-Ti maraging steel samples at strain rates of 1500 to 5000 s <sup>-1</sup> .....	271
Fig 7. 7 Strain hardening rate vs. strain curves of High-Ti maraging steel dynamically compressed at the strain rates of 1500 s <sup>-1</sup> , 2000 s <sup>-1</sup> , 2900 s <sup>-1</sup> , 3000 s <sup>-1</sup> , 3600 s <sup>-1</sup> , and 5000 s <sup>-1</sup> .....	273
Fig 7. 8 Microstructures of the deformed Low-Ti specimens at strain rates of (a) 1500, (b) 1950, (c) 2770, and (d) 2770 s <sup>-1</sup> .....	277
Fig 7. 9 Microstructures of the deformed High-Ti specimens at strain rates of (a) 1500 (b) 2000, (c) 2900, (d) 3000, (e) 3600, and (f) 5000 s <sup>-1</sup> .....	278
Fig 7. 10 SEM fractography of the fracture surfaces of Low-Ti samples deformed at the strain rates of 3150 s <sup>-1</sup> .....	279
Fig 7. 11 SEM fractography of the fracture surfaces of Low-Ti sample deformed at the strain rate of 3670 s <sup>-1</sup> .....	280
Fig 7. 12 Potentiodynamic polarization curves of Low-Ti and High-Ti, Low-Ti-1950 and High-Ti-2000, and Low-Ti-2770 and High-Ti 2900 specimens in 3.5 wt.% NaCl solution at room temperature.....	283
Fig 7. 13 EIS spectrum of the LPBF maraging steel samples before and after deformation. (a)-(g) plots before deformation, (b)-(h) Nyquist and bode plots of Low-Ti-1990 and High-Ti-2000, and	

(c)-(m) EIS plots of Low-Ti-2770 and High-Ti-3000. (a)-(c): Nyquist diagrams, (d-f): Bode, and (g)-(m): Bode phase plots. ....	285
Fig 7. 14 Equivalent circuits used to fit the experimental impedance data obtained from (a) all samples except High-Ti-2000 sample and (b) High-Ti-2000 sample. ....	287
Fig 7. 15 SEM images showing the surface morphologies of Low-Ti-2770 sample after polarization test in 3.5% NaCl solution. ....	293
Fig 7. 16 SEM images of the surface degradation of High-Ti-2900 sample after polarization test in 3.5% NaCl solution. ....	293
Fig 8. 1 Schematic of the torsional SHTB apparatus. ....	307
Fig 8. 2 The geometry of specimens in in the SHTB test. ....	308
Fig 8. 3 Schematic and real samples used for microstructural studies. ....	310
Fig 8. 4 True strain- strain rate curves of M.S samples at different angles of twist. ....	312
Fig 8. 5 Dynamic true shear strain-true shear stress curves of the M.S samples deformed at the angles of twist 3, 6, 9 and 12. The specimens' flow curves deformed at angle of twist 3 in the inset ensure repeatability. ....	316
Fig 8. 6 Microstructures of of the a) and b) M.S in as-built condition, c) and d) deformed M.S at strain rates of $260 \text{ s}^{-1}$ . ....	319
Fig 8. 7 Microstructures of the deformed M.S samples at strain rates of a) and b) $650 \text{ s}^{-1}$ , c) and d) $720 \text{ s}^{-1}$ . ....	321
Fig 8. 8 Fractography of the deformed M.S samples at angle of twist of 12 and strain rates of $650 \text{ s}^{-1}$ . ....	323
Fig 8. 9 IPF-Z maps of LBPF-M.S samples after torsion test at the angle of twist of (a) 3, (b) 6 and (c) 9 degrees and strain rate of a) 260, b) 650 and c) $720 \text{ s}^{-1}$ , respectively. ....	325
Fig 8. 10 (001), (110) and (111) pole figure of LBPF-M.S samples after torsion test at strain rate of a) 260, b) 650 and c) $720 \text{ s}^{-1}$ . ....	326
Fig 8. 11 The $\phi_2=0^\circ$ and $45^\circ$ sections of the ODF maps of LBPF-M.S samples after torsion test at strain rate of a) 260, b) 650 and c) $720 \text{ s}^{-1}$ . ....	328
Fig 8. 12 KAM maps of LBPF-M.S samples after torsion test at strain rate of a) 260, b) 650 and c) $720 \text{ s}^{-1}$ . ....	330
Fig 8. 13 Comparison between the tested flow stress curves and the Kobayashi-Odd model description for (a) 3degree- $260 \text{ s}^{-1}$ , (b) 6 degree- $650 \text{ s}^{-1}$ , (c) 9 degree- $720 \text{ s}^{-1}$ , (d) 12 degree- $650 \text{ s}^{-1}$ . ....	332

Fig 8. 14 Comparison between the tested flow stress curves and the Nemat-Nasser model description for (a) 3degree-260 s <sup>-1</sup> , (b) 6 degree-650 s <sup>-1</sup> , (c) 9 degree-720 s <sup>-1</sup> , (d) 12 degree-650 s <sup>-1</sup> .....	335
Fig 8. 15 Threshold stress of Peierls stress and work hardening coefficient as function of angle of twist.....	336

## Nomenclature

AM: Additive Manufacturing
LPBF: Laser powder bed fusion
CAD: Computer-aided design
EBM: Electron beam melting
DED: Directed energy deposition
WAAM: Wire Arc Additive Manufacturing (WAAM)
SCC : Stress corrosion cracking
$\gamma$ : Austenite phase
SEM: Scanning Electron Microscope
XRD: X-ray Diffraction
EBSD: Electron Backscattered Diffraction
TEM: Transmission Electron Microscope
$\alpha'$ : Martensite phase
$k_0$ : Equilibrium partition coefficient
$\Delta T_C$ : Constitutional undercooling
SAAD : Selected area diffraction
ODF : Orientation distribution function
IPF : Inverse Pole Figure
EDS : Energy-dispersive X-ray spectroscopy

SHPB: Split Hopkinson Pressure Bar

ASBs: Adiabatic Shear Bands

DRV: Dynamic Recovery

DRX: Dynamic Recrystallization

KAM : Kernel average misorientation

CPE : Constant phase element

SHTB : Split Hopkinson torsion bar

## Chapter 1: Introduction

Additive manufacturing (AM), also known as 3D printing, is a fast-developing technology that enables the creation of lighter yet stronger parts. One of the key advantages of 3D printing is the ability to produce very complex shapes or geometries with reduced cost and time. Laser powder bed fusion (LPBF) is one of the additive manufacturing (AM) procedures to fabricate three-dimensional objects directly from a metal powder feedstock using a computer-aided design (CAD) model. Due to high heating and cooling rates inherent in LPBF (up to  $10^8$  °C/s), a very fine cellular structure is produced, which results in improving the mechanical behavior of the LPBF-parts compared to conventional counterparts [1]. The LPBF process can be used to fabricate different alloys such as aluminum, titanium, maraging steels, and stainless steels [2][3][4].

Maraging steel is a class of low carbon iron-nickel alloys with high strength and toughness, which is primarily alloyed with Ni, as well as Co, Mo, Ti, and Al. Maraging steel parts can be produced using the LPBF process and can be used as a suitable candidate for demanding applications such as aerospace, military, nuclear, tooling, and transportation [5][6]. C300 is a traditional maraging steel grade with 18 wt.% Ni, along with 8.5-9.5 wt.% Co, 4.6-5.2 wt.% Mo and smaller amounts of Ti and Al. The LPBF of C300 steels has received much interest because it offers a reasonable deposition rate and a broad process window to develop ultrafine microstructures leading to enhanced mechanical properties.

Marginal changes in the chemical composition in alloys, such as the maraging steel family, can often significantly change the mechanical properties. Among the investigations carried out on the role of alloying elements on the microstructural and strengthening mechanisms of maraging steels, the majority were focused on the trace of Ni, Mn, and Ti

after aging heat treatments [7–13]. Besides, in many maraging steel structural applications, maraging steel parts experienced elevated and high strain-rate impact loadings. For instance, in tool and dies (automotive) and landing gears (aerospace), maraging steel parts are subjected to high strain-rate compressive and torsion loadings, and their response is important for designers and engineers. Furthermore, incidents like car accidents, bird strikes, and airplane collisions are examples of dynamic events in our life that needs to be investigated.

### **1.1 Maraging steels**

Among the ultra-high strength steels, the maraging class is a special alloying system in which the low carbon content (good weldability) makes this material a preferred candidate for LPBF process [1,2]. Over the last decades, the ultra-high-strength 18Ni grades of maraging steels are widely credited for their good sintering properties, low porosity levels, and low vulnerability to hot cracking allowing the industries to implement them in their supply chain [13,15–17]. In this category, the C300 maraging steels in which 300 is referred to its ultimate tensile strength (in ksi) is broadly used in tooling applications and aerospace industry, where its toughness and strength make it a good candidate for various parts of landing gears as well as punching and forming dies [18–21]. During the LPBF process, due to repeated heating and cooling cycles, stress is accumulated, which is a concerning issue. To relieve high residual stresses within LPBF products, subsequent heat treatments are usually needed. The maraging steels gain their ultra-high strength through the precipitation of phases within post-processing heat treatment, e.g.,  $\text{Ni}_3\text{Ti}$ ,  $\text{Ni}_3\text{Mo}$ ,  $\text{Fe}_2\text{Mo}$  [14,22,23]. Besides, the presence of alloying elements such as Ni, Co, Mo, Ti, and Al promotes the formation of martensite by air-cooling and the formation of fine particles

of intermetallic compounds [24]. The presence of high Ni content, on the other hand, broaden the  $\gamma$  single-phase region to room temperature and, consequently, facilitates martensitic transformation [25,26]. According to the American Society for Metals (ASM) handbook, to have the optimum mechanical properties, it is recommended to conduct an age-hardening heat treatment for 3 to 8 hours at a temperature between 460 °C and 510 °C [27]. The LPBF of maraging steel introduces a promising opportunity to build parts with superior mechanical properties compared to conventionally built maraging steels [13]. Due to high cooling rates present during the LPBF process, martensitic matrix rapidly quenched from the austenite region and LPBF-maraging steel parts have high strength compared to conventional parts [13].

## **1.2 Literature review**

### **1.2.1 Additive manufacturing**

Additive manufacturing has recently attracted attention as a cost-effective method for the fabrication of metals and alloys due to the reduction of production time and waste material and consolidation of assemblies into single parts. Metal additive manufacturing techniques are a form of near-net-shape manufacturing to fabricate three-dimensional objects directly from a powder or wire feedstock using a CAD model. Additive Manufacturing evolution goes back almost 150 years [28]. Research efforts provided the first modern AM process, known as Stereolithography in the late 1960s. Stereolithography (SL) is an additive technique, which an ultraviolet (UV) laser has been employed to selectively polymerize a vat of photopolymer resin [29]. As stereolithography was expensive and time consuming, in order to respond to the need of industrial requirements, more efficient technologies have emerged [29]. The 2000s were a period of growth for

AM, and new processes such as electron beam melting (EBM) were introduced [28]. Nowadays, with the improvement in computing power, additive technologies have become a promising method for manufacturers looking to save significant time and money on the production of parts.

### **1.2.2 Different additive manufacturing techniques**

AM technologies are generally categorized into seven groups. 1) Binder jetting, 2) Directed energy deposition (DED), 3) Material extrusion, 4) Material jetting, 5) Sheet lamination, 6) Vat polymerization, and 7) Powder bed fusion. Between these techniques, powder bed fusion and direct energy deposition are the two most promising fabrication processes that offer high flexibility in geometric design [29].

### **1.2.3. Powder bed fusion**

Powder bed fusion (PBF) is an additive manufacturing technique in which an energy source is exposed to the surface of a powder bed to bind material. A schematic of the PBF process is shown in Fig. 1.1. Among all AM processes, powder bed fusion is popular for manufacturers because of the wide range of materials that can potentially be processed. In the PBF process, the energy source, e.g., laser or electron beam, selectively melts and fuses powder particles to create a solid structure. PBF processes are used in aerospace and biomedical applications due to their ability to produce customized and complex geometries with excellent material properties compared with traditional metal manufacturing techniques [30]. Depending on the type of power source (laser or electron beam), PBF can be divided into two major techniques: laser powder bed fusion (LPBF) and electron beam melting (EBM) [30].

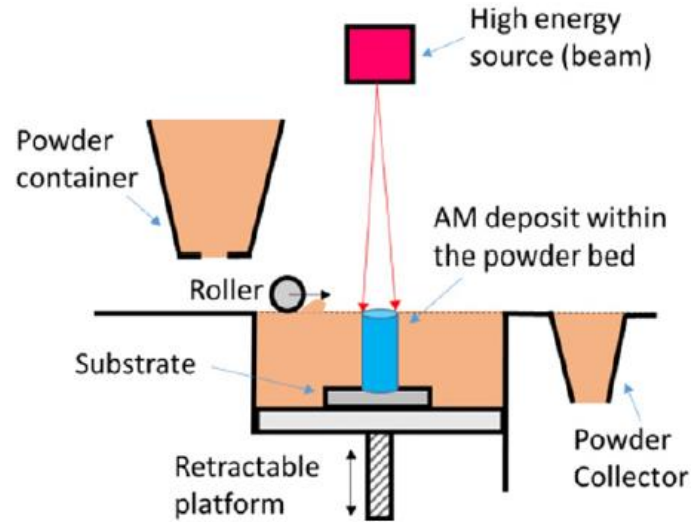


Fig 1. 1 Generic illustration of BPF system [30].

#### 1.2.4. Laser powder bed fusion technique

The laser powder bed fusion technique is one of the powder bed fusion techniques in which the successive layers of metal powders are melted on top of each other by a high-power laser beam with the use of the CAD model. In the LPBF process, a substrate is placed inside a chamber, and due to the high reactivity of materials in high temperatures, an inert gas (either argon or nitrogen at oxygen levels below 500 parts per million) is purged to prevent the formation of various impurities, such as oxides and nitrides. This process is accompanied by a high-power laser beam, usually an ytterbium fiber laser with hundreds of watts. Laser power, scanning speed, scan line spacing (hatch distance), thickness of powder layer, scanning strategy, working atmosphere, and temperature of powder bed are process parameters of LPBF, which directly affect the microstructure, density, mechanical behavior, strength, and surface quality of the final product and need to be optimized, for each material, to achieve a successful fabrication [31][32]. The primary goal in additive

manufacturing is always to achieve a high-density part and, in most cases, laser power and scanning speed are the most influential parameters on density. Studies have shown that higher laser power, higher layer thickness, lower scan speed, and lower hatch spacing results in better strength [33]. Measuring energy density is one of the best predictors for parts relative density. As for maraging steel, when the energy density is over 180 J/mm<sup>2</sup>, the part density almost reaches 100% [34]. The low energy led to insufficient melting, while too high energy resulted in shrinkage and burnt surface.

### **1.2.5 LPBF-maraging steel**

#### **1.2.5.1 Microstructure of maraging steel**

Microstructure of maraging steel parts consists of equiaxed, cellular, and columnar grains. During the solidification process, grains tend to grow along the maximum heat flow, which results in different grain morphologies with respect to thermal gradient and cooling rate. Columnar grains tend to form at the bottom of a meltpool due to high thermal gradient and fine equiaxed grains are mainly appearing at the top of the meltpool due to high cooling rates. The cellular structure was predicted to form at the meltpools' core [13]. Fractography of as-built and aged maraging steel samples were conducted by Kucerova *et al.* [9]. They found that failure in as-built samples is governed by ductile dimples, while in aged condition, brittle fracture happened for maraging steels. Crystal structure of maraging steel consists of martensite phase with body-centered tetragonal (BCT) structure and austenite phase with face-centered cube (FCC) structure. Austenite is the softer part, which accommodates most of the deformation [35].

#### **1.2.5.2. Process parameters**

There have been many studies conducted to assess the effect of process parameters on the properties of the additively manufactured maraging steels. For instance, Bai *et al.* [5,6] analyzed the relative density of LPBF-maraging steel alloys by changing processing parameters, i.e. laser power, scanning speed, and hatch distance. They found that there is a reciprocal effect between these parameters and the density, where their increase firstly improves the relative density and then drops it due to keyhole formation and balling effects [36]. Furthermore, Kempen *et al.* [37] investigated the influence of laser scan speed and powder layer thickness in combination with various age-hardening treatments. Bhardwaj and Shukla [38,39] also evaluated the influence of the building direction on the physical and mechanical behavior of AM maraging steels. They concluded that the vertically printed samples showed lower residual stresses than horizontally printed ones. They also investigated the effect of laser scan strategy on mechanical properties of maraging steels, where scan strategy showed to have a significant influence on texture and grain growth. Mooney *et al.* [17] studied the mechanical properties, anisotropic behavior, and fracture of two maraging steel parts additively manufactured using two types of feedstock powders with slightly different chemical compositions. They have developed a modeling framework suitable to study the elastic and plastic anisotropic behaviors of these alloys. Tan *et al.* [40] also evaluated the effect of building direction on the mechanical properties of maraging steels. They found out that in the direction perpendicular to the building direction maximum temperature gradient exists and grains tend to grow in this direction.

### **1.2.5.3. Heat treatment**

Aging treatments can modify microstructure through phase transformation and the introduction of different precipitations. The mechanical strength of maraging steels

increases with aging treatment due to the formation of precipitates. Heat treatment can reduce the ductility of maraging steels as well and is shown to transform a portion of martensite to austenite [13]. There are many studies on the effect of the heat treatment process on the mechanical behavior of LPBF-maraging steels. Tan *et al.* [13] reported that the integrated solution-aging treatment was a more preferable heat treatment recipe than only aging for LPBF-maraging steel 300. Conde *et al.* [41] studied the effect of different heat treatment schedules on LPBF-maraging steel 300. Their results showed that the promotion of martensite-to-austenite reversion is beneficial to enhance the ductility and toughness of maraging steel parts. Mooney *et al.* [42] investigated different heat treatment procedures on LPBF-maraging steel 300 to identify the optimum combinations of time and temperature, which can reduce anisotropy. They reported, aging at 490 °C for 8 hours is offered an optimal strength (yield strength >1900 MPa) whereas aging at 525 °C for 8 hours provides a trade-off between yield strength and ductility (yield strength >1700 MPa and at  $\approx$  10% strain). Mutua *et al.* [43] investigated the effect of post-heat treatment on microstructure and mechanical properties of maraging steel 300. They found that after solution treatment and aging, the maximum tensile strength obtained was 2033 MPa.

#### **1.2.6. Chemical composition of maraging steel**

Maraging steel is a class of low-carbon steels in which Ni, Mo, and Co are primary elements. Each alloying element has its effect on materials behavior and change in alloy content can significantly change the mechanical behavior of the final part. Ni is the most important element, which helps in the formation of precipitates and is the austenite stabilizing element and controls the austenite reversion process during heat treatment. The effect of chemical composition on the mechanical behavior of maraging steels produced

using conventional manufacturing methods was investigated in detail before [22]. Galindo-Nava *et al.* [14] elucidated that the reverted  $\gamma$  kinetics promoted by Ti addition has the highest hardening effect via Ni<sub>3</sub>Ti precipitation in the matrix. Schober *et al.* [11] reported an accelerated coarsening of precipitates, and consequently, a fast drop in the hardness of Ti-bearing maraging steels due to a broad variety of phases during ageing. Carvalho *et al.* [44] showed that Co and Ti contents strongly influence lattice diffusion in maraging steels 300 and 350. Ahmed *et al.* [26] confirmed that Ni and Mo act as strong austenite stabilizers, where Sha *et al.* [45] also reported this effect and explained a similar strengthening role for Ti as other researchers.

#### **1.2.7. Dynamic behavior of maraging steel**

In-service impact loading situations can expose maraging steel parts to dynamic loading. Therefore, it is crucial to investigate the deformation behavior of this alloy under these complex loading conditions. Few researchers have studied the effect of compression loading on the mechanical properties of maraging steels fabricated by conventional methods. Song *et al.* [46] employed a Kolsky compression bar test to investigate the compressive response of C250 maraging steel alloy at two strain rates. Their observations revealed that the dynamic strength increased with an increase in strain rate. Schnitzer *et al.* [47] studied the effect of high strain rate compression loadings on aged maraging steels. They observed that with increasing strain, strain rate sensitivity decreased, which is related to the pinning of dislocations by precipitates.

#### **1.2.8. Corrosion behavior of maraging steel**

Relatively few researchers reported on corrosion behavior of LPBF fabricated maraging steel parts. In the application of maraging steel in pressure vessels, gas turbines, aircraft, these components are exposed to corrosive environments in the presence of external loading. Due to a variety of applications, the corrosion resistance properties of maraging steel have received a considerable amount of attention. Bouzakis *et al.* [48] conducted research regarding corrosion fatigue of additively manufactured maraging steel. They observed that additively manufactured parts show lower corrosion fatigue performance due to cellular-dendritic structure and multiple melt pools. Avelino *et al.* [49] investigated the corrosion behavior of maraging steels in NaCl solution and they found out that the austenite phase formed during heat treatment is detrimental to corrosion properties and it is better to conduct solution treatment to remove the austenite phase. Florez *et al.* [50] achieved the same results in HF medium for maraging steel. Their results showed that solution annealed maraging steels have more noble behavior. In addition, they found out that a higher amount of cobalt and titanium in grade 350 maraging steel leads to inferior corrosion resistance due to rendering a higher driving force for microgalvanic corrosion due to precipitates. In some applications, load from operation along with corrosive environments provide the opportunity for stress corrosion cracking (SCC). Zhao *et al.* [51] investigated the SCC behavior of maraging steels and they found out that SCC behavior of maraging steels under the effect of hydrogen is related to precipitates, dislocations, austenite grains.

### **1.3. Gap of knowledge**

Since maraging steel components fabricated by the LPBF process have only recently been introduced to industrial applications, there is little information regarding the effect of

dynamic loading on the mechanical behavior of LPBF-maraging steel. Maraging steel parts are used in applications where they are subjected to dynamic loading such as compression and torsion. Multiple studies on mechanical properties and microstructure of additively manufactured 18 Ni-300 maraging steels were conducted as discussed in previous sections. However, most of these studies focused on the quasi-static behavior of LPBF-maraging steels and there are not any studies on the dynamic behavior of LPBF-maraging steels.

Despite the available investigations on maraging steels, there is a knowledge gap on the effect of chemical composition (Ti content) on mechanical behavior and microstructure of LPBF-maraging steels. Therefore, a comprehensive study on the effect of chemical composition would help the industry to benefit from the results. Besides, comprehensive knowledge about maraging steel behavior in the presence of dynamic loading would be beneficial for designing parts.

In this thesis, the maraging steel powders containing two different contents of Ti element were fused and printed using the LPBF process. In the first paper in chapter two, the effect of Ti on microstructure and mechanical properties of as-built parts were investigated. The second paper's subject in chapter three is a comprehensive study about the effect of Ti on heat-treated LPBF-maraging steels. Due to the necessity to investigate the dynamic behavior of LPBF-maraging steels in industry, the third paper is about the effect of high strain rate compressive loading on microstructure and mechanical behavior of as-built and heat-treated maraging steels. Material response to high-speed deformation processes depends on many factors such as microstructure, texture, grain size, etc. In additive manufactured samples, a hierarchical microstructure is predictable involving cells, grains, and melt pools. The hierarchical structures in stainless steel and AlSi10Mg parts

produced by additive manufacturing have been shown by Wang [52] and Hadadzadeh [53], respectively. As a result of these studies, it is generally accepted that grain size, orientation, and morphology can affect the mechanical behavior of the final product. It is also believed that superior mechanical properties of additively manufactured parts are related to their hierarchical structure [54]. Thus, the effect of a hierarchical microstructure on the dynamic loading behavior of the material and the correlation between the mechanical behavior of the alloy and microstructural changes need to be investigated. Thus, paper four aimed to study the texture evolution during high strain rate compressive loading of as-built and heat-treated LPBF-maraging steel samples. As discussed, building direction is an important parameter that affects the mechanical behavior of the additively manufactured parts. In the fifth paper, the effect of building direction on the dynamic compressive behavior of LPBF-maraging steels were investigated. Furthermore, as maraging steel samples are subjected to both loading and corrosive environments in some industrial application, corrosion behavior of LPBF-maraging steel was investigated in 3.5% wt. NaCl solution. The effect of prior deformation and strain rate on corrosion behavior of LPBF-maraging steel have been evaluated in detail in the sixth paper. It should be noted that in practice, maraging steel parts tend to be applied in complex loading environments, which involve a torsional mode of deformation. Almost no work has been reported on the dynamic torsion on maraging steel. In the last paper, dynamic torsion behavior of LPBF-maraging steel parts was investigated using Split Hopkinson torsion bar apparatus. Based on the results of studies on the effect of Ti element on quasi-static and dynamic compression behavior of LPBF-maraging steels, a dynamic torsion test was conducted on Ti-rich maraging steel samples. Developing new LPBF fabricated C300 components from powders with a higher

concentration of Ti and the same price, which has better mechanical properties, can be the main contribution of this thesis.

#### **1.4. Contributions**

Different chapters of this thesis were written in collaboration with different team members. For clarification, the contribution of the author of this thesis is specified in each paper separately.

Paper one in chapter two was written in collaboration with Mohammadhossein Ghonche, Dr. Amir Hadadzadeh, Dr. Mehdi Sanjari, Dr. Babak Shalchi Amirkhiz, and Dr. Mohsen Mohammadi. The first author (author of this thesis) conducted all the experimental tests except the TEM and XRD studies. Moreover, the author of this thesis interpreted and wrote the manuscript of the paper. The co-authors helped with the interpretation of the data.

The second paper was written in collaboration with Dr. Mehdi Sanjari, Mohammadhossein Ghonche, Dr. Babak Shalchi Amirkhiz, and Dr. Mohsen Mohammadi. The first author (author of this thesis) conducted all the experimental tests except the TEM and XRD studies. The author of the thesis interpreted and wrote the manuscript of the paper, and the co-authors helped with the interpretation of the data.

The third paper in chapter four was written in collaboration with Reza Alaghmandfard, Joey Tallon, Dr. Akindele Odeshi, and Dr. Mohsen Mohammadi. The first author (author of this thesis) conducted all the experimental tests where the Split Hopkinson test was conducted with the help of Dr. Akindele Odeshi and the numerical modeling was done with

the help of Reza Alaghmandfard. The first author interpreted and wrote the manuscript of the paper. The co-authors helped with the interpretation of the data.

The fourth paper was written in collaboration with Dr. Hadi Pirgazi, Dr. Mehdi Sanjari, Reza Alaghmandfard, Joey Tallon, Dr. Akindele Odeshi, Dr. Leo Kestens, and Dr. Mohsen Mohammadi. The first author (author of this thesis) conducted all the experimental tests where the Split Hopkinson test was conducted with the help of Dr. Akindele Odeshi and EBSD analysis were done with the help of Dr. Hadi Pirgazi and Dr. Leo Kestens.

The fifth paper was written in collaboration with Dr. Hadi Pirgazi, Dr. Mehdi Sanjari, Payam Seraj, Dr. Akindele Odeshi, Dr. Leo Kestens, and Dr. Mohsen Mohammadi. The first author (author of this thesis) conducted all the experimental tests, where the Split Hopkinson test was conducted with the help of Dr. Akindele Odeshi and EBSD analysis were done with the help of Dr. Hadi Pirgazi and Dr. Leo Kestens. Furthermore, TEM analysis was conducted by Dr. Vitaliy Bliznuk. Besides, numerical modeling was done with the help of Payam Seraj.

The sixth paper was written in collaboration with Ayda Shahriari, Dr. Akindele Odeshi, and Dr. Mohsen Mohammadi. The first author (author of this thesis) conducted all the experimental tests where the Split Hopkinson test was conducted with the help of Dr. Akindele Odeshi and electrochemical tests were done with the help of Ayda Shahriari.

The seventh paper was written in collaboration with Dr. Hadi Pirgazi, Dr. Mehdi Sanjari, Payam Seraj, Dr. Akindele Odeshi, Dr. Leo Kestens, and Dr. Mohsen Mohammadi. The first author (author of this thesis) conducted all the experimental tests where the Split Hopkinson test was conducted with the help of Dr. Akindele Odeshi and

EBSD analysis were done with the help of Dr. Hadi Pirgazi and Dr. Leo Kestens. Besides, numerical modeling was done with the help of Payam Seraj.

### **1.5. Study outline**

A comprehensive study on the high strain rate compression and torsion of additively manufactured 18 Ni-300 maraging steel (MS1) was performed in this research. A study on the effect of chemical composition (Ti content) on the mechanical properties in quasi-static and dynamic conditions is presented in this research as well. The effects of the high strain rate compressive loading on the mechanical behavior of as-built and heat treated maraging steels were evaluated and the effect of the building direction on quasi-static and also dynamic behavior was investigated in this work. Besides, the electrochemical behavior of LPBF-maraging steels was studied and the effect of simultaneous corrosion and dynamic test was inspected.

Initially, two gas atomized maraging steel powders with different Ti content (0.72 and 1.17 wt.%) were used to additively manufacture maraging steel samples via laser powder bed fusion (LPBF) technique. The effect of Ti addition on microstructural and mechanical properties of the additively manufactured (AM) maraging steel was investigated. Then the effect of heat treatment on Ti addition was evaluated through different microstructural analyses. At the first step to characterize the dynamic behavior of additively manufactured maraging steels, a high strain rate compression test was conducted on as-built and heat-treated maraging steel samples. Furthermore, the effect of building direction on the dynamic compressive behavior of LPBF-maraging steels was studied. Besides, corrosion tests were conducted on LPBF-maraging steels in 3.5 wt.% NaCl to analyze the electrochemical behavior of maraging steel parts. The effect of prior deformation (high

strain rate compression test) on corrosion behavior of maraging steels was evaluated. In the end, the high strain rate torsion behavior of LPBF-maraging steels was studied.

This thesis is presented in a paper-based format in 10 chapters. Chapter 1 contains an introduction to additive manufacturing as well as the maraging steel family of alloys. Chapter 2 presents a study on the effect of Ti addition on the mechanical properties and microstructure of as-built maraging steels. Chapter 3 is a study on the effect of Ti addition on microstructure and mechanical properties of heat-treated maraging steels. In chapter 4, a study is presented on the high strain rate compression behavior of as-built and heat-treated LPBF-maraging steels. Chapter 5 discusses the effect of texture evolution on the high strain rate compressive behavior of as-built and heat-treated maraging steels. Chapter 6 shows the effect of building direction on dynamic compressive behavior of heat-treated maraging steels. Chapter 7 presents a study on corrosion behavior of maraging steels and chapter 8 is about dynamic torsion behavior of LPBF-maraging steels. Finally, in chapter 9, this study is summarized and in chapter 10, conclusions and future works are presented.

## **1.6. Hypothesis**

The result of this research might be used as a guide for mechanical engineers efficiently design procedures for using AM techniques. Production of new maraging steels with improved mechanical properties at the same price can be a significant step for AM engineers. To examine this hypothesis, a series of sub-studies were defined to address the original question of whether a change of chemical composition (Ti content) is beneficial or not. A series of experiments were designed to investigate the effect of Ti addition on the quasi-static and dynamic behavior of additively manufactured maraging steels. Based on the available information, it was assumed that the most important loading mode for

maraging steels is torsion mode. In this study, a new maraging steel alloy with superior mechanical behavior under dynamic loading was introduced. To achieve this goal, the effect of Ti on quasi-static and high strain rate compression behavior of as-built and heat-treated maraging steels was studied, and at the final step, Ti-rich maraging steels were used for high strain rate torsion test.

### 1.7. References

- [1] G. Casalino, S.L. Campanelli, N. Contuzzi, A.D. Ludovico, Experimental investigation and statistical optimisation of the selective laser melting process of a maraging steel, *Opt. Laser Technol.* 65 (2015) 151–158. <https://doi.org/10.1016/j.optlastec.2014.07.021>.
- [2] A. Hadadzadeh, B.S. Amirkhiz, A. Odeshi, M. Mohammadi, Dynamic loading of direct metal laser sintered AlSi10Mg alloy: Strengthening behavior in different building directions, *Mater. Des.* 159 (2018) 201–211. <https://doi.org/10.1016/j.matdes.2018.08.045>.
- [3] A. Hadadzadeh, A. Shahriari, B.S. Amirkhiz, J. Li, M. Mohammadi, Additive manufacturing of an Fe–Cr–Ni–Al maraging stainless steel: Microstructure evolution, heat treatment, and strengthening mechanisms, *Mater. Sci. Eng. A.* (2020) 139470.
- [4] C. Dharmendra, R. Alaghmandfard, A. Hadadzadeh, B.S. Amirkhiz, M. Mohammadi, Influence of build orientation on small-scale properties of electron beam melted Ti-6Al-4V, *Mater. Lett.* (2019) 126970. <https://doi.org/10.1016/j.matlet.2019.126970>.

- [5] Y. Bai, D. Wang, Y. Yang, H. Wang, Effect of heat treatment on the microstructure and mechanical properties of maraging steel by selective laser melting, *Mater. Sci. Eng. A.* 760 (2019) 105–117. <https://doi.org/10.1016/j.msea.2019.05.115>.
- [6] Y. Bai, Y. Yang, D. Wang, M. Zhang, Influence mechanism of parameters process and mechanical properties evolution mechanism of maraging steel 300 by selective laser melting, *Mater. Sci. Eng. A.* 703 (2017) 116–123. <https://doi.org/10.1016/j.msea.2017.06.033>.
- [7] G.H. de O. Freitas, C.A.S. de Oliveira, Effect of Hot Deformation on Microstructure, Hardness and Precipitation Kinetics in a C350 Maraging Steel Modified by Titanium Addition, *Mater. Res.* 21 (2018) 1–9. <https://doi.org/10.1590/1980-5373-mr-2018-0120>.
- [8] E.A. Jäggle, Z. Sheng, P. Kürnsteiner, S. Ocylok, A. Weisheit, D. Raabe, Comparison of maraging steel micro- and nanostructure produced conventionally and by laser additive manufacturing, *Materials (Basel)*. 10 (2017) 2–15. <https://doi.org/10.3390/ma10010008>.
- [9] L. Kučerová, I. Zetková, A. Jandová, M. Bystrianský, Microstructural characterisation and in-situ straining of additive-manufactured X3NiCoMoTi 18-9-5 maraging steel, *Mater. Sci. Eng. A.* 750 (2019) 70–80. <https://doi.org/10.1016/j.msea.2019.02.041>.
- [10] N. Takata, R. Nishida, A. Suzuki, M. Kobashi, M. Kato, Crystallographic features of microstructure in maraging steel fabricated by selective laser melting, *Metals (Basel)*. 8 (2018) 1–10. <https://doi.org/10.3390/met8060440>.
- [11] M. Schober, R. Schnitzer, H. Leitner, Precipitation evolution in a Ti-free and Ti-

- containing stainless maraging steel, *Ultramicroscopy*. 109 (2009) 553–562.  
<https://doi.org/10.1016/j.ultramic.2008.10.016>.
- [12] W. Sha, Z. Guo, *Maraging steels: Modelling of microstructure, properties and applications*, Woodhead Publishing Limited, 2009.
- [13] C. Tan, K. Zhou, W. Ma, P. Zhang, M. Liu, T. Kuang, Microstructural evolution, nanoprecipitation behavior and mechanical properties of selective laser melted high-performance grade 300 maraging steel, *Mater. Des.* 134 (2017) 23–34.  
<https://doi.org/10.1016/j.matdes.2017.08.026>.
- [14] E.I. Galindo-Nava, W.M. Rainforth, P.E.J. Rivera-Díaz-del-Castillo, Predicting microstructure and strength of maraging steels: Elemental optimisation, *Acta Mater.* 117 (2016) 270–285. <https://doi.org/10.1016/j.actamat.2016.07.020>.
- [15] K.S. Cho, S.S. Park, D.H. Choi, H. Kwon, Influence of Ti addition on the microstructure and mechanical properties of a 5% Cr-Mo-V steel, *J. Alloys Compd.* 626 (2015) 314–322. <https://doi.org/10.1016/j.jallcom.2014.12.040>.
- [16] C. Du, R. Petrov, M.G.D. Geers, J.P.M. Hoefnagels, Lath martensite plasticity enabled by apparent sliding of substructure boundaries, *Mater. Des.* 172 (2019) 1–12. <https://doi.org/10.1016/j.matdes.2019.107646>.
- [17] B. Mooney, K.I. Kourousis, R. Raghavendra, D. Agius, Process phenomena influencing the tensile and anisotropic characteristics of additively manufactured maraging steel, *Mater. Sci. Eng. A.* 745 (2019) 115–125.  
<https://doi.org/10.1016/j.msea.2018.12.070>.
- [18] E. Cyr, H. Asgari, S. Shamsdini, M. Purdy, K. Hosseinkhani, M. Mohammadi, Fracture behaviour of additively manufactured MS1-H13 hybrid hard steels, *Mater.*

- Lett. 212 (2018) 174–177. <https://doi.org/10.1016/j.matlet.2017.10.097>.
- [19] H. Azizi, R. Ghiaasiaan, R. Prager, M.H. Ghoncheh, K.A. Samk, A. Lausic, W. Byleveld, A.B. Phillion, Metallurgical and mechanical assessment of hybrid additively-manufactured maraging tool steels via selective laser melting, *Addit. Manuf.* 27 (2019) 389–397. <https://doi.org/10.1016/j.addma.2019.03.025>.
- [20] X. Xu, S. Ganguly, J. Ding, S. Guo, S. Williams, F. Martina, Microstructural evolution and mechanical properties of maraging steel produced by wire + arc additive manufacture process, *Mater. Charact.* 143 (2018) 152–162. <https://doi.org/10.1016/j.matchar.2017.12.002>.
- [21] A. Ebrahimi, M. Mohammadi, Numerical tools to investigate mechanical and fatigue properties of additively manufactured MS1-H13 hybrid steels, *Addit. Manuf.* 23 (2018) 381–393. <https://doi.org/10.1016/j.addma.2018.07.009>.
- [22] M.K. El-Fawkhry, M. Eissa, A. Fathy, T. Mattar, Development of Maraging Steel with Retained Austenite in Martensite Matrix, *Mater. Today Proc.* 2 (2015) S711–S714. <https://doi.org/10.1016/j.matpr.2015.07.381>.
- [23] D.G. Lee, K.C. Jang, J.M. Kuk, I.S. Kim, The influence of niobium and aging treatment in the 18% Ni maraging steel, *J. Mater. Process. Technol.* 162–163 (2005) 342–349. <https://doi.org/10.1016/j.jmatprotec.2005.02.102>.
- [24] A. Jakus, A. Fredenburg, N. Thadhani, High-strain-rate behavior of maraging steel linear cellular alloys: Mechanical deformations, *Mater. Sci. Eng. A.* 534 (2012) 452–458.
- [25] S. Shamsdini, S. Shakerin, A. Hadadzadeh, B.S. Amirkhiz, M. Mohammadi, A trade-off between powder layer thickness and mechanical properties in additively

- manufactured maraging steels, *Mater. Sci. Eng. A.* 776 (2020) 139041.  
<https://doi.org/10.1016/j.msea.2020.139041>.
- [26] M. Ahmed, I. Nasim, S.W. Husain, Influence of nickel and molybdenum on the phase stability and mechanical properties of maraging steels, *J. Mater. Eng. Perform.* 3 (1994) 248–254. <https://doi.org/10.1007/BF02645850>.
- [27] A.S.M.H. Committee, *ASM Handbook Volume 4 Heat Treating*, ASM Stand. Am. Soc. Met. Mater. Park. OH. (1991).
- [28] M.K. Thompson, G. Moroni, T. Vaneker, G. Fadel, R.I. Campbell, I. Gibson, A. Bernard, J. Schulz, P. Graf, B. Ahuja, Design for Additive Manufacturing: Trends, opportunities, considerations, and constraints, *CIRP Ann.* 65 (2016) 737–760.
- [29] D. Bourell, J.P. Kruth, M. Leu, G. Levy, D. Rosen, A.M. Beese, A. Clare, Materials for additive manufacturing, *CIRP Ann.* 66 (2017) 659–681.
- [30] J.-Y. Lee, J. An, C.K. Chua, Fundamentals and applications of 3D printing for novel materials, *Appl. Mater. Today.* 7 (2017) 120–133.
- [31] A.C.F. on A.M. Technologies, A.C.F. on A.M.T.S.F. 91 on Terminology, Standard terminology for additive manufacturing technologies, Astm International, 2012.
- [32] P. Mercelis, J. Kruth, Residual stresses in selective laser sintering and selective laser melting, *Rapid Prototyp. J.* (2006).
- [33] H. Shipley, D. McDonnell, M. Culleton, R. Coull, R. Lupoi, G. O'Donnell, D. Trimble, Optimisation of process parameters to address fundamental challenges during selective laser melting of Ti-6Al-4V: A review, *Int. J. Mach. Tools Manuf.* 128 (2018) 1–20.
- [34] Y. Yao, Y. Huang, B. Chen, C. Tan, Y. Su, J. Feng, Influence of processing

- parameters and heat treatment on the mechanical properties of 18Ni300 manufactured by laser based directed energy deposition, *Opt. Laser Technol.* 105 (2018) 171–179.
- [35] S. Shamsdini, M.H. Ghoncheh, M. Sanjari, H. Pirgazi, B.S. Amirkhiz, L. Kestens, M. Mohammadi, Plastic deformation throughout strain-induced phase transformation in additively manufactured maraging steels, *Mater. Des.* 198 (2020) 109289.
- [36] T. DebRoy, H.L. Wei, J.S. Zuback, T. Mukherjee, J.W. Elmer, J.O. Milewski, A.M. Beese, A. Wilson-Heid, A. De, W. Zhang, Additive manufacturing of metallic components – Process, structure and properties, *Prog. Mater. Sci.* 92 (2018) 112–224. <https://doi.org/10.1016/j.pmatsci.2017.10.001>.
- [37] K. Kempen, E. Yasa, L. Thijs, J.P. Kruth, J. Van Humbeeck, Microstructure and mechanical properties of selective laser melted 18Ni-300 steel, *Phys. Procedia.* 12 (2011) 255–263. <https://doi.org/10.1016/j.phpro.2011.03.033>.
- [38] T. Bhardwaj, M. Shukla, Effect of laser scanning strategies on texture, physical and mechanical properties of laser sintered maraging steel, *Mater. Sci. Eng. A.* 734 (2018) 102–109. <https://doi.org/10.1016/j.msea.2018.07.089>.
- [39] T. Bhardwaj, M. Shukla, Direct Metal Laser Sintering of Maraging Steel: Effect of Building Orientation on Surface Roughness and Microhardness, *Mater. Today Proc.* 5 (2018) 20485–20491. <https://doi.org/10.1016/j.matpr.2018.06.425>.
- [40] C. Tan, K. Zhou, M. Kuang, W. Ma, T. Kuang, Microstructural characterization and properties of selective laser melted maraging steel with different build directions, *Sci. Technol. Adv. Mater.* 19 (2018) 746–758.

- [41] F.F. Conde, J.D. Escobar, J.P. Oliveira, M. Béréš, A.L. Jardini, W.W. Bose, J.A. Avila, Effect of thermal cycling and aging stages on the microstructure and bending strength of a selective laser melted 300-grade maraging steel, *Mater. Sci. Eng. A.* 758 (2019) 192–201.
- [42] B. Mooney, K.I. Kourousis, R. Raghavendra, Plastic anisotropy of additively manufactured maraging steel: Influence of the build orientation and heat treatments, *Addit. Manuf.* 25 (2019) 19–31. <https://doi.org/10.1016/j.addma.2018.10.032>.
- [43] J. Mutua, S. Nakata, T. Onda, Z.C. Chen, Optimization of selective laser melting parameters and influence of post heat treatment on microstructure and mechanical properties of maraging steel, *Mater. Des.* 139 (2018) 486–497. <https://doi.org/10.1016/j.matdes.2017.11.042>.
- [44] L.G. de Carvalho, M.S. Andrade, R.L. Plaut, F.M. Souza, A.F. Padilha, A dilatometric study of the phase transformations in 300 and 350 maraging steels during continuous heating rates, *Mater. Res.* 16 (2013) 740–744.
- [45] Y. He, K. Yang, W. Sha, Transmission Electron Microscopy of New High-Strength Grade Maraging Steels, *Microsc. Anal.* 118 (2007) 5.
- [46] B. Song, B. Sanborn, P.E. Wakeland, M.D. Furnish, Dynamic Characterization and Stress-Strain Symmetry of Vascomax® C250 Maraging Steel in Compression and Tension, *Procedia Eng.* 197 (2017) 42–51.
- [47] R. Schnitzer, G.A. Zickler, E. Lach, H. Clemens, S. Zinner, T. Lippmann, H. Leitner, Influence of reverted austenite on static and dynamic mechanical properties of a PH 13-8 Mo maraging steel, *Mater. Sci. Eng. A.* 527 (2010) 2065–2070.
- [48] E. Bouzakis, A. Arvanitidis, F. Kazelis, G. Maliaris, N. Michailidis, Comparison of

- Additively Manufactured vs. Conventional Maraging Steel in Corrosion-Fatigue Performance after various surface treatments, *Procedia CIRP*. 87 (2020) 469–473.
- [49] A.F. Avelino, W.S. Araújo, D.F. Dias, L.P.M. dos Santos, A.N. Correia, P. de Lima-Neto, Corrosion investigation of the 18Ni 300 grade maraging steel in aqueous chloride medium containing H<sub>2</sub>S and CO<sub>2</sub>, *Electrochim. Acta*. 286 (2018) 339–349.
- [50] M.A.C. Florez, Ú.C. Pereira, J.L. Cardoso, F.J. dos Santos Oliveira, W.S. Araújo, G.F. Ribas, H.F.G. de Abreu, M.J.G. da Silva, Microstructural characterization of grade 300 and grade 350 maraging steels and electrochemical study in hydrofluoric solution, *J. Fluor. Chem.* 243 (2021) 109738.
- [51] T. Zhao, S. Wang, Z. Liu, C. Du, X. Li, Effect of cathodic polarisation on stress corrosion cracking behaviour of a Ni (Fe, Al)-maraging steel in artificial seawater, *Corros. Sci.* 179 (2021) 109176.
- [52] Y.M. Wang, T. Voisin, J.T. McKeown, J. Ye, N.P. Calta, Z. Li, Z. Zeng, Y. Zhang, W. Chen, T.T. Roehling, Additively manufactured hierarchical stainless steels with high strength and ductility, *Nat. Mater.* 17 (2018) 63–71.
- [53] A. Hadadzadeh, B.S. Amirkhiz, A. Odeshi, J. Li, M. Mohammadi, Role of hierarchical microstructure of additively manufactured AlSi10Mg on dynamic loading behavior, *Addit. Manuf.* 28 (2019) 1–13.
- [54] P. Bajaj, A. Hariharan, A. Kini, P. Kürnsteiner, D. Raabe, E.A. Jäggle, Steels in additive manufacturing: A review of their microstructure and properties, *Mater. Sci. Eng. A*. 772 (2020) 138633. <https://doi.org/10.1016/j.msea.2019.138633>.

# **Chapter 2: The Role of Titanium on the Microstructure and Mechanical Properties of Additively Manufactured C300 Maraging Steels**

## **2.1. Introduction**

Among the ultra-high strength steels, the maraging class are special alloying systems in which the carbon is not acting a role in their hardening potential [1,2]. In fact, there have been many efforts to keep this impurity element as low as possible, where the maraging steels gain their ultra-high strength through the precipitation of phases within post-processing heat treatment e.g.  $\text{Ni}_3\text{Ti}$ ,  $\text{Ni}_3\text{Mo}$ ,  $\text{Fe}_2\text{Mo}$  [2–4]. The infinitesimal content of carbon leads to significantly better hardenability, formability, and toughness [5]. The presence of high Ni content, on the other hand, broaden the austenite ( $\gamma$ ) single-phase region to the room temperature and, consequently, facilitates martensitic transformation [6,7]. As a result, the microstructure of maraging steels usually contains different types of precipitates embedded into a soft ductile martensitic matrix that is heavily dislocated [1]. Over the last decades, the ultra-high strength 18Ni grades of maraging steels are widely taken into account due to their good sintering properties, low porosity levels, and low vulnerability to hot cracking allowing the industries to implement them in their supply chain [8–11]. In this category, the C300 maraging steels in which 300 is referred to its ultimate tensile strength (in ksi) is broadly used in tooling applications and aerospace industry, where its good toughness and strength make it a good candidate for various parts of landing gears as well as punching and forming dies [12–15].

The presence of a number of alloying elements in the C300 steels makes this alloy expensive compared to many other engineering materials; therefore, choosing a beneficial

fabrication method that could be cost-, and energy effective should be highly considered. Recently, additive manufacturing (AM) techniques have been widely used to manufacture maraging steels [13,16–18]. Among AM techniques, laser powder bed fusion (LPBF) has received much interest, not only due to a broad processing window, which could allow the operator to engineer different microstructures, but it also offers consistent physical and mechanical properties over well-defined processing parameters [19–22]. Towards this end, there have been many studies conducted to assess the properties of the additively manufactured maraging steels [11,17,18,23]. For instance, Bai *et al.* [20,21] analyzed the relative density of AM C300 alloys by changing LPBF processing parameters, i.e. laser power, scanning speed, and hatch distance. They found that there is a reciprocal effect between these parameters and the density, where their increase firstly improves the relative density and then drops it due to keyhole formation and balling effects [24]. Bhardwaj and Shukla [17,23] also evaluated the influence of the building direction on the physical and mechanical behavior of AM maraging steels. They concluded that the vertically printed samples showed lower residual stresses than horizontally printed ones.

Among the investigations carried out on the role of alloying elements on the microstructural and strengthening mechanisms of maraging steels, the majority were focused on the trace of Ni, Mn, and Ti after ageing heat treatments [1,10,25–29]. Galindo-Nava *et al.* [2] elucidated that the reverted  $\gamma$  kinetics promoted by Ti addition has the highest hardening effect via  $\text{Ni}_3\text{Ti}$  precipitation in the matrix, while Schober *et al.* [29] reported an accelerated coarsening of precipitates, and consequently, a fast drop in the hardness of Ti-bearing maraging steels due to a broad variety of phases during ageing. In spite of the most studies on the post-processing heat treatment of maraging steels, there has

been a lack of knowledge on the effect of chemical composition on the mechanical and microstructural properties of the as-built AM C300 alloys. In this case, the role of Ti content on the volume fraction of compounds' clusters, which could be in-situ formed within the ultra-fast solidification during the LPBF can be taken into account, because these clusters can act as suitable sites to expedite precipitation during the ageing process [5,26,30].

In this study, the C300 alloy powders containing two contents of Ti element were fused and printed using the LPBF process. To study the effect of Ti concentration on the mechanical, microstructure, phase distribution, and texture of the AM C300 alloy, the specimens were vertically and horizontally printed using similar processing parameters and laser scanning strategy. As an objective of this research, the role of Ti addition and building direction on the presence of Ti-rich precipitates into the matrix has been assessed using a combination of multiscale electron microscopy techniques including scanning electron microscopy (SEM), electron backscatter diffraction (EBSD), and transmission electron microscopy (TEM) along with X-ray diffraction (XRD) procedures.

## **2.2. Experimental Methodology**

The gas atomized C300 steel powders with size distribution of 10-63  $\mu\text{m}$  and 0.72 wt. % Ti content supplied by EOS GmbH (Low Ti content) and 1.17 wt. % Ti content supplied by Praxair (High Ti content) were used to produce the printed parts via the LPBF process. In order to compare microstructural and mechanical properties of a chemically modified C300 maraging steel powder and the conventional one, which are both commercially supplied, two types metal powders with various Ti contents were chosen. As

given in Table 2.1., the chemical composition of the powders with various contents of titanium, abbreviated as HighTi and LowTi, has been compared with the nominal one reported by the ASM international [31]. The chemical composition of the powders was determined using an inductively coupled plasma – optical emission microscopy (ICP-OES), where an Agilent ICAP-E725 was used according to the ASTM E1019-18, ASTM E1097-12, and ASTM E1479-16 [32–34]. Besides from that, combustion infrared detection (CID) technique was conducted to identify the carbon and sulfur contents via a LECO CS-844 apparatus.

An EOS M290 additive machine located at Additive Metal Manufacturing Inc., Concord, ON, was employed to fabricate the cube and tensile samples. The machine was equipped with a 400W Yb-fiber laser and spot size of 100  $\mu\text{m}$ . Based on the instruction by EOS GmbH [35], the LPBF process was conducted using 285 W as the laser power, scanning speed of 960  $\text{mm}\times\text{s}^{-1}$ , 40  $\mu\text{m}$  and 110  $\mu\text{m}$  as layer thickness and hatch space, respectively. The process parameters were chosen so that the maximum density, minimum volume fraction of porosity, and suitable surface quality could be simultaneously satisfied. In this regard, some literature recommended 250-300 W, 850-1000  $\text{mm}\times\text{s}^{-1}$ , and 80-120  $\mu\text{m}$  as the laser power, scanning speed and hatch space, respectively [36–38]. Out from the optimized window, the more laser power, the more probability of keyhole defect and entrapped gas porosity [39,40]. The lower laser power, on the other side, promotes lack of fusion, balling effect, and consequently, surface roughness [40]. The strip scanning pattern, i.e. the laser beam was rotated 67° after each step layer deposition [41,42], was applied throughout the process. As schematically shown in Figure 2.1., a set of solid cubes with 15 mm dimension was printed to study the microstructure, porosity area fraction, and hardness

of both materials, while the cylindrical rods with 12 mm diameter and L/D ratio of 10 were both horizontally and vertically printed to provide the uniaxial tensile samples. In all cases, the LPBF process was done under a protective atmosphere (99.999% high purity of argon gas) and the building plate with 250×250×325 dimensions (in mm) was preheated and held at 40°C during the process.

Table 2. 1. Chemical composition of the standard C300 maraging steel and virgin powders used in this study.

Elements (wt.%)											
	Ni	Co	Mo	Ti	Si	Mn	C	Al	S	P	Cr
<b>Standard</b>	18.0-19.0	8.5-9.5	4.6-5.2	0.55-0.8	0.1	0.1	0.03	0.05-0.15	0.01	0.01	-
<b>LowTi</b>	17.98	8.85	4.85	0.72	0.09	0.06	0.016	0.09	0.008	-	0.15
<b>HighTi</b>	17.68	9.26	4.82	1.17	0.06	0.03	0.012	0.11	0.011	-	0.11

In order to identify phases preexisted in the powder particles or those in-situ formed during the processing, the X-ray diffraction (XRD) analysis was carried out using a Bruker D8 Discover instrument equipped with Davinci-Design diffractometer, where the Cobalt sealed tube source with  $\lambda_{\text{mean}}=1.79026\text{\AA}$  was utilized. The analysis was conducted over a range of  $40 < 2\theta < 110^\circ$  with step size and time of  $0.02^\circ$  and 1 s, respectively.

To measure the hardness of the samples, a Clark macrohardness machine (CRM12) was employed, where the applied load was 150 Kg. The HRC hardness of the cubic samples was reported as a mean value of ten measurements. The tensile samples were collected and machined out from the printed cylindrical rods based upon the ASTM E8/E8M-15a standard [43]. A universal hydraulic controlled Instron 1332 apparatus equipped with a 25 mm extensometer was used to test the tensile samples (with 32, and 6 mm dimensions in their gauge length and diameter) at a quasi-static strain rate of  $9 \times 10^{-4} \text{ s}^{-1}$ .

To determine the area fraction of porosity in un-etched AM C300 cubes, the optical microscopy along with the ImageJ image processing and a Zeta-20 microscope was used. The size distribution and microstructure of the metal powders, which were hot mounted, regularly polished, and etched via the Nital 3% (3 ml HNO<sub>3</sub> + 97 ml ethanol) was assessed through SEM using a JEOL 6400 microscope. This apparatus was also employed to do fractography on the tensile samples. In addition, a Hitachi SU-70 field emission gun (FEG) ultra-high-resolution SEM was employed to evaluate the microstructure of the printed cubes, over which the texture analysis was also carried out with an Oxford instrument C-nano EBSD detector. An area of 175×175 μm<sup>2</sup> was collected to do the EBSD analysis with 350 nm step size. Further analysis on the presence of precipitates in the LowTi and HighTi samples was proceeded using a Tecnai Osiris TEM equipped with a 200 keV X-FEG and super-X windowless energy-dispersive X-ray spectroscopy (EDS) detector. For TEM sample preparation, 2 mm thick, AM samples were further ground and subsequently ion milled via a Gatan 691 PIPS. The effect of Ti on microstructural changes was observed in cube samples, where the same dimension in different directions let to investigate the microstructure features regardless of building direction. In other words, along with different build orientations, the resulting microstructure is the same.

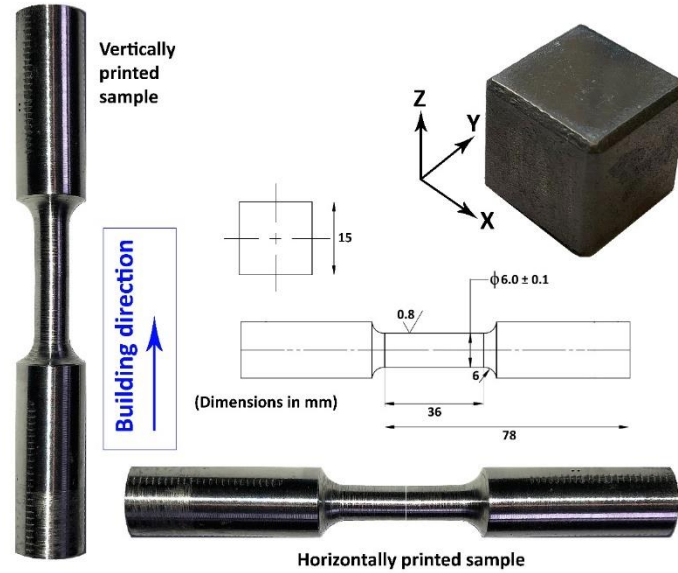


Fig 2. 1 The geometry of the AM tensile and cubic samples.

## 2.3. Results and Discussions

### 2.3.1. Phase Identification

As can be seen in the XRD patterns (Figure 2.2.), the C300 maraging powders contain almost 9% volume fraction  $\gamma$  existed in the martensite ( $\alpha'$ ) matrix. High content of nickel (17-18 wt.%) as a strong  $\gamma$  stabilizer element broadens the single-phase  $\gamma$  region at ambient temperatures in C300 maraging steels. A high cooling rate applied during the powder atomization and the LPBF suppresses diffusional phase changes, where the most probable transformation is an athermal  $\gamma \rightarrow \alpha'$ . Low percentage of carbon in C300 chemical composition, on the other hand, increases the  $\alpha'$  start temperature ( $M_s$ ). A combination between all mentioned phenomena leads to enhanced hardenability of the C300 maraging steel. As given in Table 2.2., by comparing the phase fraction in the HighTi and LowTi powders, there has been almost the same percentage of the  $\gamma$  phase. Jagle *et al.* [26] and

Liu *et al.* [44] showed that the  $M_s$  of ultra-low carbon steels diminishes in the presence of higher contents of Ti, Mo, and Ni, which means that Ti in these steel grades acts as  $\gamma$  stabilizer. On the other side, higher content of Ni as a strong  $\gamma$  stabilizing element promotes more retained  $\gamma$  phase in the LowTi powders; however, the same values of  $(\sum Ni + Ti) \%$  for both compositions cause no significant difference in  $\gamma$  or  $\alpha'$  phases.

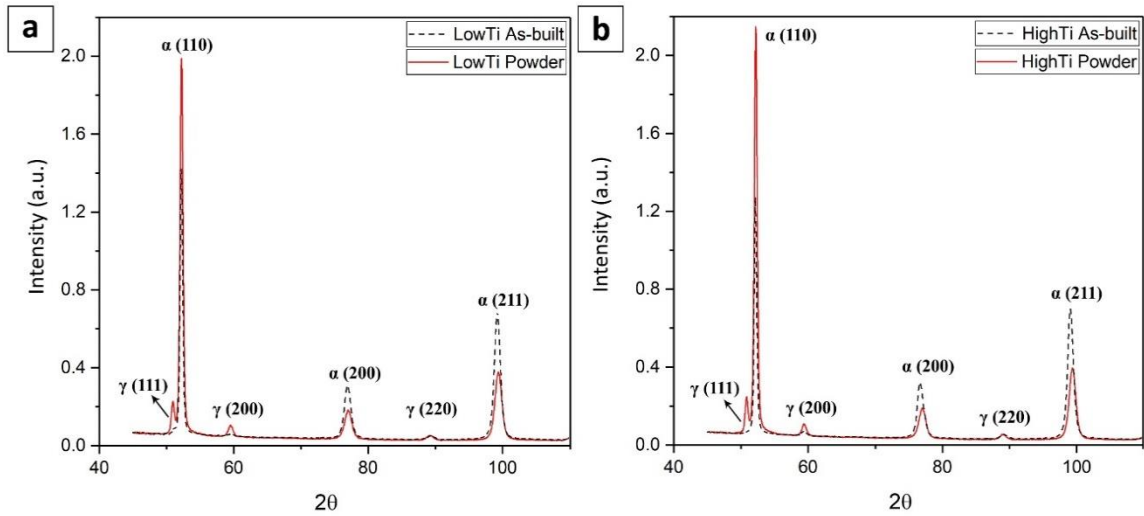


Fig 2. 2 The XRD profiles of (a) C300 powders, and (b) as-built sample at different Ti contents.

Table 2. 2. Volumetric percentage of phases presented in the C300 maraging powders and AM products.

Sample	$\alpha'$ volume fraction (%)	$\gamma$ volume fraction (%)
LowTi powder	91.09	8.91
HighTi powder	91.28	8.71
LowTi AM cube	97.03	2.97
HighTi AM cube	96.06	3.94

The XRD patterns of the as-built AM C300 samples also confirm the presence of  $\gamma$  and  $\alpha'$  in the microstructure, in which the  $\gamma$  (111) peak has been vanished in the HighTi AM alloy. As a comparison between the XRD data achieved from metal powders and printed samples, lower  $\gamma$  fraction in the printed samples is distinguishable. To discuss this

difference, the effect of solidification rate, equilibrium partition coefficient ( $k_0$ ), and the trace of alloying elements on the hardenability of the C300 steel should be taken into account. Since the cooling rate during the gas atomization ( $10^3$ - $10^5$  °C×s<sup>-1</sup>) [45] is much lower than the LPBF process ( $10^5$ - $10^7$  °C×s<sup>-1</sup>) [15,24,46], the initial microstructure formed through the isomorphous phase transformation around 18 wt.% Ni in Fe-Ni phase diagram, where  $L \rightarrow L + \gamma$ , is coarser in the atomized powders. Higher diffusion rate of alloying elements in the gas atomization rather than the LPBF process affects the degree of microsegregation during the isomorphous transformation. Based on  $k_0$  value in the  $\gamma$  phase, the rate of segregation is different from a specific element to another one [47,48]. In this case,  $k_{0,Ti}^{\gamma}$  is equal to 0.07, while for both strong  $\gamma$  stabilizers of Ni and Mn is 0.95 [49,50]. Lower  $k_0$  means higher severity of segregation due to the following equation [47],

$$k_{0,i} = \frac{C_{S,i}}{C_{L,i}} \quad (2-1)$$

where,  $C_S$  and  $C_L$  are the concentration of element (i) in the solid and liquid phases. Regarding the unequilibrium solidification condition during both processes, equation (1) should be rewritten as a function of the solid/liquid interface velocity (R) [51],

$$k_{R,i} = \frac{(k_{0,i} + \frac{a_0 R}{D_{L,i}})}{(1 + \frac{a_0 R}{D_{L,i}})} \quad (2-2)$$

in which,  $a_0$  and  $D_{L,i}$  are referred to a constant on the order of the interatomic distance, and the solute diffusivity of element i at the solid/liquid interface. Considering quantities of  $10^{-9}$  m, and  $5.5 \times 10^{-9}$  m<sup>2</sup>×s<sup>-1</sup> as  $a_0$  and  $D_{L, Ti}$  in the Fe liquid at 1550°C [45,46], respectively, the R-dependent partition coefficient is correlated to  $k_0$  and R values. The ultra-fast interface velocity through the LPBF process brings higher  $k_{R,i}$  values compared to gas

atomization, consequently, leads to more reluctancy in elements' segregation. In this regard, solute trapping, i.e. the solute atoms substitutionally entrapped in the lattice structure [47,48], would be a prevalent phenomenon occurring during both processes, particularly the LPBF. The solute trapping is dominant for those elements that have high  $k_R$  and low  $D_L$ , e.g. Ni and Mn with  $3.1 \times 10^{-9}$  and  $3.9 \times 10^{-9} \text{ m}^2 \times \text{s}^{-1}$  diffusion coefficient, respectively [45,46]. Although the probability of Ti rejection to the solidification front is greater in the atomized powders, the layer-by-layer reheating cycles during the LPBF process leads to Ti atoms segregate within intercellular and intercolumnar regions, as Jagle *et al.* also presented [26,30,54]. Notwithstanding the Ti element, Ni and Mn experience trapping even during layer-by-layer reheating. Most solute elements, except Co, that substitutionally located in the  $\gamma$  lattice brings higher hardenability, consequently, induces further  $\alpha'$  formation [5,30,55,56], while those that can have a chance to be segregated, such as Ti and Mo, act as high potential sites for keeping the  $\gamma$  phase [26].

The microstructure of both HighTi and LowTi powders are supposed to be interdendritic-intercolumnar austenitic due to the high concentration of Ti and other elements segregated into these channels. The AM products, on the other hand, are expected to be less prone to keep the  $\gamma$  phase within transgranular regions due to solute trapping of Ni and Mn, while the intercellular and intercolumnar regions are thought to be austenitic because of Ti segregation during remelting cycles. A comparison between LowTi and HighTi AM products shows that the HighTi sample presents higher  $\gamma$  percentage, since more titanium atoms can be rejected into intercellular regions, hence, the fraction of high potential sites for keeping the retained  $\gamma$  can be enhanced.

### **2.3.2. Powders Shape and Size Distribution**

Figure 2.3. demonstrates size and shape of the LowTi and HighTi powders to better understand the powder size distributions that directly affects the soundness of the AM products. The powders are mostly spherical within a broad range of size that is appropriate in terms of their flowability, packing density, and uniformity in layer deposition during the LPBF process. Some of the fine powders in both feedstocks are stuck to each other and form the satellite-shape colonies (marker (i)), while few of those show irregular shapes (marker (ii)) probably due to any inhomogeneity in the gas pressure or heat extraction during the powder atomization process [45]. The image processing on the low-magnified SEM images allows to identify powder size distribution, as revealed in Figure 2.4. As can be seen, there has been a homogenous distribution of the particles mostly ranged between 5 and 35  $\mu\text{m}$ , where  $D_{\text{Mean}}^{\text{LowTi}} = 15.1 \pm 9.2$  and  $D_{\text{Mean}}^{\text{HighTi}} = 15.8 \pm 8.7$   $\mu\text{m}$  (D is diameter). Homogenous distribution of the powders results in a suitable interlayer mechanical bonding, which ultimately leads to superior mechanical properties and monolithic integrity of the microstructure [24].

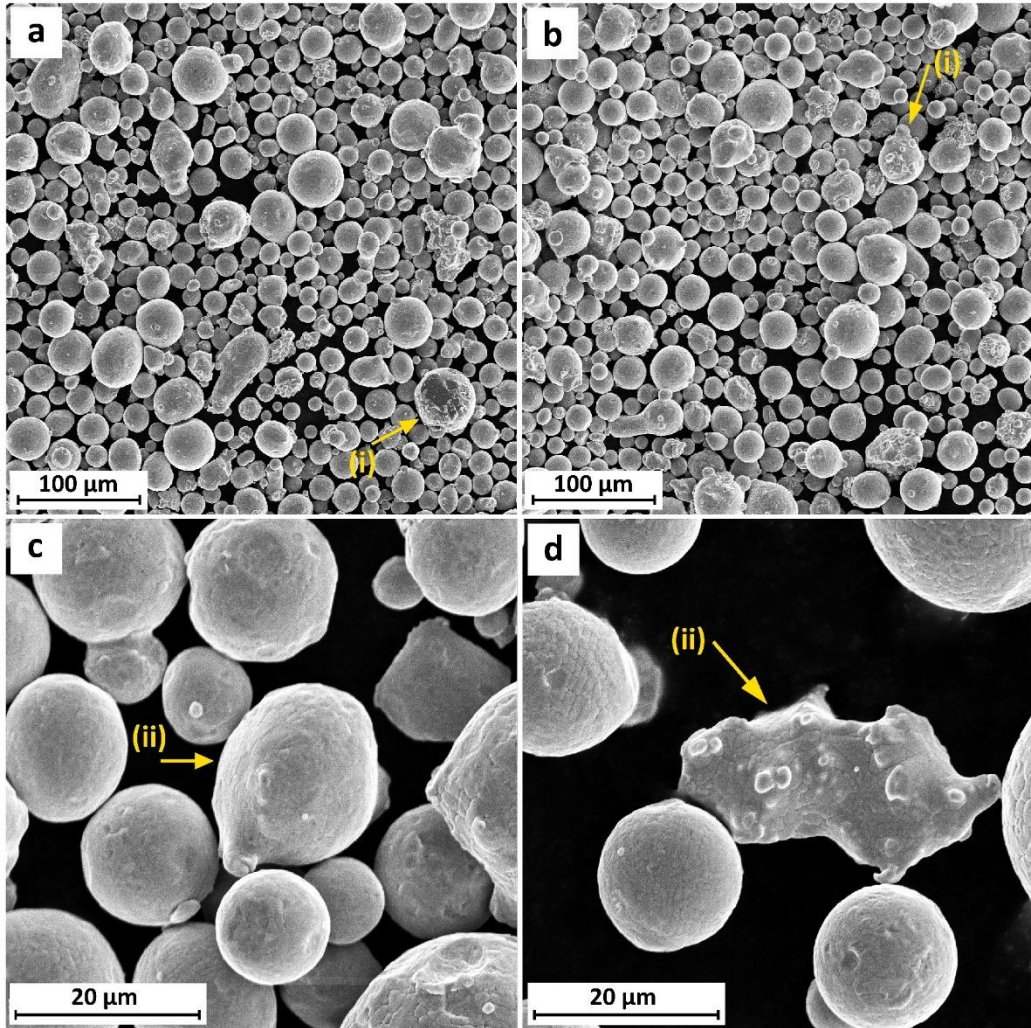


Fig 2. 3 The SEM micrographs of the LowTi and HighTi powders at two magnifications (i) satellite-shape, and (ii) irregular powders.

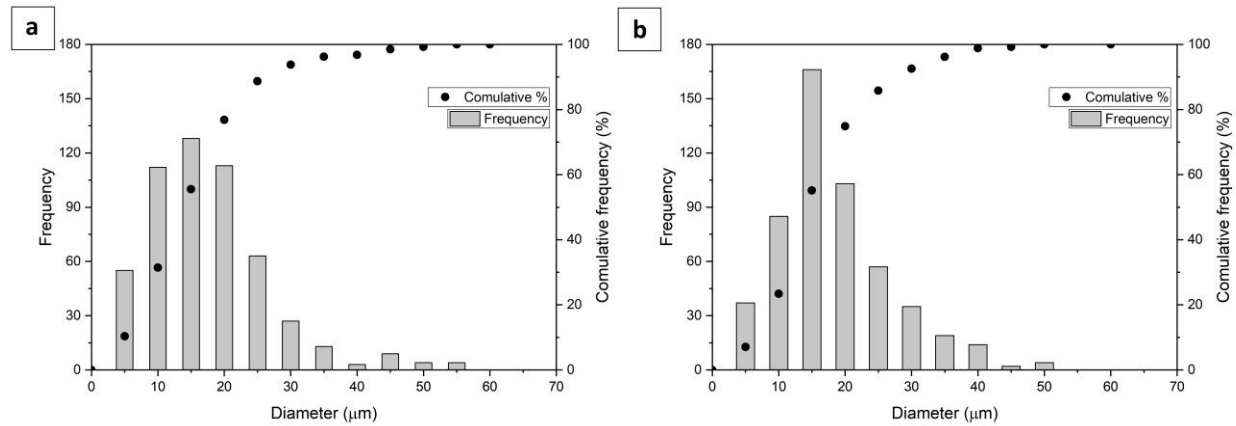


Fig 2. 4 Size distribution and cumulative frequency of (a) LowTi, and (b) HighTi alloy powders.

The micrographs of the LowTi and HighTi powders are shown in Figure 2.5. The microstructure of both materials is mostly columnar-dendritic, where the area fraction of the equiaxed grains in the HighTi powder is obviously higher. In terms of the thermal gradient ( $G$ ) and solid/liquid interface velocity ( $R$ ), both types of powders experienced similar situations providing almost the same size distribution, so the constitutional undercooling,  $\Delta T_C$ , during solidification is postulated as the main reason causing the morphological changes. To show this, the Fe-Ni isopleth for both chemical compositions is given in Figure 2.6. By focusing on the isomorphous reaction zone, it has been revealed that the HighTi shows broader mushy zone at 18 wt.% Ni in which liquid and  $\gamma$  phase are coexisted. The broad mushy-state interval exposes the solidifying material to longer solidification time, where the more fraction of solute can be

rejected to the solid/liquid front. As can be seen, the interval expanding is highly caused by the solidus line deviation, where the nickel content in the  $\gamma$  phase shifts to lower concentration. Therefore, based on equation (1),  $C_s$  and  $k_0$  are reduced. Lower  $k_0$  or more segregation presents higher amounts of  $\Delta T_C$ , over which the tendency of equiaxed growing is raised [28,47,57,58]. In other words, the more  $\Delta T_C$ , the more probability of unconstrained growth [48]. Although the morphology shown in Figure 5 belongs to  $\alpha' + \gamma$ , this could be representative of the initial microstructure formed through  $L \rightarrow L + \gamma$  reaction, where the  $\gamma$  phase continuously nucleates and grows within the liquid, and subsequently, transforms to  $\alpha'$  phase. The LowTi microstructure, on the other hand, tends to be dendritic and equiaxed in some places due to narrower freezing zone and shallower  $\Delta T_C$ . It is worth noting that,  $\Delta T_C$  is directly affected by  $k_0$ , in which decrease in the distribution coefficient leads to a steeper deviation in solidus line bringing higher solute rejection, and consequently, higher  $\Delta T_C$  values [9,48]. The equilibrium liquidus and solidus temperatures of the studying materials are given in Table 2.3.

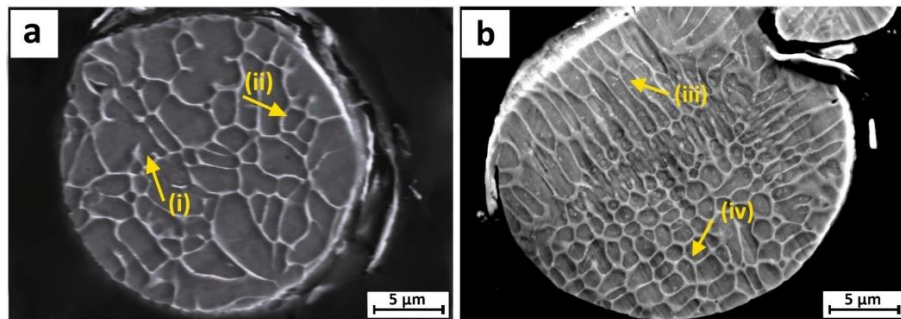


Fig 2. 5 The SEM micrographs of (a) LowTi, and (b) HighTi alloy powders (i: dendritic, ii: equiaxed, iii: columnar, and iv: equiaxed morphologies).

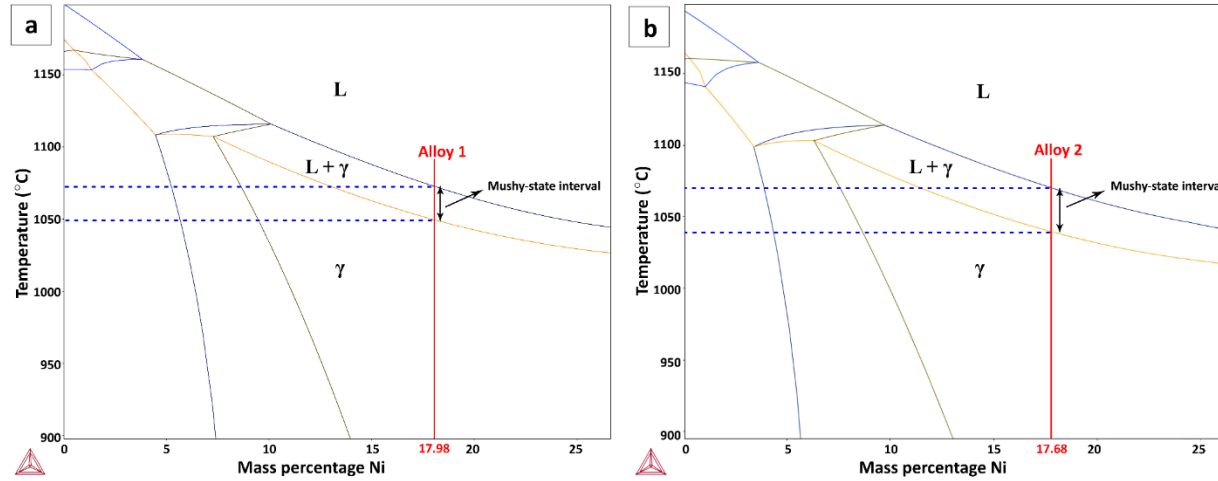


Fig 2. 6 The Fe-Ni isopleth of (a) LowTi, and (b) HighTi alloying systems indicating the liquidus and solidus temperatures of the studied materials.

Table 2. 3. Thermal properties of the AM LowTi and HighTi samples.

Alloy	Liquidus temperature (°C)	Solidus temperature (°C)	Mushy range (°C)
<b>LowTi</b>	1440.6	1384.6	56.0
<b>HighTi</b>	1433.2	1360.7	72.5

### 2.3.3. As-built Microstructural Characteristics and Porosity Formation

In order to present the nominal density of the as-built AM samples, pore area fraction measured by the image processing technique has been reported according to the optical micrographs in Figure 2.7. The area fraction of porosity is measured using image processing technique on the top surface of the unetched as-built samples. Both LowTi and HighTi AM cubes show high nominal densities, where  $\rho_{\text{Nom}}^{\text{LowTi}}$  and  $\rho_{\text{Nom}}^{\text{HighTi}}$  are 99.927% and 99.952%. The results show that processing parameters are properly chosen in such a way that the occurrence of some common processing defects like balling effect and lack of fusion was minimized. As seen in this figure, the porosities are mostly formed in spherical and wormy shapes in which the round ones are mainly caused by the protective gas entrapment, while the irregular wormy shapes are corresponding to solidification defects e.g. lack of fusion, keyhole porosity, and volumetric changes induced by solidification shrinkage and phase transformation. Other studies also reported some of these sources of porosity formation during the AM of maraging steels [49,54–56].

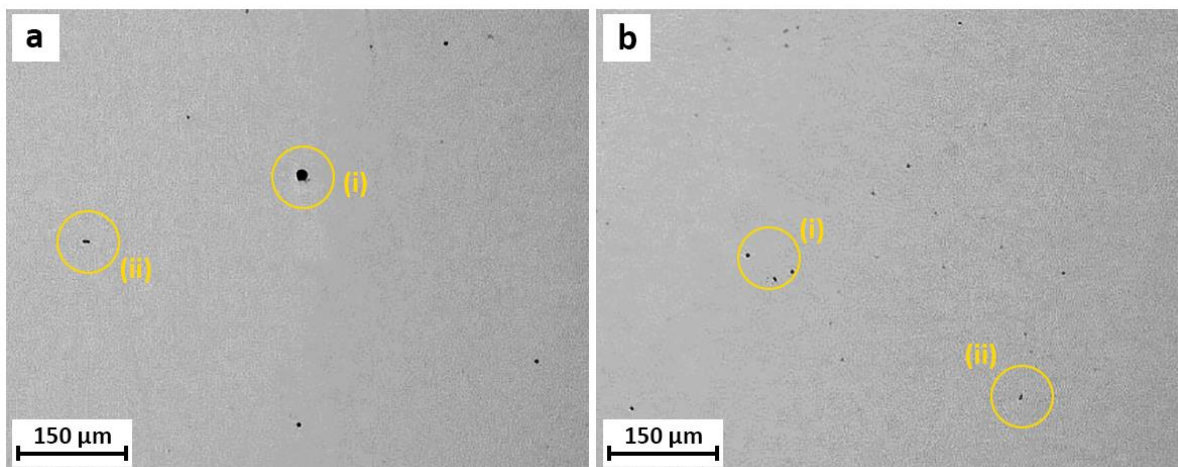


Fig 2. 7 The OM micrographs of (a) LowTi, and (b) HighTi as-built structure revealing the presence of porosities (i: spherical gas porosity, ii: irregular shrinkage porosity).

According to the SEM micrographs given in Figure 2.8., a mixed microstructure containing columnar, and equiaxed morphologies is observable in both LowTi and HighTi AM samples. Within a single melt pool, the  $\gamma$  solid/liquid front moves toward the opposite direction of the heat extraction, i.e. from the peripheral regions to the center of the melt pool surface [51]. The C300 maraging steel with almost 18 wt.% Ni shows  $\gamma$  phase nucleation and growth within an isomorphous reaction. At ultra-high cooling rates during the LPBF process, once the  $\gamma$  phase starts to form, the solute rejection during solidification occurs. This is with regards to the diffusion coefficient and partition coefficient of alloying elements. At the vicinity of the melt pool boundaries, particularly at the bottom, the high value of G/R motivates the columnar morphology over which the primary columns start to grow toward the top central zones. The solute rejection taking place during the  $\gamma$  columns growth leads to an increase in  $\Delta T_C$  ahead of solid/liquid front, where the G/R is gentle, and consequently, the equiaxed  $\gamma$  phase starts to form at top central regions. Solute partition within the intercolumnar regions also provides high  $\Delta T_C$ , particularly next to the roots of the columns in which the metallostatic pressure is dropped and the fresh liquid with less solute concentration cannot be sucked into these regions [62]. High G/R, and high frequency of nucleation due to severe  $\Delta T_C$  are responsible for nucleation of fine cellular  $\gamma$  phase in contact with the solidified columns [51]; however, the cellular structure is not observable in Figure 2.9.

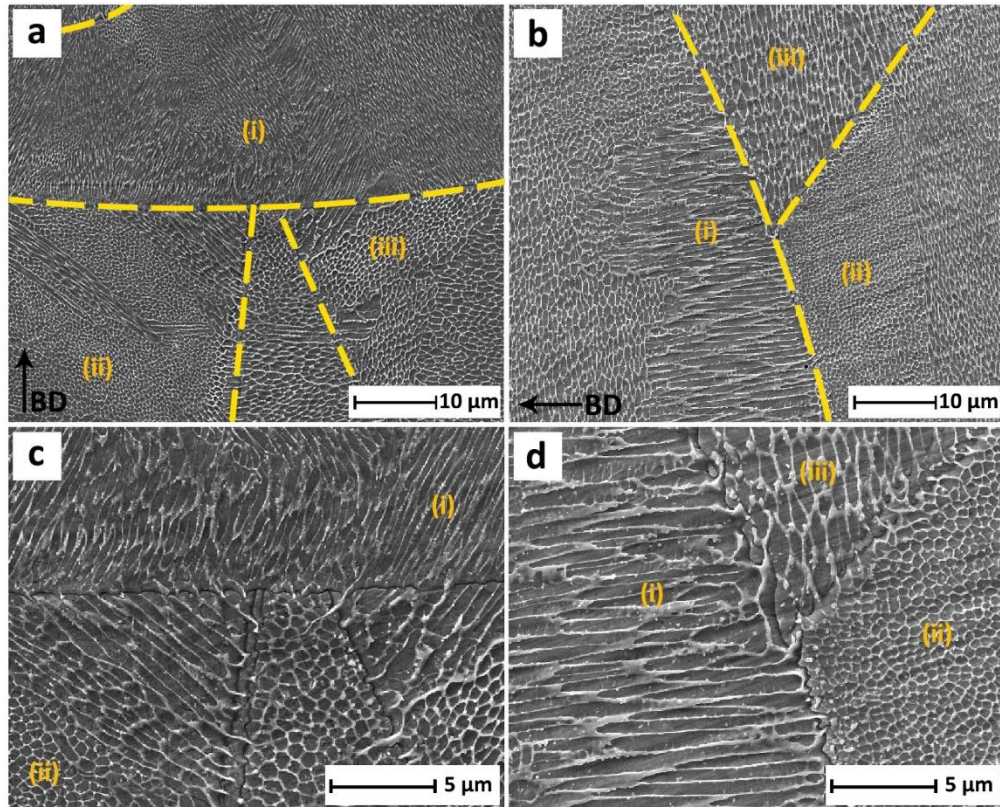


Fig 2. 8 Microstructure of the as-built (a, c) LowTi, and (b, d) HighTi samples (i: columnar, ii: fine equiaxed, iii: coarse equiaxed morphologies).

### 2.3.4. Texture Analysis and Grain Morphology

The inverse pole figure (IPF) along with the building direction of the as-built cubes is revealed in Figure 2.9. As can be observed, the texture analysis through the longitudinal direction allows better understanding of the grain shape, size and orientation. The melt pool boundaries, identified by dash lines, properly define the areas at which the initiation of different morphologies has taken place. The LowTi and HighTi IPF patterns confirm the coexistence of columnar, cellular, and equiaxed morphologies, similar to the SEM micrographs. As previously discussed, the structure is supposed to be martensitic in style

of numerous fine lathes that are highly dislocated, and some austenitic grains isolated at intergranular regions.

To make the columnar and equiaxed grains as distinguishable as possible, the grain shape aspect ratio ( $\phi$ ), defined as  $\phi = L_2/L_1$  is considered, where  $L_1$  and  $L_2$  are referred to the dimension of the major and minor axes of an ellipse fitted to each grain, respectively. According to the available literature [63],  $\phi = 0.33$  is defined as the critical grain shape aspect ratio, at which the columnar ( $\phi \leq 0.33$ ) to equiaxed ( $\phi > 0.33$ ) transition takes place. In both samples, there has been similar fraction of columnar and equiaxed grains, 12% and 88%, respectively. Since the cellular grains, i.e. short grown arms over which the nucleation and growth of secondary and ternary arms have been avoided due to high G values [47,48], are hard to identify via the term  $\phi$ , this semi-quantitative technique is conducted to distinguish the columnar from equiaxed grains. The grain area distribution in both LowTi and HighTi AM cubes are also reported in this figure, where  $D_{\text{Mean}}^{\text{LowTi}}$  and  $D_{\text{Mean}}^{\text{HighTi}}$  are 5.02 and 9.40  $\mu\text{m}^2$ , respectively.

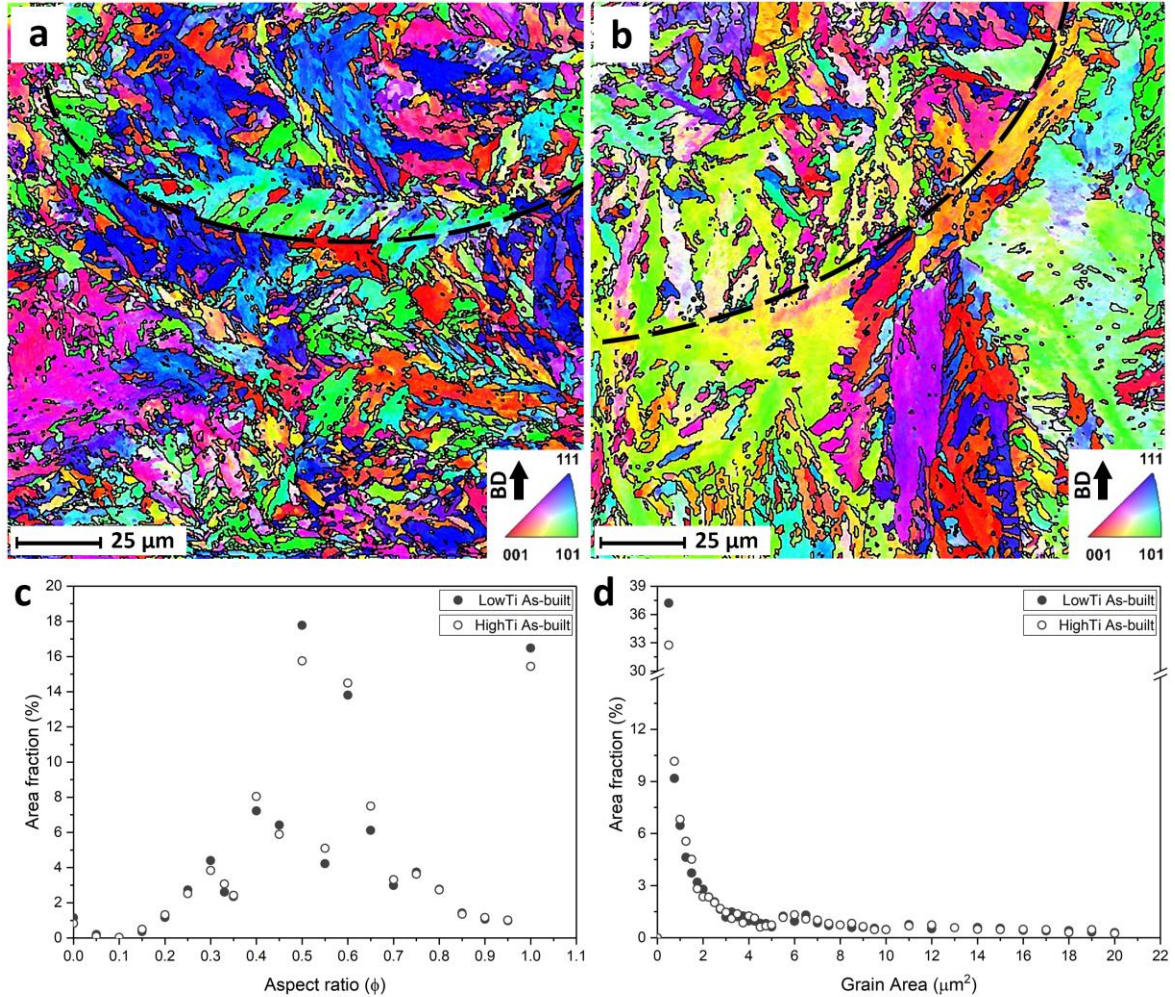


Fig 2. 9 The IPF-Z maps of the as-built (a) LowTi, and (b) HighTi structures along with the building direction (BD), followed by distribution maps of (c) columnar/equiaxed grains, and (d) grain area.

According to Figure 2.10., there is a weak random texture alongside the building direction of the LowTi sample, while the HighTi sample shows a more textured microstructure in which a tilted fibrous texture is developed. Based on Figures 2.8-2.10, it seems that the HighTi sample has coarser microstructure that can be attributed to its broader solidification interval demonstrated in Figure 2.6. Figures 2.10c and 10d show the grain boundary misorientation maps of the cube samples identifying low-, and high angle grain boundaries (LAGBs and HAGBs). The misorientation angle ( $\theta$ ) is used to represent

the difference between these two types of GBs, where  $2.5^\circ < \theta < 15^\circ$  and  $15^\circ \leq \theta$  are referred to LAGBs and HAGBs, respectively. The percentage of LAGBs in the LowTi sample (60%) is more than the HighTi one (56%). According to Rappaz *et al.* [64,65], the HAGBs are more prone to hot cracking during solidification that is also intensified by broadening the mushy-state range. Hence, this is another proof to show that the HighTi alloy reveals wider solidification temperature interval. Mutua *et al.* [60] also reported 51% LAGBs for the as-built maraging steel with a chemical composition very close to the LowTi sample.

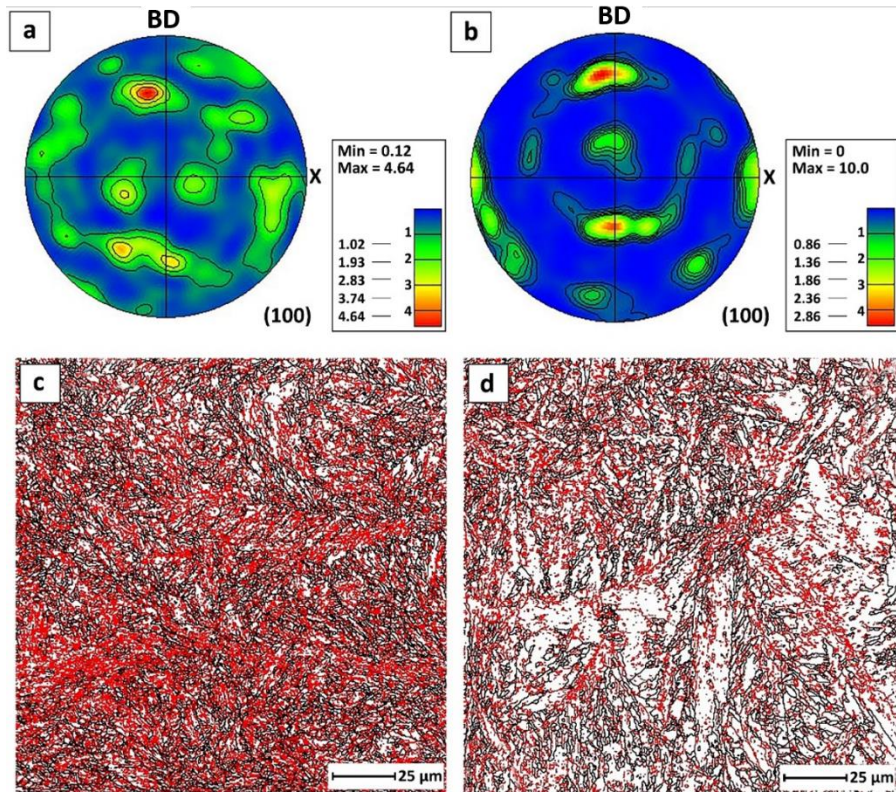


Fig 2. 10{100} pole figures and the grain boundary map of the as-built (a, c) LowTi, and (b, d) HighTi samples (In subfigures c and d, red and black lines indicate the LAGBs and HAGBs, respectively).

### 2.3.5. Solute Clustering and Precipitates Formation

As illustrated in the STEM-bright field (BF) images in Figure 2.11., the AM structure of the LowTi alloy shows intercolumnar solute-rich zones, especially of Ni, Mo, and Ti, due to cyclic reheating during the LPBF process. However, the  $\alpha'$  matrix also contains highly distributed Mo and Ni atoms, which indicates solute trapping or banding phenomenon taking place because of the ultra-fast solidification velocity ( $R$ ) and slow diffusion rate of those elements. Ti, on the other hand, does not show trapping within the matrix, as a result of its low partition coefficient and high diffusion coefficient, as previously discussed. Layer-by-layer remelting cycles during LPBF facilitates solute partition of Ti and Mo, and subsequently, intensifies equiaxed morphological growth, while there have always been some columns epitaxially or independently form next to the melt pool boundaries (which was seen in SEM images). In spite of the elements mentioned above, Al and Co could not find a chance to get rejection into the intercolumnar regions during solidification. As another observation, the intercolumnar regions are high-potential sites to keep retained  $\gamma$ , while the  $\alpha'$  lathes cover the rest of the AM structure. In the elemental maps, there have been also some round particles that are mostly Ti-, and N-rich, as well as Al and O-bearing compounds in some locations. The titanium nitride (TiN) is the most reported inclusion easily formed during the LPBF of C300 maraging steels that effectively affects the mechanical properties. Hence, the as-built samples are better to be heat treated to dissolve the inclusions and redistribute their containing elements [13]. In those places that Al, O, Ti, and N are coexisted, some studies reported the presence of core/shell  $\text{Al}_2\text{O}_3/\text{TiN}$  inclusions [14]. The nitrogen and oxygen impurities in the protective Ar gas can be easily dissolved into the liquid metal, and subsequently, react with the elements present in the alloy. In this regard, the mixing enthalpy of Ti-N is almost -190

$\text{kJ}\cdot\text{mol}^{-1}$  that brings negative Gibbs free energy of mixing [66], and Al is an active element that can be easily oxidized [14].

In Figure 2.12., the STEM-BF images illustrate the elemental distribution maps in the HighTi AM cube. The most important observable feature is Ni and Co atoms clustering, formed as the ultra-fine CoNi precipitates with 2nm in their size. These precipitates have been reported for the first time in the Ti-rich AM maraging steels; however, the LowTi alloy did not show the same feature in its microstructure. Galindo-Nava *et al.* [2] reported that increasing Ti content improves the strength of maraging steel by forming  $\eta\text{-Ni}_3\text{Ti}$  precipitates in conventional heat-treated maraging steels. It can be postulated that, the CoNi precipitates in the AM C300 is a metastable phase forming due to a lack of Ti element in the matrix. As previously discussed, Ti with its low partition coefficient and high diffusion rate can be easily segregated toward the intergranular regions, which intensifies Ti depletion within the transgranular zones [49,50]. Among all intermetallic compounds presented in the maraging steels,  $\text{Ni}_3\text{Ti}$  is the most probable one to be precipitated due to its low Gibbs free energy of formation [67]; however, Ti depletion suppresses the nucleation of the  $\text{Ni}_3\text{Ti}$  phase. In this case, Co and Ni elements react within the matrix to form the ultra-fine CoNi precipitates. Therefore, it is reasonable to report that the addition of Ti can induce CoNi formation, as also discussed by Tian *et al.* [67]. The CoNi precipitate with its high formation energy compared with the other common phases in the C300 maraging steel such as FeCo, FeNi and  $\text{Ni}_3\text{Ti}$  [59,60], act as suitable nucleation sites for those that show the lowest formation energy during the direct ageing treatment. The metastable CoNi with 0.185 eV formation energy could be transformed to  $\text{Ni}_3\text{Ti}$ , FeTi, and CoTi with -0.538, -0.475, and -0.457 eV energy level, respectively [67]. Within the

temperature range of 500-650°C that is usually used to age the as-built maraging steels [13], more stable precipitates can be formed at the expense of primary intermetallics nucleated and grew during solidification. Since all of these stable phases are Ti-rich, ageing process at high temperature for sufficient holding time leads an increase in Ti solid-state diffusion from the intergranular to transgranular regions.

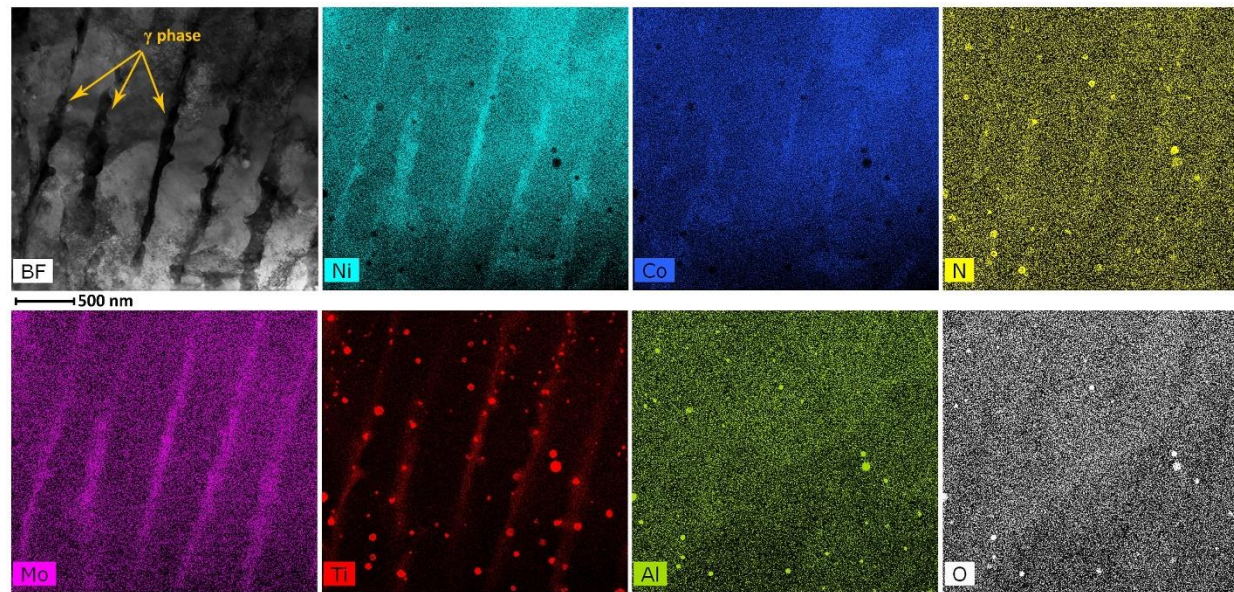


Fig 2. 11The STEM-BF image and its corresponding elemental distribution maps showing the existence of  $\gamma$  phase between  $\alpha'$  pockets in the as-built LowTi sample.

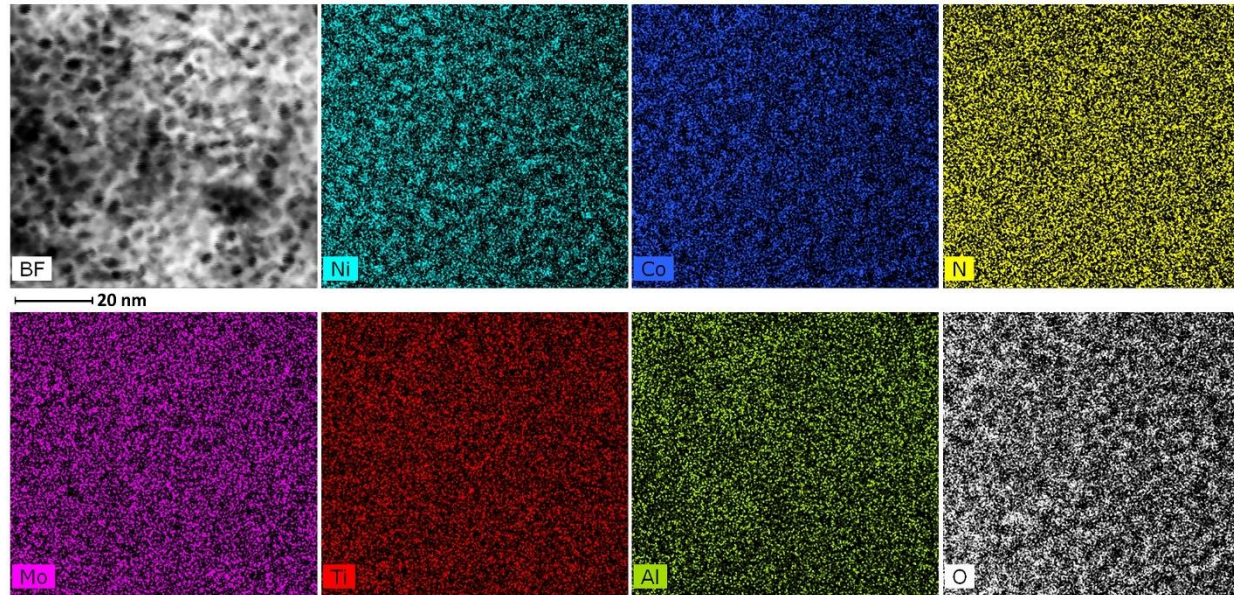


Fig 2. 12 The STEM-BF image and its corresponding elemental distribution maps showing the existence of ultra-fine CoNi precipitates in the as-built HighTi sample.

The small size of CoNi clusters made them cumbersome to be visible in the EDS maps, where the selected area diffraction (SAAD) technique can help for further characterization. To confirm the presence of the ultra-fine CoNi clusters in the Ti-rich sample, the superlattice reflection of the clusters is further analyzed using the SAAD technique, as shown in Figure 2.13a. The pattern showing the presence of the CoNi precipitates in the HighTi matrix is identified due to the ordered structure of this phase.

Figure 2.13b shows a typical TEM-dark field image of the austenitic regions in the  $\alpha'$  matrix. The width of  $\alpha'$  laths is calculated for both samples, where the average thickness of each lath is almost 500 nm. Due to the accumulation of Ti in the  $\gamma$  region, increasing the titanium content does not affect the  $\alpha'$  lath size. This observation confirms the grain size results calculated from the EBSD and confirms the previous studies [9,39]. Figure 2.13c reveals a TEM-bright field image to calculate the dislocation density ( $\rho_D$ ). Ultra-fast solidification during the LPBF process causes an extreme increase in  $\rho_D$  because of severe thermal shocks associated with residual stresses by volume changes during solidification and phase transformation [27]. Based on equation (3) [69],  $\rho_D$  can be correlated to the thickness (t) of the TEM foil using electron-energy loss spectroscopy (EELS) log-ratio technique. For this purpose, a grid with horizontal and vertical lines is superimposed on the TEM micrograph, followed by counting the number of vertical and horizontal intersections of dislocations the grid lines ( $N_{\text{vertical}}$  and  $N_{\text{horizontal}}$ ) and the dislocation density can be written as

$$\rho_D = \frac{1}{t} \left( \frac{N_{\text{vertical}}}{\sum L_{\text{vertical}}} + \frac{N_{\text{horizontal}}}{\sum L_{\text{horizontal}}} \right) \quad (2-3)$$

where,  $\sum L_{\text{vertical}}$  and  $\sum L_{\text{horizontal}}$  are the total length of vertical and horizontal grid lines. The average  $\rho_D$  for LowTi and HighTi samples are calculated as  $1.4 \times 10^{15} \text{ m}^{-2}$  and  $2.4 \times 10^{15} \text{ m}^{-2}$ , respectively, in which a significant increase in  $\rho_D$  is achieved at higher Ti content.

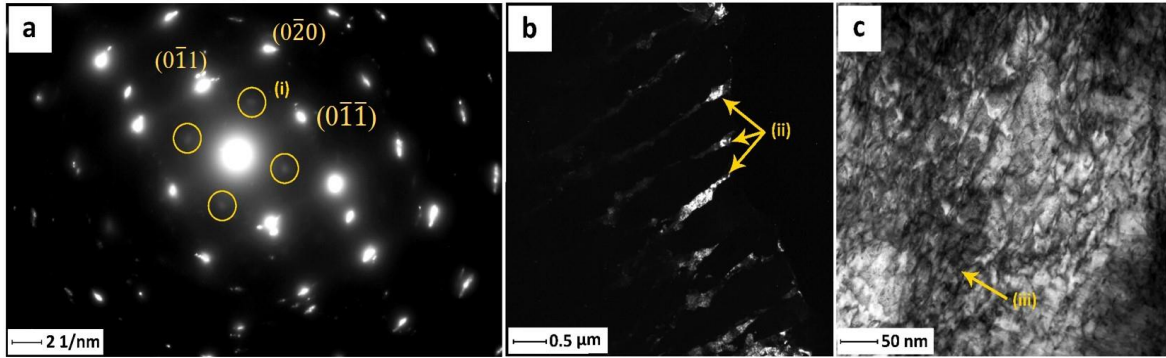


Fig 2. 13 (a) Diffraction pattern of the HighTi sample and its corresponding Miller index (i: superlattice reflections showing the presence of CoNi clusters), (b, c) TEM-DF and TEM-BF images of the LowTi matrix (ii:  $\gamma$  phase, iii: dislocations networks).

### 2.3.6. Mechanical Properties

The hardness of the AM cubes is reported as an average of ten measurements, where the LowTi and HighTi alloys show  $33.3 \pm 1.1$  and  $40.3 \pm 2.4$  HRC, respectively. The sample with higher Ti content presents almost 20% higher hardness value that can be caused by hardening effect of Ti-rich intergranular zones and those hard CoNi precipitates with Body Centered Cubic (BCC) structure well dispersed into the matrix. As another reason, higher dislocation density in the HighTi alloy can be taken into account, in which the strain hardening rate increasingly raises during the indentation. This can be assigned to the intensified dislocations entanglement that induces higher values of stored stresses during the deformation of material beneath the surface. It is well understood that Ti has a positive effect on the toughness and hardness of C300 maraging steels [25,27].

The results of the uniaxial tensile testing under quasi-static strain rate is demonstrated in Figure 2.14. As can be observed, those tensile samples horizontally printed show higher yield and ultimate tensile stresses, meantime more toughness due to higher

under-curve surface area compared to the vertical samples. The vertically printed samples, on the other hand, shows gentler strain hardening rate ( $d\sigma/d\epsilon$ ) before the maximum tensile stress. This means that the vertical samples present lower strain hardening capability that can be caused by some microstructural defects e.g. porosities and internal cracks, or the grains morphology that all are highly affected by G and R changes along with the building direction. In this regard, it has been reported that the volume fraction of the columnar grains that are highly susceptible to epitaxial growth, hot cracking, intercolumnar void formation, and segregation is much higher in the vertically printed samples [12,30,46]. Despite these samples that show a strong anisotropy in their mechanical properties, the horizontal samples usually propose less anisotropic properties accompanied by their cellular and equiaxed grain morphologies [23]. Generally, in spite of the vertical samples in which the loading and building directions are parallel, the orientation in the horizontal samples is perpendicular. Therefore, cracks and voids in the vertical samples more likely act as stress risers and produce a drastically drop in the tensile strength owing to the reduction in effective cross-sectional area [70].

As another result, Ti element better elucidates its influence on the vertical samples, where the HighTi vertical sample shows higher values of elongation and toughness compared with the LowTi one. Mooney *et al.* [16] also observed the same trend and suggested that this variation is due to the presence of planar heat generation in the LPBF process along with the constrained movement of the build platform solely in the vertical direction. As previously mentioned, both Ti-containing samples showed a small volume fraction of porosity. Both gas and shrinkage porosities inevitably formed during the solidification of the melt pools and have detrimental effects on the mechanical properties,

as they act as stress localization sites [71,72]. The CoNi clusters uniformly distributed in the matrix of the HighTi sample can increase the shear strength of the lattice by interaction with dislocations during the uniaxial tensile test. In other words, the more Peierls stress, the more resistance of the lattice against the dislocation's mobility [73].

The coexistence of this precipitate and pre-existed porosities in the HighTi samples induces a better balance between hardening and softening phenomena during tensile deformation, which provides better elongation than the LowTi samples. The importance of this synergy should be considered, when the matrix is intrinsically high strength and brittle like the martensitic matrix in C300 maraging steels. This is because the  $\alpha'$  pockets are very prone to the propagation of the microcracks generated neighboring the porosities during the deformation. Tey *et al.* [74] also reported the effect of precipitates and porosity on crack growth in AM Titanium-Steel-Copper sandwich materials, where the deleterious role of porosity on sample strength was controlling the brittle amorphous interface of studied material. To compare the mechanical properties reported in this study with some other research, Tables 2.4 and 2.5 present the average values of the elastic modulus (E), yield and ultimate tensile stresses (YS and UTS), elongation percentage at failure point, and toughness for both materials. Higher values of toughness and elongation percentage have been achieved by increasing the Ti content; however, this melioration is more significant in the vertical samples. Besides, the horizontal samples generally show better mechanical properties, particularly in load-bearing applications, where the absorbed energy before failure should be high.

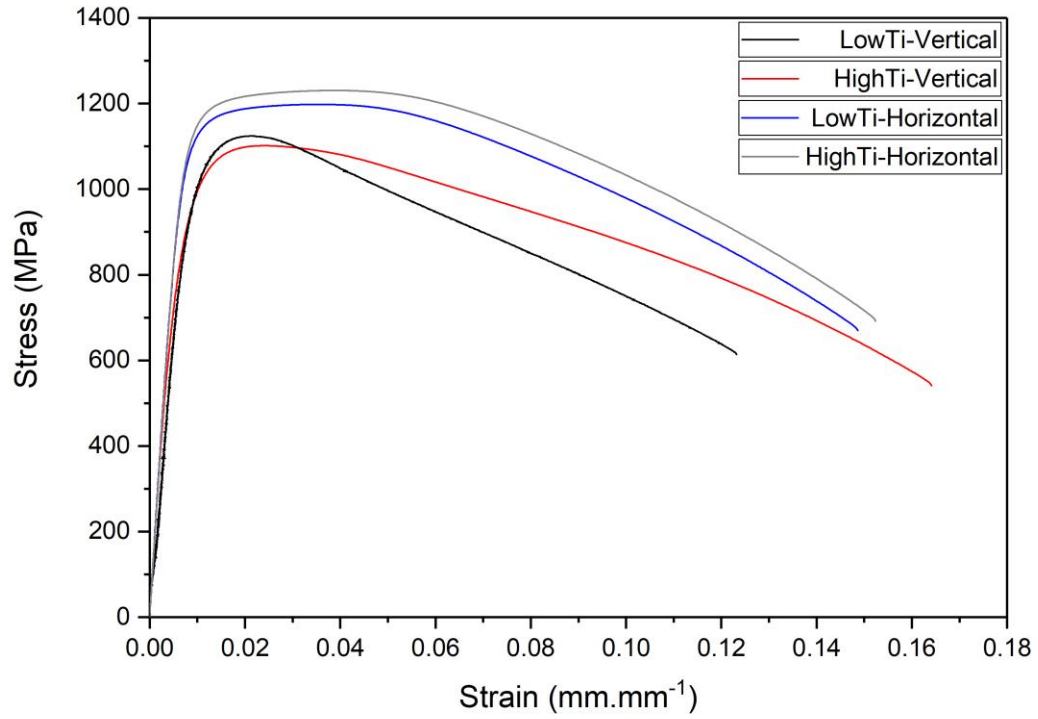


Fig 2. 14 Stress-strain curves of the AM as-built samples.

Table 2. 4. Mechanical properties of the AM LowTi and HighTi tensile samples.

Sample	E (GPa)	YS (MPa)	UTS (MPa)	Failure elongation (%)	Toughness (MJ.m <sup>-3</sup> )
<b>LowTi – Horizontal</b>	173.117±5.3	988.48±177.3	1196.37±4.6	15.1±1.0	150.19
<b>HighTi – Horizontal</b>	172.997±1.3	1113.79±11.0	1217.72±11.7	15.39±1.2	159.22
<b>LowTi – Vertical</b>	140.144±1.0	1033.438±12.6	1134.453±22.6	11.68 ±1.0	108.66
<b>HighTi – Vertical</b>	146.631±5.5	962.66±12	1087.31±13.2	15.49±1.0	144.47

Table 2. 5. Comparison between mechanical properties of the AM maraging steel at various Ti contents, reported in some studies.

	Ti content (wt.%)	Hardness (HRC)	UTS (MPa)	Failure elongation (%)
<b>Current study – V/H (LowTi)</b>	0.72	33.3	1134/1196	11.7/15.1
<b>Current study – V/H (HighTi)</b>	1.17	40.3	1087/1217	15.5/15.4
<b>Mooney <i>et al.</i> (LowTi) [11,16]</b>	0.87	39.8	1174	15.7
<b>Mooney <i>et al.</i> (HighTi) [11,16]</b>	1.05	38.8	1172	12.9
<b>Casalino <i>et al.</i> [19]</b>	0.88	35.0	1192	8.0
<b>Yuchao bai <i>et al.</i> [20,21]</b>	0.80	39.8	1178	7.9
<b>Casati <i>et al.</i> [22]</b>	0.70	38.8	1187	6.1
<b>Mutua <i>et al.</i> [60]</b>	0.62	38.1	1125	10.4
<b>Kučerová <i>et al.</i> [27]</b>	0.60-0.80	38.8	1050	8.0
<b>Bhardwaj <i>et al.</i> [17,23]</b>	0.60-0.80	39.8	1021	19.0

The fractographs of the as-built LowTi and HighTi samples are given in Figure 2.15., where both vertical and horizontal samples show ductile fracture identified with deep dimples generating during the plastic deformation (see subfigures 15a-c). In some locations, microvoids formation and coalescence are responsible for the formation of abnormally huge dimples (blue arrows). An area marked with dash oval in the HighTi fractographs experienced decohesion during the tensile testing, which can be assigned to a scan track of the melt pools exposed to a large plastic deformation occurring through the necked area. This fact has been also reported in some studies [6,46,69]. The intergranular fracture is the dominant mode throughout the surface, locally associated with wavy-like feature of plastic deformation over some narrow places next to the edges (red arrows). The

wavy feature can be ascribed to a very small change in stress at its maximum value over a certain range of strain in the horizontally printed samples. This is due to a balance between softening and hardening phenomena, which are competitive at peak stress. The vertical HighTi sample shows a lower area fraction of abnormally grown microvoids, higher uniformity in ductile fracture, and less probability of abrupt decohesion.

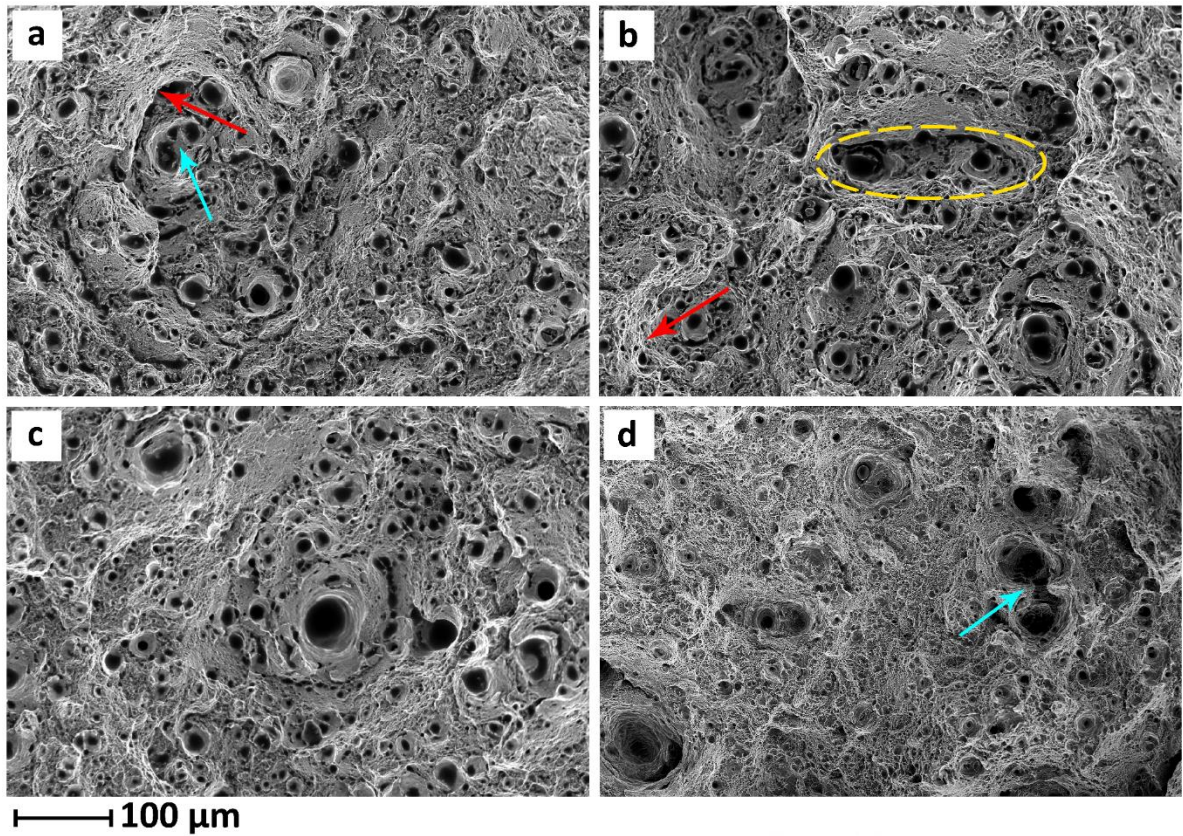


Fig 2. 15 The SEM fractographs of (a) LowTi-horizontal, (b) HighTi-horizontal, (c) LowTi-vertical, and (d) HighTi-vertical samples.

## 2.4. Conclusions

C300 maraging steels with two various Ti contents was horizontally and vertically produced via the LPBF process, and their microstructure, mechanical properties, fracture

behavior, texture and orientation were studied. The following conclusions can be drawn from this study:

- i. The volume fraction of martensite ( $\alpha'$ ) in both LowTi and HighTi powders is almost the same, while the HighTi AM sample shows lower percentage of  $\alpha'$  compared to the LowTi AM sample. This difference is resulted by higher severity of Ti rejection into the intergranular regions of the HighTi alloy microstructure, and consequently enhancing the number of high potential sites of the retained austenite ( $\gamma$ ).
- ii. The volume fraction of  $\gamma$  phase in the C300 alloy powders is much higher than that in the AM samples due to higher solid/liquid interface velocity (R) and partition coefficient (k) of the solute elements during the LPBF process rather than gas atomization, which brings higher probability of the solute trapping or banding effect. Therefore, more substitutional atoms are trapped within the lattice structure, bringing higher hardenability in the additively manufactured samples.
- iii. The micrographs of both LowTi and HighTi AM samples show a combination of columnar and equiaxed morphologies due to variation of the G and R over the length of the AM product, where the columnar grains are mostly formed at high G/R values, while equiaxed grains nucleate and grow at low G/R and high constitutional undercooling ( $\Delta T_c$ ).
- iv. Both manufactured samples show similar fractions of the columnar and equiaxed grains in their microstructure, in which the fraction of columnar and equiaxed grains are 12% and 88%, respectively. The grain size distribution of the LowTi and HighTi samples are reported within 1 to 5  $\mu\text{m}^2$ .

- v. The HighTi sample shows numerous ultra-fine CoNi precipitates through its TEM micrograph, which is a metastable phase in the maraging steels. Therefore, it has been postulated that this phase can be transformed to more stable precipitates like Ni<sub>3</sub>Ti, FeTi, and CoTi during direct ageing, where Ti element can diffuse from the intergranular to transgranular regions induced by a sufficient holding time at high temperatures.
- vi. The hardness of the HighTi sample shows higher values than the LowTi one. The HighTi sample also reveals higher dislocation density that provides higher ultimate tensile strength. The stress-strain curve of the HighTi sample shows more scattered trend between the horizontal and vertical directions in comparison with the LowTi sample. In terms of toughness, UTS, and elongation, the samples horizontally printed overall present better mechanical properties and propose steeper rate of strain hardening before the peak stress. The mode of fracture for both materials is ductile transgranular accompanied by dimples formation.

## 2.5. References

- [1] W. Sha, Z. Guo, Maraging steels: Modelling of microstructure, properties and applications, Woodhead Publishing Limited, 2009.
- [2] E.I. Galindo-Nava, W.M. Rainforth, P.E.J. Rivera-Díaz-del-Castillo, Predicting microstructure and strength of maraging steels: Elemental optimisation, *Acta Mater.* 117 (2016) 270–285. <https://doi.org/10.1016/j.actamat.2016.07.020>.
- [3] M.K. El-Fawkhry, M. Eissa, A. Fathy, T. Mattar, Development of Maraging Steel with Retained Austenite in Martensite Matrix, *Mater. Today Proc.* 2 (2015) S711–

- S714. <https://doi.org/10.1016/j.matpr.2015.07.381>.
- [4] D.G. Lee, K.C. Jang, J.M. Kuk, I.S. Kim, The influence of niobium and aging treatment in the 18% Ni maraging steel, *J. Mater. Process. Technol.* 162–163 (2005) 342–349. <https://doi.org/10.1016/j.jmatprotec.2005.02.102>.
- [5] S.J. Midea, G.D. Pfaffmann, *Heat Treating: Including Steel Heat Treating in the New Millennium*, ASM International, 2000.
- [6] S. Shamsdini, S. Shakerin, A. Hadadzadeh, B.S. Amirkhiz, M. Mohammadi, A trade-off between powder layer thickness and mechanical properties in additively manufactured maraging steels, *Mater. Sci. Eng. A.* 776 (2020) 139041. <https://doi.org/10.1016/j.msea.2020.139041>.
- [7] M. Ahmed, I. Nasim, S.W. Husain, Influence of nickel and molybdenum on the phase stability and mechanical properties of maraging steels, *J. Mater. Eng. Perform.* 3 (1994) 248–254. <https://doi.org/10.1007/BF02645850>.
- [8] K.S. Cho, S.S. Park, D.H. Choi, H. Kwon, Influence of Ti addition on the microstructure and mechanical properties of a 5% Cr-Mo-V steel, *J. Alloys Compd.* 626 (2015) 314–322. <https://doi.org/10.1016/j.jallcom.2014.12.040>.
- [9] C. Du, R. Petrov, M.G.D. Geers, J.P.M. Hoefnagels, Lath martensite plasticity enabled by apparent sliding of substructure boundaries, *Mater. Des.* 172 (2019) 1–12. <https://doi.org/10.1016/j.matdes.2019.107646>.
- [10] C. Tan, K. Zhou, W. Ma, P. Zhang, M. Liu, T. Kuang, Microstructural evolution, nanoprecipitation behavior and mechanical properties of selective laser melted high-performance grade 300 maraging steel, *Mater. Des.* 134 (2017) 23–34. <https://doi.org/10.1016/j.matdes.2017.08.026>.

- [11] B. Mooney, K.I. Kourousis, R. Raghavendra, D. Agius, Process phenomena influencing the tensile and anisotropic characteristics of additively manufactured maraging steel, *Mater. Sci. Eng. A.* 745 (2019) 115–125. <https://doi.org/10.1016/j.msea.2018.12.070>.
- [12] E. Cyr, H. Asgari, S. Shamsdini, M. Purdy, K. Hosseinkhani, M. Mohammadi, Fracture behaviour of additively manufactured MS1-H13 hybrid hard steels, *Mater. Lett.* 212 (2018) 174–177. <https://doi.org/10.1016/j.matlet.2017.10.097>.
- [13] H. Azizi, R. Ghiaasiaan, R. Prager, M.H. Ghoncheh, K.A. Samk, A. Lausic, W. Byleveld, A.B. Phillion, Metallurgical and mechanical assessment of hybrid additively-manufactured maraging tool steels via selective laser melting, *Addit. Manuf.* 27 (2019) 389–397. <https://doi.org/10.1016/j.addma.2019.03.025>.
- [14] X. Xu, S. Ganguly, J. Ding, S. Guo, S. Williams, F. Martina, Microstructural evolution and mechanical properties of maraging steel produced by wire + arc additive manufacture process, *Mater. Charact.* 143 (2018) 152–162. <https://doi.org/10.1016/j.matchar.2017.12.002>.
- [15] A. Ebrahimi, M. Mohammadi, Numerical tools to investigate mechanical and fatigue properties of additively manufactured MS1-H13 hybrid steels, *Addit. Manuf.* 23 (2018) 381–393. <https://doi.org/10.1016/j.addma.2018.07.009>.
- [16] B. Mooney, K.I. Kourousis, R. Raghavendra, Plastic anisotropy of additively manufactured maraging steel: Influence of the build orientation and heat treatments, *Addit. Manuf.* 25 (2019) 19–31. <https://doi.org/10.1016/j.addma.2018.10.032>.
- [17] T. Bhardwaj, M. Shukla, Direct Metal Laser Sintering of Maraging Steel: Effect of Building Orientation on Surface Roughness and Microhardness, *Mater. Today Proc.*

- 5 (2018) 20485–20491. <https://doi.org/10.1016/j.matpr.2018.06.425>.
- [18] K. Kempen, E. Yasa, L. Thijs, J.P. Kruth, J. Van Humbeeck, Microstructure and mechanical properties of selective laser melted 18Ni-300 steel, *Phys. Procedia*. 12 (2011) 255–263. <https://doi.org/10.1016/j.phpro.2011.03.033>.
- [19] G. Casalino, S.L. Campanelli, N. Contuzzi, A.D. Ludovico, Experimental investigation and statistical optimisation of the selective laser melting process of a maraging steel, *Opt. Laser Technol.* 65 (2015) 151–158. <https://doi.org/10.1016/j.optlastec.2014.07.021>.
- [20] Y. Bai, D. Wang, Y. Yang, H. Wang, Effect of heat treatment on the microstructure and mechanical properties of maraging steel by selective laser melting, *Mater. Sci. Eng. A*. 760 (2019) 105–117. <https://doi.org/10.1016/j.msea.2019.05.115>.
- [21] Y. Bai, Y. Yang, D. Wang, M. Zhang, Influence mechanism of parameters process and mechanical properties evolution mechanism of maraging steel 300 by selective laser melting, *Mater. Sci. Eng. A*. 703 (2017) 116–123. <https://doi.org/10.1016/j.msea.2017.06.033>.
- [22] R. Casati, J.N. Lemke, A. Tuissi, M. Vedani, Aging behaviour and mechanical performance of 18-Ni 300 steel processed by selective laser melting, *Metals (Basel)*. 6 (2016) 1–13. <https://doi.org/10.3390/met6090218>.
- [23] T. Bhardwaj, M. Shukla, Effect of laser scanning strategies on texture, physical and mechanical properties of laser sintered maraging steel, *Mater. Sci. Eng. A*. 734 (2018) 102–109. <https://doi.org/10.1016/j.msea.2018.07.089>.
- [24] T. DebRoy, H.L. Wei, J.S. Zuback, T. Mukherjee, J.W. Elmer, J.O. Milewski, A.M. Beese, A. Wilson-Heid, A. De, W. Zhang, Additive manufacturing of metallic

- components – Process, structure and properties, *Prog. Mater. Sci.* 92 (2018) 112–224. <https://doi.org/10.1016/j.pmatsci.2017.10.001>.
- [25] G.H. de O. Freitas, C.A.S. de Oliveira, Effect of Hot Deformation on Microstructure, Hardness and Precipitation Kinetics in a C350 Maraging Steel Modified by Titanium Addition, *Mater. Res.* 21 (2018) 1–9. <https://doi.org/10.1590/1980-5373-mr-2018-0120>.
- [26] E.A. Jäggle, Z. Sheng, P. Kürnsteiner, S. Ocylok, A. Weisheit, D. Raabe, Comparison of maraging steel micro- and nanostructure produced conventionally and by laser additive manufacturing, *Materials (Basel)*. 10 (2017) 2–15. <https://doi.org/10.3390/ma10010008>.
- [27] L. Kučerová, I. Zetková, A. Jandová, M. Bystrianský, Microstructural characterisation and in-situ straining of additive-manufactured X3NiCoMoTi 18-9-5 maraging steel, *Mater. Sci. Eng. A.* 750 (2019) 70–80. <https://doi.org/10.1016/j.msea.2019.02.041>.
- [28] N. Takata, R. Nishida, A. Suzuki, M. Kobashi, M. Kato, Crystallographic features of microstructure in maraging steel fabricated by selective laser melting, *Metals (Basel)*. 8 (2018) 1–10. <https://doi.org/10.3390/met8060440>.
- [29] M. Schober, R. Schnitzer, H. Leitner, Precipitation evolution in a Ti-free and Ti-containing stainless maraging steel, *Ultramicroscopy*. 109 (2009) 553–562. <https://doi.org/10.1016/j.ultramic.2008.10.016>.
- [30] P. Bajaj, A. Hariharan, A. Kini, P. Kürnsteiner, D. Raabe, E.A. Jäggle, Steels in additive manufacturing: A review of their microstructure and properties, *Mater. Sci. Eng. A.* 772 (2020) 138633. <https://doi.org/10.1016/j.msea.2019.138633>.

- [31] ASM-International, ed., Properties and Selection: Irons, Steels, and High-Performance Alloys, 10th ed., 2006. <https://doi.org/10.31399/asm.hb.mhde2.a0003107>.
- [32] ASTM-International, ASTM E1479-16 Standard Practice for Describing and Specifying Inductively Coupled Plasma Atomic Emission Spectrometers, 2016.
- [33] ASTM-International, ASTM E1097-12 Standard Guide for Determination of Various Elements by Direct Current Plasma Atomic Emission Spectrometry, 2017.
- [34] ASTM-International, ASTM E1019-11 Standard test methods for determination of carbon, sulfur, nitrogen, and oxygen in steel, iron, nickel, and cobalt alloys by various combustion and fusion techniques, 2018.
- [35] E.O.S.N.I.D. Sheet, EOS GmbH-Electro Optical Systems, (2014).
- [36] C.N. Kuo, C.K. Chua, P.C. Peng, Y.W. Chen, S.L. Sing, S. Huang, Y.L. Su, Microstructure evolution and mechanical property response via 3D printing parameter development of Al–Sc alloy, *Virtual Phys. Prototyp.* 15 (2020) 120–129. <https://doi.org/10.1080/17452759.2019.1698967>.
- [37] M. Huang, Z. Zhang, P. Chen, Effect of selective laser melting process parameters on microstructure and mechanical properties of 316L stainless steel helical micro-diameter spring, *Int. J. Adv. Manuf. Technol.* 104 (2019) 2117–2131. <https://doi.org/10.1007/s00170-019-03928-3>.
- [38] Z. Sun, X. Tan, S.B. Tor, C.K. Chua, Simultaneously enhanced strength and ductility for 3D-printed stainless steel 316L by selective laser melting, *NPG Asia Mater.* 10 (2018) 127–136. <https://doi.org/10.1038/s41427-018-0018-5>.
- [39] P. Laakso, T. Riipinen, A. Laukkanen, T. Andersson, A. Jokinen, A. Revuelta, K.

- Ruusuvuori, Optimization and simulation of SLM process for high density H13 tool steel parts, *Phys. Procedia.* 83 (2016) 26–35. <https://doi.org/10.1016/j.phpro.2016.08.004>.
- [40] M. Narvan, K.S. Al-Rubaie, M. Elbestawi, Process-structure-property relationships of AISI H13 tool steel processed with selective laser melting, *Materials (Basel)*. 12 (2019) 1–20. <https://doi.org/10.3390/ma12142284>.
- [41] W. Yu, S. Leong, C. Kai, X. Tian, Influence of re-melting on surface roughness and porosity of AlSi10Mg parts fabricated by selective laser melting, *J. Alloys Compd.* 792 (2019) 574–581. <https://doi.org/10.1016/j.jallcom.2019.04.017>.
- [42] A. Salmi, E. Atzeni, A. Salmi, E. Atzeni, Residual stress analysis of thin AlSi10Mg parts produced by Laser Powder Bed Fusion Residual stress analysis of thin AlSi10Mg parts produced by Laser Powder Bed Fusion, *Virtual Phys. Prototyp.* 0 (2019) 1–13. <https://doi.org/10.1080/17452759.2019.1650237>.
- [43] ASTM-International, ASTM E8/E8M-16a standard test methods for tension testing of metallic materials, 2016.
- [44] C. Liu, Z. Zhao, D.O. Northwood, Y. Liu, A new empirical formula for the calculation of MS temperatures in pure iron and super-low carbon alloy steels, *J. Mater. Process. Technol.* 113 (2001) 556–562. [https://doi.org/10.1016/S0924-0136\(01\)00625-2](https://doi.org/10.1016/S0924-0136(01)00625-2).
- [45] A.M. Mullis, L. Farrell, R.F. Cochrane, N.J. Adkins, Estimation of cooling rates during close-coupled gas atomization using secondary dendrite arm spacing measurement, *Metall. Mater. Trans. B Process Metall. Mater. Process. Sci.* 44 (2013) 992–999. <https://doi.org/10.1007/s11663-013-9856-2>.

- [46] H. Asgari, M. Mohammadi, Microstructure and mechanical properties of stainless steel CX manufactured by Direct Metal Laser Sintering, *Mater. Sci. Eng. A.* 709 (2018) 82–89. <https://doi.org/10.1016/j.msea.2017.10.045>.
- [47] D.M. Stefanescu, *Science and engineering of casting solidification: Third edition*, 2015. <https://doi.org/10.1007/978-3-319-15693-4>.
- [48] M.. Glicksman, *Principles of Solidification: An Introduction to Modern Casting and Crystal Growth Concepts*, Springer, 2011. <https://doi.org/10.1017/CBO9781107415324.004>.
- [49] T. Saito, Y. Kawai, K. Maruya, M. Maki, Diffusion of Some Alloying Elements in Liquid Iron, *Sci. Reports Res. Institutes, Tohoku Univ. Ser. A, Physics, Chem. Metall.* (1959) 401–410.
- [50] Z. Liu, H. Fredriksson, On the kinetics of carbide precipitation during reaction between graphite and Fe-Ti liquids under microgravity, *Metall. Mater. Trans. A Phys. Metall. Mater. Sci.* 28 (1997) 707–719. <https://doi.org/10.1007/s11661-997-0057-y>.
- [51] P. Mohammadpour, A. Plotkowski, A.B. Phillion, Revisiting solidification microstructure selection maps in the frame of additive manufacturing, *Addit. Manuf.* 31 (2020) 100936. <https://doi.org/10.1016/j.addma.2019.100936>.
- [52] R. Zhang, T. Jing, W. Jie, B. Liu, Phase-field simulation of solidification in multicomponent alloys coupled with thermodynamic and diffusion mobility databases, *Acta Mater.* 54 (2006) 2235–2239. <https://doi.org/10.1016/j.actamat.2006.01.029>.
- [53] O. Hunziker, Theory of plane front and dendritic growth in multicomponent alloys,

- Acta Mater. 49 (2001) 4191–4203. [https://doi.org/10.1016/S1359-6454\(01\)00313-5](https://doi.org/10.1016/S1359-6454(01)00313-5).
- [54] P. Kürsteiner, M.B. Wilms, A. Weisheit, P. Barriobero-Vila, E.A. Jäggle, D. Raabe, Massive nanoprecipitation in an Fe-19Ni-xAl maraging steel triggered by the intrinsic heat treatment during laser metal deposition, *Acta Mater.* 129 (2017) 52–60. <https://doi.org/10.1016/j.actamat.2017.02.069>.
- [55] G. Krauss, *Steels: processing, structure, and performance*, Second, 2015. <https://doi.org/10.5860/choice.43-6550>.
- [56] G.. Totten, *Steel Heat treatment handbook*, Second, Taylor & Francis, 2006.
- [57] R. Mahshid, H.N. Hansen, K.L. Højbjerg, Strength analysis and modeling of cellular lattice structures manufactured using selective laser melting for tooling applications, *Mater. Des.* 104 (2016) 276–283. <https://doi.org/10.1016/j.matdes.2016.05.020>.
- [58] Y. Lian, Z. Gan, C. Yu, D. Kats, W.K. Liu, G.J. Wagner, A cellular automaton finite volume method for microstructure evolution during additive manufacturing, *Mater. Des.* 169 (2019) 107672. <https://doi.org/10.1016/j.matdes.2019.107672>.
- [59] F. Hengsbach, P. Koppa, K. Duschik, M.J. Holzweissig, M. Burns, J. Nellesen, W. Tillmann, T. Tröster, K.P. Hoyer, M. Schaper, Duplex stainless steel fabricated by selective laser melting - Microstructural and mechanical properties, *Mater. Des.* 133 (2017) 136–142. <https://doi.org/10.1016/j.matdes.2017.07.046>.
- [60] J. Mutua, S. Nakata, T. Onda, Z.C. Chen, Optimization of selective laser melting parameters and influence of post heat treatment on microstructure and mechanical properties of maraging steel, *Mater. Des.* 139 (2018) 486–497.

<https://doi.org/10.1016/j.matdes.2017.11.042>.

- [61] H. Fayazfar, M. Salarian, A. Rogalsky, D. Sarker, P. Russo, V. Paserin, E. Toyserkani, A critical review of powder-based additive manufacturing of ferrous alloys: Process parameters, microstructure and mechanical properties, *Mater. Des.* 144 (2018) 98–128. <https://doi.org/10.1016/j.matdes.2018.02.018>.
- [62] S.G. Shabestari, M.H. Ghoncheh, Investigation on the Effect of Cooling Rate on Hot Tearing Susceptibility of Al2024 Alloy Using Thermal Analysis, *Metall. Mater. Trans. B Process Metall. Mater. Process. Sci.* 46 (2015) 2438–2448. <https://doi.org/10.1007/s11663-015-0450-7>.
- [63] A. Hadadzadeh, B.S. Amirkhiz, J. Li, M. Mohammadi, Columnar to equiaxed transition during direct metal laser sintering of AlSi10Mg alloy: Effect of building direction, *Addit. Manuf.* 23 (2018) 121–131. <https://doi.org/10.1016/j.addma.2018.08.001>.
- [64] M. Rappaz, J.M. Drezet, M. Gremaud, A new hot-tearing criterion, *Metall. Mater. Trans. A Phys. Metall. Mater. Sci.* 30 (1999) 449–455. <https://doi.org/10.1007/s11661-999-0334-z>.
- [65] M. Rappaz, A. Jacot, W.J. Boettinger, Last-stage solidification of alloys: Theoretical model of dendrite-arm and grain coalescence, *Metall. Mater. Trans. A Phys. Metall. Mater. Sci.* 34 A (2003) 467–479. <https://doi.org/10.1007/s11661-003-0083-3>.
- [66] A. Takeuchi, A. Inoue, Classification of Bulk Metallic Glasses by Atomic Size Difference, Heat of Mixing and Period of Constituent Elements and Its Application to Characterization of the Main Alloying Element, *Mater. Trans.* 46 (2005) 2817–2829.

- [67] J. Tian, M.B. Shahzad, W. Wang, L. Yin, Z. Jiang, K. Yang, Role of Co in formation of Ni-Ti clusters in maraging stainless steel, *J. Mater. Sci. Technol.* 34 (2018) 1671–1675. <https://doi.org/10.1016/j.jmst.2018.04.020>.
- [68] C. Dharmendra, R. Alaghmandfard, A. Hadadzadeh, B.S. Amirkhiz, M. Mohammadi, Influence of build orientation on small-scale properties of electron beam melted Ti-6Al-4V, *Mater. Lett.* (2019) 126970. <https://doi.org/10.1016/j.matlet.2019.126970>.
- [69] A. Hadadzadeh, B.S. Amirkhiz, A. Odeshi, M. Mohammadi, Dynamic loading of direct metal laser sintered AlSi10Mg alloy: Strengthening behavior in different building directions, *Mater. Des.* 159 (2018) 201–211. <https://doi.org/10.1016/j.matdes.2018.08.045>.
- [70] A. Pineau, A.A. Benzerga, T. Pardoen, Failure of metals I: Brittle and ductile fracture, *Acta Mater.* 107 (2016) 424–483. <https://doi.org/10.1016/j.actamat.2015.12.034>.
- [71] W.H. Yu, S.L. Sing, C.K. Chua, C.N. Kuo, X.L. Tian, Progress in Materials Science Particle-reinforced metal matrix nanocomposites fabricated by selective laser melting: A state of the art review, 104 (2019) 330–379. <https://doi.org/10.1016/j.pmatsci.2019.04.006>.
- [72] C. Qiu, Z. Wang, A.S. Aladawi, M.A.L. Kindi, I.A.L. Hatmi, H.U. Chen, L.E.I. Chen, Influence of Laser Processing Strategy and Remelting on Surface Structure and Porosity Development during Selective Laser Melting of a Metallic Material, *Metall. Mater. Trans. A.* (n.d.). <https://doi.org/10.1007/s11661-019-05348-0>.
- [73] R. Hertzberg, R. Vinci, J. Hertzberg, Deformation and fracture mechanics of

engineering materials, 2013. <https://doi.org/10.1016/b978-0-08-026167-6.50013-8>.

- [74] C.F. Tey, X. Tan, S.L. Sing, W.Y. Yeong, Additive manufacturing of multiple materials by selective laser melting: Ti-alloy to stainless steel via a Cu-alloy interlayer, *Addit. Manuf.* 31 (2020) 100970. <https://doi.org/10.1016/j.addma.2019.100970>.

# **Chapter 3: Concurrent improvement of strength and ductility in heat-treated C300 maraging steels produced by laser powder bed fusion technique**

## **3.1. Introduction**

Maraging steel is a class of low carbon iron-nickel alloys with high strength and toughness, which are primarily alloyed with Ni, as well as Co, Mo, Ti, and Al [1][2]. The ultra-high-strength of this class of material is achieved by aging treatment resulted in the formation of intermetallic precipitates such as Ni<sub>3</sub>Ti [3][4]. High strength and superior toughness of maraging steels made them suitable candidates for demanding applications such as aerospace, marine, nuclear, tooling, and transportation [5][6][7]. In this category, maraging steel 300 (300 is the yield strength in ksi) is a traditional maraging steel grade with 18 wt.% Ni along with 8.5-9.5 wt.% Co, 4.6-5.2 wt.% Mo and smaller amounts of Ti and Al [5][8].

Recently, additive manufacturing (AM) techniques have been widely used to manufacture maraging steels [9][10]. Laser powder bed fusion technique (LPBF) is one of the AM procedures to fabricate three-dimensional objects directly from a powder or wire feedstock using a computer aided design (CAD) model [11][12]. Different thermal gradient, cooling rates and solidification front velocities across the melt pool results in evolution of a heterogeneous microstructure (both chemical and structural) during LPBF [13] [14]. As a result of this effect a very fine cellular structure has been formed during LPBF reportedly improving the mechanical behavior of the manufactured parts [15]. However, in the LPBF process, due to the large thermal gradients, residual stresses

developed in as-built samples whereby some cracks may be created within the material [16][17][18]. To relieve these high residual stresses within the LPBF products, usually subsequent heat treatments needed after the LPBF process [19]. On the other hand, to optimize the physical and mechanical properties of maraging steel, it is essential to understand aging behavior during the heat treatment process [20]. In maraging steel, heat treatment is an effective way to improve mechanical properties through the formation of intermetallic precipitates [21]. Solution treatment/aging [22] and direct aging [23] are two common post heat treatment procedures that were introduced for LPBF of maraging steel. Solution treatment which is heating to temperature higher than austenite finish temperature (750 °C), results in the elimination of austenite phase. However, aging results in the formation of precipitates and martensite to austenite reversion.

To date, several studies have been carried out to investigate the heat treatment process of additively manufactured maraging steel. For example, Conde *et al.* [24] studied the effect of different heat treatment schedules on LPBF-maraging steel 300. Their results showed that the promotion of martensite-to-austenite reversion is beneficial to enhance the ductility and toughness of maraging steel parts. In another study, Conde *et al.* [10] investigated austenite reversion in maraging steel 300 produced by selective laser melting. They concluded that martensite-to-austenite reversion between 610 and 690 °C results in gradual martensite to austenite reversion with high thermal stability. Mooney *et al.* [25] investigated different heat-treatment procedures on LPBF-maraging steel 300 to identify the optimum combinations of time and temperature, which can reduce anisotropy. They reported that, aging at 490 °C for 8 hours offered an optimal strength (yield strength ( $R_{p0.2}$ )>1900 MPa) whereas aging at 525 °C for 8 hours provided a trade-off between yield

strength and ductility ( $R_{p0.2} > 1700$  MPa and  $A_t \approx 10\%$ ). Mutua *et al.* [22] studied the effect of post-heat treatment (solution treatment at 820 °C for 1 h and aging at 460 °C for 5 h) on the microstructure and mechanical properties of maraging steel 300. They found that after solution treatment and aging, the maximum tensile strength obtained was 2033 MPa.

Increasing both the ductility and strength of heat-treated maraging steel parts simultaneously has been a challenge for researchers [26]. It was reported that reverted austenite and precipitation formation are two factors, which affect the mechanical behavior of maraging steels significantly [1][23]. Previous studies on conventional maraging steels reveal that reverted austenite formation and subsequent phase transformation also change the texture development and subsequent mechanical behavior [27][28][29]. Although the previous studies investigated the effect of heat treatment in improving the mechanical behavior of maraging steel, only a few studies have focused on the texture development manufactured by the LPBF process [19][24][22]. Thus, the effect of reverted austenite in the texture development of additively manufactured maraging steel was not studied before. Furthermore, the strength of maraging steels can notably be improved by precipitate formation after heat treatment. Maraging steel is strengthened by the precipitation of intermetallics at temperature of about 455–510 °C. Depending on aging time and temperature, different precipitates such as  $Ni_3Ti$ ,  $Ni_3Mo$ ,  $Ni_3Al$ ,  $Fe_2Mo$  can be embedded in the martensite matrix [14][30]. There are many studies, which focused on precipitate evolution, and strengthening on conventional [20] and additively manufactured [31] maraging steels. However, few studies have been published regarding the effect of chemical composition on precipitate evolution.

Chemical composition can have a significant effect on reverted austenite and precipitation formation. Galindo-Nava *et al.* [32] conducted a critical assessment of the individual contributions of Ni, Cr, Al, and Ti on the mechanical behavior of maraging steels. They concluded that the reverted austenite kinetics promoted by Ni and Ti additions have the highest strengthening effect by precipitating Ni<sub>3</sub>Ti in the matrix. Gray *et al.* [33] studied the effect of chemical composition on the volume fraction and precipitate chemistry of maraging steels. They concluded that decreasing Mo and W elements (crucial elements in forming laves) could reduce the formation of the laves phase and increase the formation of precipitates, which affect mechanical properties. Escobar *et al.* [34] investigated the effect of austenite-stabilizing (Ni, Mn, Cu), ferrite stabilizing (Cr, Mo), and carbide forming elements (Ti, N) on the formation of reverted austenite in super martensitic stainless steels. Their results showed that carbon and titanium have essential roles in stabilization of austenite during the reversion process with precipitation of Ti(C, N).

Despite the available studies on maraging steels, there is a knowledge gap on the effect of chemical composition (Ti content) on reverted austenite and precipitate formation of LPBF-maraging steels. Therefore, in this work, the effect of Ti content on the microstructure and mechanical properties of as-built and heat-treated 18Ni-300 maraging steels produced by LPBF is discussed. Using X-ray diffraction and advanced electron microscopy techniques, the submicron changes of reverted austenite and precipitates are investigated. The heat treatment process of 490° C and 6 h (recommended by EOS GmbH) was chosen for the study.

## 3.2. Experiments

### 3.2.1 Sample preparation

C300 maraging steel powders with a size distribution of 10–50  $\mu\text{m}$  was used for the LPBF process. As given in Table 3.1., the two different metal powders were chosen with 0.72 to 1.17 wt.% titanium content. The chemical composition was identified via an inductively coupled plasma-optical emission spectrometry (ICP-OES), in which an Agilent ICAP 725 was employed. In terms of Ti content, HighTi composition was chosen in such a way to make sure that Ti wt.% is far enough from 0.72 wt. % to avoid the probability of elemental loss during the LPBF. Also, 1.17 wt. % is not too high to induce a significant difference in phase stability and phase transformation.

Table 3. 1. Chemical composition of powders used in this study.

	Elements (wt.%)										
	Ni	Co	Mo	Ti	Si	Mn	C	Al	S	P	Cr
<b>Standard</b>	18.0-	8.5-	4.6-	0.55-	0.1	0.1	0.03	0.05-	0.01	0.01	-
	19.0	9.5	5.2	0.8				0.15			
<b>LowTi</b>	17.98	8.85	4.85	0.72	0.09	0.06	0.016	0.09	0.008	-	0.15
<b>HighTi</b>	17.68	9.26	4.82	1.17	0.06	0.03	0.012	0.11	0.011	-	0.11

Cubic and rod samples were additively manufactured using an EOS M290 additive machine at Additive Metal Manufacturing Inc. (AMM) in Concord, ON. The same process parameters recommended by EOS GmbH [35] to achieve the minimum porosity volume

fraction were used (listed in table 3.2.). Stripe scanning strategy by rotating the laser beam  $67^\circ$  between the successive layers was utilized during the process. Sample cube ( $a=15$  mm) and the rods ( $D=12$  mm,  $L/D=10$ ) were printed on the top of a build plate preheated at  $40^\circ\text{C}$ . Fig. 3.1. shows the schematic of the cubes and rods that were fabricated.

A Calvin 1543 heat treatment chamber was used to perform the heat treatment procedure. The heat treatment schedule recommended by EOS GmbH [35] for the C300 maraging steel consists of heating the sample at  $490^\circ\text{C}$  for 6 h, followed by furnace cooling.

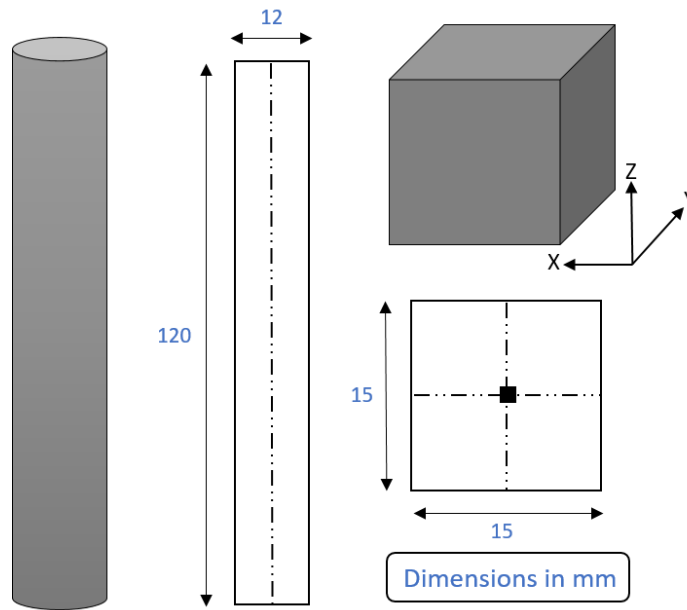


Fig 3. 1 Schematic of cube and rod fabricated samples in the LPBF process.

Table 3. 2. Process parameters of the LPBF process.

Laser power (W)	Scanning speed (mm/s)	Layer thickness ( $\mu\text{m}$ )	Hatch distance ( $\mu\text{m}$ )
285	960	40	110

### 3.2.2. Phase and microstructural analyses

Phase analysis was implemented using the X-ray diffraction (XRD) technique using a Bruker D8 DISCOVER instrument Located at McMaster Analytical X-Ray Diffraction (MAX) facility. This instrument, equipped with DAVINCI.DESIGN diffractometer using a Cobalt Sealed Tube Source ( $\lambda_{\text{avg}} = 1.79026\text{\AA}$ ), was utilized for texture macroanalysis and phase identification.  $2\theta$  range of  $40\text{--}110^\circ$  at 35kV and 45mA power settings was used to collect the data. XRD data were then analyzed with Rietveld analysis through Topas software Version 4.2.

The microstructure of the as-built and heat-treated maraging steels was characterized using scanning electron microscopy (SEM), electron backscatter diffraction (EBSD), and transmission electron microscopy (TEM). SEM and EBSD were performed using a Hitachi SU-70 Field Emission Gun (FEG) ultra-high-resolution. The results were processed with Oxford Instruments HKL Flamenco software. EBSD scans were performed at both low (x300) and high magnifications (x5000) over areas of  $420\ \mu\text{m} \times 315\ \mu\text{m}$  (500 nm step size) and  $30\ \mu\text{m} \times 20\ \mu\text{m}$  (50 nm step size), respectively. A standard metallography procedure was applied to the EBSD samples. Further investigations on the microstructural features of the samples were done using an FEI Tecnai Osiris TEM with a 200 keV X-FEG gun coupled with a Super-X windowless EDS detector. Ion milling was used for preparing the

TEM samples using a Gatan Precision Ion Polishing System (PIPS) model 691. The effect of Ti on microstructural changes was observed in the cube samples to avoid any interference between the effect of building direction and Ti. Therefore, SEM, EBSD and TEM were conducted on the cuboidal samples.

### **3.2.3. Mechanical properties**

A CLARK CRM12 Rockwell hardness machine with a diamond indenter head and 150 kg load was used for hardness measurements. The hardness measurements were performed on the cuboidal samples, where the mean value of at least 10 measurements was reported.

Dog-bone tensile samples with 6mm gauge diameter and 32mm gauge length were machined from the cylindrical rods according to the ASTM E8/E8M-15a standard [36]. A universal hydraulic controlled Instron 1332 machine with a 25 mm extensometer was used for conducting the uniaxial tensile test at a quasi-static  $9 \times 10^{-4} \text{ s}^{-1}$  strain rate. Each test was repeated 3 times to ensure reproducibility. In addition, the gauge sections along the tensile axis of the samples were cut and polished for texture macroanalysis.

## **3.3. Results**

### **3.3.1. Mechanical properties of as-built and heat treated samples**

As the first step to characterize the mechanical properties, the hardness of cube samples is measured on the top surface in as-built and heat-treat conditions. The hardness

for LowTi and HighTi samples in the as-built condition is  $33\pm 1.1$  HRC and  $40\pm 2.4$  HRC, respectively, which shows an increase of about 21.21% with the addition of Ti. Furthermore, the hardness in the heat-treated samples is  $55\pm 0.68$  HRC for LowTi and  $57\pm 0.63$  HRC for HighTi, which shows an increase of about 3.63% with Ti addition after heat treatment. It should be noted that, although hardness HRC values are similar between LowTi and HighTi, there is still a consistent difference between them in HV (649 HV for LowTi and 727 HV for HighTi).

Fig. 3.2. shows a typical stress-strain curve for two HighTi and LowTi maraging steel samples in the as-built and heat-treated conditions. Increasing Ti content in this maraging steel resulted in increasing the ultimate tensile strength (UTS) and elongation compared to LowTi counterpart in both as-built and heat-treat conditions. With regards to mechanical properties in the as-built condition, HighTi samples exhibit higher strength and elongation (1215.51MPa and 14.23%) than the LowTi sample (1192.51MPa and 14.05%). After heat treatment, the UTS was 2057.74MPa for the HighTi sample compared to the LowTi sample with 1938.14MPa (Showing an increase of 6.14%). Furthermore, as can be seen, the tensile ductility decreased after heat treatment to 4.05% and 1.94% for the HighTi and LowTi samples respectively (showing an increase of nearly double).

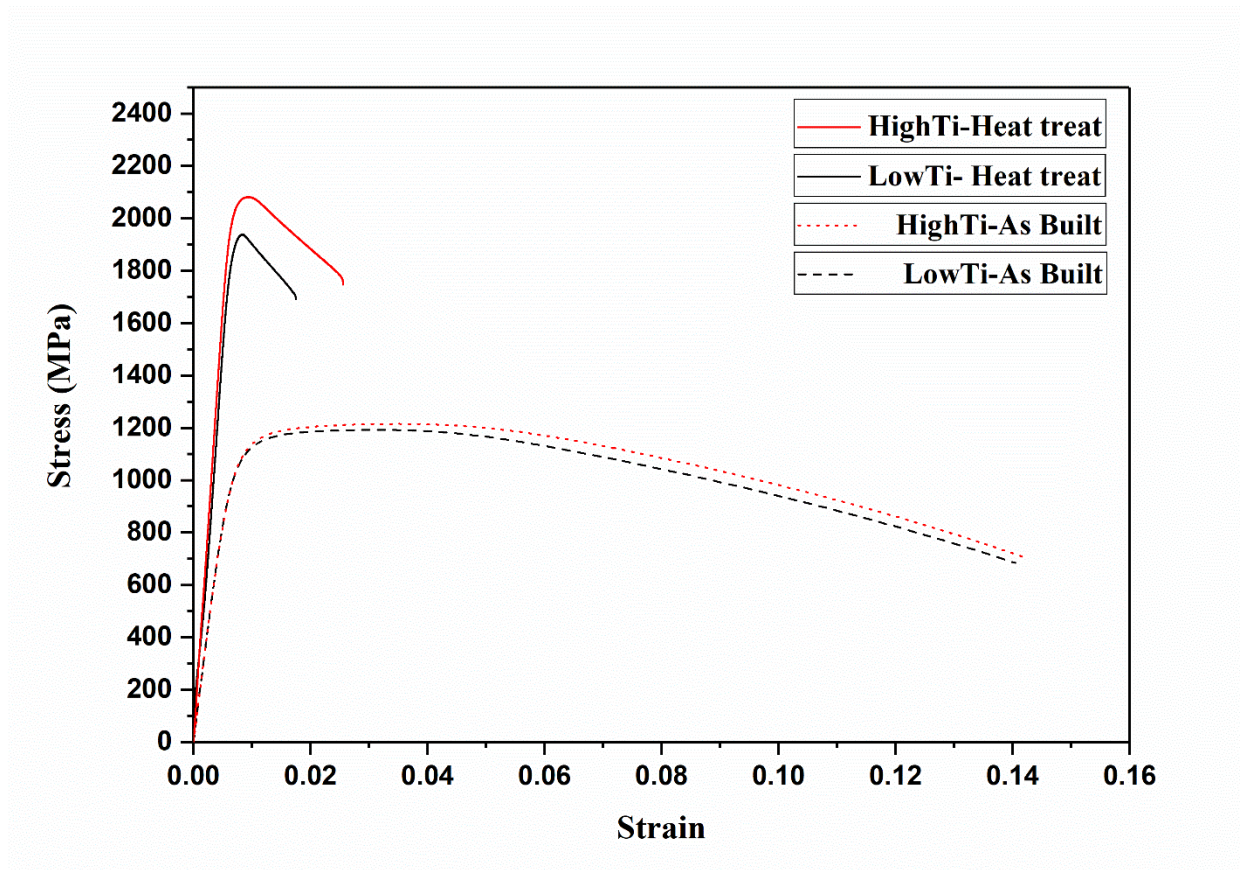


Fig 3. 2 Uniaxial tensile stress-strain curves in as-built and heat-treat conditions.

### 3.3.2. Microstructure

Fig. 3.3. shows the SEM images of the side view (i.e. parallel to building direction (BD)) of the as-built and heat-treated cube samples. As it can be seen, three different zones across the melt pools (MP) can be observed in the microstructure: columnar dendritic structures at the bottom of the melt pools (area (i)), cellular structures between columns (area (iii)), and equiaxed morphology at the top central zone (area (ii)) [23]. Grain boundaries of heat-treated samples are vague and irregular, which can be due to the homogenization of microsegregation at high temperatures during heat treatment [23]. It seems that HighTi heat treated sample has more equiaxed grains based on Fig 3.3(d).

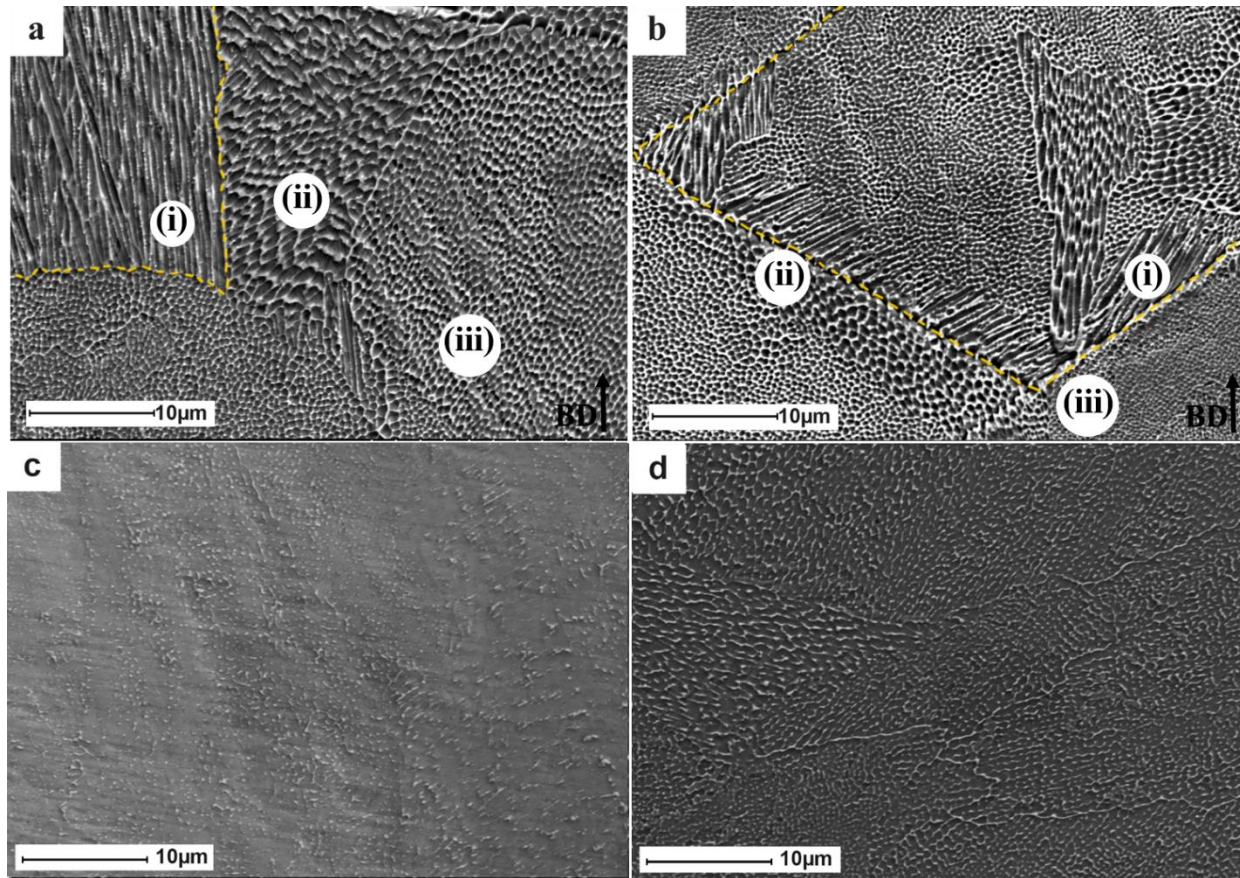


Fig 3. 3 SEM images of the microstructure of the as-built and heat-treated samples. (a) LowTi as-built, b) HighTi as-built, c) LowTi heat treated, d) HighTi heat treated. ((i) Columnar structure at the bottom of the melt pools, (ii) Equiaxed structure at the top of the MP borders, (iii) Cellular structure inside the MP).

### 3.3.3 Crystallographic orientation

To determine the morphology and orientation of the microstructure, electron backscatter diffraction (EBSD) is performed on the longitudinal cross section of the as-built and heat-treated cube samples (i.e parallel to BD). Inverse Pole Figure (IPF-Z maps) are used in these figures since the preferable growth direction is parallel to the building direction in the LPBF process. Fig. 3.4. and 3.5. shows the IPF-Z maps and corresponding pole figures of maraging steel samples in as-built and heat-treated conditions. As can be seen in these two figures, pronounced crystallographic orientation are observed after Ti addition; while a weak texture is seen in the LowTi maraging steel, a preferred {111} texture is developed in HighTi alloy (in both as-built and heat treated conditions). Therefore, by adding Ti,  $\langle 111 \rangle$   $\gamma$  fibre texture (blue color) and a copper component ( $\{112\}$   $\langle 111 \rangle$ ) were developed.

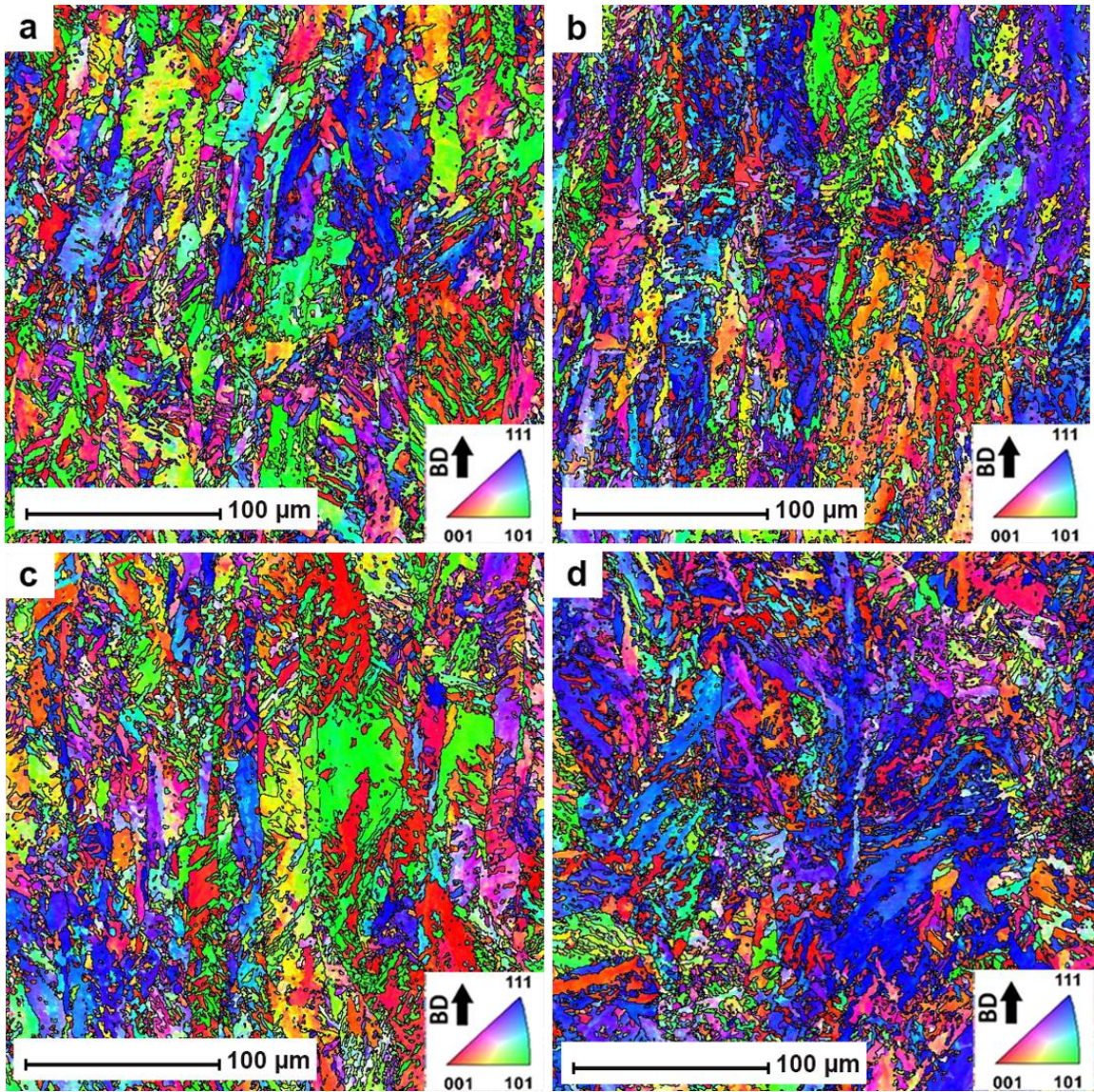


Fig 3. 4 EBSD results of the side of the samples at  $\times 300$  magnification. IPF-Z map of the HighTi and LowTi samples in as-built and heat-treat conditions. Build direction (z-axis) is marked as BD in the IPF maps. (a) LowTi-as built, b) HighTi- as built, c) LowTi heat treat, d) HighTi-heat treat.

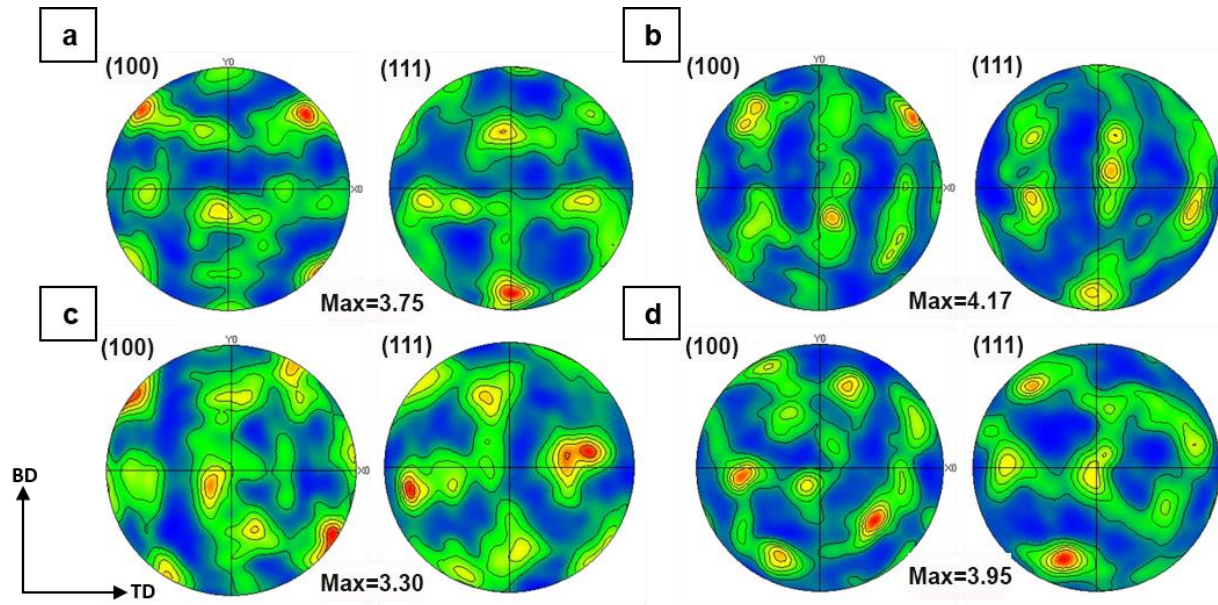


Fig 3. 5 EBSD results of the side of the samples at  $\times 300$  magnification. (100) and (111) Pole figure maps of HighTi and LowTi samples in as-built and heat-treat conditions. (a) LowTi-as built, b) HighTi- as built, c) LowTi heat treat, d) HighTi-heat treat.

To achieve deeper details of crystallographic orientations and fibers, orientation distribution function (ODF) maps in  $\phi = 45^\circ$  section in the as-built and heat-treated conditions were presented in Fig. 6. ODF maps also prove that the Ti addition can change the

crystallographic texture. As can be seen in Fig. 3.5., in the HighTi sample, fibre, and copper texture developed which is consistent with previous analysis. As can be seen by adding Ti, a relatively strong  $\gamma$ -fiber developed, where a strong near-rotated cube texture ( $\{001\}\langle 110\rangle$ ) formed in as-built and heat treated samples for the LowTi sample.

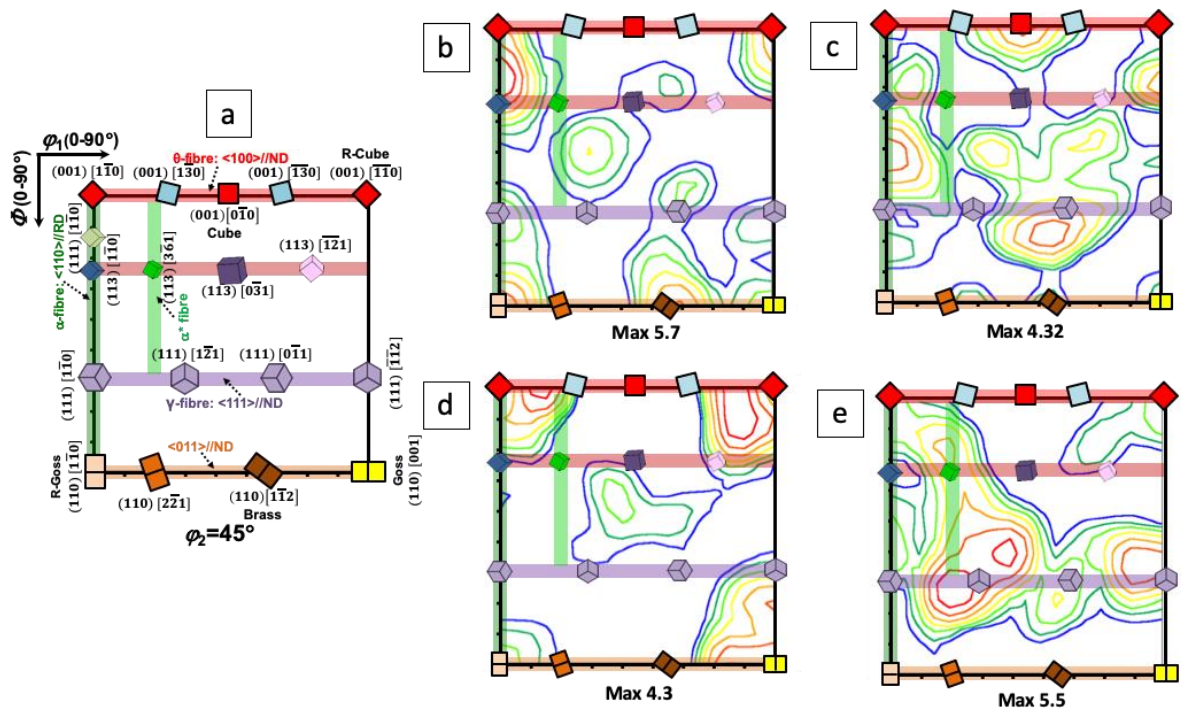


Fig 3. 6 EBSD results of the side of the samples at  $\times 300$ . ODF maps ( $\phi_2=45^\circ$ ) of the HighTi and LowTi samples in as-built and heat-treat conditions. (a) texture component key (b) LowTi-as built, c) HighTi- as built, d) LowTi heat treat, e) HighTi-heat treat.

### 3.3.4. Grain morphology

Oxford Instruments HKL Flamenco software was used for processing the EBSD scans. The fraction of columnar and equiaxed grains was evaluated for both samples before and after the heat treatment from the IPF-Z maps and is shown in Table 3.3. To identify the columnar and equiaxed grains, the grain shape aspect ratio ( $\phi$ ), defined as  $\phi = L_2/L_1$ , is considered, where  $L_1$  is the major axis, and  $L_2$  is the minor axis of an ellipse fitted to each grain, respectively. Columnar grains are determined with  $\phi \leq 0.33$  ( $L_2:L_1=1:3$  and lower), while equiaxed grains are identified by  $\phi > 0.33$  [37]. As can be seen from Table 3.3., equiaxed grains fraction increased after heat treatment for both alloys (about 6.12% for HighTi sample and 8.32% for LowTi sample), which indicates that partial recrystallization occurred.

Table 3. 3. Area fraction of columnar and equiaxed grains in the as-built and heat-treat conditions.

Sample	Fraction of columnar grains	Fraction of equiaxed grains
<b>LowTi-as-built</b>	8.14	91.85
<b>HighTi-as-built</b>	5.80	94.19
<b>LowTi-heat treated</b>	0.50	99.5
<b>HighTi-heat treated</b>	0.37	99.96

### 3.3.5. Phase identification of as-built and heat treated samples

To evaluate the effect of heat treatment on the phase transformation, X-ray diffraction analysis was employed. Fig. 3.7. shows the XRD spectrum in the  $2\theta$  range of

40°-110° for the as-built and heat-treated conditions of both LowTi and HighTi alloys. XRD spectra show that the as-built microstructure of both alloys consists of austenite and martensite. The results show that after heat treatment, no significant change in the intensity of martensite peaks is observed and intensity of {200}, {111}, and {220} peaks of austenite were increased. Furthermore, no sign of the peaks for precipitates were observed in the heat-treated samples, which might be due to the small size and volume fraction of precipitates. During heat treatment, the temperature increased to above  $M_s$ , and some amount of martensite phase in the microstructure transformed back to the austenite, which is called reverted austenite [38].

Table 3.4. shows the volumetric percentage of phases based on Rietveld refinement analysis. As can be noted, after heat treatment, austenite fraction increases significantly for both LowTi and HighTi samples. In the case of LowTi, the austenite volume fraction increased from 2.9% to 8.88%, whereas in the case of HighTi sample, the austenite fraction changed between 3.94% and 17.89%. This shows that heat treatment resulted in an increase of austenite fraction for both alloys, which this increase was about twice for the HighTi alloy.

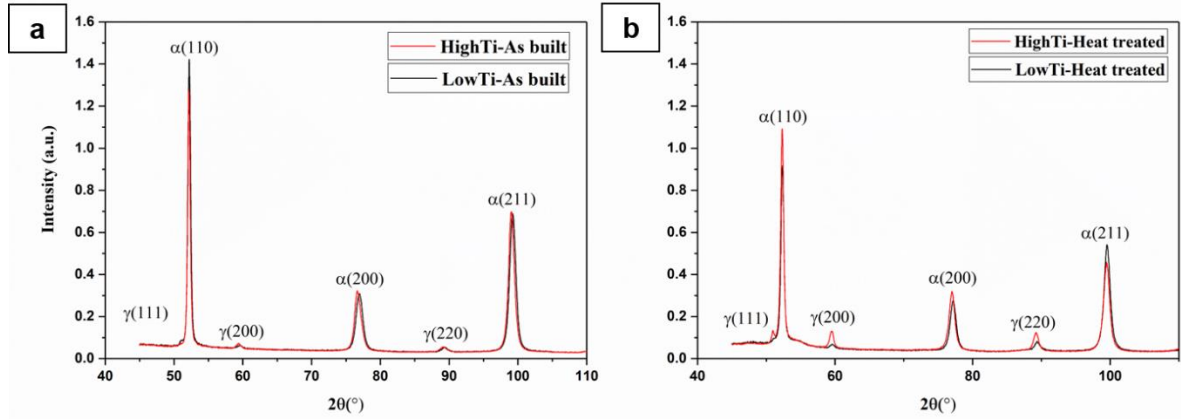


Fig 3. 7 XRD pattern of HighTi and LowTi LPBF-maraging steel samples in (a) as-built and (b) heat-treated conditions.

Table 3. 4. Volumetric percentage of phases in the as-built and heat-treat conditions.

Sample	$\alpha'$ volume fraction (%)	$\gamma$ volume fraction (%)
<b>LowTi as-built</b>	97.03	2.97
<b>HighTi as-built</b>	96.06	3.94
<b>LowTi heat treated</b>	91.12	8.88
<b>HighTi heat treated</b>	82.01	17.89

To analyze the effect of Ti content on the phase fraction of reverted austenite, high magnification EBSD analysis for heat-treated LowTi and HighTi samples was performed. As can be seen in Fig. 3.8., heat-treated maraging steel consists of  $\alpha$ -martensite (red color) and  $\gamma$ -austenite (yellow color) and precipitates (here  $\text{Ni}_3\text{Ti}$  as green color). It is noteworthy to mention that, after heat treatment of 6 h at 490 °C, two types of precipitates ( $\text{Ni}_3\text{Mo}$  and  $\text{Ni}_3\text{Ti}$ ) were reported in maraging steel [23] (one of them identified as hexagonal  $\text{Ni}_3\text{Ti}$  in EBSD maps). The areas near cell boundaries, identified as austenite (yellow spots), are

formed, which all of austenite grains in each sample have same crystallographic orientation; this has been observed before [19][39]. Crystallographic orientations of the austenite grains are changed in LowTi and HighTi samples. In the LowTi sample, all austenite grains have the same  $\langle 100 \rangle$  orientation (red color). However, in the HighTi sample, all austenite grains in this area have the same  $\langle 111 \rangle$  orientation (blue color), which is consistent with the pole figure in 300X magnification (Fig. 4). We can conclude that Ti not only can increase the volume fraction of austenite grains, but also it can change the orientation of austenite grains too. This change of orientation is the reason for the development of fibre texture in the HighTi sample. The difference between the X-ray diffraction and EBSD results in term of phase area fraction is because of significantly smaller areas that were scanned in the EBSD maps (due to the small size of austenite grains, high magnification EBSD was needed). The small austenite grains are detected mainly in intercellular and intercolumnar regions. Previous studies also reported the exclusive presence of austenite at the cell or dendrite boundaries for AM maraging steels [19][40].

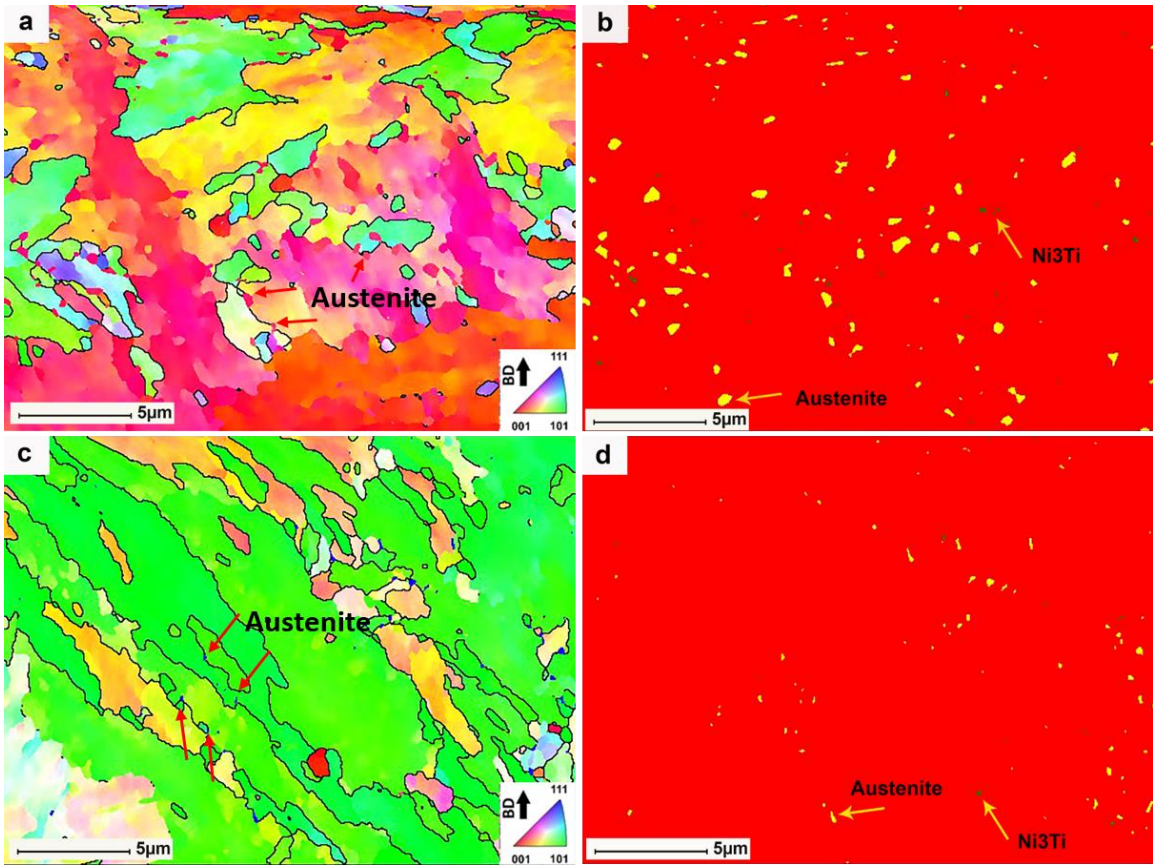


Fig 3. 8 EBSD results of the side of the samples at  $\times 5000$  magnification. (a) IPF-Z map of heat-treated LowTi sample (b) Phase map of heat-treated LowTi sample. (c) IPF-Z map of heat-treated HighTi sample and (d) phase map of heat-treated HighTi sample. Yellow spots represent reverted austenite, and green spots represent  $\text{Ni}_3\text{Ti}$  precipitates.

### 3.3.6. TEM analysis in the heat treated samples

Further analysis is conducted using the TEM technique to study austenite and precipitate formation in maraging steel samples during heat treatment. Fig. 3.9. shows scanning transmission electron microscopy (STEM) image and energy-dispersive X-ray spectroscopy (EDS) mappings of LowTi sample showing chemical composition and

morphology of austenite grains after heat treatment. As can be seen, austenite grains located within intercellular and intercolumnar regions which was seen before [40]. Ni with a high partition coefficient and low diffusion rate has more tendency for trapping in lattice structure. However, Ti with a lower partition coefficient and high diffusion rate, has more tendency to segregate in intercellular and intercolumnar regions [41]. As can be seen, Ti, on the other hand, does not show trapping within the matrix. Intergranular regions are enriched of Ti, Mo and Ni in which Ti in the presence of Ni and Mo promotes the austenite formation. This is the reason for higher fraction of austenite in HighTi sample.

TEM bright field of LowTi sample along with SAAD pattern and dark field images of the matrix (a) and austenite grains (b) are presented in Fig 3.10. It is clear that the martensite matrix that is heavily dislocated contains nano precipitates. However, austenite grains are free of precipitates and dislocations, which was reported before [26].

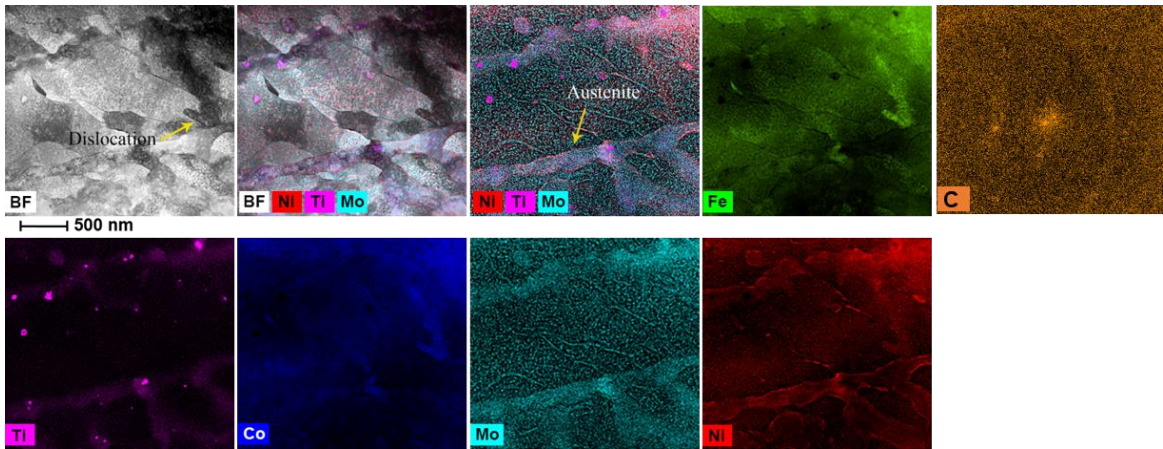


Fig 3. 9 STEM image along with EDS mapping from LowTi heat-treated specimen along with a compositional map of Ni, Ti, Mo showing the distribution of alloying elements in austenite.

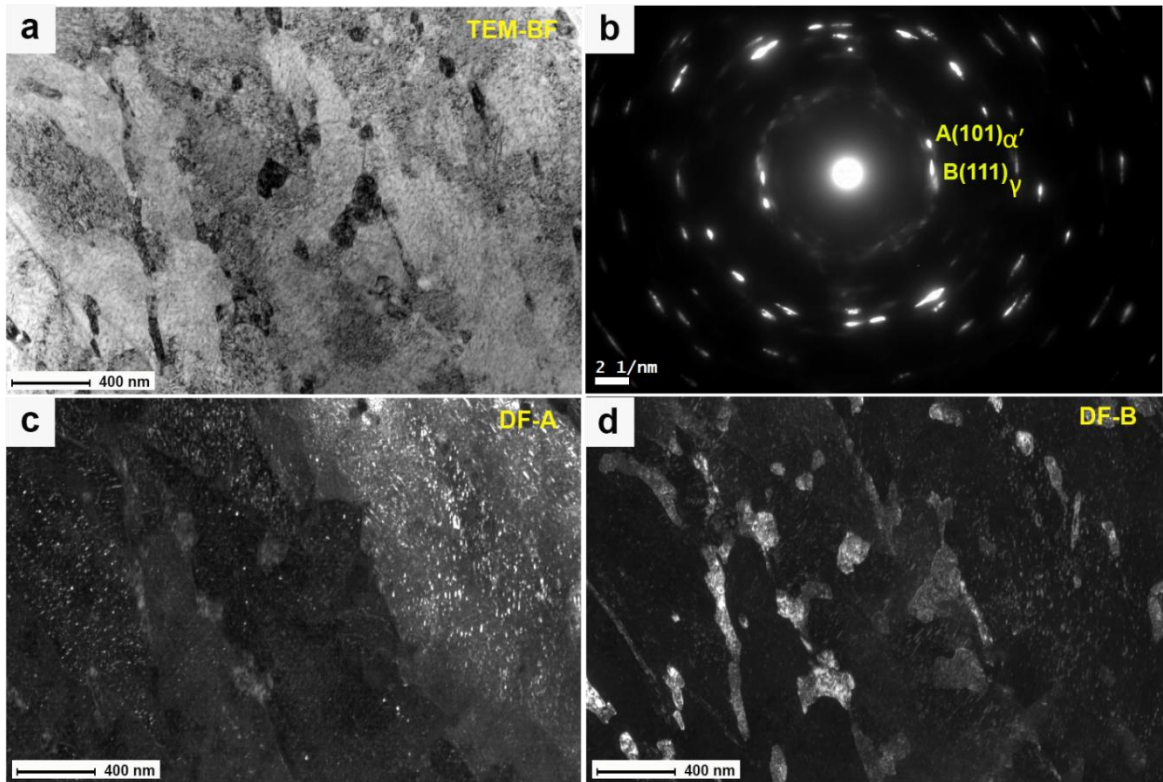


Fig 3. 10 TEM micrograph of LowTi heat-treated maraging steel showing (a) TEM-Bright field, (b) Corresponding SAAD pattern. (c) Dark filed A as matrix, (d) Dark field B as austenite.

To study the effect of heat treatment on the composition of nano-sized precipitates, a high magnification STEM image along with energy-dispersive X-ray spectroscopy (EDS) mappings of the HighTi sample is presented in Fig 3.11. This figure clearly shows the composition and morphology of precipitates in the structure of maraging steel samples. Two types of precipitates are found in this microstructure. First, spherical precipitates enriched in Mo with a lower amount of Ti and Ni, which is reported to be  $Ni_3Mo$ . Second, needle-shaped precipitates enriched in Ti and Ni with a lower amount of Mo, which is proposed to be  $Ni_3Ti$ . Needle-shaped  $Ni_3Ti$  precipitates are observed in both HighTi and LowTi samples, which was reported before in the maraging steel heat-treated

microstructure [23]. The  $\text{Ni}_3\text{Mo}$  precipitates are observed in both LowTi and HighTi samples, were reported by Yen *et al.*[21].

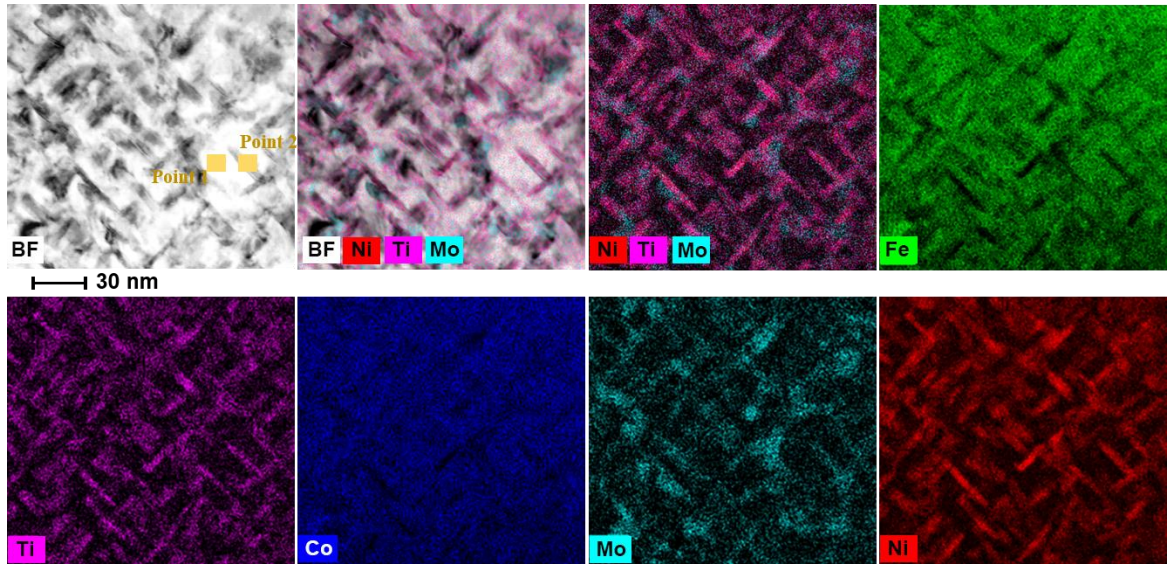


Fig 3. 11 STEM image along with EDS mapping from the HighTi specimen along with a compositional map of Ni, Mo, Ti, showing composition and morphology of precipitates after heat treatment.

Because of precipitate formation during the aging process, the concentration of different elements might change in the matrix. From Table 3.5., it can be seen that the concentration of Mo, Ti, and Ni are generally higher in precipitates. However, the concentration of Fe and Co are lower in the precipitates than in the matrix. It can be confirmed that, two types of precipitates formed during aging,  $\text{Ni}_3\text{Mo}$  and  $\text{Ni}_3\text{Ti}$ .  $\text{Ni}_3\text{Ti}$  forms very quickly during aging, which can act as a nucleation site for  $\text{Ni}_3\text{Mo}$  precipitates [23].

Table 3. 5. Chemical composition (wt. %) by EDS/TEM of heat-treated maraging 300 steel extracted from Fig13.

Elements	Fe	Ni	Mo	Ti	Co
<b>Matrix (point 1)</b>	72.14	14.94	1.59	0.36	10.84
<b>Precipitate (point 2)</b>	48.86	31.34	8.45	3.03	8.22

To study the morphology of precipitates some additional TEM analyses were done on both samples. Fig. 3.12. (a) shows a bright field (BF) micrograph of the LowTi sample, in which needle-shaped precipitates can be seen. The bright region refers to the martensitic matrix, whereas the dark areas represent the dislocation network and precipitates. As can be seen in Fig. 3.12. (b), the diffraction pattern of martensite showing the most intense spots and superlattices, which is related to  $\text{Ni}_3\text{Ti}$  precipitates, are also visible in this image. In addition, dark filed images of A and B diffracted spot are shown. It is worth mentioning that, the dark area represents the martensite, and the distributed white particles are the needle-shaped precipitates found after aging treatment.

Fig. 3.13. (a) shows a bright field (BF) micrograph of the HighTi sample, in which spherical  $\text{Ni}_3\text{Mo}$  precipitates can be seen. Superlattices, which are related to  $\text{Ni}_3\text{Mo}$  precipitates, are visible in Fig. 3.13. (b). In addition, dark filed images of A, B, C diffracted spots are shown where dark area represents the martensite, and the distributed white particles are the spherical precipitates found after aging treatment. At aging above  $450^\circ\text{C}$ , hexagonal  $\eta\text{-Ni}_3\text{Ti}$  is the main precipitate phase responsible for the strengthening of the maraging steels (compared to  $\text{Ni}_3\text{Mo}$ ) [23], which grew along specific orientation direction relative to martensite matrix and make a coherent interface with martensite. The orientation

relationship is reported to be  $\{0001\}_{\text{Ni}_3\text{Ti}} // \langle 001 \rangle_{\text{martensite}}$  and  $\{112\bar{0}\}_{\text{Ni}_3\text{Ti}} // \langle 111 \rangle_{\text{martensite}}$ . It was concluded that, both types of morphologies were found in both HighTi and LowTi samples.

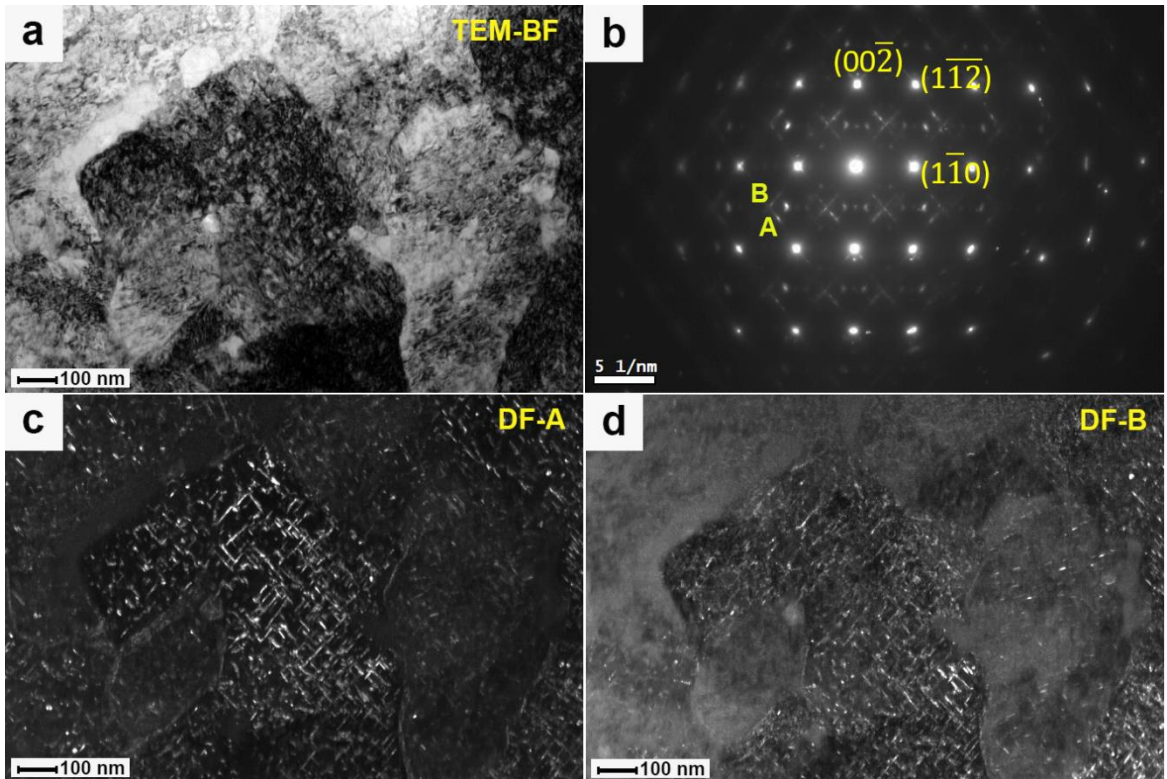


Fig 3. 12 TEM micrograph of LowTi heat-treated maraging steel showing (a) TEM-Bright field of LowTi sample. (b) Corresponding SAAD pattern where the superlattice spots represent needle-shaped precipitates ( $\text{Ni}_3\text{Ti}$ ), (c) Dark field from reflection A (d) Dark field from reflection B.

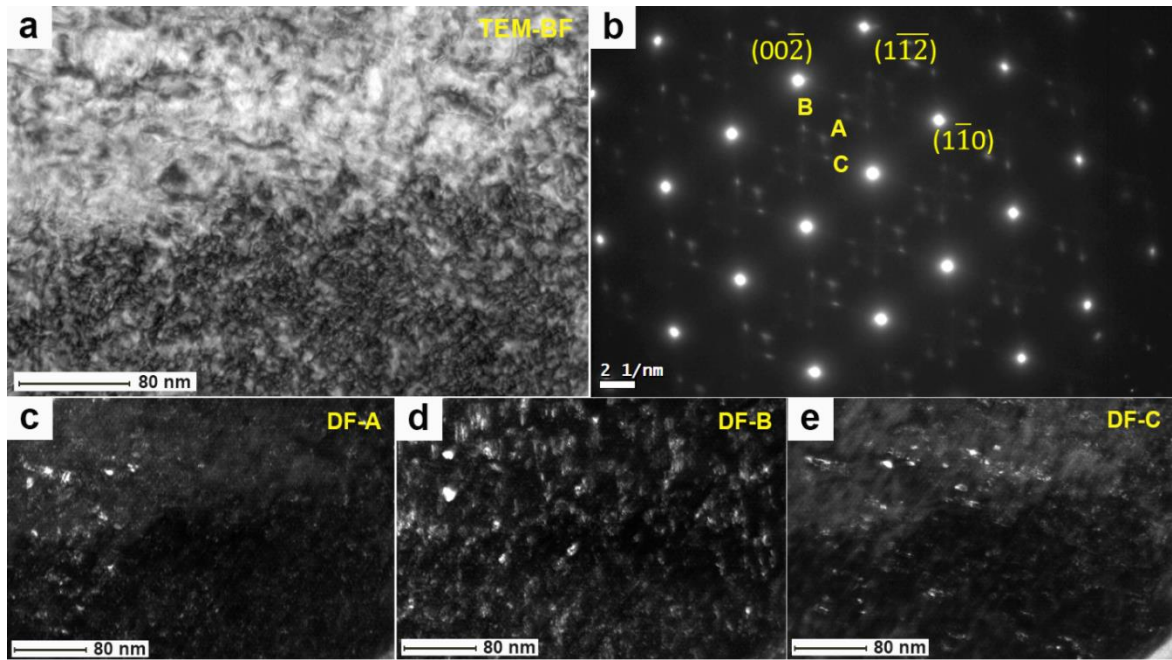


Fig 3. 13 TEM micrograph of HighTi heat-treated maraging steel showing (a) TEM-Bright field of HighTi sample. (b) Corresponding SAAD pattern where the superlattice spots represent spherical precipitates ( $\text{Ni}_3\text{Mo}$ ). (c), (d), (e) Dark filed from reflections A, B, C respectively.

Fig. 3.14. shows STEM-EDS images of both LowTi and HighTi samples in the same magnification to study volume fraction of precipitates. As can be seen, in the HighTi heat-treated sample, the volume fraction of  $\text{Ni}_3\text{Ti}$  precipitates increased; however, there is no noticeable difference in the morphology and chemical composition of precipitates in the two alloys. Besides, some Ti and Al nano-particles were found in Fig.14 that can be formed due to the fast diffusion rate of Ti and Al which was reported before [23].

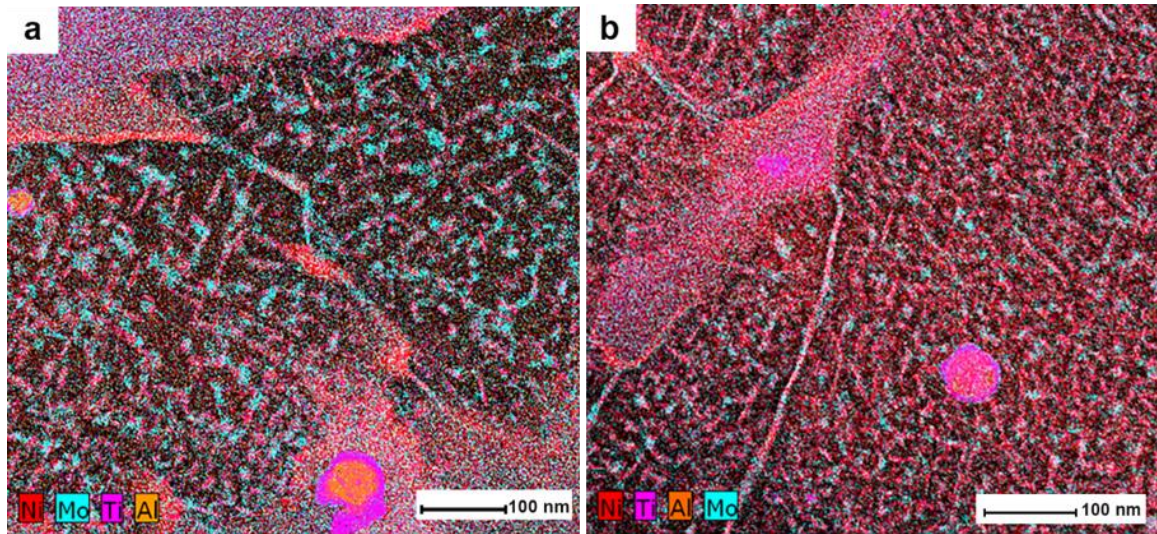


Fig 3. 14 STEM image along with EDS mapping. a) LowTi, b) HighTi samples showing the difference in precipitate volume fraction.

### 3.3.7. Texture evolution during the deformation

To study phase transformation and macrotexture development during the deformation, XRD analysis was employed. Fig. 3.15. shows  $\{200\}$  and  $\{110\}$  pole figures of the as-built samples in undeformed and deformed parts after the uniaxial tensile test (after the completion of the tensile tests). In these pole figures, x-axes represent loading direction, and y represent the building direction. The orientation of grains relative to the tensile axis can affect the strength and ductility of the samples during the tensile test. As can be seen, due to the Ti addition, the number of grains, which orientated in the direction of the tensile axis, is different. The dominant slip system in martensite is  $\langle 111 \rangle \{110\}$ [42]. Based on the components that can be seen from the  $\{200\}$  and  $\{110\}$  pole figures, in the HighTi sample, intensity of  $\{110\}$  planes are higher (Max intensity = 2.5) than the LowTi sample, and this is the reason for the higher strength of the HighTi sample. In addition, the

location of {110} poles indicates that the majority of {110} planes oriented at about  $45^\circ$  to the loading direction (x-axis in pole figures), which is favorable for activation of slip system in martensite [43]. The orientation of grains rotates to a specific direction during deformation. The {110} poles of LowTi sample does not show a strong texture, showing that the {110} poles are not oriented in a favorable direction for slip mechanism.

Fig. 3.16. shows {200} and {110} pole figures of the heat-treated samples in undeformed and deformed parts after the uniaxial tensile test (after the completion of tensile tests). In heat-treat condition, in the pole figures, x-axis is parallel to the loading and y-axis is parallel building direction. In the heat-treat condition, orientation for {110} planes in deformed samples is not significant, which is the reason for brittleness of the heat treat samples. In other words, during the deformation, slip planes are not in favorable orientation, which leads to lower ductility of heat-treated samples. However, in the HighTi sample, {110} planes orientated about  $20-30^\circ$  to the loading direction, which could be the reason for better ductility of this sample compared to the LowTi sample.

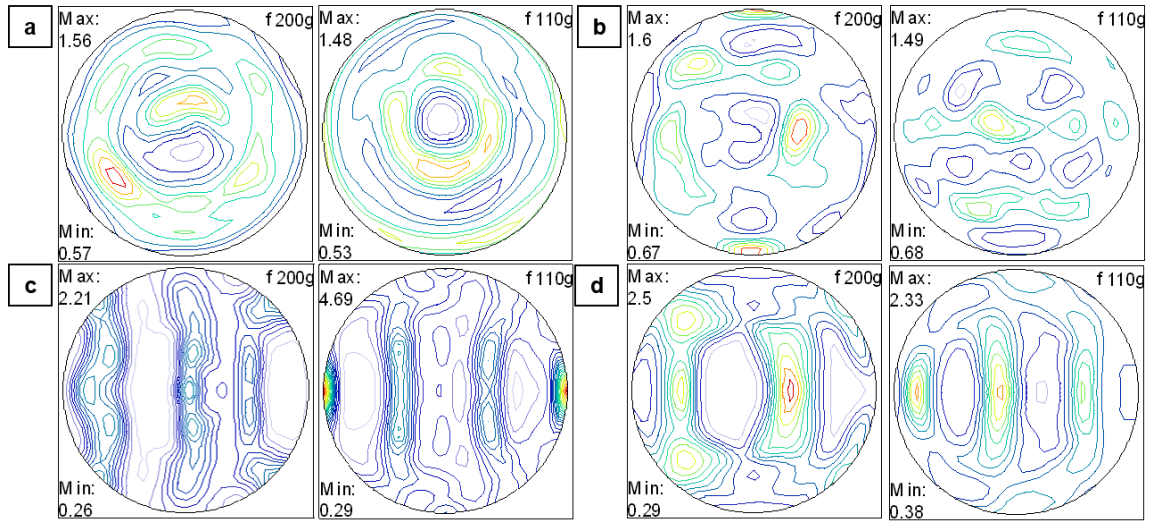


Fig 3. 15 XRD pole figures of as-built samples before and after uniaxial tensile test. (a) LowTi- as-built - undeformed, b) HighTi- as-built - undeformed, c) LowTi- as-built - deformed, d) HighTi- as-built - deformed.

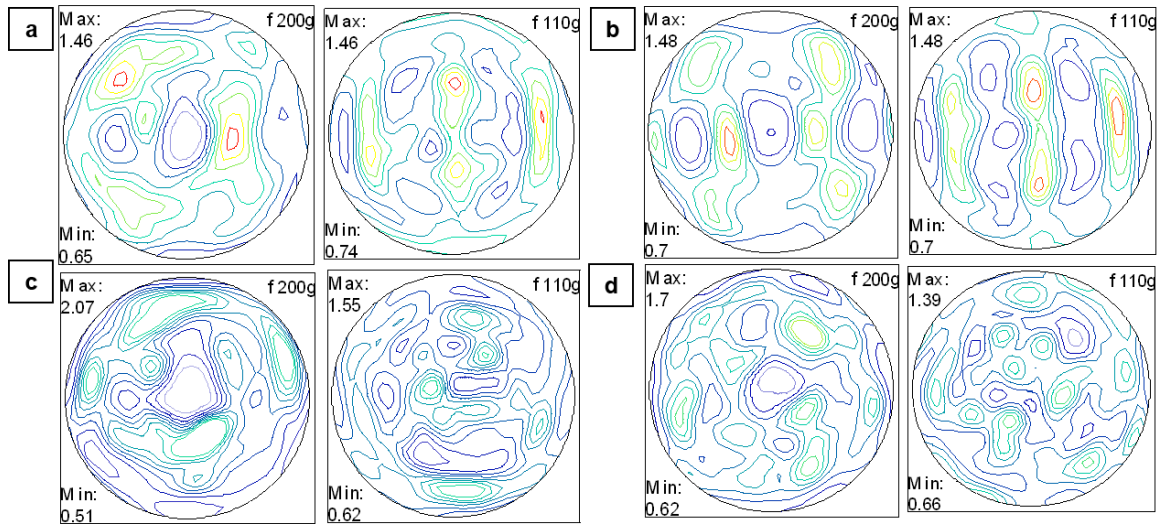


Fig 3. 16 XRD pole figures of heat-treated samples before and after uniaxial tensile test. (a) LowTi- heat treat- undeformed, b) HighTi- heat treat- undeformed, c) LowTi- heat treat- deformed, d) HighTi- heat treat- deformed.

Table 3.6. and 3.7. lists the phase fractions before and after deformation extracted from XRD test. As can be seen in table 3.6. and 3.7., the amount of austenite decreased

after deformation and austenite phase transform to martensite during deformation. In the HighTi sample, this effect is more pronounced. In other words, after deformation, the amount of austenite decreased more in the HighTi sample (with 16.36 wt. % austenite fraction before deformation and 11.31% austenite fraction after deformation). In addition, in comparison with the as-built condition, although volume fraction of austenite is higher in the heat-treated samples, austenite did not completely transform to martensite during deformation and this could be the reason for the lower ductility of the heat-treated samples.

Table 3. 6. Phase analysis before and after deformation in as-built condition.

Sample	$\alpha'$ volume fraction (%)	$\gamma$ volume fraction (%)
<b>LowTi- un deformed</b>	95.3	4.70
<b>HighTi- un deformed</b>	93.17	6.83
<b>LowTi-deformed</b>	100	0
<b>HighTi- deformed</b>	100	0

Table 3. 7. Phase analysis before and after deformation in heat treat condition.

Sample	$\alpha'$ volume fraction (%)	$\gamma$ volume fraction (%)
<b>LowTi- un deformed</b>	90.88	9.12
<b>HighTi- un deformed</b>	83.64	16.36
<b>LowTi-deformed</b>	93.99	6.01
<b>HighTi- deformed</b>	88.69	11.31

### 3.3.8. The effect of Ti content on recrystallization fraction

To study static recovery and recrystallization of samples during heat treatment, recrystallization and kernel average misorientation (KAM) maps of samples were used. Fig. 3.18. presents recrystallization maps of both maraging steels in the as-built and heat-treated conditions. During the LPBF process, due to high heating and cooling rates, residual stress exists in the samples [19]. Martensite matrix in maraging steel has a high density of dislocations, which is the reason for the higher amount of deformed grains in these samples [26]. As can be seen in Fig. 17, partial recrystallization happens during aging at 490 °C, and more blue grains, which represent recrystallized grains, can be seen in the HighTi sample. This recrystallization results in the formation of strain-free grains in the microstructure of the HighTi sample, which was seen in the SEM images (Fig. 3.3.).

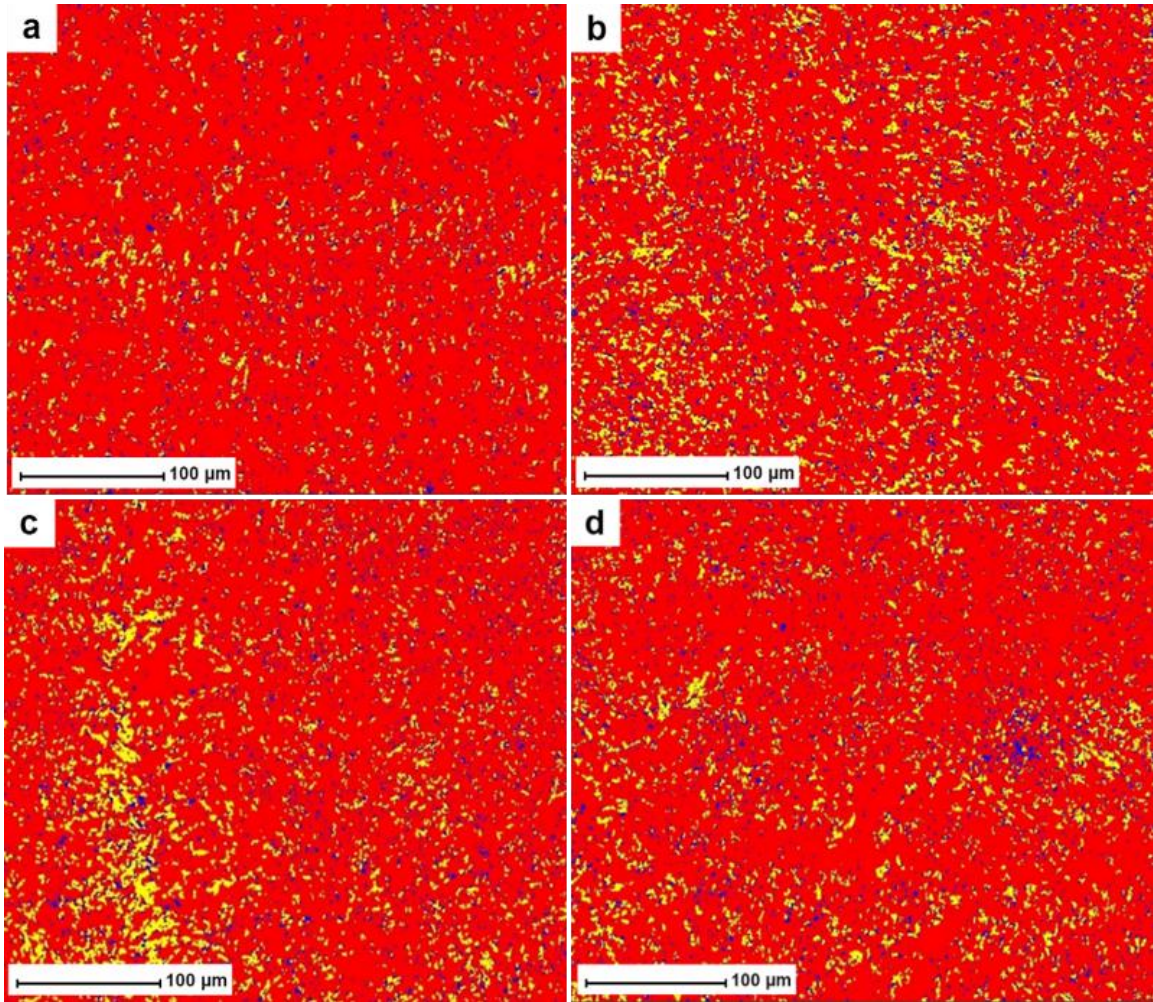


Fig 3. 17 EBSD results of the side of the samples at  $\times 300$  magnification. Recrystallization maps of the HighTi and LowTi samples in as-built and heat-treat conditions. (a) LowTi-as built, b) HighTi- as built, c) LowTi heat treat, d) HighTi-heat treat. (Red represent deformed grains, Blue represent recrystallized grains, and Yellow represent sub structured grains).

The dislocation density can be analyzed by EBSD using KAM value for presenting local dislocation density. Based on KAM graphs in Fig 3.18, a higher KAM value in the grains indicates a higher degree of misorientation, implying higher stored energy in the grain [44]. Low KAM values ( $KAM < 1^\circ$ ) show low internal energy due to the small number of dislocations. However, high KAM values ( $KAM > 3^\circ$ ) show strain accumulation, dislocation walls, and dislocation structures near grain boundaries. In the as-built

condition, the KAM value is more significant in the HighTi sample, which indicates that Ti addition increased the dislocation density which was reported before [41]. However, after heat treatment, the KAM value of both samples decreases, which indicates partial recrystallization, occurred in these samples, and this recrystallization is more pronounced in the HighTi sample due to higher driving force for recrystallization. This dislocation network can provide nucleation sites for precipitate formation during the heat treatment procedure.

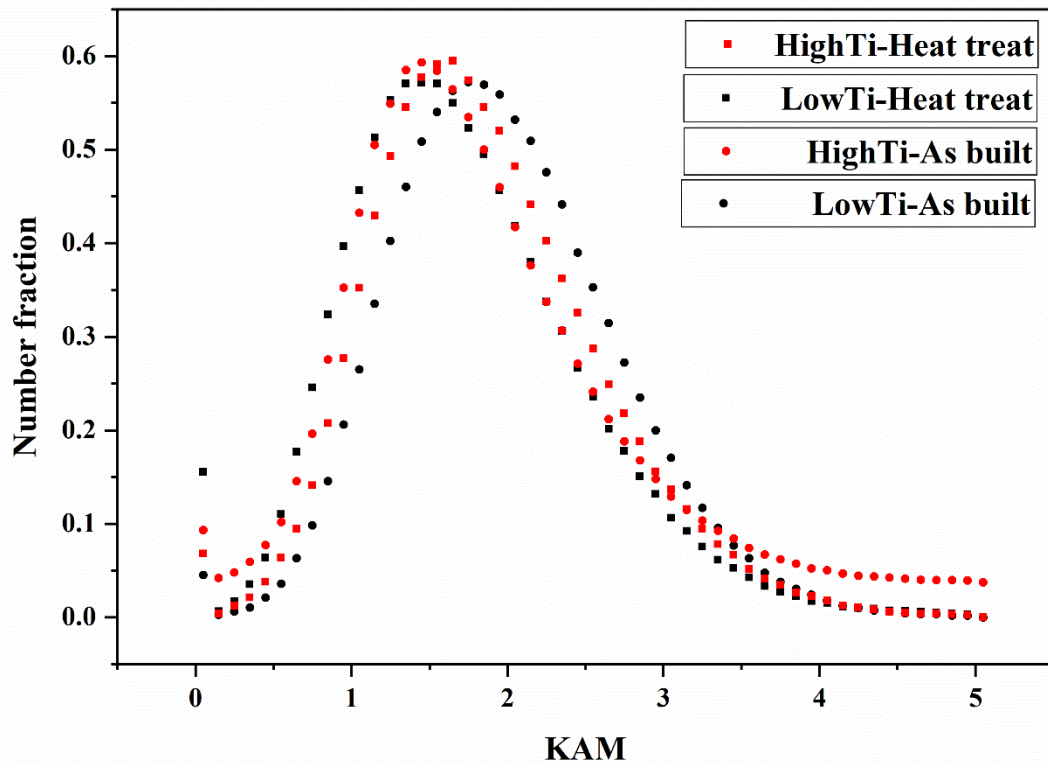


Fig 3. 18 EBSD results of the side of the samples at  $\times 300$  magnification. KAM graphs for as-built and heat-treat samples.

### 3.4. Discussion

As shown in Fig 3.2., mechanical properties characterization of the C300 maraging steel alloy with a higher amount of Ti shows better ductility and strength in the heat-treat condition. It has been reported that, an increase in UTS is accompanied by a reduction of ductility [21]. However, in this work, the HighTi sample showed better ductility and higher strength simultaneously in the heat-treated condition. In this section, the effect of Ti content on reverted austenite and subsequently its effect on the mechanical properties is discussed.

#### 3.4.1. The effect of Ti content on reverted austenite formation

Ti is usually considered as a ferrite stabilizer in steels [45]; however, Ti in the intercellular and intercolumnar regions act as austenite stabilizer [40]. Although Ti is a ferrite stabilizer, thermodynamic calculations showed that Ti, Mo and Ni solutes in intergranular regions can favor austenite retention as Jagle *et al.*[40] and Liu *et al.* [46] reported. They showed that martensite start temperature of ultra-low carbon steels diminishes in the presence of higher contents of Ti, Mo, and Ni, which means that higher amount of Ti in these steel grades facilitates austenite retention. As a result, in HighTi sample where interdenritic areas are enriched with Ti, Mo and Ni, the fraction of austenite increased. Interestingly the results of XRD (Table 3.4.), and TEM (Fig 3.9.) showed that the material with a higher amount of Ti showed a higher amount of reverted austenite in both as-built and heat-treated HighTi samples. This behavior is mainly due to the segregation of Ti elements in the intercellular and intercolumnar regions, leading to the formation of more reverted austenite [40][47]. Ti rejection into these regions is higher in HighTi alloy due to its higher severity of segregation, which consequently enhanced the

number of high potential sites of the austenite formation. As Ti has a higher diffusion coefficient compared to other elements in maraging steels, it is responsible for a higher fraction of reverted austenite in the HighTi sample [32]. Li *et al.* [3] observed the same amount of reverted austenite after the aging treatment of 6 hours at 490°C for LPBF-maraging steel with the same chemical composition as LowTi powder in this work. In addition, Rohit *et al.* [38] achieved higher reverted austenite with the addition of Ti at the weld joint due to the segregation of Ti at dendritic cell boundaries occurring in the fusion zone. They concluded that Ti have a high tendency to get enriched in interdendritic areas and provide nucleation site for austenite formation.

In one study, Song *et al.* suggested a mechanism of the formation of the reversed austenite in low carbon martensite steels. They suggested that Lath martensite boundaries are energetically favorable for nucleation of carbides and  $M_nC_m$  carbides precipitate, which results in Ni-enrichment and this is the main reason for the formation of austenite [48]. In another study, it was postulated that Ni diffusion into the Fe matrix accompanied by the transformation of  $Ni_3(Mo, Ti)$  to the more stable  $Fe_2Mo$  precipitates.  $Fe_2Mo$  phase precipitates caused local enrichment of the Ni, resulting in the formation of reverted austenite [38][49]. However, in this study, as there is no evidence of the carbides in austenite region or  $Fe_2Mo$  (based on STEM image in Fig 3.9.), these two mechanisms cannot be considered as a principal mechanism for the formation of austenite. Escobar *et al.* [34] introduced three types of mechanisms for the formation of reversed austenite. First, the shear reversion mechanism, which is reversion by shear from martensite to austenite. This mechanism is aided by strong interface segregation of elements. Second, nucleation of austenite by precipitation of carbides in which precipitates act as nucleation sites for

austenite reversion. Third, the retained austenite mechanism, which is the growth of existing retained austenite [34].

In this study (based on Fig 3.8. and Fig 3.9. and elemental segregation), it is assumed that the first mechanism of Escobar is active, which results in the formation of austenite grains with the same orientation as parent austenite grains before martensite transformation. As carbide precipitates was not observed and change of orientation of austenite grains was observed, the other two mechanisms of Escobar cannot be considered. In this mechanism, reverted austenite grains have an orientation relationship with the martensite matrix, which is called Kurdjumov–Sachs (K–S) relationship ( $\{111\} \gamma // \{011\} \alpha, \langle \bar{1}10 \rangle \gamma // \langle \bar{1}\bar{1}1 \rangle \alpha$ ). As the first mechanism is activated by the segregation of elements, Ti plays a fundamental role in the formation of austenite. Due to the higher severity of Ti segregation in grain boundaries, potential sites for the formation of reverted austenite increased, and a higher fraction of austenite in HighTi sample can be achieved [41].

### **3.4.2. The effect of reverted austenite on mechanical properties**

The effect of reverted austenite on strength and toughness has been a controversial issue. Wang *et al.* [26] demonstrated that a higher amount of reverted austenite leads to better strength by transformation induced plasticity mechanism. However, others believe that reverted austenite decreased the tensile strength of maraging steel; see e.g. [38].

One of the mechanisms contributing to the strength of the samples was resulted from austenite to martensite phase transformation during deformation. During deformation, the soft austenite phase first transforms into hexagonal close-packed (hcp)  $\epsilon$

martensite, then transform to  $\alpha$  martensite phase. Shoji–Nishiyama orientation relationship exist between  $\gamma$ -austenite and  $\varepsilon$ -martensite, while between  $\alpha$ -martensite and  $\gamma$ -austenite a Kurdjumov–Sachs orientation relationship exists. Indeed, during deformation, the stacking sequence of  $\{111\}$  planes in austenite changes from ABCABC to ABAB, which is a stacking sequence of hcp [50]. As was seen in tables 3.6. and 3.7., after deformation, the intensity of FCC peaks decreased, and the intensity of BCC peaks increased and no  $\varepsilon$  martensite was observed in the deformed specimens. It should be noted that, grains with preferred orientation has higher chance for phase transformation.

Knijf *et al.* [51] investigated the effect of texture on strain-induced martensitic transformation in low carbon steels. They showed that materials with Cube and Goss texture have a higher driving force for martensite transformation compared to the material with Copper and Brass texture. In addition, Hilkhuijsen *et al.* [52] reported that materials with Copper texture have a higher driving force for martensite transformation compared to un-textured materials. It can be concluded that, HighTi sample, which showed Copper texture, has more driving force for the TRIP mechanism, which involved in the strengthening of this material. As was seen in tables 3.6. and 3.7., the HighTi sample is a suitable candidate for the martensite phase transformation due to Copper texture. Indeed, during deformation, grains orientated in  $\{112\} \langle 111 \rangle$  are more prone to transform first to  $\varepsilon$  martensite through Shoji–Nishiyama orientation relationship and then to  $\alpha$  martensite through the Kurdjumov–Sachs orientation relationship.

Phase transformation is triggered in early uniform deformation regime in which at these lower strains, some austenite grains transformed depending on their crystal orientation. However, dislocation plasticity is triggered in later uniform deformation

regime (in other words, TRIP occurred in the early stages of deformation and slip occurred in final stages) [26]. Wang *et al.* reported that an increase of reverted austenite could increase plastic strain (both uniform elongation and post-necking elongation) by TRIP mechanisms [26]. This emphasizes the effect of a higher amount of austenite in the deformation process. In addition, maraging steel have low work hardening ability, which means that maraging steel has a peak stress at small plastic strains. It was proven that austenite in maraging steel could improve work hardening behavior through TRIP effect, which means that austenite can delay strain localization in maraging steels [26][53]. As was seen in Fig 3.6., the HighTi sample showed higher work hardening rate compared to the LowTi sample, which can be attributed to the higher TRIP effect, which enhances the excellent combination of strength and ductility [54].

### **3.4.3. The effect of microstructure characteristic on mechanical properties**

Martensite lath in the as-built maraging steel contains high dislocation density in the order of  $10^{11-12}$   $\text{cm}^{-2}$ , which contributes to strain hardening mechanism [23]. As KAM and recrystallization maps (Fig 3.17. and 3.18.) showed, the HighTi sample in the as-built condition showed higher dislocation density compared to the LowTi as-built sample (quantified in [41]) . Liu *et al.* [55] investigated the effect of segregation of alloying elements on dislocation network and they reported that in complex thermal cycles in the LPBF process, segregation of alloying elements leads to the formation of a dislocation network due to cellular growth mode. Higher content of Ti in cell boundaries in the HighTi sample, cause an increase of dislocation density in this sample. During heat treatment, due to the restoration process, dislocation density decreased, which lead to partial

recrystallization and forming of equiaxed grains. Mutua *et al.* [22] also reported that the elongated grains morphology replaced by equiaxed grain after heat treatment for maraging steel. Furthermore, the HighTi sample, which has more dislocation density, is more prone to recrystallization and showed more equiaxed grains in SEM and more recrystallized grains (blue grain) in recrystallization map after heat treatment. However, in heat treat condition, due to the reduction of dislocation density and not enough preferred orientation planes (as was seen in XRD macro textures in Fig 3.16.), the slip of dislocation could not be considered as a strong deformation mechanism.

Furthermore, during the heat treatment process, precipitates generate on dislocations and grow up by pipe diffusion [23]. In the HighTi sample, which has higher dislocation density, more nucleation sites provided and higher volume fraction of precipitates is expected.

#### **3.4.4. The effect of precipitate formation on mechanical properties**

The interaction of precipitates with dislocations is the primary strengthening mechanism in maraging steels. In this study, two types of precipitates were found in both maraging steel samples in the heat-treat condition (Fig 3.14.). First spherical Ni<sub>3</sub>Mo precipitates and second needle shaped Ni<sub>3</sub>Ti precipitates. Bodziak *et al.* [31] studied different types of precipitates in LPBF-maraging steels after heat treatment of 510 °C for 2 hours. Their results revealed that three different types of precipitates could be found in the maraging steel: (i) spherical precipitates enriched of Ti and Ni, (ii) plate-like precipitates enriched of Ti and Ni with a low amount of Mo and (iii) spherical precipitates enriched in Mo, which two later types were observed in this study [5]. Ni<sub>3</sub>Ti precipitates

are stable due to the coherency with the martensite matrix. These Ni<sub>3</sub>Ti intermetallics precipitates in the martensite matrix owing to the high initial dislocation density and make a coherent interface with the matrix, which makes them the main strengthening phase in maraging steel [56].

As shown in Fig 3.14., the volume fraction and the size of precipitates in the two samples is different, which can influence the mechanical response of the materials. Depending on the size of precipitates, different models can be used to relate precipitate distribution to strength [20]. Bodziak *et al.* [31] reported that diameters of spherical precipitates (Ni<sub>3</sub>Mo) are 9 nm and 5 nm, and plate-like precipitates (Ni<sub>3</sub>Ti) are 9 nm and 22 nm. Tan *et al.* [23] reported that needle-shaped precipitates (Ni<sub>3</sub>Ti) are about 6-10 nm diameter, 15-45 length, interspacing of precipitates of about 25 nm and spherical precipitates are the about 40-80nm diameter. However, in this study, nano precipitates in the HighTi sample are about 7.76 nm diameter, which the distance between them is approximately 12.13 nm. For the LowTi sample, nano precipitates are in 7.97 nm diameter and distance between them is about 25.04 nm (Fig 3.14.).

HighTi sample showed higher strength, which is related to higher volume fraction of precipitation of Ni<sub>3</sub> (Ti, Mo) precipitates. The contribution of precipitates in the overall strength of the material can be studied by the Orowan relationship. Based on equations (1) and (2), Orowan strengthening can be calculated as follows [23]:

$$\sigma_A = \sigma_0 + \frac{Gb}{2\pi k(\lambda-d)} \ln \frac{(\lambda-d)}{2b} \quad (3-1)$$

$$\frac{1}{k} = \frac{1}{2} \left( \frac{1}{1-\nu} + 1 \right) \quad (3-2)$$

where  $\sigma_0$  is the yield strength of the martensite matrix,  $G$  is the shear modulus of the matrix,  $b$  is the Bergers vector,  $\lambda$  is the interspace of precipitates, and  $\nu$  is the Poisson's ratio.  $G$  is about 71 GPa, Poisson's ratio for steels is 0.3, and Bergers vector for maraging steel is approximately 0.249 nm [23][57]. Based on the Orowan relationship, the increase of the strength in the HighTi sample due to precipitates is about 1692 MPa, and for LowTi sample is about 706 MPa. Such a significant difference between the strength increments due to the precipitate volume fraction is the reason for different mechanical behavior.

The addition of Ti results in an increase of  $\text{Ni}_3\text{Ti}$  precipitates volume fraction in microstructure, leading to improved strength. The formation energy of  $\text{Ni}_3\text{Ti}$  is the lowest among all binary alloys in maraging steels [58], and this is the reason for the formation of  $\text{Ni}_3\text{Ti}$  precipitates after Ti addition. As Galindo-Nava *et al.* [32] reported, with increasing Ti content, the strength of maraging steel improved by forming  $\text{Ni}_3\text{Ti}$  precipitates in conventional heat-treated maraging steels. As previously observed,  $\text{Ni}_3\text{Ti}$  due to lower lattice misfit formed in the early stage of aging and act as a nucleation site for  $\text{Ni}_3\text{Mo}$  precipitates [14]. Dehgahi et al [41] reported that  $\text{CoNi}$  metastable precipitates were seen in HighTi maraging steel in the as-built condition which these precipitates can act as a nucleation site for more stable precipitates such as  $\text{Ni}_3\text{Ti}$  in HighTi heat treated sample and this can be the reason for more volume fraction of precipitates in HighTi sample.

### 3.4.5. The effect of preferred orientation on mechanical properties

Texture is another factor, which affects the mechanical behavior of LPBF-maraging steel parts [59]. Austenite plays another role in the mechanical behavior of maraging steel through a texture change, which leads to an increase of ductility. It was observed that Ti not only increase volume fraction of austenite but also it can change the crystallographic texture of austenite grains from  $\{100\} \langle uvw \rangle$  orientation to  $\{111\} \langle uvw \rangle$  orientation. Due to this texture change,  $\{111\} \gamma$  fibre developed in the HighTi sample, which is the compact direction and has the highest Young's modulus and is responsible for better strength and toughness. In the cold rolled maraging steel 350, the intensity of  $\gamma$  fibre ( $\{111\} //$  normal direction) texture of martensite is reduced in the sample with a higher amount of reverted austenite [27]. In other words, martensite with  $\{111\} \langle uvw \rangle$  orientation is more prone to transform to austenite [27]. However, in the case of LPBF because of local residual stresses, the intensity of  $\gamma$  fibre ( $\{111\} //$  normal direction) texture is increased in the sample with a higher fraction of reverted austenite. In addition, texture component of  $\{112\} \langle 111 \rangle$  texture (referred to as copper texture), which is the characteristic of FCC alloys, is increased in material with a high amount of reverted austenite, which was seen before in the cold rolled maraging steel 350 [27].

It is well known that, grains oriented with  $\{111\}$  and  $\{110\}$  have better mechanical properties due to activated slip systems in BCC structures [60]. As a matter of fact,  $\langle 111 \rangle$  direction has the highest Young's modulus, and  $\langle 001 \rangle$  has lower Young's modulus in iron, and this texture change is the reason for the increase of strength and ductility in HighTi sample. Specifically, from ODF maps (Fig 3.5.), it can be concluded that after Ti addition,  $\{111\} \langle 0\bar{1}1 \rangle$  texture component was increased, which improves mechanical behavior due

to an increase of available slip systems in martensite. Masoumi *et al.* [60] reported that the increase in the toughness behavior is associated with the increase of the orientation of {111}, {112}, and {110}//ND components in maraging steel 300, which happened for HighTi sample. In other words, more slip systems are activated in the HighTi sample, which facilitates dislocation movement and is the reason for the higher ductility of this material. In addition, ODF maps of the LowTi sample indicate that reduction in toughness is related to an increase of undesirable {001} planes (rotated cube) in these samples.

Furthermore, heat treatment causes the development of {110} texture, which could be the reason for the strength of heat-treated maraging steel samples. It should be noted that, the reason for brittleness of the heat-treated samples is the presence of grains orientated along {001} (cleavage planes), which promotes brittle fracture in steel due to the lowest Young's modulus.

As it was seen in this study, two mechanisms are contributed in the strength of HighTi heat-treated maraging steel: phase transformation (TRIP) and precipitate formation. It was observed that, material with a higher amount of Ti showed more fraction of reverted austenite, which led to better strength and ductility. Austenite contributes to strength through the TRIP effect and contribute to ductility through texture change.

### **3.5. Conclusion**

In the current study, reverted austenite and precipitation formation in heat-treated LPBF-maraging steels was studied. The main purpose of this investigation was to achieve high strength and high ductility material through the LPBF process. It was found that, with the addition of Ti, strength and ductility enhanced simultaneously. By using multi-scale

characterization techniques including XRD, EBSD, and TEM, the mechanisms of strengthening and deformation of maraging steel evaluated. The followings were the main findings of the current study:

- As the addition of Ti, the fraction of austenite phase increased after heat treatment in HighTi sample due to the higher severity of Ti rejection into the intergranular regions where Ti in the presence of Ni and Mo promotes austenite formation.
- As a result of the addition of Ti, not only the volume fraction of reverted austenite increased in heat-treated maraging steel, but also the orientation of austenite grains changed too.
- It was found that in HighTi material, ductility improved as a results of Copper and fibre texture development, which facilitate dislocation movement through the activation of more slip systems.
- Both spherical ( $\text{Ni}_3\text{Mo}$ ) and needle-shaped ( $\text{Ni}_3\text{Ti}$ ) precipitates were found in both samples. However, a higher volume fraction of  $\text{Ni}_3\text{Ti}$  precipitates was observed in the HighTi sample.
- The HighTi sample showed better strength than the LowTi sample due to two mechanisms: martensite phase transformation (due to more austenite), and precipitation hardening.
- Reverted austenite contributed to the strength through the TRIP effect and contributed to ductility through texture change.

### 3.5. References

- [1] J. Song, Q. Tang, Q. Feng, S. Ma, R. Setchi, Y. Liu, Q. Han, X. Fan, M. Zhang, Effect of heat treatment on microstructure and mechanical behaviours of 18Ni-300 maraging steel manufactured by selective laser melting, *Opt. Laser Technol.* 120 (2019) 105725.
- [2] S. Shamsdini, S. Shakerin, A. Hadadzadeh, B.S. Amirkhiz, M. Mohammadi, A trade-off between powder layer thickness and mechanical properties in additively manufactured maraging steels, *Mater. Sci. Eng. A.* 776 (2020) 139041. <https://doi.org/10.1016/j.msea.2020.139041>.
- [3] J. Li, X. Wang, W. Qi, J. Tian, S. Gong, Laser nanocomposites-reinforcing/manufacturing of SLM 18Ni300 alloy under aging treatment, *Mater. Charact.* 153 (2019) 69–78.
- [4] S. Shakerin, A. Hadadzadeh, B.S. Amirkhiz, S. Shamsdini, J. Li, M. Mohammadi, Additive manufacturing of maraging steel-H13 bimetal using laser powder bed fusion technique, *Addit. Manuf.* 29 (2019) 100797.
- [5] A.G. Dos Reis, D.A.P. Reis, A.J. Abdalla, J. Otubo, High-temperature creep resistance and effects on the austenite reversion and precipitation of 18 Ni (300) maraging steel, *Mater. Charact.* 107 (2015) 350–357.
- [6] C.N. Hsiao, C.S. Chiou, J.R. Yang, Aging reactions in a 17-4 PH stainless steel, *Mater. Chem. Phys.* 74 (2002) 134–142.
- [7] A. Ebrahimi, M. Mohammadi, Numerical tools to investigate mechanical and

- fatigue properties of additively manufactured MS1-H13 hybrid steels, *Addit. Manuf.* 23 (2018) 381–393. <https://doi.org/10.1016/j.addma.2018.07.009>.
- [8] J. Tallon, E. Cyr, A. Lloyd, M. Mohammadi, Crush performance of additively manufactured maraging steel microlattice reinforced plates, *Eng. Fail. Anal.* 108 (2020) 104231.
- [9] A. Shahriari, L. Khaksar, A. Nasiri, A. Hadadzadeh, B.S. Amirkhiz, M. Mohammadi, Microstructure and corrosion behavior of a novel additively manufactured maraging stainless steel, *Electrochim. Acta.* 339 (2020) 135925.
- [10] F.F. Conde, J.D. Escobar, J.P. Oliveira, A.L. Jardini, W.W. Bose Filho, J.A. Avila, Austenite reversion kinetics and stability during tempering of an additively manufactured maraging 300 steel, *Addit. Manuf.* 29 (2019) 100804.
- [11] Y. Bai, D. Wang, Y. Yang, H. Wang, Effect of heat treatment on the microstructure and mechanical properties of maraging steel by selective laser melting, *Mater. Sci. Eng. A.* 760 (2019) 105–117. <https://doi.org/10.1016/j.msea.2019.05.115>.
- [12] H. Asgari, M. Mohammadi, Microstructure and mechanical properties of stainless steel CX manufactured by Direct Metal Laser Sintering, *Mater. Sci. Eng. A.* 709 (2018) 82–89. <https://doi.org/10.1016/j.msea.2017.10.045>.
- [13] Y.M. Wang, T. Voisin, J.T. McKeown, J. Ye, N.P. Calta, Z. Li, Z. Zeng, Y. Zhang, W. Chen, T.T. Roehling, Additively manufactured hierarchical stainless steels with high strength and ductility, *Nat. Mater.* 17 (2018) 63–71.
- [14] T. Allam, K.G. Pradeep, P. Köhnen, A. Marshal, J.H. Schleifenbaum, C. Haase,

Tailoring the nanostructure of laser powder bed fusion additively manufactured maraging steel, *Addit. Manuf.* 36 (2020) 101561.

- [15] M. Sanjari, A. Hadadzadeh, H. Pirgazi, A. Shahriari, B.S. Amirkhiz, L.A.I. Kestens, M. Mohammadi, Selective laser melted stainless steel CX: Role of built orientation on microstructure and micro-mechanical properties, *Mater. Sci. Eng. A.* (2020) 139365.
- [16] J.P. Oliveira, T.G. Santos, R.M. Miranda, Revisiting fundamental welding concepts to improve additive manufacturing: From theory to practice, *Prog. Mater. Sci.* 107 (2020) 100590.
- [17] V. V Zhukov, G.M. Grigorenko, V.A. Shapovalov, Additive manufacturing of metal products, *Pat. Weld. J.* 5 (2016) 137–142.
- [18] J.P. Oliveira, A.D. LaLonde, J. Ma, Processing parameters in laser powder bed fusion metal additive manufacturing, *Mater. Des.* 193 (2020) 108762.
- [19] L. Kučerová, I. Zetková, A. Jandová, M. Bystrianský, Microstructural characterisation and in-situ straining of additive-manufactured X3NiCoMoTi 18-9-5 maraging steel, *Mater. Sci. Eng. A.* 750 (2019) 70–80. <https://doi.org/10.1016/j.msea.2019.02.041>.
- [20] T.H. Simm, L. Sun, D.R. Galvin, E.P. Gilbert, D.A. Venero, Y. Li, T.L. Martin, P.A.J. Bagot, M.P. Moody, P. Hill, A SANS and APT study of precipitate evolution and strengthening in a maraging steel, *Mater. Sci. Eng. A.* 702 (2017) 414–424.
- [21] S. Yin, C. Chen, X. Yan, X. Feng, R. Jenkins, P. O'Reilly, M. Liu, H. Li, R. Lupoi,

The influence of aging temperature and aging time on the mechanical and tribological properties of selective laser melted maraging 18Ni-300 steel, *Addit. Manuf.* 22 (2018) 592–600.

- [22] J. Mutua, S. Nakata, T. Onda, Z.C. Chen, Optimization of selective laser melting parameters and influence of post heat treatment on microstructure and mechanical properties of maraging steel, *Mater. Des.* 139 (2018) 486–497. <https://doi.org/10.1016/j.matdes.2017.11.042>.
- [23] C. Tan, K. Zhou, W. Ma, P. Zhang, M. Liu, T. Kuang, Microstructural evolution, nanoprecipitation behavior and mechanical properties of selective laser melted high-performance grade 300 maraging steel, *Mater. Des.* 134 (2017) 23–34. <https://doi.org/10.1016/j.matdes.2017.08.026>.
- [24] F.F. Conde, J.D. Escobar, J.P. Oliveira, M. Béréš, A.L. Jardini, W.W. Bose, J.A. Avila, Effect of thermal cycling and aging stages on the microstructure and bending strength of a selective laser melted 300-grade maraging steel, *Mater. Sci. Eng. A.* 758 (2019) 192–201.
- [25] B. Mooney, K.I. Kourousis, R. Raghavendra, Plastic anisotropy of additively manufactured maraging steel: Influence of the build orientation and heat treatments, *Addit. Manuf.* 25 (2019) 19–31. <https://doi.org/10.1016/j.addma.2018.10.032>.
- [26] M.-M. Wang, C.C. Tasan, D. Ponge, A.-C. Dippel, D. Raabe, Nanolaminate transformation-induced plasticity–twinning-induced plasticity steel with dynamic strain partitioning and enhanced damage resistance, *Acta Mater.* 85 (2015) 216–228.
- [27] H.F.G. Abreu, J.J. Silva, M.R. Silva, M.J.G. da Silva, Influence of reverted austenite

- on the texture and magnetic properties of 350 maraging steel, *J. Magn. Magn. Mater.* 393 (2015) 99–104.
- [28] Y. Tomota, W. Gong, S. Harjo, T. Shinozaki, Reverse austenite transformation behavior in a tempered martensite low-alloy steel studied using in situ neutron diffraction, *Scr. Mater.* 133 (2017) 79–82.
- [29] K. Li, L. Wei, B. Yu, R.D.K. Misra, Reverted austenite with distinct characteristics in a new cobalt-free low lattice misfit precipitate-bearing 19Ni3Mo1.5Ti maraging steel, *Mater. Lett.* 257 (2019) 126692.
- [30] M.N. Rao, Progress in understanding the metallurgy of 18% nickel maraging steels, *Zeitschrift Für Met.* 97 (2006) 1594–1607.
- [31] S. Bodziak, K.S. Al-Rubaie, L. Dalla Valentina, F.H. Lafratta, E.C. Santos, A.M. Zanatta, Y. Chen, Precipitation in 300 grade maraging steel built by selective laser melting: Aging at 510 C for 2 h, *Mater. Charact.* 151 (2019) 73–83.
- [32] E.I. Galindo-Nava, W.M. Rainforth, P.E.J. Rivera-Díaz-del-Castillo, Predicting microstructure and strength of maraging steels: Elemental optimisation, *Acta Mater.* 117 (2016) 270–285. <https://doi.org/10.1016/j.actamat.2016.07.020>.
- [33] V. Gray, D. Galvin, P. Hill, M. Rawson, K. Perkins, Impact of targeted chemistries on maraging steel precipitation evolution observed using SANS and APT, *Mater. Charact.* 139 (2018) 208–220.
- [34] J.D. Escobar, J.D. Poplawsky, G.A. Faria, J. Rodriguez, J.P. Oliveira, C.A.F. Salvador, P.R. Mei, S.S. Babu, A.J. Ramirez, Compositional analysis on the reverted

- austenite and tempered martensite in a Ti-stabilized supermartensitic stainless steel: Segregation, partitioning and carbide precipitation, *Mater. Des.* 140 (2018) 95–105.
- [35] E.O.S.N.I.D. Sheet, EOS GmbH-Electro Optical Systems, (2014).
- [36] ASTM-International, ASTM E8/E8M-16ae1 standard test methods for tension testing of metallic materials, 2016.
- [37] A. Hadadzadeh, B.S. Amirkhiz, J. Li, M. Mohammadi, Columnar to equiaxed transition during direct metal laser sintering of AlSi10Mg alloy: Effect of building direction, *Addit. Manuf.* 23 (2018) 121–131. <https://doi.org/10.1016/j.addma.2018.08.001>.
- [38] B. Rohit, N.R. Muktinutalapati, Austenite reversion in 18% Ni maraging steel and its weldments, *Mater. Sci. Technol.* 34 (2018) 253–260.
- [39] F. Qian, W.M. Rainforth, The formation mechanism of reverted austenite in Mn-based maraging steels, *J. Mater. Sci.* 54 (2019) 6624–6631.
- [40] E.A. Jäggle, Z. Sheng, P. Kürnsteiner, S. Ocylok, A. Weisheit, D. Raabe, Comparison of maraging steel micro- and nanostructure produced conventionally and by laser additive manufacturing, *Materials (Basel)*. 10 (2017) 2–15. <https://doi.org/10.3390/ma10010008>.
- [41] S. Dehgahi, M.H. Ghoncheh, A. Hadadzadeh, M. Sanjari, B.S. Amirkhiz, M. Mohammadi, The role of titanium on the microstructure and mechanical properties of additively manufactured C300 maraging steels, *Mater. Des.* (2020) 108965.
- [42] S. Suwas, R.K. Ray, *Crystallographic texture of materials*, Springer, 2014.

- [43] G.E. Dieter, D.J. Bacon, Mechanical metallurgy, McGraw-hill New York, 1986.
- [44] Y.L. Hu, X. Lin, Y.L. Li, J. Wang, S.Y. Zhang, X.F. Lu, W.D. Huang, Effect of heat treatment on the microstructural evolution and mechanical properties of GH4099 additive-manufactured by directed energy deposition, *J. Alloys Compd.* 800 (2019) 163–173.
- [45] Y. Kang, W.M. Mao, Y.J. Chen, J. Jing, M. Cheng, Effect of Ti content on grain size and mechanical properties of UNS S44100 ferritic stainless steel, *Mater. Sci. Eng. A.* 677 (2016) 211–221.
- [46] C. Liu, Z. Zhao, D.O. Northwood, Y. Liu, A new empirical formula for the calculation of MS temperatures in pure iron and super-low carbon alloy steels, *J. Mater. Process. Technol.* 113 (2001) 556–562. [https://doi.org/10.1016/S0924-0136\(01\)00625-2](https://doi.org/10.1016/S0924-0136(01)00625-2).
- [47] C.R. Shamantha, R. Narayanan, K.J.L. Iyer, V.M. Radhakrishnan, S.K. Seshadri, S. Sundararajan, S. Sundaresan, Tensile properties and fracture toughness of 18Ni (250 grade) maraging steel weldments, *Sci. Technol. Weld. Join.* 5 (2000) 329–337.
- [48] Y. Song, X. Li, L. Rong, Y. Li, The influence of tempering temperature on the reversed austenite formation and tensile properties in Fe–13% Cr–4% Ni–Mo low carbon martensite stainless steels, *Mater. Sci. Eng. A.* 528 (2011) 4075–4079.
- [49] J.M. Pardal, S.S.M. Tavares, M.P.C. Fonseca, H.F.G. Abreu, J.J.M. Silva, Study of the austenite quantification by X-ray diffraction in the 18Ni-Co-Mo-Ti maraging 300 steel, *J. Mater. Sci.* 41 (2006) 2301–2307.

- [50] Z. Wang, A.M. Beese, Stress state-dependent mechanics of additively manufactured 304L stainless steel: Part 1—characterization and modeling of the effect of stress state and texture on microstructural evolution, *Mater. Sci. Eng. A.* 743 (2019) 811–823.
- [51] D. De Knijf, T. Nguyen-Minh, R.H. Petrov, L.A.I. Kestens, J.J. Jonas, Orientation dependence of the martensite transformation in a quenched and partitioned steel subjected to uniaxial tension, *J. Appl. Crystallogr.* 47 (2014) 1261–1266.
- [52] P. Hilkhuijsen, H.J.M. Geijselaers, T.C. Bor, The influence of austenite texture on the martensitic transformation of an austenitic stainless steel, *J. Alloys Compd.* 577 (2013) S609–S613.
- [53] S.W. Ooi, P. Hill, M. Rawson, H. Bhadeshia, Effect of retained austenite and high temperature Laves phase on the work hardening of an experimental maraging steel, *Mater. Sci. Eng. A.* 564 (2013) 485–492.
- [54] D. Mohr, J. Jacquemin, Large deformation of anisotropic austenitic stainless steel sheets at room temperature: multi-axial experiments and phenomenological modeling, *J. Mech. Phys. Solids.* 56 (2008) 2935–2956.
- [55] L. Liu, Q. Ding, Y. Zhong, J. Zou, J. Wu, Y.-L. Chiu, J. Li, Z. Zhang, Q. Yu, Z. Shen, Dislocation network in additive manufactured steel breaks strength–ductility trade-off, *Mater. Today.* 21 (2018) 354–361.
- [56] W. Xu, P.E.J. Rivera-Díaz-del-Castillo, W. Wang, K. Yang, V. Bliznuk, L.A.I. Kestens, S. Van der Zwaag, Genetic design and characterization of novel ultra-high-strength stainless steels strengthened by Ni<sub>3</sub>Ti intermetallic nanoprecipitates, *Acta Mater.* 58 (2010) 3582–3593.

- [57] K. Li, L. Wei, B. An, B. Yu, R.D.K. Misra, Aging phenomenon in low lattice-misfit cobalt-free maraging steel: Microstructural evolution and strengthening behavior, *Mater. Sci. Eng. A.* 739 (2019) 445–454.
- [58] J. Tian, M.B. Shahzad, W. Wang, L. Yin, Z. Jiang, K. Yang, Role of Co in formation of Ni-Ti clusters in maraging stainless steel, *J. Mater. Sci. Technol.* 34 (2018) 1671–1675. <https://doi.org/10.1016/j.jmst.2018.04.020>.
- [59] T. Bhardwaj, M. Shukla, Effect of laser scanning strategies on texture, physical and mechanical properties of laser sintered maraging steel, *Mater. Sci. Eng. A.* 734 (2018) 102–109. <https://doi.org/10.1016/j.msea.2018.07.089>.
- [60] M. Masoumi, I.F. de Barros, L.F.G. Herculano, H.L.F. Coelho, H.F.G. de Abreu, Effect of microstructure and crystallographic texture on the Charpy impact test for maraging 300 steel, *Mater. Charact.* 120 (2016) 203–209.

## **Chapter 4: Microstructural evolution and high strain rate compressive behavior of as-built and heat-treated additively manufactured maraging steels**

### **4.1. Introduction**

Among different types of steel, maraging steel shows a significant combination of attractive mechanical properties, such as high strength, high fracture toughness, hardenability, and weldability [1]. This leads to their application in the aircraft landing gears, motor racing applications, molds, metal casting dies, protective armor plates, and other structural parts. The low carbon content of maraging steels accounts for their good toughness and formability [2]. Besides, the presence of alloying elements such as Ni, Co, Mo, Ti, and Al promotes the formation of martensite by air-cooling and the formation of fine particles of intermetallic compounds like FeTi [3], Fe<sub>2</sub>Mo [4], Ni<sub>3</sub>T [5], and Ni<sub>3</sub>Mo [6] during aging. The combination of strong martensite with the strengthening effect of the fine intermetallic compounds is responsible for the high strength and good toughness of maraging steels [7]. High fabrication costs and a significant amount of waste during conventional fabrication processes are a few concerns of the manufacturers.

Additive manufacturing (AM) is a rapidly advancing technique to produce complex or desirable shapes using a computer-aided design (CAD) model and by stacking of materials layer-by-layer in a short production time [8]. AM techniques can be divided based on the energy source used into Direct Metal Laser Sintering (DMLS) [9], Laser powder bed fusion (LPBF) [10], Wire Arc Additive Manufacturing (WAAM) [11], and

Electron Beam Melting (EBM) [12]. AM can also be classified based on the material feedstock into wire feed and powder feed techniques [13, 14].

Laser powder bed fusion (LPBF) is a powder-bed fusion technique where the source of heating is a laser beam. In general, the LPBF system includes a powder delivery system, a building platform, a roller to deposit the powder, a controlling system, an inert gas system, and focusing lenses and Galvano-mirrors, which control the focus and movement of the laser beam. Each AM process has its advantages and disadvantages. However, LPBF has become more popular as it can be a suitable method for a wide variety of materials [13]. The mechanical properties of LPBF parts depend strongly on process parameters such as scanning speed, hatch spacing, layer thickness, and laser power [15], [16]. An inappropriate selection of process parameters can result in poor quality parts. Measuring energy density is one of the best predictors for the relative density of parts. Maraging steel, for instance, requires an energy density higher than  $180 \text{ J/mm}^2$  in order to obtain a part with 100% density [17].

In many of their structural applications, maraging steel parts experienced elevated and high strain-rate impact loadings. For instance, in tools and dies (automotive) and landing gears (aerospace), maraging steel parts are subjected to high strain-rate compressive loadings, and their response is important for designers. Few researchers have studied the quasi-static, static, and compressive mechanical properties of maraging steel parts fabricated by conventional processes [18–21] and AM techniques [22]. The majority of these studies concentrated on macroscopic features or only focused on the behavior of maraging steels at a limited range of strain rates. Song *et al.* [19] employed a Kolsky compression bar test to investigate the compressive response of C250 maraging steel alloy

at two strain rates. Their observations revealed that the dynamic strength increased with an increase in strain rate. Schnitzer *et al.* [21] studied the effect of high strain rate compression loadings on aged maraging steels. They observed that with increasing strain, strain rate sensitivity decreased, which is related to the pinning of dislocations by precipitates. There has not been any in-depth microstructural characterization and comprehensive study on the compressive dynamic mechanical behavior of LPBF maraging steels at a wide range of strain rates to the authors' best knowledge.

Compared to conventionally built maraging steel parts, higher strength is attainable in LPBF maraging steel parts [23]; it may be possible to achieve superior mechanical properties in LPBF maraging steels by conducting post-processing heat-treatments. There are many studies on the investigation of heat-treatment on maraging steels [15] [24]. According to the ASM handbook, to have the optimum mechanical properties, it is recommended to conduct an age-hardening heat treatment for 3 to 8 hours at a temperature between 460 °C and 510 °C [25]. Therefore, precipitation refinement, such as Ni<sub>3</sub>Ti in the martensite matrix, can cause an increase in strength due to age-hardening. Conde *et al.* [26] investigated the effect of different heat treatment routes on LPBF-maraging steel where they focused on martensite to austenite reversion, and they found out that presence of austenite slightly increase ductility at the expense of the strength of maraging steel parts. In another study [27], these researchers studied the effect of different heat treatment processes on stability of austenite in martensite-to-austenite process. They showed that soaking temperatures of between 610 °C and 650 °C results in the formation of austenite with high stability based on thermodynamic calculations. It should be noted that, the dynamic behavior of heat-treated LPBF maraging steel has not been reported in the

literature. Most of the studies limited their investigation to the effect of process parameters on the mechanical properties of maraging steel. However, due to the wide range of LPBF maraging steels used in structural applications and to have a better understanding of the deformation behavior of LPBF maraging steels under a wide range of strain rates, predictions based on mathematical modeling is required. Constitutive modeling is an essential and useful quantitative tool, which enables predicting the response of LPBF maraging steels at any strain rate.

As a result, this research aims to determine the effect of dynamic compressive loadings on the microstructure and texture evolution, as well as the deformation and failure modes of as-built LPBF maraging steel. In addition, the effect of heat-treatment on the mechanical behavior and microstructure evolution under compressive loadings is discussed. Constitutive modeling based on the Chang-Asaro equation is used to predict the dynamic behavior of as-built and heat-treated LPBF maraging steels under elevated and high strain rate deformations.

## **4.2. Experimental procedure**

### **4.2.1. Laser powder bed fusion (LPBF) process and maraging steel rods fabrication**

Cylindrical high strength martensitic 300-grade maraging steel rods with the dimension of 120 mm × 12 mm length and diameter and chemical composition listed in Table 4.1. were printed through the LPBF process using an EOS M290 additive machine located at Additive Metal Manufacturing Inc. (AMM) in Concord, ON. The rods were

printed using the process parameters recommended by EOS GmbH, shown in Table 4.2., to fabricate low-porosity samples (nominal density of 99.95%) [28]. The scanning strategy used was the stripes strategy, i.e., the laser beam was rotated  $67^\circ$  after each consecutive layer. Maraging steel rods were printed along the horizontal direction, as can be seen in Fig. 4.1., where the loading direction is perpendicular to the building direction.

Table 4. 1. Chemical composition of maraging steel 300 based on EOS datasheet.

Element	Fe	Ni	Co	Mo	Ti	Al	C
<b>Composition (wt. %)</b>	balance	17-19	8.5-9.5	1.5-5.2	0.6-0.8	0.05-0.15	<0.03

Table 4. 2. Process parameter of the LPBF process.

Laser power (W)	Scanning speed (mm/s)	Layer thickness ( $\mu\text{m}$ )	Hatch distance ( $\mu\text{m}$ )
<b>285</b>	960	40	110

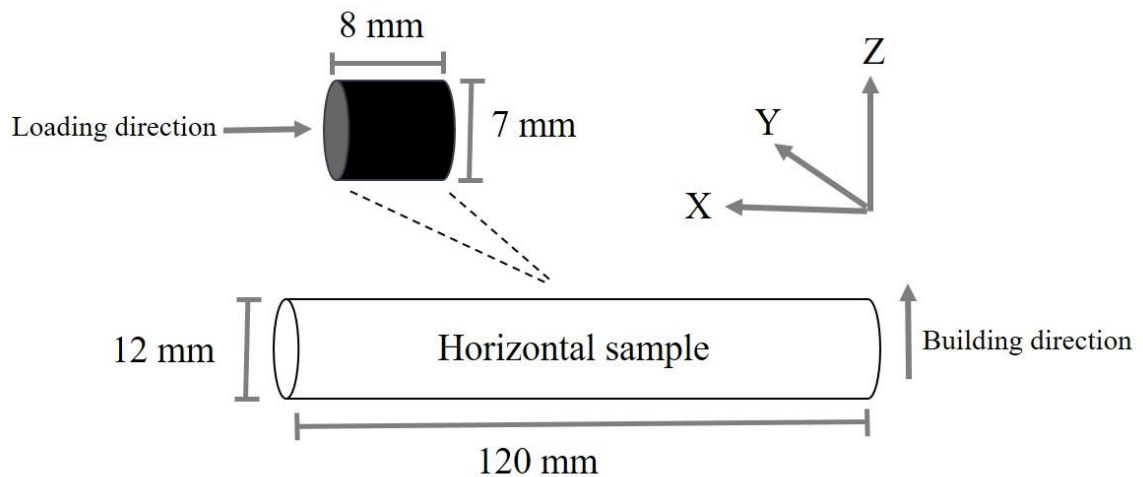


Fig 4. 1 Schematic of an LPBF-Maraging steel rod fabricated in the horizontal direction. The schematic of samples cut for dynamic impact loading is illustrated.

### **4.2.2. Heat-treatment**

A Calvin 1543 heat treatment chamber was used for the heat treatment procedure. The heat treatment procedure recommended by EOS was implemented, which consists of heating the sample at 490 °C for 6 hrs, followed by furnace cooling. The heating rate in the tests was set as 15 °C/min.

### **4.2.3. Dynamic compression tests**

Cylindrical rods with a diameter 7 mm and a length of 8 mm were machined for the mechanical tests. High strain rate tests using a split-Hopkinson Pressure Bar (SHPB) system were conducted at room temperature. As-built samples were subjected to firing pressures of 100 kPa, 120 kPa, 160 kPa, 180 kPa, and 200 kPa, which generated strain rates of 1500 s<sup>-1</sup>, 2000 s<sup>-1</sup>, 3200 s<sup>-1</sup>, 3500 s<sup>-1</sup>, and 4000 s<sup>-1</sup> in the impacted samples, respectively. The heat-treated samples were subjected to high strain-rate loading at strain rates of 150 s<sup>-1</sup>, 400 s<sup>-1</sup>, 670 s<sup>-1</sup>, 890 s<sup>-1</sup>, and 1930 s<sup>-1</sup> generated by the firing pressures of 50 kPa, 60 kPa, 70 kPa, 80 kPa, and 90 kPa, respectively. For each strain rate, three tests were conducted to ensure repeatability. Lower firing pressures were utilized for heat-treated samples due to their lower ductility. In other words, choices of firing pressures were made based on the ductility of as-built and heat-treated maraging steel samples based on literature.

Fig. 4.2. shows a schematic of the SHPB apparatus used in this study. A projectile is fired by a gas gun and strikes the incident bar, which results in deforming the sample sandwiched between the incident and the transmitter bars. Striking the projectile to the incident bar led to the generation of elastic waves, which are first captured by the incident

bar's strain gauge as the incident waves ( $\epsilon_I$ ). Some portions of these waves traveled through the specimen into the transmitted bar and were recorded via a strain gauge on the transmitted bar as the transmitted waves ( $\epsilon_T$ ). The rest of the waves were reflected and recorded as reflected waves ( $\epsilon_R$ ) by the same strain gauge on the incident bar. The nominal values of stress, strain, and strain rate data can be calculated based on the theory of one-dimensional wave propagation using the following equations [29]:

$$\sigma(t) = \left(\frac{A_B}{A_S}\right) \cdot E_B \cdot \epsilon_T \quad (4-1)$$

$$\epsilon(t) = \left(-2 \frac{C_B}{L_S}\right) \cdot \int_0^t \epsilon_R \cdot dt \quad (4-2)$$

$$\dot{\epsilon}(t) = \left(-2 \frac{C_B}{L_S}\right) \cdot \epsilon_R \quad (4-3)$$

In these equations,  $A_B$  and  $A_S$  are cross-sectional areas of the bars and specimen.  $C_B$ ,  $E_B$ ,  $L_S$ , and  $t$  are the velocity of elastic waves in bars, the elastic modulus of the bar material, the initial length of the specimen, and the deformation time. The true stress, true strain, and true strain rate can be calculated using the following equations:

$$\sigma = \sigma(t)(1 - \epsilon(t)) \quad (4-4)$$

$$\epsilon = -\ln(1 - \epsilon(t)) \quad (4-5)$$

$$\dot{\epsilon} = \dot{\epsilon}(t)/(1 - \epsilon(t)) \quad (4-6)$$

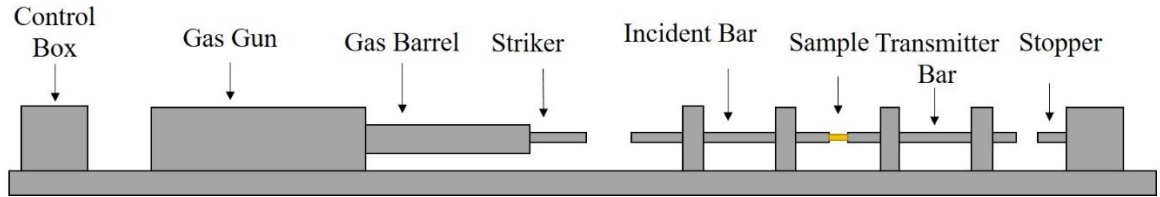


Fig 4. 2 Schematic of a split-Hopkinson Pressure Bar (SHPB) apparatus.

Fig 4.3. shows as-built and heat-treated samples after different dynamic compressive loadings. As can be seen, in the as-built condition, fracture occurred at the strain rate of  $3500 \text{ s}^{-1}$  for all three samples in which one of them was melted. However, in the heat-treated condition, all three specimens fragmented into two halves when subjected to the strain rate of  $1930 \text{ s}^{-1}$ .

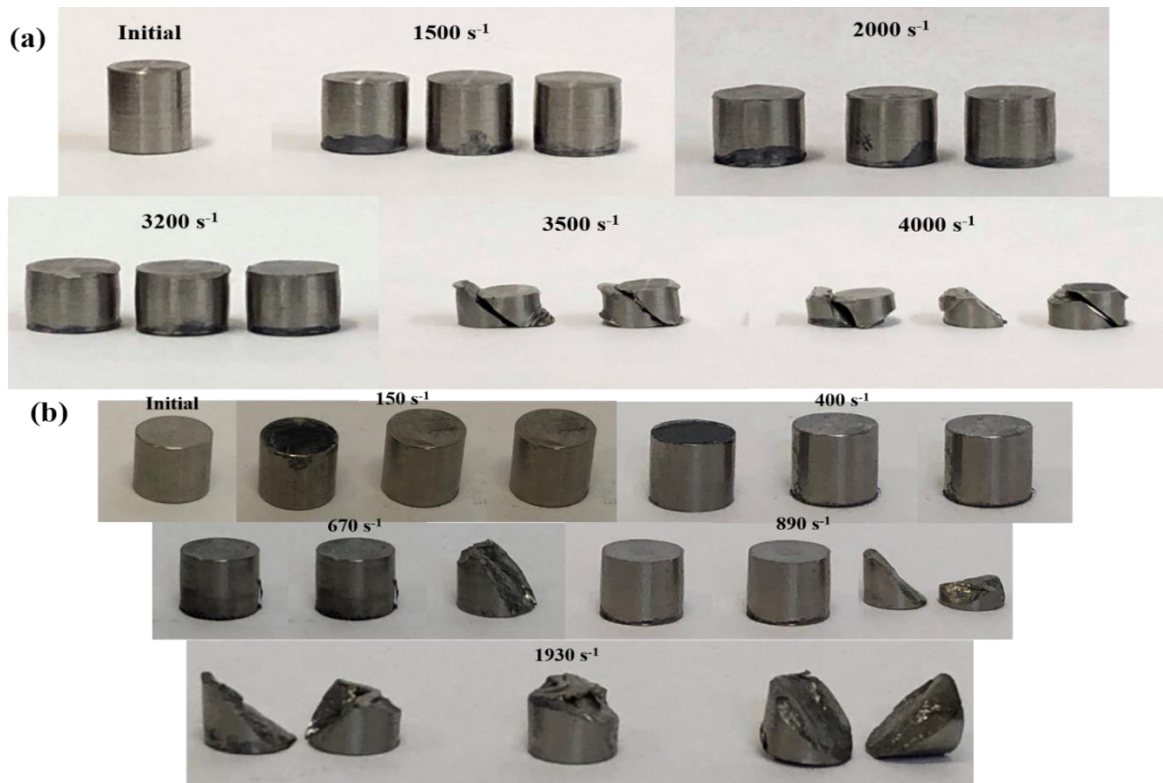


Fig 4. 3 Pictures of deformed samples after dynamic compressive loading. a) as-built maraging steel samples. b) heat-treated maraging steel samples.

#### **4.2.4. Microscopy**

For microstructural studies, samples were sectioned along with loading direction using a wafering blade. Surface preparation for microscopic investigations started with grinding using SiC papers, followed by polishing using diamond paste and finally etching with 3% Nital. The microstructural examination of the initial and impacted specimens along the loading direction was performed using a Thermo-Fisher Scientific/FEI's Scios 2 Dual Beam system. For EBSD analysis, a mirror-like surface was achieved using a vibratory polisher. EBSD characterization was carried out using a Thermo-Fisher Scientific/FEI's Scios 2 Dual-beam focused ion beam scanning electron microscopy (FIB-SEM) equipped with an integrated Oxford/HKL EBSD detector. Raw data were post-processed using Channel 5 software. To obtain statistically relevant crystallographic information, a relatively large area of  $400\ \mu\text{m} \times 300\ \mu\text{m}$  with a step size of 100 nm was chosen for the EBSD measurements.

### **4.3. Results**

#### **4.3.1. Dynamic compression behavior of LPBF-maraging steel**

##### **4.3.1.1. Dynamic flow curves**

The true strain rate-true strain curves of the dynamically deformed LPBF-maraging steel samples at the strain rates of  $1500\ \text{s}^{-1}$ ,  $2000\ \text{s}^{-1}$ ,  $3200\ \text{s}^{-1}$ ,  $3500\ \text{s}^{-1}$ , and  $4000\ \text{s}^{-1}$  are presented in Fig. 4.4. At different firing pressures, strain rate increased with strain in the first step of deformation, followed by a plateau, demonstrating the equilibrium between strain hardening and thermal softening [12]. Finally, because of the unloading, the strain

rate decreased. Each curve is an average of three conducted tests. In this study, the maximum value of the strain rate is representative of the experiment.

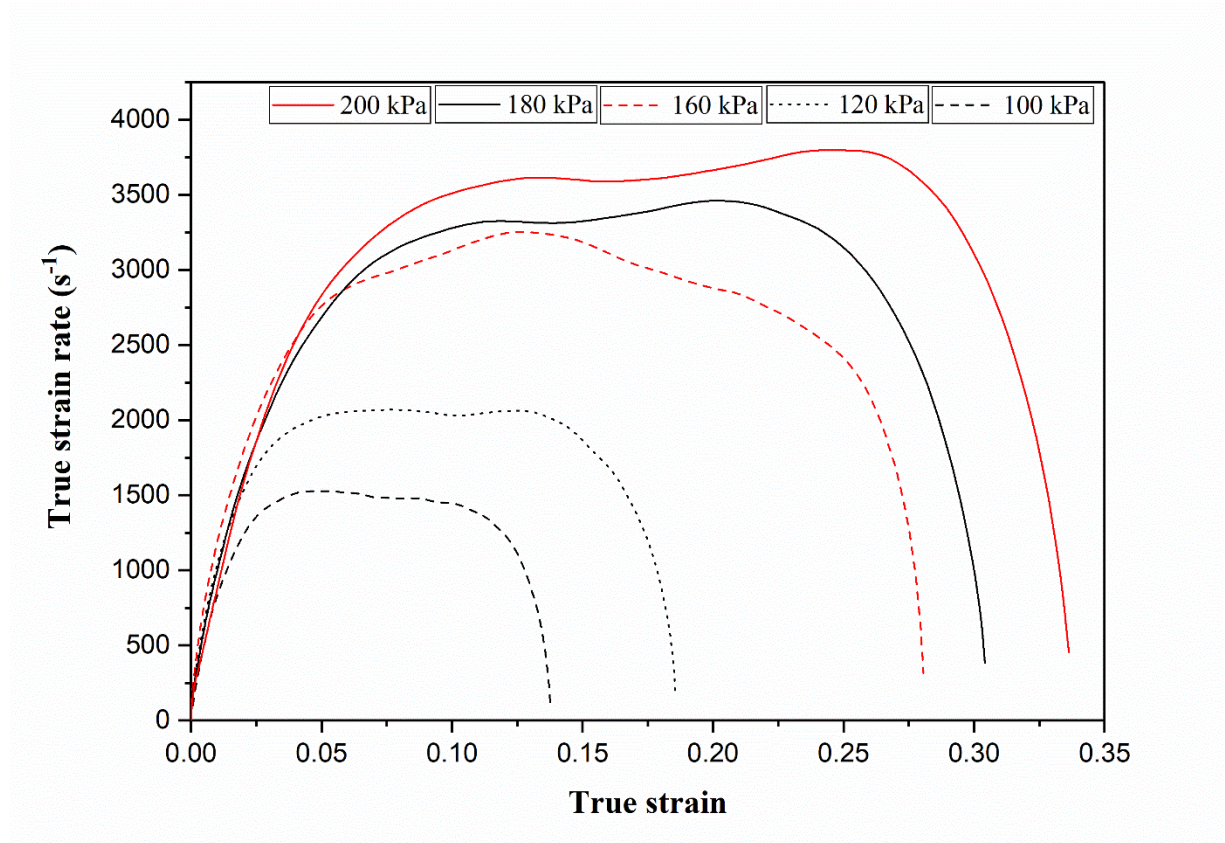


Fig 4. 4 Strain rate-strain curves of LPBF-maraging steel samples at different firing pressure bars, showing the strain rate variation during high strain rate compression loadings.

The true stress-true strain curves of dynamically deformed as-built LPBF-maraging steel samples at the strain rates of  $1500 \text{ s}^{-1}$ ,  $2000 \text{ s}^{-1}$ ,  $3200 \text{ s}^{-1}$ ,  $3500 \text{ s}^{-1}$ , and  $4000 \text{ s}^{-1}$  are presented in Fig 4.5. Each strain rate condition was tested at least three times, as shown in the inset in Fig 4.5., for the sample deformed at the strain rate of  $1500 \text{ s}^{-1}$ . As-built maraging steel samples were fragmented into pieces at the strain rate of  $3500 \text{ s}^{-1}$ , as shown in Fig 4.5. Table 4.3. shows flow stress, total strain, toughness, and temperature rise within

the samples at different strain rates. Generally, the ultimate compressive strength (UCS) and strain increased with increasing strain rate, which is an established behavior for strain rate sensitive materials. The increase of strength with increasing strain rate can be explained by dislocation-dislocation interaction, dislocation multiplication, and grain refinement [30]. The continuous dynamic recrystallization-induced grain refinement contributes to the increase in strength based on the Hall-Petch relationship. In addition, with the increase of strain rate, the heat generated in the sample increased, which leads to thermal softening and an increase in strain.

For the sample deformed at the strain rate of  $1500 \text{ s}^{-1}$ , the flow curve started with a considerable initial strain hardening, followed by a maximum peak. With increasing the strain, flow stress decrement can be observed, which indicates a competition between strain hardening due to the dynamic deformation and thermal softening as a result of the temperature rise inside the specimen during the high strain rate deformation process.

During dynamic deformation of metals and alloys at high strain rates, a considerable portion of the plastic work converts into heat, and an adiabatic condition develops in which there is a local rise in temperature resulting in localized loss of load-carrying capacity. As a result, plastic deformation becomes inhomogeneous, and strain localization occurs along narrow bands called adiabatic shear bands occurs [31] [32]. As deformation proceeds, the heat generated as a result of severe plastic deformation will not be dissipated quickly, leading to heat accumulation and a local temperature rise in the deformed specimen. Temperature rise can be calculated using the following equation [32]:

$$\Delta T = T - T_0 = \frac{\beta W_p}{\rho \cdot c_v} \quad (4-7)$$

where  $T_0$  is the room temperature,  $T$  is the temperature of the sample after dynamic compression tests,  $W_p$  is the plastic work of the high strain rate deformation,  $\rho$  and  $c_v$  are mass density and specific heat capacity at a constant volume, which are  $8 \text{ g/cm}^3$  and  $450 \pm 20 \text{ J/kg.}^\circ\text{C}$  in maraging steel C300, respectively. The Taylor-Quinney parameter ( $\beta$ ) is defined as the fraction of the plastic deformation that converts into thermal energy and can be calculated as follows:

$$\beta = \frac{Q_p}{W_p} \quad (4-8)$$

$$W_p = \int \sigma \cdot d\varepsilon \quad (4-9)$$

where  $Q_p$  is the heat, which is converted from plastic work; also  $\sigma$  and  $\varepsilon$ , are stress and strain. The Taylor–Quinney coefficient is assumed to be 0.9 in this work, which means 90% of the projectile's kinetic energy converted into heat energy [12] [32]. The temperature increase comes from the heat converted from plastic work and phase transformation. However, as maraging steel contains about 95% martensite (stable phase) [10], [33], heat from phase transformation can be neglected. The temperature rise of deformed samples is provided in Table 4.3.

Continuing with the discussion on the deformation behavior of the deformed samples using the stress-strain curves in Fig 4.5., with an increase of the strain rate to  $2000 \text{ s}^{-1}$ , the same behavior as the previous sample can be observed. As deformation proceeds, an increase of flow stress (as a result of strain hardening) and the subsequent decrease in flow stress (resulting from thermal softening) can be observed. However, a slight improvement in the ultimate compressive strength and the total strain can be observed.

Considering the flow curve of the specimen deformed at the strain rate of  $3200 \text{ s}^{-1}$ , the effect of thermal softening (drop-in flow stress) is more pronounced. In this strain rate, sample exhibited  $\sim 40\%$  higher total strain compared to the sample deformed at the strain rate of  $2000 \text{ s}^{-1}$  since thermal softening has been increased with the increase of strain rate. Due to the dominancy of thermal softening at this strain rate, the temperature rise within the specimen is significant  $\sim 150 \text{ }^\circ\text{C}$  (Table 4.3.).

By increasing the strain rate to  $3500 \text{ s}^{-1}$  and  $4000 \text{ s}^{-1}$ , the dynamic deformation ultimately resulted in the test samples' failure. A drop in the flow stress after initial strain hardening, followed by a rise of flow stress, can be seen in both flow curves, indicating the competition between strain hardening and thermal softening for deformation at these strain rates, where the effect of thermal softening became more intense. At the strain rates of  $3500 \text{ s}^{-1}$  and  $4000 \text{ s}^{-1}$ , UCS values are much higher than the previous strain rates. Significant increases in UCS and total strain were recorded in the specimen failed at the strain rate of  $4000 \text{ s}^{-1}$  (UCS by  $\sim 19.5\%$  and total strain by  $\sim 22\%$ ).

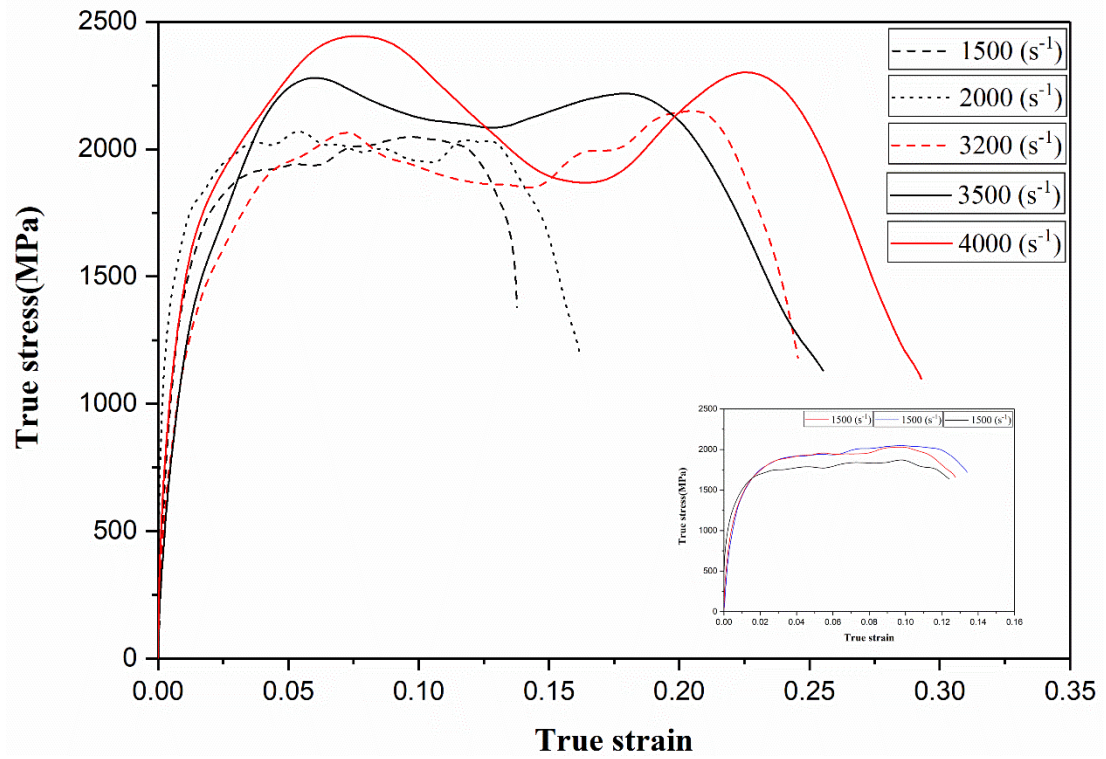


Fig 4. 5 True stress vs. true strain curves of LPBF-maraging steel dynamically compressed at the strain rates of  $1500 \text{ s}^{-1}$ ,  $2000 \text{ s}^{-1}$ ,  $3200 \text{ s}^{-1}$ ,  $3500 \text{ s}^{-1}$ , and  $4000 \text{ s}^{-1}$ . The specimens' flow curves deformed at the strain rate of  $1500 \text{ s}^{-1}$  in the inset ensure repeatability.

Table 4. 3. Dynamic mechanical properties of compressed LPBF-maraging steel.

Pressure (kPa)	Strain rate (s <sup>-1</sup> )	Yield stress (MPa)	UCS (Mpa)	Total strain (%)	Toughness (MJ/m <sup>3</sup> )	Temperature rise (°C)
100	1500	1232 ± 11.7	2005 ± 10.4	13.76 ± 1.2	245.3± 6.8	61.3± 3.2
120	2000	1424 ± 7.9	2070 ± 13.7	18.48 ± 2.1	348.7± 11.6	87.1± 10.2
160	3200	1528 ± 5.2	2126 ± 13.5	28.05 ± 3.3	519± 8.3	144.1± 11.5
180	3500	1872 ± 6.3	2279 ± 15.6	29.17 ± 2.9	566.5± 12.5	157.3± 11.3
200	4000	2004 ± 7.4	2493 ± 12.2	33.46 ± 3.1	647.7± 13.8	179.9± 15.4

The strain hardening rate vs. strain curves of the LPBF-maraging steel samples is presented in Fig 4.6. to comprehend the hardening and softening behavior during high strain rate deformation under compressive loadings. The strain hardening rate curves consist of three regimes of initial strain hardening drop, a plateau, and a final strain hardening drop resulting from thermal softening dominancy [34]. As the strain increases, the strain hardening rate dropped due to the transition from elastic to elastoplastic behavior (stage 1). It reached a steady-state condition because of the dynamic equilibrium between strain hardening and thermal softening, which results in dislocation recovery (stage 2). Finally, it decreased again (stage 3) that is due to the occurrence of stress concentration in microstructure [34], more severe dislocation annihilation, dynamic recrystallization (DRX), and adiabatic shear bands (ASBs) formation

caused by intense strain localization [35], which are mostly due to temperature rise during dynamic deformation. At the strain rate of  $1500 \text{ s}^{-1}$ , the strain hardening rate intercepted the x-axis at the strain of  $\sim 11\%$ , which shows thermal softening's dominant role in the deformation process over strain hardening.

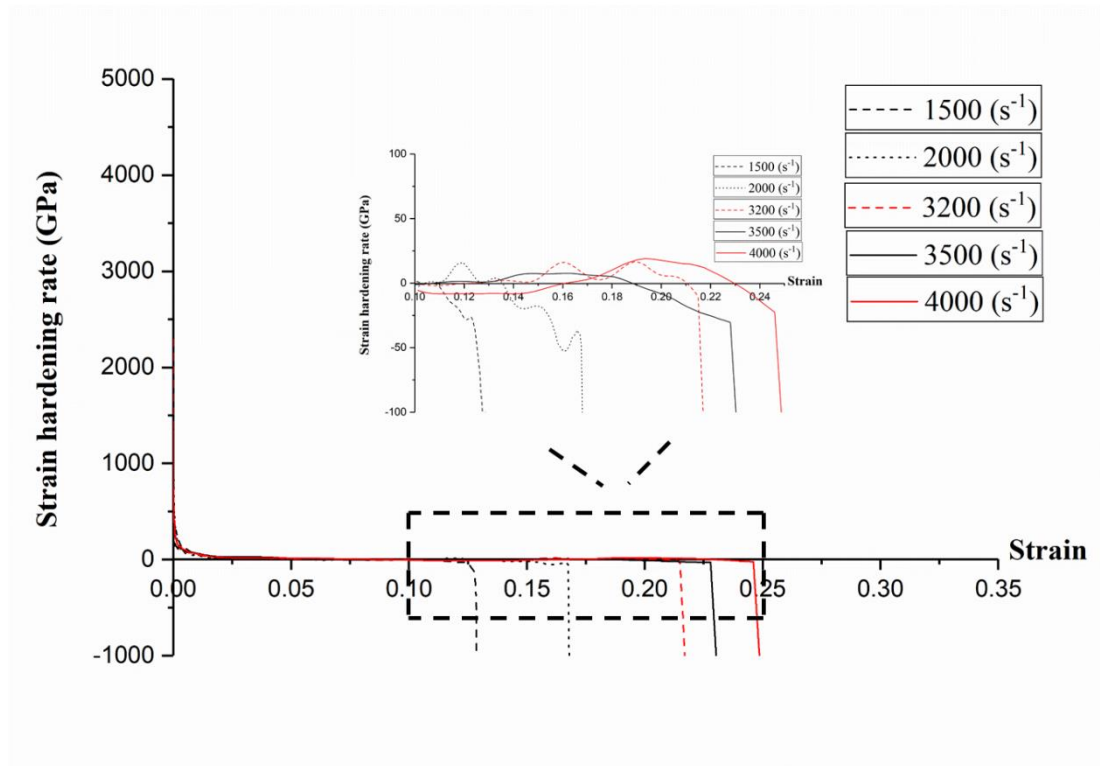


Fig 4. 6 Strain hardening rate vs. strain curves of LPBF-maraging steel dynamically compressed at the strain rates of  $1500 \text{ s}^{-1}$ ,  $2000 \text{ s}^{-1}$ ,  $3200 \text{ s}^{-1}$ ,  $3500 \text{ s}^{-1}$ , and  $4000 \text{ s}^{-1}$ .

#### 4.3.1.2. Microstructure features of as-built and dynamically deformed LPBF-maraging steel

SEM micrographs showing the typical microstructures of the as-built and dynamically deformed LPBF-maraging steel specimens are presented in Fig 4.7. It should be noted that the building and loading directions are perpendicular to each other in the deformed specimens. The initial microstructure (Fig 4.7.a) consists of the columnar and fine equiaxed grains. Columnar and equiaxed grains were observed at the bottom and top of the melt pool, respectively. Besides, the cellular grains were formed between columnar grains [10]. The fine equiaxed grains are mainly appearing due to the high cooling rate during melt pool formation [36]. The orientation of the columnar grain is almost along with the building direction. This phenomenon occurs because of the preferential cooling direction along the building direction, as the powder surrounding the part acts as an isolation layer, and the only heat loss modes are conduction through substrate and convection/radiation from the top of the part.

Fig 4.7.(b-d) exhibits the SEM micrographs of the cross-sectional area of the samples compressed at the strain rates of  $1500 \text{ s}^{-1}$ ,  $2000 \text{ s}^{-1}$ , and  $3200 \text{ s}^{-1}$ . More intense grain refinement by increasing strain rate can be observed. Using the ImageJ software, the grain size diameter at each strain rate was calculated. At the strain rates of  $1500 \text{ s}^{-1}$ ,  $2000 \text{ s}^{-1}$  and  $3200 \text{ s}^{-1}$ , grain size diameter was  $0.57 \pm 0.14 \text{ }\mu\text{m}$ ,  $0.44 \pm 0.10 \text{ }\mu\text{m}$  and  $0.30 \pm 0.06 \text{ }\mu\text{m}$ , respectively. According to the Hall-Petch equation, grain refinement can be responsible for higher UCS and strength at higher strain rates [12]. Also, in extremely deformed regions, due to the grains fragmentation, melt pool boundaries are not visible after deformation, notably in the specimen deformed at the strain rate of  $3200 \text{ s}^{-1}$ . Adiabatic shear bands (ASBs) were observed in strain rates of  $1500 \text{ s}^{-1}$ ,  $2000 \text{ s}^{-1}$  and  $3200 \text{ s}^{-1}$ . Severe shear strain localization and formation of adiabatic shear bands (ASBs) occur as a result of

thermomechanical instability caused by a local temperature rise and the associated local thermal softening. Moreover, the microstructure of the adiabatic shear bands was found to be finer compared to the other regions of the material. The finer grain structure of ASBs has been attributed to dynamic recovery and dynamic recrystallization [37].

It should be noted that, because of the microstructural heterogeneities induced by localized shear band formation, shear bands are undesirable in the microstructure as they lead to the fracture of the material. Elliptical or circular micro-voids were observed inside the ASBs (Fig 4.7.b) due to tensile force generated as a result of the difference in the plasticity ASB and that of the adjacent region. These voids eventually elongated along the ASBs at higher loadings, coalescing to form cracks, which propagated and led to failure [12].

By the strain rate increment, thermal softening becomes the prominent deformation mechanism, and at the strain rate of  $3200 \text{ s}^{-1}$  (Fig 4.7.d) and due to the adiabatic heat, a wider shear band can be observed. The microstructure of ASBs is different from the matrix due to massive shear stress localization during high strain rate deformation. Besides, compared to the initial microstructure, grain refinement is noticed because of the DRX [37]. Susceptibility of material to adiabatic shear bands can be predicted from the stress-strain curve, and as it was seen in table 4.3., temperature rise in  $3200 \text{ s}^{-1}$  was significant, which is compatible with wider shear bands. It should be noted that in those localized shear regions, the temperature rise is much more than what was calculated [31], and calculated values give global temperature rise in the specimen.

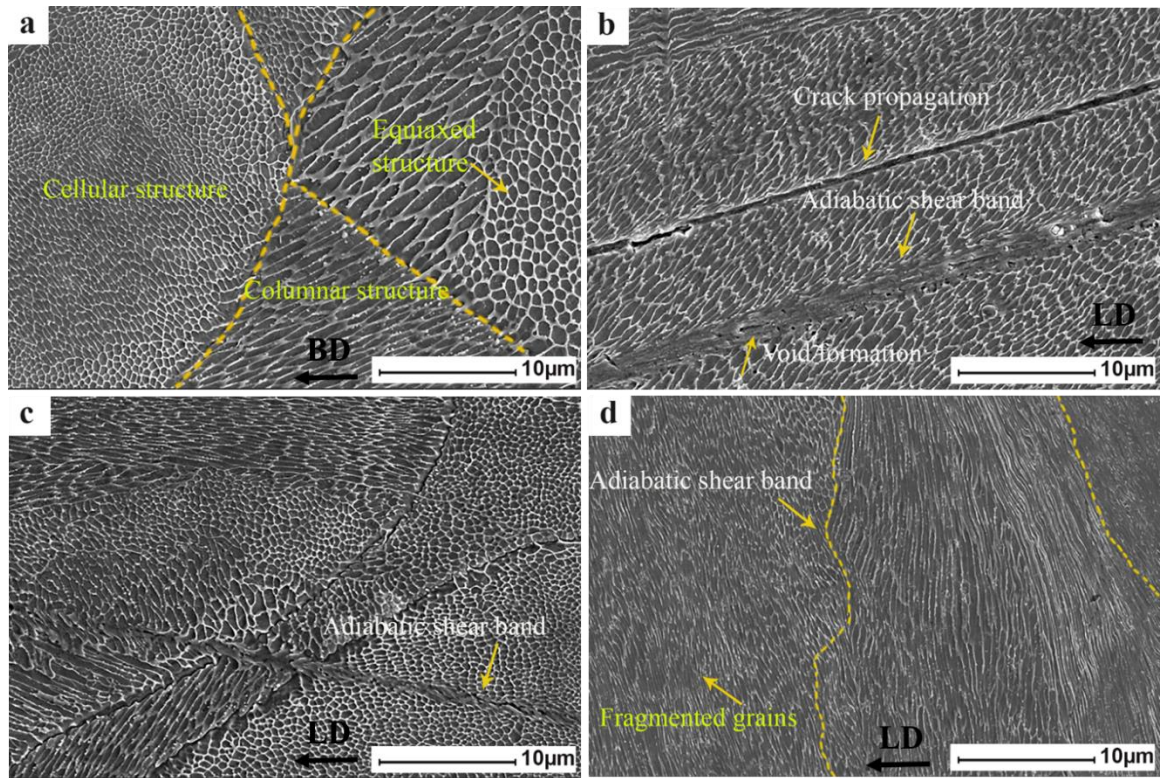


Fig 4. 7 Microstructures of the a) as-built sample, deformed specimens at strain rates of b)  $1500 \text{ s}^{-1}$ , c)  $2000 \text{ s}^{-1}$ , and d)  $3200 \text{ s}^{-1}$ . (BD and LD represent building direction and loading direction, respectively).

SEM fractography of the fragmented specimens deformed at strain rates of  $3500 \text{ s}^{-1}$  and  $4000 \text{ s}^{-1}$  are presented in Fig 4.8. In the specimen fractured at the strain rate of  $3500 \text{ s}^{-1}$  (Fig 4.8a), failure occurred because of an intensive localized shearing force oriented at  $45^\circ$  to the impact direction (maximum shear stress direction). The conical shape formed by the ASB, along which the crack propagation and fracture occurred, can be observed in the lower right region of Fig 8a. The fracture surface contains the knobby fracture feature (spherical clusters), which is evidence of intense local temperature rise in the specimen during high strain rate compressive loading (Fig 4.8b) [38]. In the fractured specimen at the strain rate of  $4000 \text{ s}^{-1}$ , crack initiation along with the ASBs was detected. These cracks can propagate by continuing deformation, resulting in the fragmentation of the specimen and the V-type shear bands (Fig 4.8b and d) [38]. In addition, in Fig 4.8c and e, ductile

dimples can be observed, indicating ductile fracture. Moreover, the knobby feature was detected in this sample, as well.

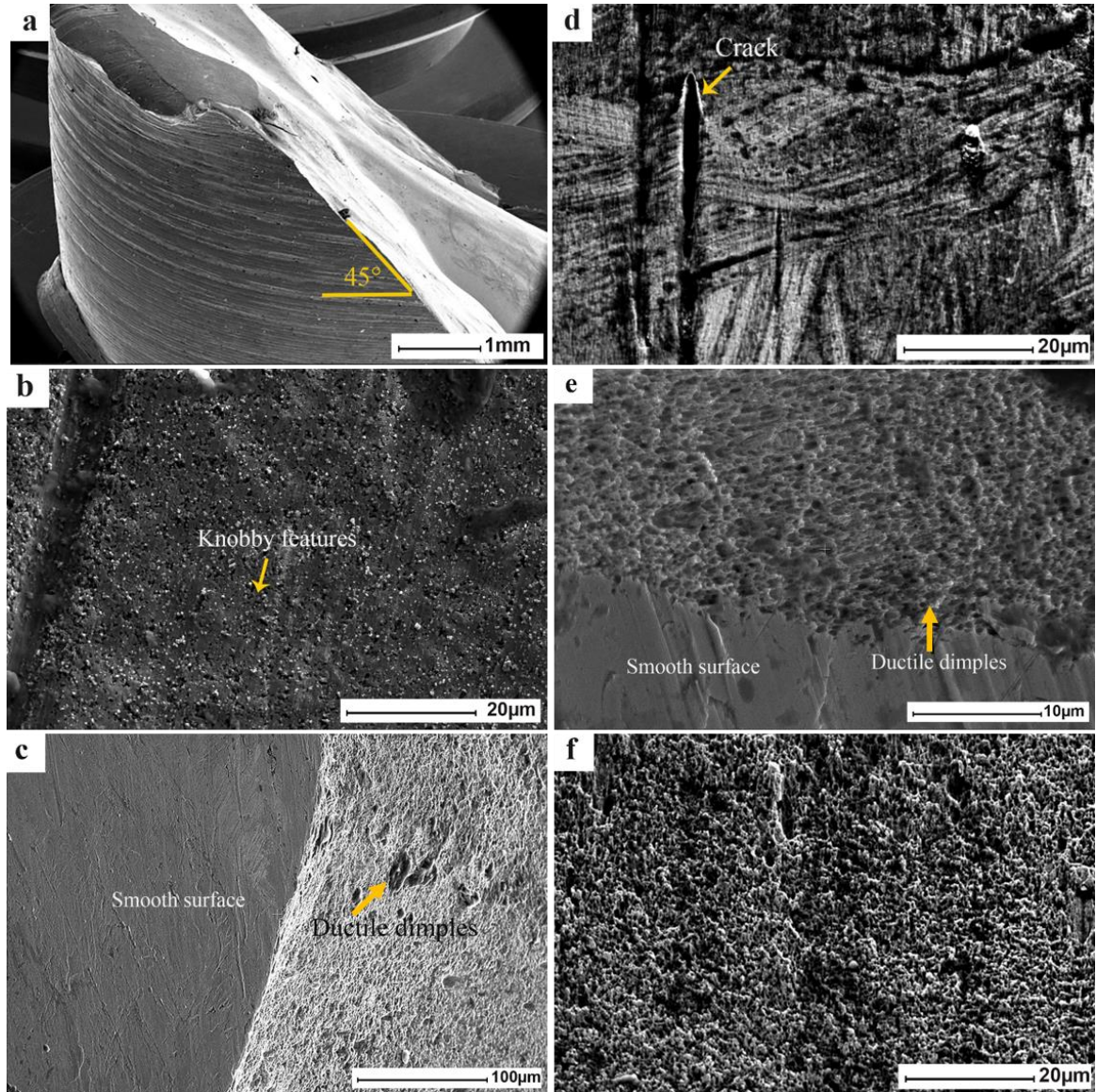


Fig 4. 8 SEM fractography of the fracture surfaces of specimens deformed at the strain rates of a, b, c) 3500  $s^{-1}$  and d, e, f) 4000  $s^{-1}$ .

#### 4.3.1.3. Texture development in the as-built deformed alloy

To understand the shear band formation mechanism, texture analysis was done on the deformed as-built sample. EBSD characterizations were conducted on the initial as-built sample and the dynamically deformed sample at the strain rate of  $3200 \text{ s}^{-1}$ . Fig 4.9. shows the pole figures and Orientation Distribution Function (ODF) of the as-built and deformed samples in which the deformed sample exhibits a more pronounced texture. The as-built sample was used as a reference for comparison with the deformed microstructures. Initially, random-oriented crystals are realigned into a preferred orientation during impact loading. Under high strain-rate testing, the maraging steel is shown to be strain rate sensitive, as observed through strong texture evolution when deformed at the strain rate of  $3200 \text{ s}^{-1}$ . The ODF of the sample deformed at the strain rate of  $3200 \text{ s}^{-1}$  shows that the dominant texture is positioned between Goss ( $\{110\} \langle 001 \rangle$ ) and Brass ( $\{110\} \langle 112 \rangle$ ) components. The intense texture observed in the deformed samples can be traced to adiabatic band formation. In other words, due to strain accumulation, grains rotate towards the shear direction to accommodate localized heat and stress. The Goss component was previously reported in materials subjected to high strain rate deformation attributed to the recrystallization in the microstructure [8]. Increasing the strain rate in the LPBF-maraging steel sample results in the alignment of  $\{110\}$  planes parallel to the loading direction and evolution of a strong texture. Saleh *et al.* also observed more pronounced texture development with an increase in strain rate for BCC steels [39]. During high strain rate compressive loadings, slip planes with high Schmid factor oriented to accommodate imposed strains, wherein these planes heat cannot dissipate, resulting in the formation of shear bands. In maraging steel with BCC structure, slip planes are  $\{110\}$ ,  $\{112\}$  and  $\{123\}$  and the slip direction is always  $\langle 111 \rangle$  (the direction of close packing) [40]. Slip planes

such as (110) will be activated during compression loading to accommodate imposed strain. From another perspective, ASBs are formed along the activated slip system to accommodate intense stress, and in this way, ASBs can relax stress concentrations [37]. Localized shear band is proposed to start with slip in favored crystallographic orientation in an individual grain, and then it propagates into adjacent grains leading to formation of macroscopic shear band [41], [31].

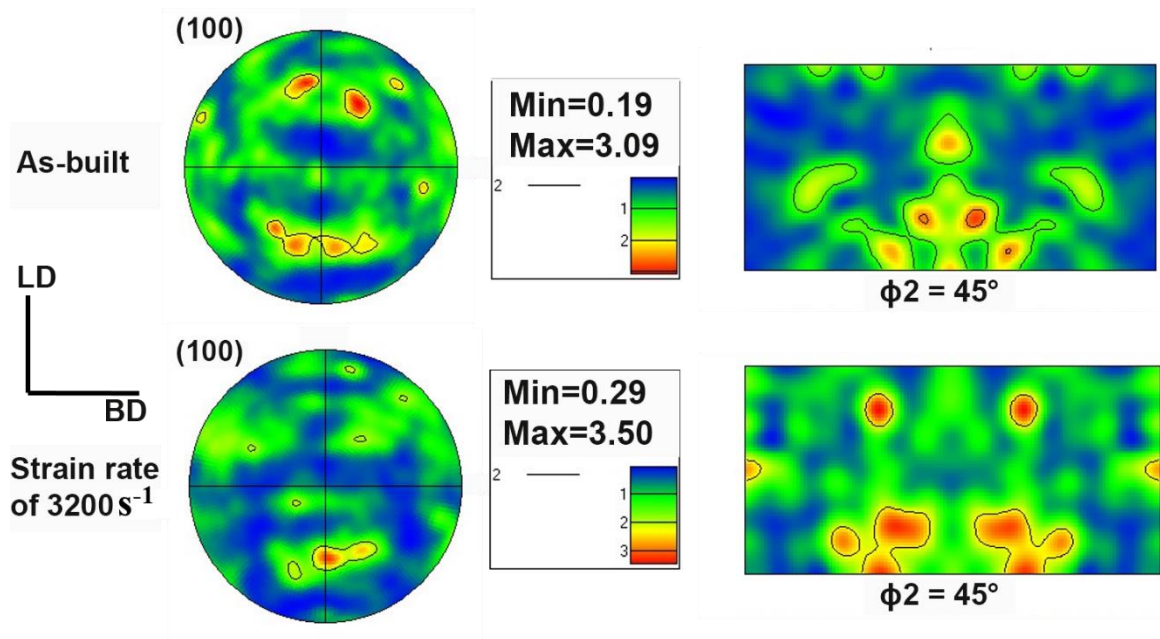


Fig 4. 9 EBSD pole figure and ODF maps of as-built and impacted maraging steel samples. (BD represents building direction and LD represents loading direction).

The microstructural changes due to the high strain rate deformation, which confirm the occurrence of dynamic recrystallization, are summarized in Table 4.4. It is believed that the temperature that dynamic recrystallization can happen decreases with the increase of dislocation density [42]. As with the increase of strain rate, dislocation density increased, it can be concluded that the temperature rises at the strain rate of  $3200 \text{ s}^{-1}$  ( $\sim 150 \text{ }^\circ\text{C}$ ) was enough for recrystallization. During the dynamic impact loading, the impact energy is

converted to thermal energy, which results in dynamic recrystallization. The grain size decreased after the deformation (average grain area of  $7.90 \pm 0.82 \mu\text{m}^2$  for the initial sample and  $1.81 \pm 0.15 \mu\text{m}^2$  for the impacted sample) and the percentage of fine equiaxed grains increased due to recrystallization (93% equiaxed grains in the impacted sample compared to 82% equiaxed grains in the initial sample). It should be noted that the high dislocation density at high strain rates can rotate the grains and accelerate recrystallization inside the adiabatic shear bands [37]. At high strain rates, adiabatic heating can occur in some narrow regions, resulting in the formation of the ASBs and the accompanying dynamic recrystallization[37]. Microstructural evolution during high strain rate includes dynamic recovery (DRV), static recrystallization (SRX), and dynamic recrystallization (DRX) [43]. As can be seen in table 4.4., higher fraction of low angle grain boundaries was found in deformed samples (64% LAGB in impacted samples compared to 44% LAGB in the initial sample). A higher fraction of LAGBs at high strain rates indicates that dynamic recovery happened near the shear bands [44].

Table 4. 4. Observations from the EBSD analysis of maraging steel original and post-impact samples.

	Grain area ( $\mu\text{m}^2$ )	Low Grain Boundary (%)	Equiaxed grains (%)
As-built sample	$7.90 \pm 0.82$	44	82
Deformed sample at the strain rate of 3200 $\text{s}^{-1}$	$1.81 \pm 0.15$	64	93

Fig. 4.10. shows the band contrast map, inverse pole figure (IPF), grain boundary map, and the corresponding kernel average misorientation (KAM) map of the impacted

sample at the strain rate of  $3200 \text{ s}^{-1}$  along the loading direction, which reveal the grain shape, size, and orientation characteristics close to the adiabatic shear band. As can be seen from the IPF map, pronounced crystallographic orientation is observed, and preferred  $\{110\}$  texture (green color) is developed adjacent to the adiabatic shear band (which is in agreement with pole figure and ODF maps). High strain accumulation inside shear bands results in a smearing of Kikuchi patterns in which some points could not be indexed. Near the adiabatic shear band, there are elongated grains perpendicular to the loading direction. Equiaxed grains developed inside the shear band, confirming dynamic recrystallized (DRX). At the strain rate of  $3200 \text{ s}^{-1}$ , the temperature of the sample increased significantly, which promotes dynamic recovery and dynamic recrystallization and the formation of new equiaxed grains. As can be seen in Fig 4.10.c, near the adiabatic shear band, the amount of low angle grain boundaries due to highly localized stress (represented by red lines) increased, which is an indication of dynamic recovery. Dynamic loading results in the generation of new dislocations and release of stored energy by dynamic recovery process and evolution of low angle grain boundaries [45]. A network of accumulated dislocations can be inferred from the presence of low-angle grain boundaries near the adiabatic shear band. This effect was confirmed from the corresponding KAM map, where KAM values represent local misorientation, which has a correlation with dislocation density. Higher KAM values suggest deformed grains with high dislocation density, which is in good agreement with the grain boundary map. High KAM values near shear bands suggest a higher driving force for dynamic recrystallization during the process of adiabatic shear band formation [37][44].

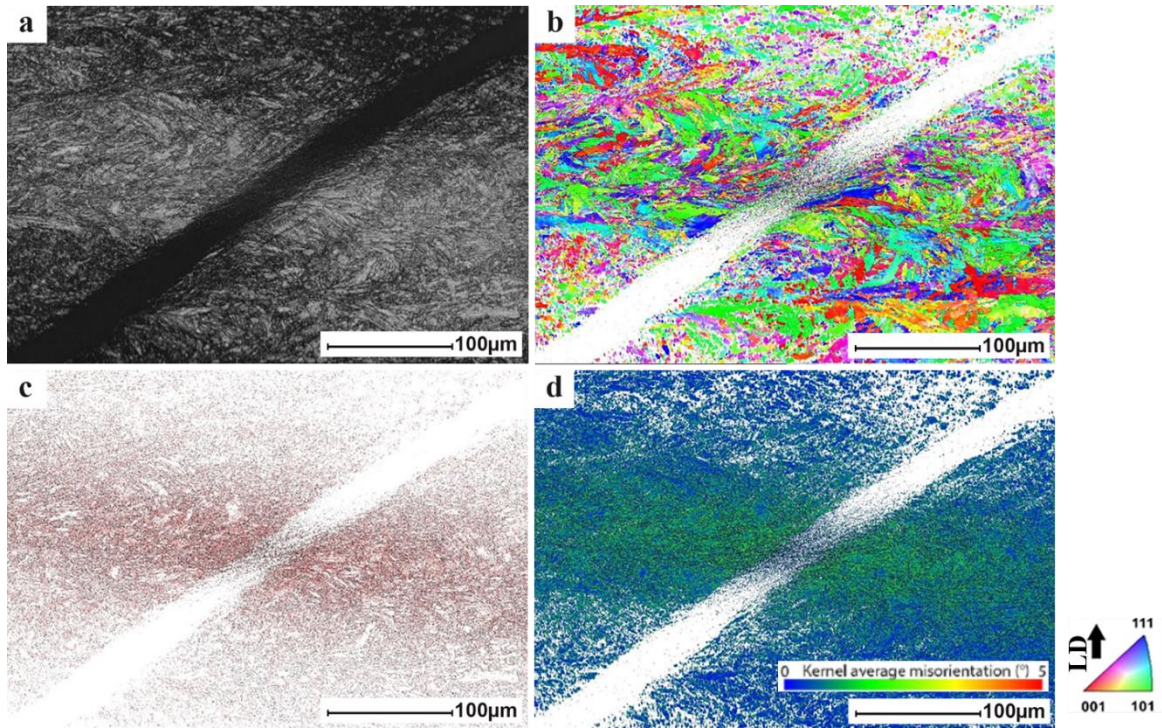


Fig 4. 10 EBSD analysis of impacted maraging steel sample at a strain rate of  $3200 \text{ s}^{-1}$  a) band contrast map, b) IPF-Y map along the loading direction, c) grain boundary map, d) KAM map.

### 4.3.2. Dynamic compression behavior of heat treated LPBF-maraging steel

#### 4.3.2.1. Dynamic flow curves

Fig 4.11. shows the strain rates achieved in the heat-treated specimens during dynamic loadings by different firing pressure of the striker bar in the SHPB test. It can be seen that the strain rate increased sharply at first and then remains constant, followed by a quick drop. Strain rates of  $150 \text{ s}^{-1}$ ,  $400 \text{ s}^{-1}$ ,  $670 \text{ s}^{-1}$ ,  $890 \text{ s}^{-1}$ , and  $1930 \text{ s}^{-1}$  were achieved by the firing pressures of 50 kPa, 60 kPa, 70 kPa, 80 kPa, and 90 kPa, respectively. Each curve's maximum value was considered the nominal strain rate, and each experiment was performed at least three times. The imposed strain rates in the heat-treated condition are

significantly lower than in the as-built ones due to lower ductility in heat-treated samples, which brings lower tolerance to high strain loads.

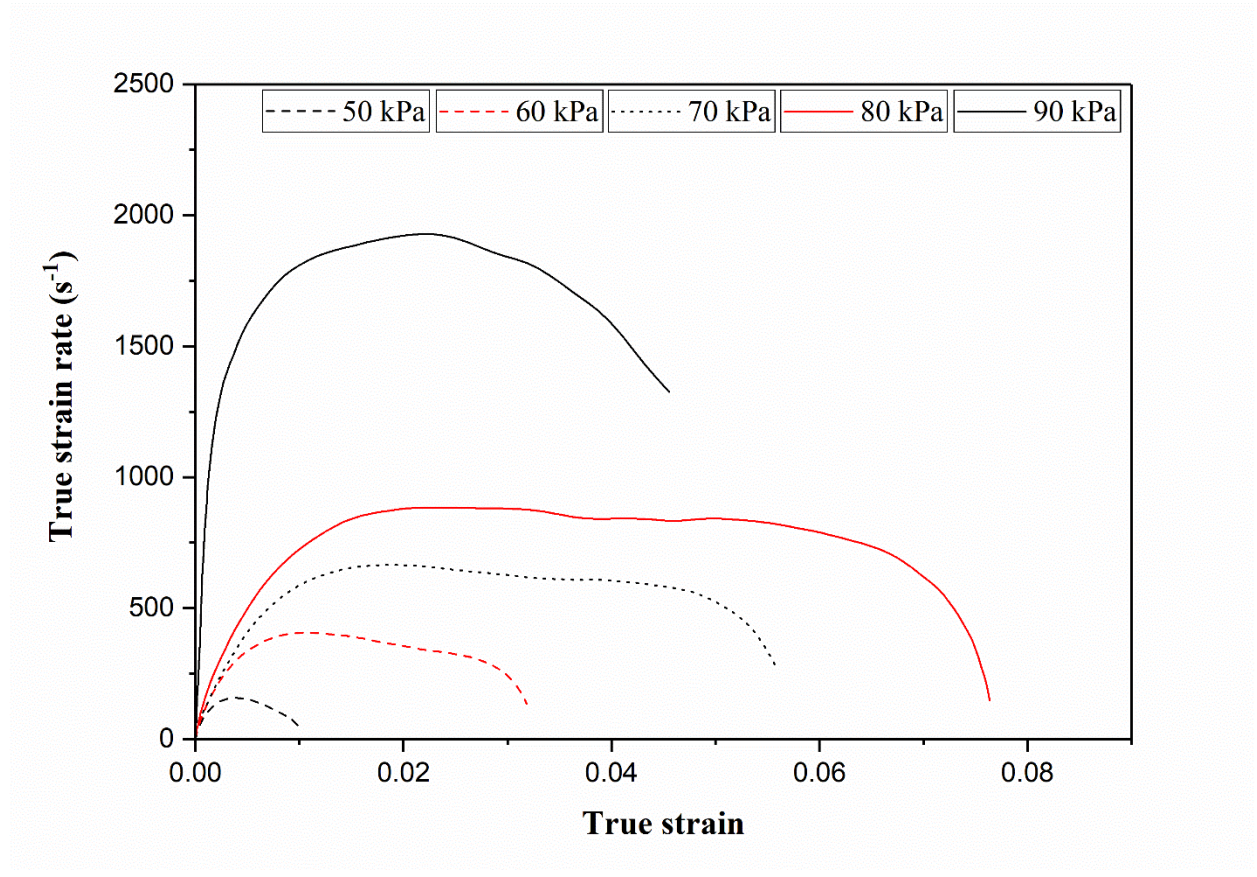


Fig 4. 11 Strain rate-strain curves of heat-treated LPBF-maraging steel samples at different firing pressure bars, showing the strain rate variation during high strain rate compression loadings.

The true stress-true strain curves of dynamically deformed heat-treated LPBF-maraging steel samples at the strain rates of  $150 \text{ s}^{-1}$ ,  $400 \text{ s}^{-1}$ ,  $670 \text{ s}^{-1}$ ,  $890 \text{ s}^{-1}$ , and  $1930 \text{ s}^{-1}$  are presented in Fig 4.12. Generally, aging at the temperature of  $490 \text{ }^{\circ}\text{C}$  results in an increase of strength and reduction of ductility in maraging steel [33]. Strength improved due to the formation of fine precipitates such as  $\text{Ni}_3\text{Ti}$  in the martensite matrix during the aging process [15][24]. Compared to the as-built deformed samples, higher UCS can be

observed in the heat-treated samples, which is associated with the precipitation hardening of the heat-treated samples. For the sample deformed at the strain rate of  $150 \text{ s}^{-1}$ , considerable initial strain hardening occurred at the beginning, followed by a maximum peak and a quick drop in stress. The small portion of the plastic deformation region is due to the negligible contribution of deformation mechanisms such as slip in the heat-treated maraging steel samples [33]. With the increase of strain rate to  $400 \text{ s}^{-1}$ , dislocation density increased, which results in the increase of total strain. By increasing the strain rate from  $400 \text{ s}^{-1}$  to  $670 \text{ s}^{-1}$ , initial strain hardening decreased, which is a sign of temperature rise and thermal softening in the samples at higher strain rates. As previously mentioned, during high strain rate loadings, competition between strain hardening and thermal softening occurs. In the sample deformed at the strain rate of  $890 \text{ s}^{-1}$ , stress remains approximately constant before a drop in stress, which shows an equilibrium state between the two mentioned phenomena. The heat-treated specimen fragmented when subjected to the strain rate of  $1930 \text{ s}^{-1}$  as shown in Fig 4.3. As presented in Table 4.5., UCS does not change significantly with the increase in strain rate. This behavior is related to the presence of precipitates in the heat-treated samples. Dislocation density increment occurred as a consequence of increasing the strain rate; however, due to the accumulation of dislocations in front of precipitates, dislocations start to annihilate, and they can not be effective as they were in other samples.

In the heat-treated LPBF-maraging steel samples, ductility is so much lower than the as-built samples, which indicates a lower number of active slip systems is involved in the plastic deformation of the heat-treated samples [33]. As was discussed in section 3.1.3, the dominance of thermal softening, accumulation of heat, and formation of adiabatic shear

bands are related to the activation of slip systems. Due to the lower active slip systems in the heat-treated condition, heat accumulation and temperature rise are lower than for the as-built samples (table 4.5.). In other words, heat dissipates due to the limited number of activated slip systems, and the formation of adiabatic shear bands is less probable. This is the reason for the small contribution of thermal softening over strain hardening in the flow curves of the strain rates from  $150 \text{ s}^{-1}$  to  $670 \text{ s}^{-1}$ . Heat accumulation in slip planes and the formation of ASBs is one way to dissipate shock energy and accommodate intense stress. As can be seen from table 4.5., due to the lower toughness of the heat-treated samples, the temperature rise in the heat-treated samples was not significant, suggesting why the adiabatic shear bands (ASBs) were not observed in the heat-treated samples at the strain rates of  $150 \text{ s}^{-1}$  to  $670 \text{ s}^{-1}$ . However, at the strain rate of  $890 \text{ s}^{-1}$ , a significant temperature rise was recorded, which indicates that heat accumulation and the formation of adiabatic shear bands can occur at this strain rate.

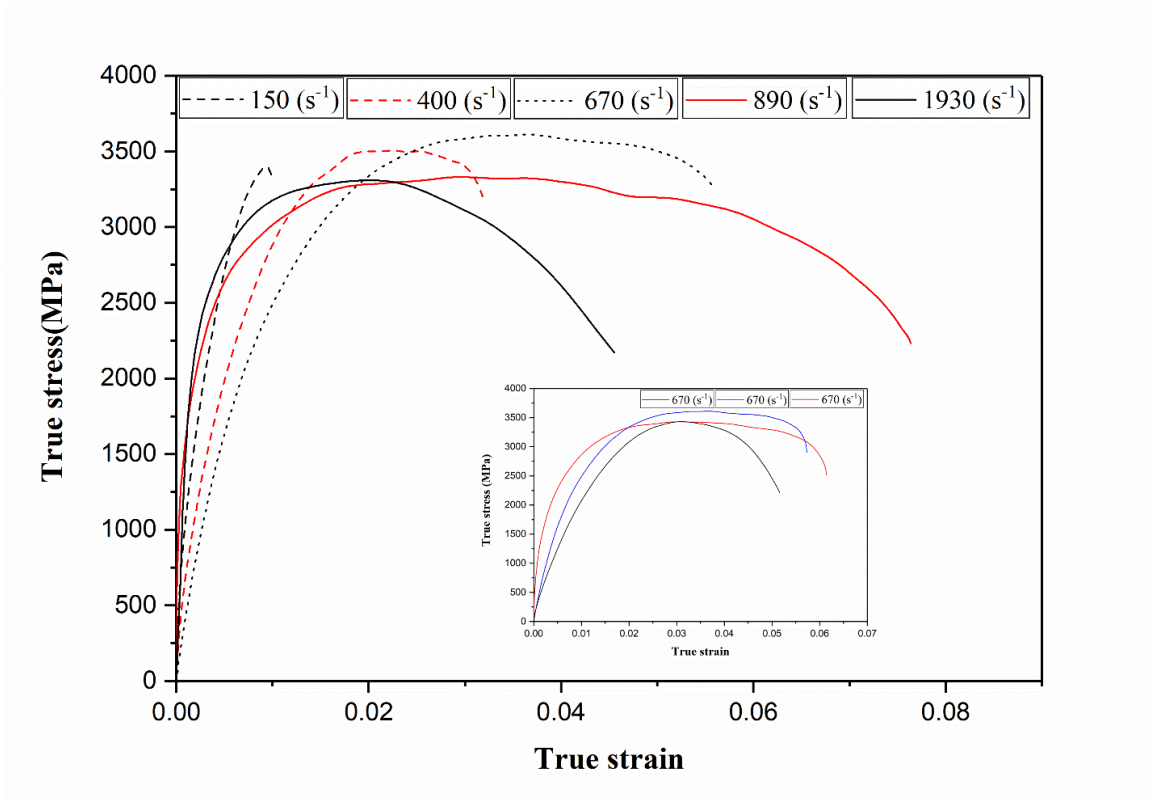


Fig 4. 12 True stress vs. true strain curves of heat-treated LPBF-maraging steel dynamically compressed at the strain rates of  $150 \text{ s}^{-1}$ ,  $400 \text{ s}^{-1}$ ,  $670 \text{ s}^{-1}$ ,  $890 \text{ s}^{-1}$ , and  $1930 \text{ s}^{-1}$ . The specimens' flow curves deformed at the strain rate of  $150 \text{ s}^{-1}$  in the inset to ensure repeatability.

To have a better understanding of the strain hardening/softening behavior of the dynamically deformed heat-treated LPBF-maraging steel samples, the strain hardening rate ( $\theta = d\sigma/d\varepsilon$ ) versus strain ( $\varepsilon$ ) is plotted in Fig 4.13. The same hardening/softening behavior was observed in the heat-treated samples as was recorded in the as-built samples. At the beginning of the deformation, samples experienced a rapid strain hardening drop (stage I) followed by a plateau (stage II). It should be noted that, at strain rates of  $150 \text{ s}^{-1}$  and  $400 \text{ s}^{-1}$ , the curves intercepted the x-axis at shorter strains. Compared to Fig 4.6., in the heat-treated samples, negative strain hardening rates occurred at lower strains as these samples are more brittle due to the presence of fine precipitates [23]. In addition, the length of stage

II is more prominent at the strain rates of  $890 \text{ s}^{-1}$ , which shows the dominance of thermal softening over the strain hardening at this strain rate.

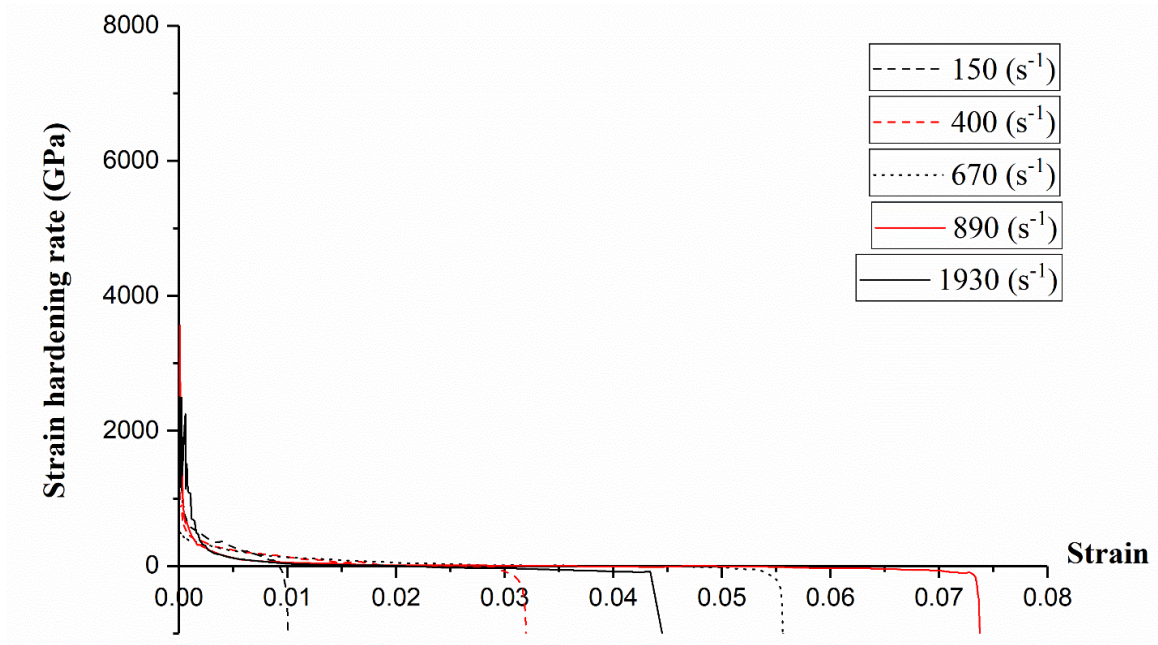


Fig 4. 13 Strain hardening rate vs. strain curves of LPBF-maraging steel dynamically compressed at the strain rates of  $150 \text{ s}^{-1}$ ,  $400 \text{ s}^{-1}$ ,  $670 \text{ s}^{-1}$ ,  $890 \text{ s}^{-1}$ , and  $1930 \text{ s}^{-1}$ .

Table 4. 5. Dynamic mechanical properties of compressed heat-treated LPBF-maraging steel.

Pressure (kPa)	Strain rate (s <sup>-1</sup> )	Yield stress (MPa)	UCS (MPa)	Total strain (%)	Toughness (MJ/m <sup>3</sup> )	Temperature rise (°C)
50	150	3271 ± 15.5	3397 ± 10.6	0.09 ± 0.05	24.0 ± 11.3	6.0 ± 2.3
60	400	3298 ± 12.3	3500 ± 22.6	3.17 ± 0.07	92.2 ± 11.7	23.0 ± 5.6
70	670	3395 ± 10.4	3611 ± 13.5	5.59 ± 0.07	171.6 ± 14.3	42.9 ± 4.2
80	890	2907 ± 33.3	3331 ± 18.3	7.63 ± 1.2	231.2 ± 18.2	57.8 ± 7.6
90	1930	2864 ± 21.7	3305 ± 14.6	4.55 ± 3.2	132.8 ± 12.3	33.2 ± 10.4

#### 4.3.2.2. Microstructure of heat treated deformed LPBF-maraging steel

Fig. 14 shows the SEM images of the initial and deformed microstructure of heat-treated LPBF-maraging specimens deformed at the strain rates of  $150 \text{ s}^{-1}$ ,  $400 \text{ s}^{-1}$ ,  $670 \text{ s}^{-1}$ . As can be seen, aging treatment resulted in the complete disappearance of scan tracks and solidification traces (Fig 4.14. a), which were observed in the as-built samples [33]. Compared to the as-built condition, in heat-treated samples, melt pool and grain boundaries are vague and irregular that can be owing to the phase transformation and residual stress releasing during the heat treatment procedure [23] [33]. ASBs were not observed in these samples (Fig 4.14. b-d), an indication that the temperature rise is not sufficient to cause heat accumulation and shear strain localization leading to the occurrence of ASBs. As was seen in table 4.5., temperature rise during dynamic compressive loadings of the heat-treated maraging steel samples was much lower than the as-built samples.

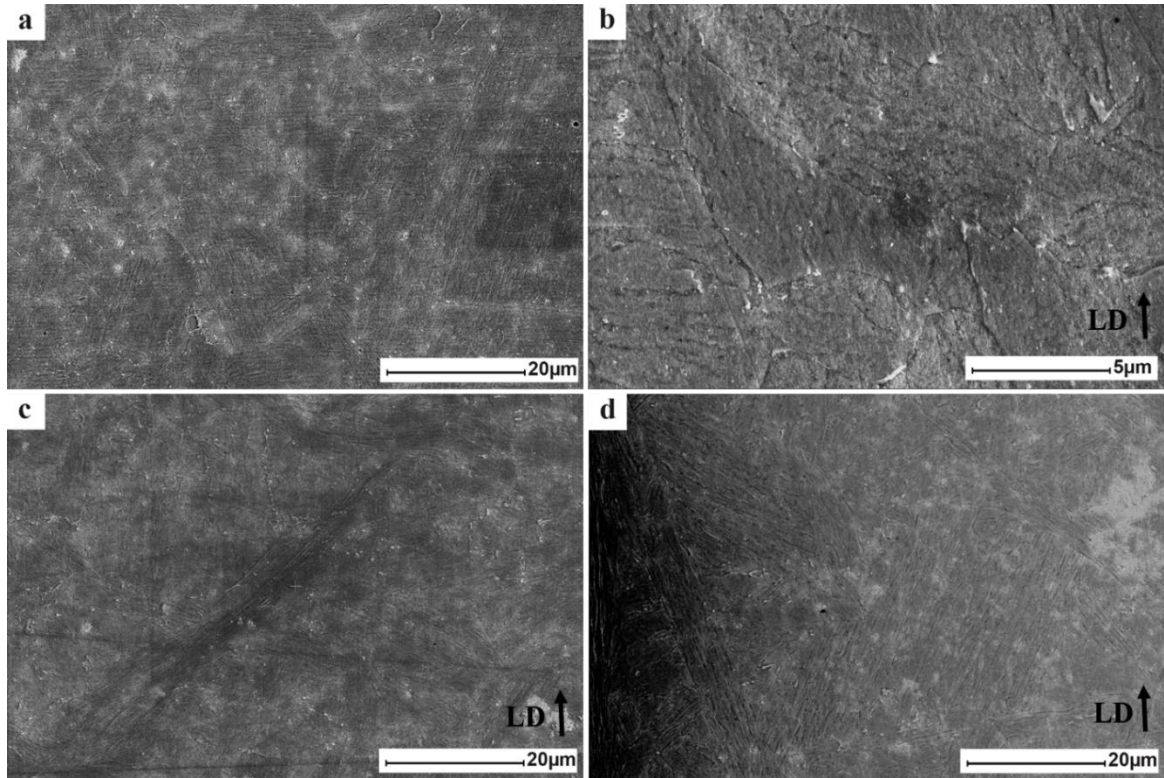


Fig 4. 14 Microstructures of the a) initial heat-treated maraging steel, b) deformed samples in strain rate of  $150 \text{ s}^{-1}$ , c) deformed sample in strain rate of  $400 \text{ s}^{-1}$ , d) deformed sample in strain rate of  $670 \text{ s}^{-1}$ .

Fig 4.15. shows the SEM images of the heat-treated LPBF-maraging steel specimens deformed at the strain rate of  $890 \text{ s}^{-1}$ , in which ASBs resulting from temperature rise and strain softening were observed (Fig 4.15. a, c, and d). Due to an intense shear strain localization at this strain rate, the temperature increased locally, resulting in the formation of ASBs. These bands are oriented at  $45^\circ$  to the compression axis. Void nucleation, growth, and coalescence occurred within the ASBs, leading to crack formation, crack propagation, and failure [12]. Fig 4.15. (b) depicts a crack propagating along with an ASB. Shear stress localization along the ASBs resulted in the formation of cracks. Cracks inside ASBs elongated and propagated in the direction of shear stress leading ultimately to fragmentation of specimen at higher strain rates. From Fig 4.15. (c) and (d), shear bands

are featureless, which indicates that dynamic recrystallization could have happened at the strain rate of  $890 \text{ s}^{-1}$ . Adiabatic heat during the strain rate of  $890 \text{ s}^{-1}$  could be high enough (based on table 4.5.) to result in dynamic recovery and dynamic recrystallization.

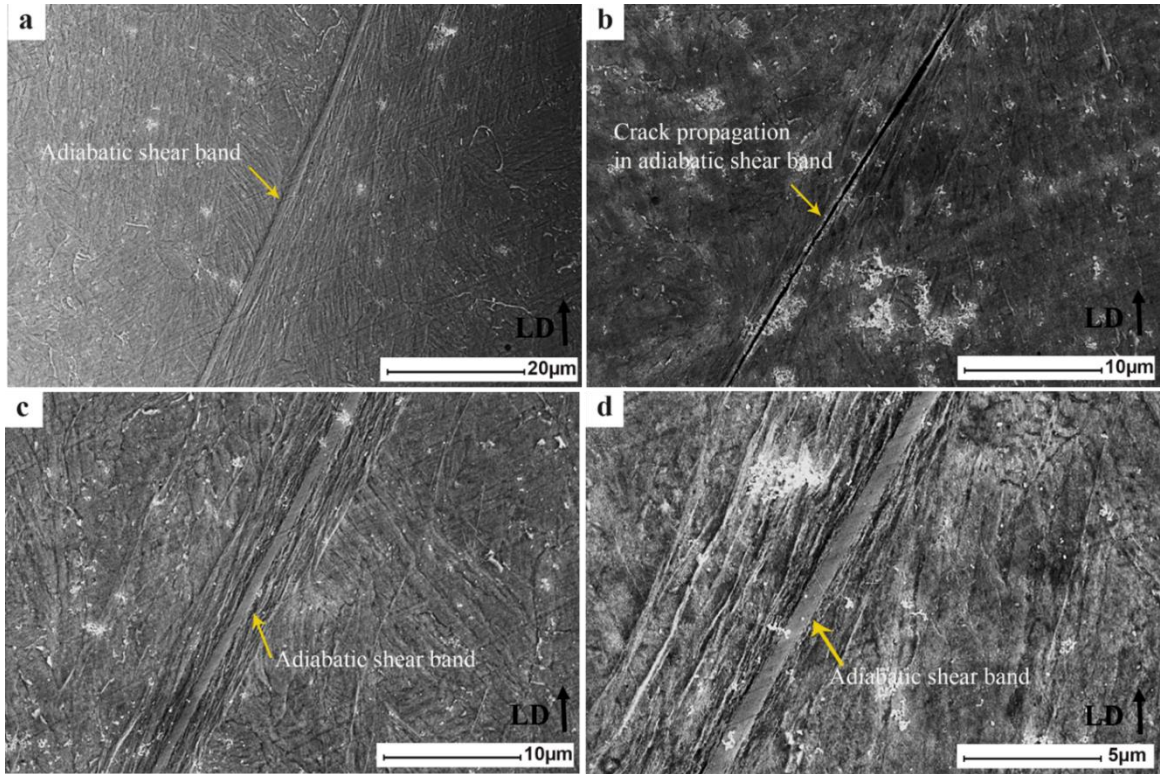


Fig 4. 15 Microstructures of the deformed specimens at strain rates of  $890 \text{ s}^{-1}$ . (LD represent loading direction).

Fig 4.16. shows the SEM fractography of the heat-treated LPBF-maraging steel specimens deformed at the strain rate of  $1930 \text{ s}^{-1}$ . The fracture occurred because of intensive shear stress along the maximum shear stress direction, which is  $45^\circ$  to impact direction (Fig 4.16. a). It can be observed that the specimen shows a small number of shallow dimples, which is a characteristic feature for transgranular ductile fracture (Fig 4.16. b-d). On the other hand, quasi-cleavages can be observed in these figures,

representing brittle fracture (Fig. 16 b-d). This confirms that the as-built samples broke after substantial plastic deformation, while in the heat-treated samples, plastic deformation is insufficient, and its dominant fracture mode is a brittle fracture. Furthermore, brittle fracture surface for the heat-treated LPBF-maraging steel samples was also observed before for uniaxial tensile test [23].

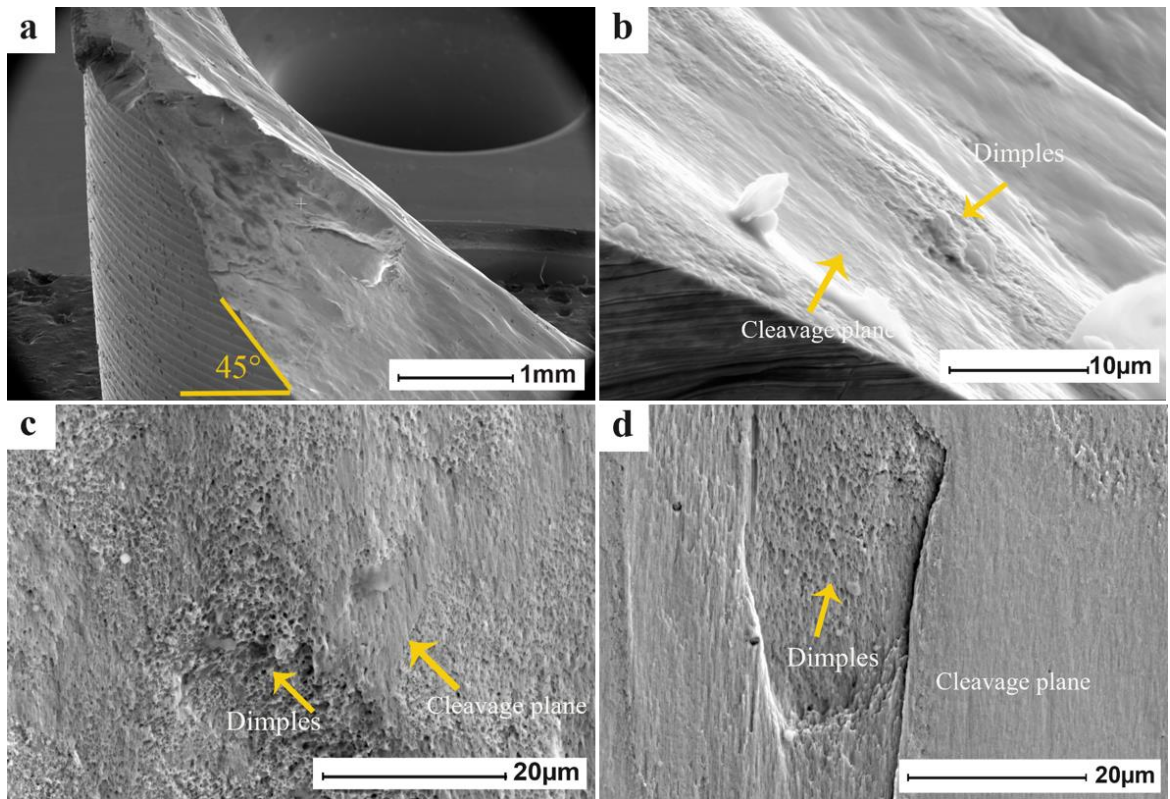


Fig 4. 16 SEM fractography of the fracture surfaces of the heat-treated specimen deformed at the strain rate of  $1930 \text{ s}^{-1}$ .

### 4.3.3. Constitutive modeling of dynamic deformation behavior

#### 4.3.3.1. Mathematical modeling development for as-built LPBF-maraging steel

For the dynamically compressed LPBF-maraging steel samples, the Chang-Asaro hardening equation was used to model the dynamic compressive behavior as significant hardening behavior was recorded in the flow curves. Eq. 10 was introduced for modeling the dynamic behavior where three brackets are responsible for changes in flow stress at the beginning (initial strain hardening), middle (thermal softening), and final part (drop) [46].

$$\bar{\sigma} = \sigma_0 + \left[ (\sigma_s - \sigma_0) \cdot \tanh \left( \frac{h_0}{\sigma_s - \sigma_0} \cdot \varepsilon_p \right) \right] \cdot \left[ \tanh^2 \left( \frac{\varepsilon_p - \varepsilon_m}{A} \right) + B \right] \cdot \left[ 1 - \exp \left( C \frac{(\varepsilon_p - \varepsilon_f)}{\varepsilon_p} \right) \right] \quad (4-10)$$

In this equation,  $\bar{\sigma}$  is the effective true stress,  $\sigma_0$  is the yield stress,  $\sigma_s$  is the saturation stress,  $h_0$  is the initial hardening rate,  $\varepsilon_p$  is the plastic strain,  $\varepsilon_m$  is a strain related to the inflection point of the trough where the softening phase returns to hardening,  $A$  controls the width of said trough, and  $B$  controls the depth of the said trough. In addition,  $C$  is a constant, which correlates to the severity of the decay, and  $\varepsilon_f$  is related to the final strain [46].

The theoretical modeling for dynamic compression data displayed a good agreement with the experimental data at all the strain rates ( $1500 \text{ s}^{-1}$ ,  $2000 \text{ s}^{-1}$ ,  $3200 \text{ s}^{-1}$ ,  $3500 \text{ s}^{-1}$ , and  $4000 \text{ s}^{-1}$ ), as shown in Fig 4.17. The effect of strain rate alteration on the initial hardening rate ( $h_0$ ) and saturation stress ( $\sigma_s$ ) are exhibited in Fig 4.18. With the increase in strain rate, saturation stress increased. However, the initial hardening rate ( $h_0$ ) decreased with increasing strain rate. The same behavior was observed in the flow curves in Fig 4.5.

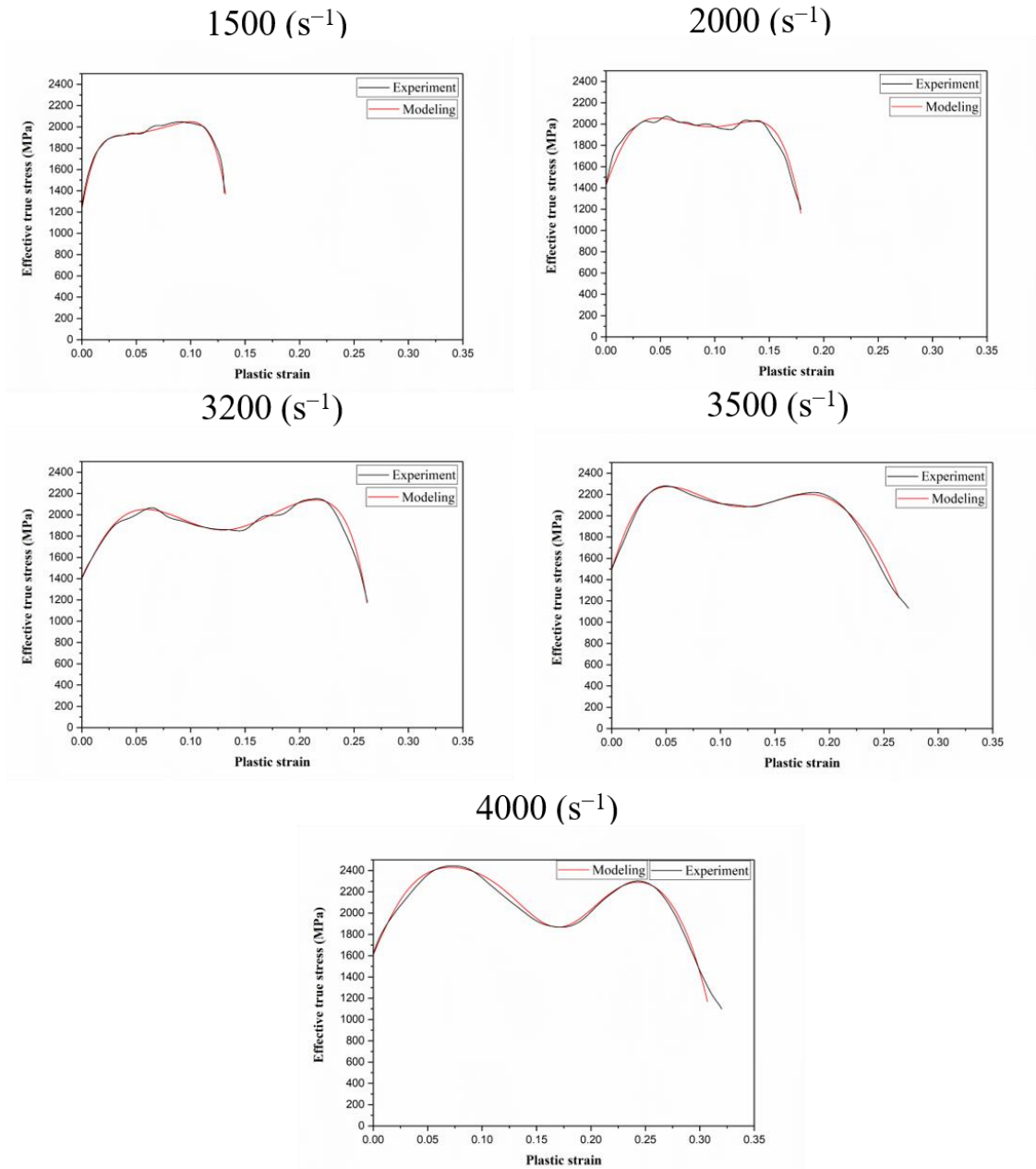


Fig 4. 17 Comparison of the Chang-Asaro modeling with the experimental data for the LPBF-maraging steel samples at the strain rates of 1500 s<sup>-1</sup>, 2000 s<sup>-1</sup>, 3200 s<sup>-1</sup>, 3500 s<sup>-1</sup>, and 4000 s<sup>-1</sup>.

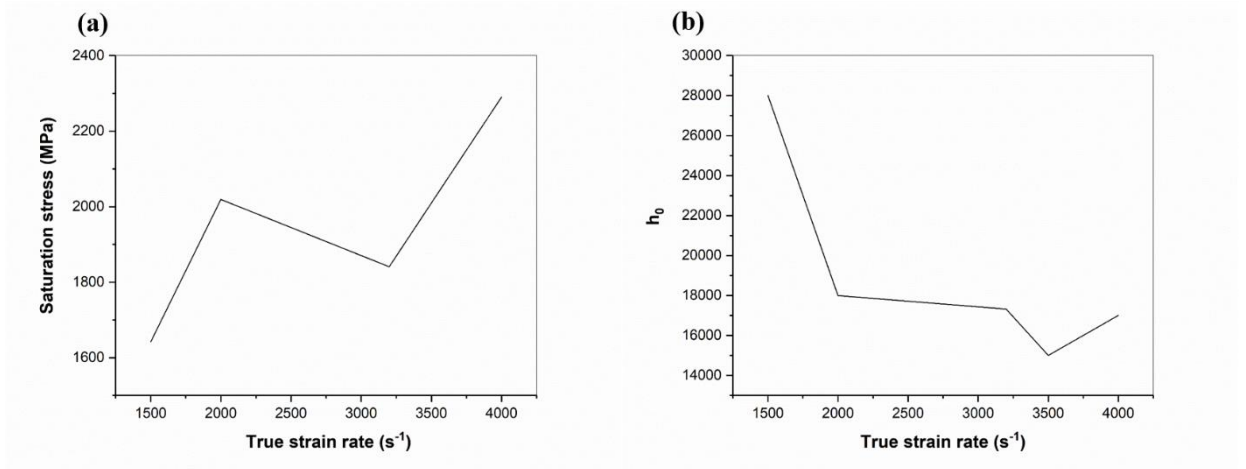


Fig 4. 18 Effect of strain rate on the (a) saturation stress and (b) initial hardening rate of dynamically deformed LPBF-maraging steel based on the Chang-Asaro model.

#### 4.3.3.2. Mathematical modeling development for heat treated LPBF-maraging steel

The Chang-Asaro hardening equation was utilized to predict the dynamic compression behavior of the heat-treated LPBF-maraging steel at the strain rates of 150 s<sup>-1</sup>, 400 s<sup>-1</sup>, 670 s<sup>-1</sup>, 890 s<sup>-1</sup>, 1930 s<sup>-1</sup>. The theoretical modeling using the Chang-Asaro equation to fit the experimental data for the heat-treated deformed samples is shown in Fig 4.19., in which good agreement between the experimental data and the modeling was obtained. Fig 4.20. shows changes in the saturation stress ( $\sigma_s$ ) and the initial hardening ( $h_0$ ) with strain rate in heat-treated LPBF-maraging steel. As can be seen, with an increase in strain rate, stress saturation increased that is because of the grain refinement. In addition, the initial hardening rate is much more significant in the heat-treated samples compared to the as-built samples, which is attributable to the brittle nature of the heat-treated samples. However, with an increase in strain rate, the initial strain hardening first decreased and then

increased at the strain rate of  $890 \text{ s}^{-1}$ , which can be attributed to the dominance of thermal softening.

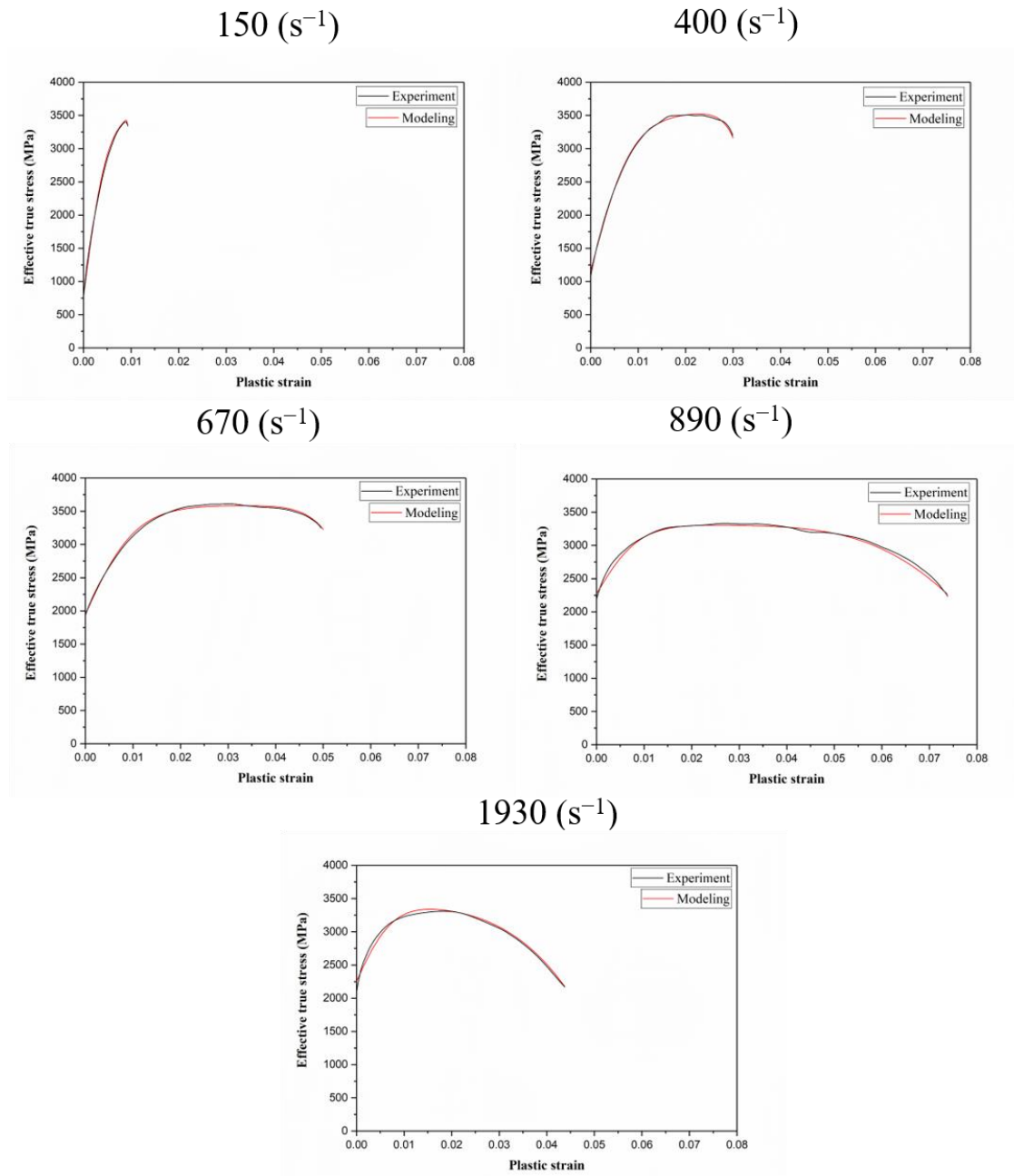


Fig 4. 19 Comparison of the Chang-Asaro modeling with the experimental data for the LPBF-maraging steel samples at the strain rates of  $150 \text{ s}^{-1}$ ,  $400 \text{ s}^{-1}$ ,  $670 \text{ s}^{-1}$ ,  $890 \text{ s}^{-1}$ , and  $1930 \text{ s}^{-1}$ .

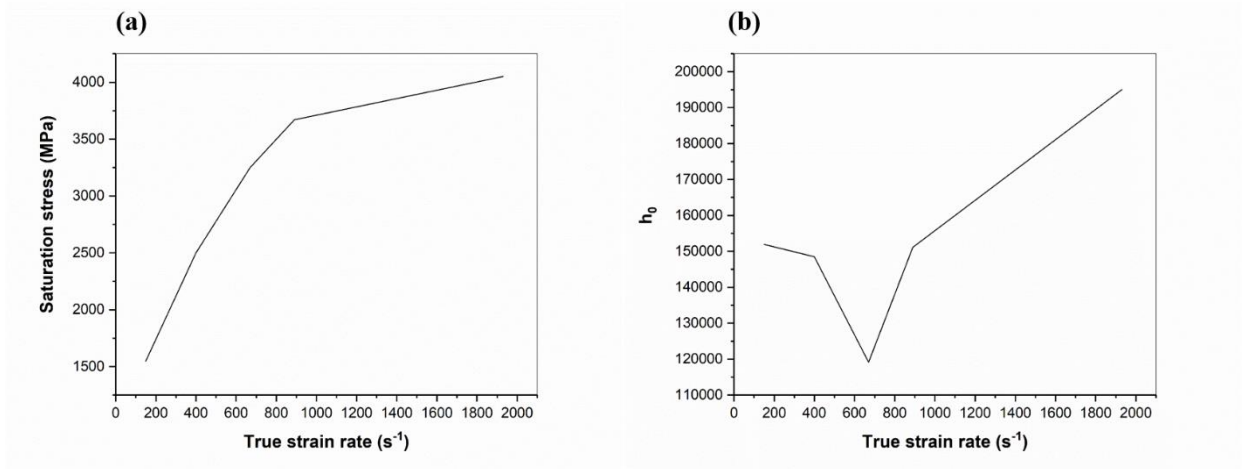


Fig 4. 20 Effect of strain rate on the (a) saturation stress and (b) initial hardening rate of dynamically deformed heat-treated LPBF-maraging steel based on the Chang-Asaro model.

#### 4.4. Conclusion

Additively manufactured as-built and heat-treated maraging steel specimens were subjected to dynamic loadings to investigate the dynamic behavior, deformation mechanisms, microstructural and texture evolution, and mechanical properties improvement. Split-Hopkinson Pressure Bar (SHPB) apparatus was used to conduct high strain rate compressive loadings on the as-built maraging steels samples at the strain rates of 1500 s<sup>-1</sup> to 4000 s<sup>-1</sup>, and the heat-treated samples at the strain rates of 150 s<sup>-1</sup> to 1930 s<sup>-1</sup>. As a result of thermomechanical instability during dynamic loading, adiabatic shear bands formed in the as-built samples at the strain rates of 1500 s<sup>-1</sup>, 2000 s<sup>-1</sup>, and 3200 s<sup>-1</sup> and in the heat-treated samples at the strain rate of 890 s<sup>-1</sup>. Although in the as-built samples, fracture occurred at the strain rate of 3500 s<sup>-1</sup>, fracture in the heat-treated samples occurred at the strain rate of 1930 s<sup>-1</sup>, which can be related to the presence of precipitates in the heat-

treated condition (brittleness of heat-treated samples). In LPBF-maraging steels, fracture occurred due to the formation of cracks along with shear bands and in the direction of the maximum shear stress, which is  $45^\circ$  to the impact direction. The ductile fracture was identified for as-built samples (due to the presence of plastic strain corresponding to high elongation), while brittle fracture was identified for heat-treated samples due to insufficient plastic deformation in the heat-treated samples. A theoretical model incorporating a Chang-Asaro hardening function was developed for both as-built and heat-treated maraging steel samples. Theoretical models showed good agreement with experimental results at all strain rates.

#### **4.5. References**

- [1] E. Yasa, K. Kempen, J. Kruth, L. Thijs, J. Van Humbeeck, Microstructure and mechanical properties of maraging steel 300 after selective laser melting, in: Solid Free. Fabr. Symp. Proc., 2010: pp. 383–396.
- [2] S.J. Midea, G.D. Pfaffmann, Heat Treating: Including Steel Heat Treating in the New Millennium, ASM International, 2000.
- [3] J.M. Chilton, C.J. Barton, Identification of strengthening precipitates in 18 Ni-250 Aluminum , Vanadium and Titanium maraging steels, ASM Trans Quart. 60 (1967).
- [4] J.B. Lecomte, C. Servant, G. Cizeron, A comparison of the structural evolution occurring during anisothermal or isothermal treatments in the case of nickel and manganese type maraging alloys, J. Mater. Sci. 20 (1985) 3339–3352.

- [5] M.J. Fleetwood, G.M. Higginson, G.P. Miller, The identification of precipitates in maraging steels by electron microscopy and electron probe X-ray microanalysis, *Br. J. Appl. Phys.* 16 (1965) 645.
- [6] K. Shimizu, H. Okamoto, Transmission electron microscopy study of strengthening precipitates in 18% Ni maraging steel, *Trans. Japan Inst. Met.* 12 (1971) 273–279.
- [7] A. Jakus, A. Fredenburg, N. Thadhani, High-strain-rate behavior of maraging steel linear cellular alloys: Mechanical deformations, *Mater. Sci. Eng. A.* 534 (2012) 452–458.
- [8] H. Asgari, A. Odeshi, K. Hosseinkhani, M. Mohammadi, On dynamic mechanical behavior of additively manufactured AlSi10Mg\_200C, *Mater. Lett.* 211 (2018) 187–190.
- [9] M. Shellabear, O. Nyrhilä, DMLS-Development history and state of the art, *Laser Assist. Netshape Eng.* 4, Proc. 4th LANE. (2004) 21–24.
- [10] S. Dehgahi, M.H. Ghoncheh, A. Hadadzadeh, M. Sanjari, B.S. Amirkhiz, M. Mohammadi, The role of titanium on the microstructure and mechanical properties of additively manufactured C300 maraging steels, *Mater. Des.* (2020) 108965.
- [11] C. Dharmendra, B.S. Amirkhiz, A. Lloyd, G.D.J. Ram, M. Mohammadi, Wire-arc additive manufactured nickel aluminum bronze with enhanced mechanical properties using heat treatments cycles, *Addit. Manuf.* 36 (2020) 101510.
- [12] R. Alaghmandfard, C. Dharmendra, A.G. Odeshi, M. Mohammadi, Dynamic mechanical properties and failure characteristics of electron beam melted Ti-6Al-

- 4V under high strain rate impact loadings, *Mater. Sci. Eng. A.* 793 (2020) 139794.
- [13] T. DebRoy, H.L. Wei, J.S. Zuback, T. Mukherjee, J.W. Elmer, J.O. Milewski, A.M. Beese, A. Wilson-Heid, A. De, W. Zhang, Additive manufacturing of metallic components – Process, structure and properties, *Prog. Mater. Sci.* 92 (2018) 112–224. <https://doi.org/10.1016/j.pmatsci.2017.10.001>.
- [14] J.P. Oliveira, T.G. Santos, R.M. Miranda, Revisiting fundamental welding concepts to improve additive manufacturing: From theory to practice, *Prog. Mater. Sci.* 107 (2020) 100590.
- [15] J. Mutua, S. Nakata, T. Onda, Z.C. Chen, Optimization of selective laser melting parameters and influence of post heat treatment on microstructure and mechanical properties of maraging steel, *Mater. Des.* 139 (2018) 486–497. <https://doi.org/10.1016/j.matdes.2017.11.042>.
- [16] J.P. Oliveira, A.D. LaLonde, J. Ma, Processing parameters in laser powder bed fusion metal additive manufacturing, *Mater. Des.* 193 (2020) 108762.
- [17] Y. Yao, Y. Huang, B. Chen, C. Tan, Y. Su, J. Feng, Influence of processing parameters and heat treatment on the mechanical properties of 18Ni300 manufactured by laser based directed energy deposition, *Opt. Laser Technol.* 105 (2018) 171–179.
- [18] K.V.A. Chakravarthi, N. Koundinya, S.V.S.N. Murty, B.N. Rao, Microstructure, properties and hot workability of M300 grade maraging steel, *Def. Technol.* 14 (2018) 51–58.

- [19] B. Song, B. Sanborn, P.E. Wakeland, M.D. Furnish, Dynamic Characterization and Stress-Strain Symmetry of Vascomax® C250 Maraging Steel in Compression and Tension, *Procedia Eng.* 197 (2017) 42–51.
- [20] S. Loewy, L. Hjortd, B. Rheingans, E.J. Mittemeijer, Modulated formation of lath martensite: Influence of uniaxial compressive load and transformation-induced plasticity, *Acta Mater.* 109 (2016) 46–54.
- [21] R. Schnitzer, G.A. Zickler, E. Lach, H. Clemens, S. Zinner, T. Lippmann, H. Leitner, Influence of reverted austenite on static and dynamic mechanical properties of a PH 13-8 Mo maraging steel, *Mater. Sci. Eng. A.* 527 (2010) 2065–2070.
- [22] E. Cyr, A. Lloyd, M. Mohammadi, Tension-compression asymmetry of additively manufactured Maraging steel, *J. Manuf. Process.* 35 (2018) 289–294.
- [23] C. Tan, K. Zhou, W. Ma, P. Zhang, M. Liu, T. Kuang, Microstructural evolution, nanoprecipitation behavior and mechanical properties of selective laser melted high-performance grade 300 maraging steel, *Mater. Des.* 134 (2017) 23–34. <https://doi.org/10.1016/j.matdes.2017.08.026>.
- [24] L. Kučerová, I. Zetková, A. Jandová, M. Bystrianský, Microstructural characterisation and in-situ straining of additive-manufactured X3NiCoMoTi 18-9-5 maraging steel, *Mater. Sci. Eng. A.* 750 (2019) 70–80. <https://doi.org/10.1016/j.msea.2019.02.041>.
- [25] A.S.M.H. Committee, *ASM Handbook Volume 4 Heat Treating*, ASM Stand. Am. Soc. Met. Mater. Park. OH. (1991).

- [26] F.F. Conde, J.D. Escobar, J.P. Oliveira, M. Béréš, A.L. Jardini, W.W. Bose, J.A. Avila, Effect of thermal cycling and aging stages on the microstructure and bending strength of a selective laser melted 300-grade maraging steel, *Mater. Sci. Eng. A.* 758 (2019) 192–201.
- [27] F.F. Conde, J.D. Escobar, J.P. Oliveira, A.L. Jardini, W.W. Bose Filho, J.A. Avila, Austenite reversion kinetics and stability during tempering of an additively manufactured maraging 300 steel, *Addit. Manuf.* 29 (2019) 100804.
- [28] E.O.S.N.I.D. Sheet, EOS GmbH-Electro Optical Systems, (2014).
- [29] R. Alaghmandfard, C. Dharmendra, A. Hadadzadeh, B.S. Amirkhiz, A. Odeshi, M. Mohammadi, Dynamic compressive response of electron beam melted Ti–6Al–4V under elevated strain rates: Microstructure and constitutive models, *Addit. Manuf.* (2020) 101347.
- [30] A. Hadadzadeh, C. Baxter, B.S. Amirkhiz, M. Mohammadi, Strengthening mechanisms in direct metal laser sintered AlSi10Mg: Comparison between virgin and recycled powders, *Addit. Manuf.* 23 (2018) 108–120.
- [31] Y. Xu, J. Zhang, Y. Bai, M.A. Meyers, Shear localization in dynamic deformation: microstructural evolution, *Metall. Mater. Trans. A.* 39 (2008) 811–843.
- [32] A.A. Tiamiyu, A.G. Odeshi, J.A. Szpunar, Multiple strengthening sources and adiabatic shear banding during high strain-rate deformation of AISI 321 austenitic stainless steel: Effects of grain size and strain rate, *Mater. Sci. Eng. A.* 711 (2018) 233–249.

- [33] S. Dehgahi, M. Sanjari, M.H. Ghoncheh, B.S. Amirkhiz, M. Mohammadi, Concurrent improvement of strength and ductility in heat-treated C300 maraging steels produced by laser powder bed fusion technique, *Addit. Manuf.* (2021) 101847.
- [34] Y.F. Shen, N. Jia, R.D.K. Misra, L. Zuo, Softening behavior by excessive twinning and adiabatic heating at high strain rate in a Fe–20Mn–0.6 C TWIP steel, *Acta Mater.* 103 (2016) 229–242.
- [35] B. Dodd, Y. Bai, *Adiabatic shear localization: frontiers and advances*, Elsevier, 2012.
- [36] S. Yin, C. Chen, X. Yan, X. Feng, R. Jenkins, P. O'Reilly, M. Liu, H. Li, R. Lupoi, The influence of aging temperature and aging time on the mechanical and tribological properties of selective laser melted maraging 18Ni-300 steel, *Addit. Manuf.* 22 (2018) 592–600.
- [37] H.-W. Son, C.-H. Cho, J.-C. Lee, K.-H. Yeon, J.-W. Lee, H.S. Park, S.-K. Hyun, Deformation banding and static recrystallization in high-strain-rate-torsioned Al-Mg alloy, *J. Alloys Compd.* 814 (2020) 152311.
- [38] W.-S. Lee, C.-F. Lin, T.-H. Chen, W.-Z. Luo, High temperature deformation and fracture behaviour of 316L stainless steel under high strain rate loading, *J. Nucl. Mater.* 420 (2012) 226–234.
- [39] M. Saleh, M.M. Kariem, V. Luzin, K. Toppler, H. Li, D. Ruan, High strain rate deformation of ARMOX 500T and effects on texture development using neutron diffraction techniques and SHPB testing, *Mater. Sci. Eng. A.* 709 (2018) 30–39.

- [40] C. Tian, D. Ponge, L. Christiansen, C. Kirchlechner, On the mechanical heterogeneity in dual phase steel grades: Activation of slip systems and deformation of martensite in DP800, *Acta Mater.* 183 (2020) 274–284.
- [41] Y.B. Xu, Y.L. Bai, Q. Xue, L.T. Shen, Formation, microstructure and development of the localized shear deformation in low-carbon steels, *Acta Mater.* 44 (1996) 1917–1926.
- [42] P.C. Brand, R.B. Helmholtz, B. Pathiraj, B.H. Kolster, Dynamic recovery and recrystallization in a cold rolled ultra low carbon steel plate: a neutron and X-ray diffraction study, *J. Mater. Sci.* 30 (1995) 1307–1312.
- [43] A.S. Taylor, P.D. Hodgson, The post-deformation recrystallization behaviour of 304 stainless steel following high strain rate deformation, *Mater. Sci. Eng. A.* 529 (2011) 164–169.
- [44] A. Hadadzadeh, B.S. Amirkhiz, J. Li, A. Odeshi, M. Mohammadi, Deformation mechanism during dynamic loading of an additively manufactured AlSi10Mg\_200C, *Mater. Sci. Eng. A.* 722 (2018) 263–268.
- [45] A. Hadadzadeh, B.S. Amirkhiz, A. Odeshi, J. Li, M. Mohammadi, Role of hierarchical microstructure of additively manufactured AlSi10Mg on dynamic loading behavior, *Addit. Manuf.* 28 (2019) 1–13.
- [46] C. Baxter, E. Cyr, A. Odeshi, M. Mohammadi, Constitutive models for the dynamic behaviour of direct metal laser sintered AlSi10Mg\_200C under high strain rate shock loading, *Mater. Sci. Eng. A.* 731 (2018) 296–308.

# **Chapter 5: Texture evolution during high strain-rate compressive loading of maraging steels produced by laser powder bed fusion**

## **5.1. Introduction**

Additive manufacturing (AM) is a layer-by-layer manufacturing technique for building parts using 3D design software, and it can be employed to produce near-net-shaped and complex components [1]. Laser powder bed fusion (LPBF) is one of AM techniques, which uses a laser as the energy source to melt layers of powder on top of each other [2]. Among AM processes, LPBF has been found to be very promising for the fabrication of metallic parts due to shorter production time and lower fabrication cost [2]. LPBF parts exhibit superior mechanical properties than their conventional counterparts due to the formation of fine and cellular microstructure as a result of a fast solidification rate up to  $10^8$  °C/s [1][2].

Maraging steels belong to the iron-nickel-based alloy family, which show an excellent combination of mechanical properties (i.e., high strength along with good toughness) [3], resulting from the low carbon content and the presence of nano-sized precipitates [4]. The LPBF can be considered as the candidate technique to fabricate maraging steel parts. LPBF-maraging steel parts have received significant attention for applications in industries such as aerospace, precision gear manufacturing, and molding [3][5]. Post-processing heat treatment is recommended for these parts to (i) relieve the residual stresses generated by rapid heating and cooling during the LPBF process and (ii) introduce nano-sized intermetallic precipitates ( $\text{Ni}_3\text{Ti}$ ,  $\text{Ni}_3\text{Mo}$ , and  $\text{Fe}_2\text{Mo}$ ) into the microstructure in order to increase their strength [4].

LPBF-maraging steels have been the subject of multiple studies in recent years. Tan *et al.* [4] studied and reported the strength improvement of aged LPBF-maraging steel parts due to the presence of nano precipitates embedded in the matrix. Their results showed that high-performance maraging steels could be produced using LPBF, which offers a higher strength than their wrought-aged counterparts. Furthermore, Mutua *et al.* [6] investigated the effect of different heat treatment procedures on LPBF-maraging steel's mechanical properties. They concluded that the maximum tensile strength could be obtained from solution treatment at 820 °C for 1 h followed by aging at 460 °C for 5 h.

Unexpected impact situation in-service can expose maraging steel parts to dynamic loading. Therefore, it is crucial to investigate the deformation behavior of this alloy under these complex loading conditions. Few researchers have studied the effect of compression loading on the mechanical properties of maraging steels fabricated by conventional methods [7][8][9]. Schnitzer *et al.* [9] studied the effect of reverted austenite on aged maraging steels' dynamic properties. They observed that with the increase of strain rate, the phase fraction of austenite decreased. Song *et al.* [7] studied the effect of high strain-rate compressive loadings on C250 maraging steel, and they observed that dynamic strength increase with increasing strain rate. These studies focused on macroscopic features, and there has not been any in-depth microstructural study on the dynamic compressive behavior of LPBF-maraging steels.

Material response to high-speed deformation processes depends on many factors such as microstructure, texture, grain size, etc. In additive manufactured samples, a hierarchical microstructure is predictable involving cells, grains, and meltpools. The hierarchical structures in stainless steel and AlSi10Mg parts produced by additive manufacturing has

been shown by Wang [10] and Hadadzadeh [11], respectively. As a result of these studies, it is generally accepted that grain size, orientation, and morphology can affect the mechanical behavior of the final product, and it is believed that superior mechanical properties of additively manufactured parts are related to their hierarchical structure [12]. Thus, the effect of a hierarchical microstructure on the dynamic loading behavior of the material and the correlation between the mechanical behavior of the alloy and microstructural changes need to be investigated. Deep knowledge of the evolved texture helps understand the relationship between the mechanical properties and microstructure of the material. Therefore, this study focuses on investigating the microstructure, texture evolution, and mechanical properties of LPBF-maraging steels during dynamic compression loadings in as-built and heat-treated conditions.

## **5.2. Experimental procedure**

### **5.2.1. Materials and the LPBF process**

Rod-shaped samples (120 mm in length and 12 mm in diameter) were built in the horizontal direction using an EOS M290 machine. The samples were fabricated using maraging steel powder with an average particle size of 20  $\mu\text{m}$  and chemical composition of Ni (18.0–19.0 wt.%), Co (8.5–9.5 wt.%), Mo (4.6–5.2 wt.%). The laser power of 285W, scanning speed of 960 mm/s, the layer thickness of 40  $\mu\text{m}$ , and hatch distance of 110  $\mu\text{m}$  were used to fabricate the samples. These process parameters were recommended by EOS GmbH to produce parts with the least amount of porosity. The well-known strip scanning strategy was employed (the laser beam was rotated 67 degrees between consecutive layers), and the building platform temperature was kept at 40°C to minimize the residual stresses.

The applied aging temperature and time were selected to be 490 °C and 6 h for LPBF-maraging steel samples. A Calvin heat treatment chamber, model 1543, was used for the aging process.

### 5.2.2. High strain rate test

The dynamic mechanical behavior of LPBF-maraging steel samples was investigated using a Split-Hopkinson Pressure Bar (SHPB) apparatus at the strain rates of 2000 s<sup>-1</sup>, 2300 s<sup>-1</sup>, 3200 s<sup>-1</sup> for the as-built samples and 650 s<sup>-1</sup>, 680 s<sup>-1</sup>, 950 s<sup>-1</sup> for the heat-treated samples. Cylindrical test specimens, 7 mm in diameter and 8 mm long, for high strain-rate tests were machined from the horizontal rod-shaped samples produced using LPBF. In all the experiments, the loading direction was perpendicular to the building direction. The dynamic impact tests were performed at room temperature, and to ensure repeatability, three tests were conducted for each strain rate. The schematic of the SHPB apparatus used in this study is shown in Fig 5.1. An elastic wave is generated, which propagates when the striker bar impacts the incident bar (creating the incident wave), a part of this wave passes through the sample and reaches the transmitted bar (transmitted wave) while the rest of that wave is reflected (reflected wave) at the specimen/incident bar interface. The strains are measured by strain gauges located on the bars and are used to calculate the nominal values of stress, strain, and strain rate by following equations [13]:

$$\sigma(t) = \left(\frac{A_B}{A_S}\right) \cdot E_B \cdot \varepsilon_T \quad (5-1)$$

$$\varepsilon(t) = \left(-2 \frac{C_B}{L_S}\right) \cdot \int_0^t \varepsilon_R \cdot dt \quad (5-2)$$

$$\varepsilon'(t) = \left(-2 \frac{C_B}{L_S}\right) \cdot \varepsilon_R \quad (5-3)$$

where  $A_B$  and  $A_S$  are the cross-sectional areas of the bars and specimen, respectively.  $E_b$  is the elastic modulus of the bar, and  $C_B$  is the velocity of the elastic wave in the bars.  $L_S$  is the initial length of the sample, and  $t$  is the time. In addition,  $\varepsilon_T$  and  $\varepsilon_R$  are transmitted wave and reflected wave, which are recorded via strain gauges on the transmitter and incident bar, respectively. True stress, strain, and strain rate values were calculated using the following equations.

$$\sigma = \sigma(t)(1 - \varepsilon(t)) \quad (5-4)$$

$$\varepsilon = -\ln(1 - \varepsilon(t)) \quad (5-5)$$

$$\dot{\varepsilon} = \varepsilon'(t)/(1 - \varepsilon(t)) \quad (5-6)$$

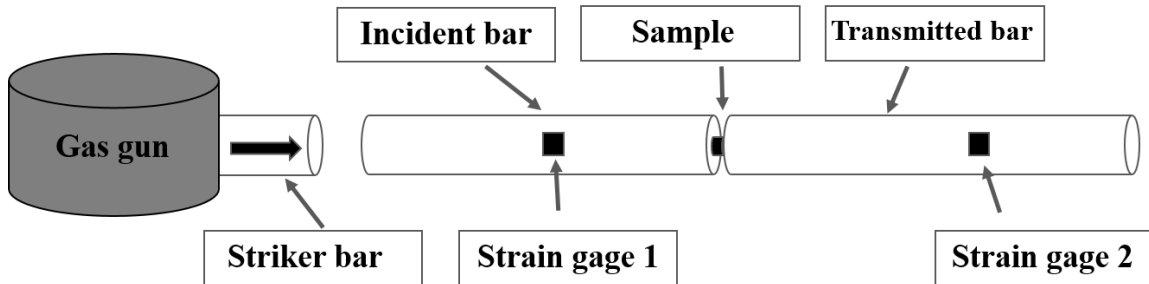


Fig 5. 1 Schematic of a Split-Hopkinson Pressure Bar (SHPB) apparatus.

### 5.2.3. Texture measurement

A Hitachi SU-70 Field Emission Gun (FEG) ultra-high-resolution SEM was utilized for microstructural studies. Furthermore, texture measurements were conducted on the impacted cylindrical samples, which were sectioned along the compression direction. The sectioned samples were prepared using standard metallographic sample preparation

techniques. A FEI Quanta™ 450 FEG-SEM microscope was employed for electron backscattering diffraction (EBSD) analysis. The diffraction patterns were collected using the TSL® OIM data collection software and were post-processed by the OIM 8 data analysis software. The crystallographic textures were calculated by harmonic series expansion with truncation at  $L = 16$ . A relatively large area of  $500 \times 500 \mu\text{m}^2$  with a step size of 500 nm and smaller step size (50 nm) in an area of  $50 \times 50 \mu\text{m}^2$  were chosen for the EBSD measurements to obtain statistically relevant crystallographic information. In all EBSD scans, Y and Z directions represent loading and building directions, respectively.

### **5.3. Results and discussion**

#### **5.3.1. Mechanical properties**

Fig 5.2. (a) shows the strain rates employed for dynamic compression tests. The strike bar was fired at firing pressures of 100, 120, and 160 kPa for the as-built maraging steel samples, which generated the strain rates of  $2000 \text{ s}^{-1}$ ,  $2300 \text{ s}^{-1}$ , and  $3200 \text{ s}^{-1}$ . It can be seen that a quick increase in the strain rate occurred in the early strain stages followed by a plateau in lower strain rates, but a fluctuated curve is seen in the highest strain rate, which demonstrates the strain hardening/thermal softening competition during dynamic compressive loading. Finally, the strain rate drops because of unloading. For consistency, the maximum strain rate was considered as the nominal strain rate in this study.

Fig 5.2. (b) shows the true dynamic stress- true strain curves of the as-built samples dynamically deformed at the strain rates of  $2000 \text{ s}^{-1}$ ,  $2300 \text{ s}^{-1}$ , and  $3200 \text{ s}^{-1}$ . The mechanical properties of the specimens (yield strength, maximum flow stress, total strain, and toughness), as recorded under the impact loading, shows the dependency of the mechanical

response of maraging steel on strain rate. The inset shows consistency, reliability, and repeatability of the data obtained in the dynamic impact tests. It can be observed that the peak flow stress of all the samples increased with increasing the strain rate, which can be related to the increase in dislocation density as plastic deformation progressed [14]. Indeed, dislocation-dislocation interactions and dislocation multiplication and grain refinement are the sources of strengthening with the increase in the strain rate [15]. The deformation behavior of the specimen deformed at the strain rate of  $2000 \text{ s}^{-1}$  commenced with an initial strain hardening, following by a plateau and a final drop. Increasing the strain rate up to  $2300 \text{ s}^{-1}$  led to a more complex deformation behavior. The same initial strain hardening was observed; however, the next deformation stage revealed a competition between initial strain hardening and thermal softening, which described slight fluctuations in the plateau section. Comparing the two mentioned samples, increasing strain rates from  $2000 \text{ s}^{-1}$  to  $3200 \text{ s}^{-1}$  led to 10% increase in maximum strength and 30% increase in strain. At the highest strain rate of  $3200 \text{ s}^{-1}$  used in this study, the effect of strain rate is apparent. In this sample, maximum flow stress and total strain increased by 27% and 24.7% compared to the samples that were deformed at the strain rate of  $2300 \text{ s}^{-1}$ . Also, the sample encountered severe thermal softening (resulting in the decrease of flow stress) and the following strain hardening (resulting in the increase of flow stress) that caused the appearance of the second peak. The total strain has been increased with an increase of strain rate and a maximum total strain of 25.1 % attained at the strain rate of  $3200 \text{ s}^{-1}$ .

The increase of strain with an increase of strain rate is related to thermal softening. In higher strain rates, the amount of generated heat in the specimen is increased, leading to thermal softening and an increase of strain. By increasing the strain rate, deformation

behavior changed, and initial strain hardening was followed by strain softening. With the increase of strain rate, thermal softening domination leads to thermo-mechanical instability resulting in intense strain localization along with narrow bands, which are called adiabatic shear bands (ASBs) [16]. Indeed, there is a critical firing pressure or strain rate at which adiabatic shear bands form. The susceptibility of the material to adiabatic shear bands can be predicted from the stress-strain curve for the specimens deformed at the strain rate of  $3200 \text{ s}^{-1}$ . Thermal softening is related to the conversion of the kinetic energy of projectile into thermal energy, which can be evaluated by the temperature rise within the bulk. The temperature rise can be calculated by the following equation [16]:

$$\Delta T = (\beta/\rho c_v) \cdot \int_0^\epsilon \sigma \cdot d\epsilon \quad (5-7)$$

where  $\beta$  (Taylor-Quinney parameter) is the fraction of plastic deformation that converted to heat. In this work, it is supposed that 90% of kinetic energy is converted to thermal energy, which means  $\beta$  is equal to 0.9. In this equation,  $\rho$  is the mass-density of maraging steel, which is  $8 \text{ g/cm}^3$ , and  $c_v$  is the specific heat capacity of maraging steel, which is  $450 \pm 20 \text{ J/kg}^\circ\text{C}$ . The integral term is toughness or the area under the true stress- true strain curve. The increase in firing pressure results in an increase in strain rate, whereby the sample temperature is raised. As can be seen from Table 5.1., at a strain rate of  $3200 \text{ s}^{-1}$ , the temperature increased significantly, which can result in the formation of ASBs. Adiabatic shear bands develop as a result of shear strain localization due to the loss of load-carrying capacity, and it is assumed that the temperature within ASBs increases much more than what is calculated from the stress-strain curve [17]. Calculation of temperature is based on total strain in the specimen, whereas strain inside shear bands is much higher.

ASBs are susceptible to cracking, and they promote the failure of materials under dynamic loading [16]. Indeed, fracture of shock-loaded samples has been reported to initiate and propagate in the ASB regions [16].

Literature shows that, compared to conventionally built maraging steel parts, LPBF maraging steel parts exhibit higher strength [4]; Song *et al.* [8] conducted a study using Split Hopkinson pressure bar apparatus regarding dynamic behavior of maraging steel 250 with a chemical composition close to the current study. They concluded that dynamic strength increased with an increase in strain rate. However, at the strain rate of  $3000 \text{ s}^{-1}$ , which is close to the strain rate of  $3200 \text{ s}^{-1}$  in our study, lower dynamic strength was achieved. This effect is attributed to the LPBF process, which offers high strength materials due to fine structure as a result of the high cooling rate in the LPBF process [18]. However, the thermal softening effect is more pronounced in LPBF maraging steels compared to conventional ones.

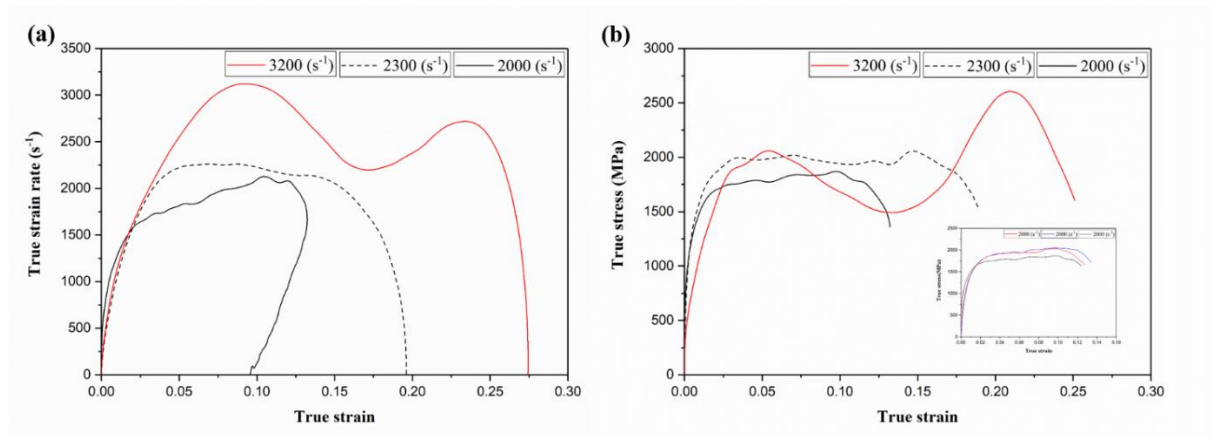


Fig 5. 2 (a) True strain rate- true strain curves of maraging steel samples at different firing pressure bar. (b) Dynamic true stress- true strain curves of the as-built maraging steel samples deformed at the strain rates of 2000, 2300, and  $3200 \text{ s}^{-1}$ . The specimens' flow curves deformed at the strain rate of  $2000 \text{ s}^{-1}$  in the inset ensure repeatability.

Table 5. 1. Dynamic mechanical properties of the compressed as-built LPBF-maraging steel samples.

Pressure (kPa)	Strain rate (s <sup>-1</sup> )	Yield stress (MPa)	Maximum flow stress (MPa)	Total strain (%)	Toughness (MJ/m <sup>3</sup> )	Temperature rise (°C)
<b>100</b>	<b>2000</b>	<b>1530.9±11.7</b>	<b>1871.2±10.4</b>	<b>13.2±1.2</b>	<b>227.4±6.8</b>	<b>56.8±3.2</b>
<b>120</b>	<b>2300</b>	<b>1737.0±7.9</b>	<b>2058.2±13.7</b>	<b>18.9±2.1</b>	<b>359.1±11.6</b>	<b>89.7±10.2</b>
<b>160</b>	<b>3200</b>	<b>1853.4±5.2</b>	<b>2604.2±13.5</b>	<b>25.1±3.3</b>	<b>466.2±8.3</b>	<b>116.5±11.5</b>

Fig. 5.3. (a) shows strain rates used for dynamic loading of heat-treated samples. The same behavior can be seen as it was observed in Fig. 5.2. The dynamic true stress- true strain curves of these samples are presented in Fig 5.3. (b). Firing pressures of 60, 70, and 80 kPa were used for heat-treated samples, which generated strain rates of 650, 680, and 950 s<sup>-1</sup>. Lower pressures were applied on heat treated samples due to the lower ductility of the heat treated samples compared to as-built samples. Table 5.2. summarizes the observations of true stress-strain curves for each strain rate. True dynamic stress- true strain curves of heat-treated samples showed different dynamic behaviors compared to as-built ones. The flow curves showed strain hardening up to the maximum flow stress and then a drop in the stress. In other words, as deformation proceeds beyond the yield point, strain hardening dominated the deformation, signs of strain-softening before reaching maximum flow stress cannot be observed.

As can be seen from Fig 5.3.(b) and Table 5.2., the heat-treated sample deformed at the strain rate of 950 s<sup>-1</sup> has a 30-40% higher flow stress than the as-built samples, which is attributed to the age-hardening process [4]. A plausible source of strengthening during high

strain rate deformation is the interaction between precipitates and dislocations in which precipitates act as a barrier to the motion of dislocations. However, with the increase in strain rate, dynamic strength decreased in the heat-treated samples. Dislocation density increases with an increase of strain rate during dynamic loading [15]. Dislocations can circumvent or pass through precipitates via different mechanisms such as Orowan looping, cross slip, or particle shearing [19]. With the increase of dislocations density, dislocations accumulate at precipitates, and a network of entangled dislocations can be formed [15]. Accumulation of dislocations and temperature increase can promote dislocation annihilation at a higher strain rate resulting in a decrease of dynamic strength with an increase of strain rate. Furthermore, it can be seen that the total strain in heat-treated samples is lower than in the as-built ones. The lower strain can be related to the precipitate hardening effect as a result of precipitate formation in maraging steels [4]. The temperature rise ( $\Delta T$ ) of heat-treated samples was estimated based on equation 4 and presented in Table 5.2. It can be concluded from Table 5.2. that the increase of strain rate does not cause a significant difference in temperature rise. The lack of evidence of competition between strain hardening and thermal softening in heat-treated samples' flow curves is an indication that generated heat during compressive loading was not enough for thermal softening.

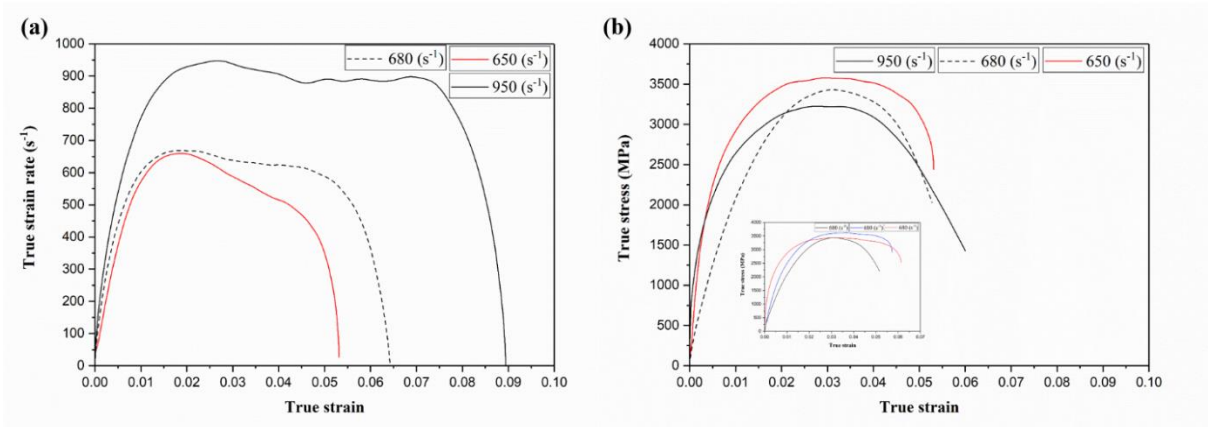


Fig 5. 3 (a) Strain rates employed for dynamic loading on the heat-treated maraging steel samples. (b) True stress- true strain curves for dynamically deformed heat-treated maraging steel samples at the strain rates of 650, 680, 950 s<sup>-1</sup>. The specimens' flow curves deformed at the strain rate of 680 s<sup>-1</sup> in the inset ensure repeatability.

Table 5. 2. Dynamic mechanical properties of the compressed heat-treated LPBF-maraging steel samples.

Pressure (kPa)	Strain rate (s <sup>-1</sup> )	Yield stress (MPa)	Maximum flow stress (MPa)	Total strain (%)	Toughness (MJ/m <sup>3</sup> )	Temperature rise (°C)
60	650	3128.6±12.3	3576.9±22.6	5.31±0.07	166.3±11.7	41.6±5.6
70	680	3067.3±10.4	3431.1±13.5	5.27±0.07	141.1±14.3	35.3±4.2
80	950	2471.9±23.3	3224.6±18.3	6±1.2	160.4±18.2	40.1±7.6

### 5.3.2. Texture analysis

Fig 5.4. shows the inverse pole figure scans (Y-IPF in which Y shows loading direction) of the undeformed as-built samples and those deformed at strain rates of 2000, 2300, 3200 s<sup>-1</sup>. The microstructure of the maraging steel sample fabricated by LPBF in an undeformed as-built state (Fig 5.4. (a)) shows random crystallographic orientations. As-built maraging

steel features a typical microstructure containing columnar, cellular, and equiaxed grains. Compared with the undeformed specimen, dynamic impact loading condition leads to the evolution of preferred crystallographic texture. As can be seen from these IPF maps along the compression direction on the longitudinal plane of the samples, strain rate has an obvious influence on the texture evolution, and a strong color gradient can be observed. These maps show that deformation is heterogeneous, as made evident by some elongated grains in some regions. It is believed that the temperature at which dynamic recrystallization can happen decreases with the increase of dislocation density [20]. As can be seen, at the strain rate of  $3200 \text{ s}^{-1}$ , the microstructure shows some elongated grains, which can be related to the occurrence of dynamic recovery and recrystallization processes. Nesterenko *et al.* [21] suggested a mechanism for dynamic recrystallization and formation of equiaxed grains during high strain rate. They believed that, because of imposed stress, dislocations accumulate and then rearrange to elongated dislocation cells. With further deformation, these elongated dislocation cells become elongated grains and break up to equiaxed grains. These elongated grains developed along the shear direction are characteristics of a deformed shear band [22]. Indeed, equiaxed grains can be generated from these elongated grains. Considering the high temperature-rise in the sample that was shock-loaded at the strain rate of  $3200 \text{ s}^{-1}$ , the occurrence of dynamic recrystallization (DRX) could result in pronounced texture evolution [23]. In these regions, thermomechanical instability leads to severe shear localization, leading to the formation of ASBs. As can be seen in Fig 5.6. (c), with a strain rate of  $3200 \text{ s}^{-1}$  and strain of 25%, pronounced crystallographic orientations are observed, and the preferred  $\{111\}||\text{LD}$  fibre texture (blue color) and  $\{100\}||\text{LD}$  fibre texture (red color) is developed which can be

related to the formation of ASBs. Fig 5.5. shows (001) and (111) pole figures of undeformed as-built samples and shock-loaded as-built samples at strain rates of 2000, 2300, 3200  $s^{-1}$ . As can be seen in Fig 5.5. (a), the undeformed as-built sample shows random crystallographic orientations. These figures show the effect of strain rate on microstructural evolution in which substantial change in the texture with an increase in strain rate is observed. For the specimen deformed at 3200  $s^{-1}$  (which shows the strain of 25%), strong texture with the maximum intensity of 5.512 located at {111} and {100} poles can be observed. Indeed, the critical true strain at which texture evolution becomes dominant is also confirmed by the calculated pole figures. In other words, larger fraction of grains aligned along {111} and {100} poles. As can be seen during compression loading, grains with {111} and {100} orientations rotate along the loading direction, and their rotation can be related to the formation of shear bands and increase of temperature. As shown in Fig 5.5. (d), the intensity of texture components increases significantly in the strain rate of 3200  $s^{-1}$ . Sonkusare *et al.* [24] and Bhattacharyya *et al.* [25] studied the effect of high strain rate on texture evolution of FCC materials, and they observed weakening of texture during high strain-rate deformation. However, Saleh *et al.* [26] observed texture sharpening with an increase in strain rate for BCC steels during the SHPB test. In addition, they observed that in BCC material, with increase of strain rate, {211} <110> and {111} <112> crystallographic texture are strengthened.

EBSB with a smaller step size (50 nm) in area of  $50 \times 50 \mu m^2$  was conducted on the as-built sample at the strain rate of 3200  $s^{-1}$  to observe the microstructure inside the shear band (due to severe plastic deformation, bands can not be detected in this scan). As it was reported, fine grains developed inside the shear band, confirming dynamic

recrystallization, which has been observed and reported before [27]. Also, grain fragmentation can be noticed, which is a result of severe plastic deformation.

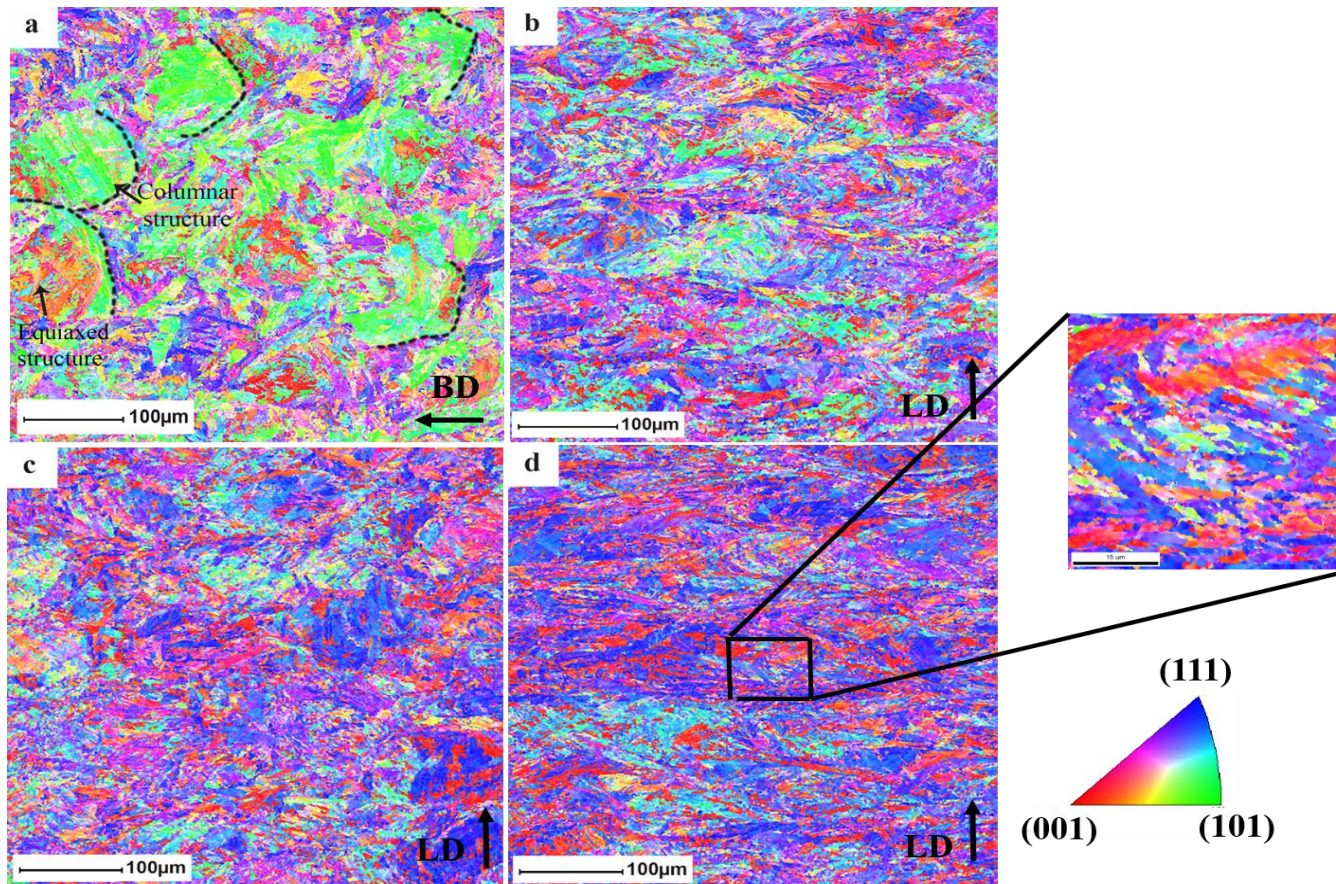


Fig 5. 4 The Y-IPF map of as-built maraging steel samples during high strain rate test (a) undeformed and deformed in strain rates of (b) 2000, (c) 2300, (d) 3200 s<sup>-1</sup> (LD represents the loading direction and BD represents building direction). The building direction is perpendicular to the loading direction.

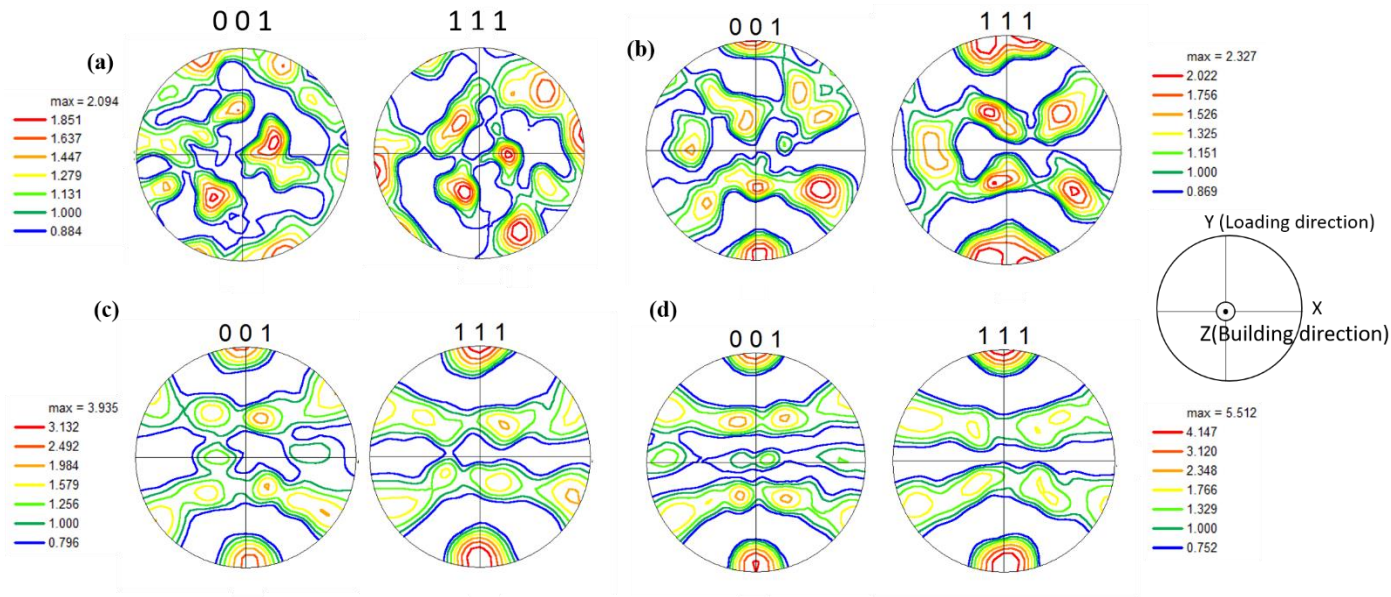


Fig 5. 5 The (001) and (111) pole figures of as-built maraging steel samples during high strain rate test (a) undeformed and deformed in strain rates of (b) 2000, (c) 2300, and (d) 3200 s<sup>-1</sup>.

Fig 5.6. shows the IPF-Y (in which Y shows loading direction) maps of undeformed and deformed heat-treated samples at strain rates of 650, 680, 950 s<sup>-1</sup>. The undeformed heat-treated maraging steel shows a random texture. With the increase in strain rate, microstructure and grain morphology of deformed heat-treated maraging steel samples did not change significantly, and no preferred orientation is observed in these figures. Fig 5.7. shows (001) and (111) pole figures of the above-mentioned samples. With the increase of strain rate, no preferred orientation can be observed in these pole figures.

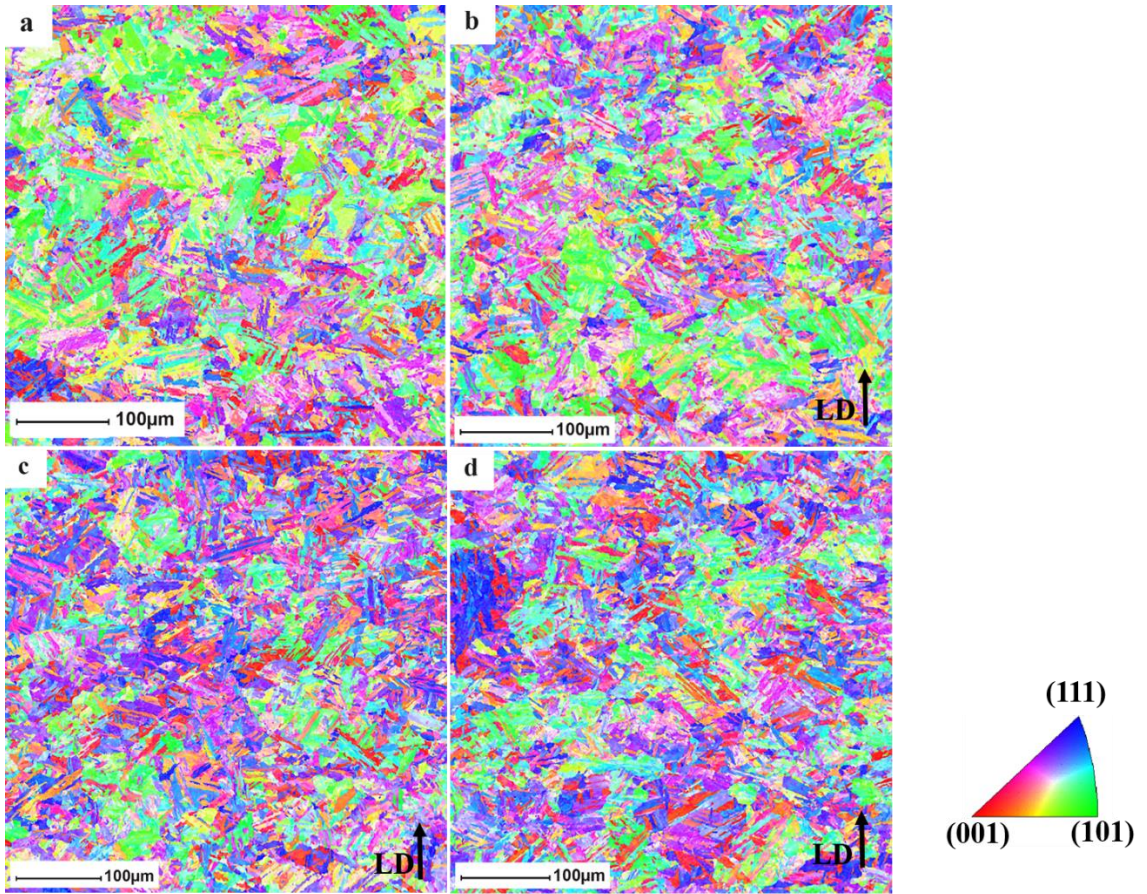


Fig 5. 6 The Y-IPF map of heat-treated maraging steel samples during high strain rate test (a) undeformed and deformed in strain rates of (b) 650, (c) 680, (d) 950  $s^{-1}$  (LD represents the loading direction). The building direction is perpendicular to the loading direction.

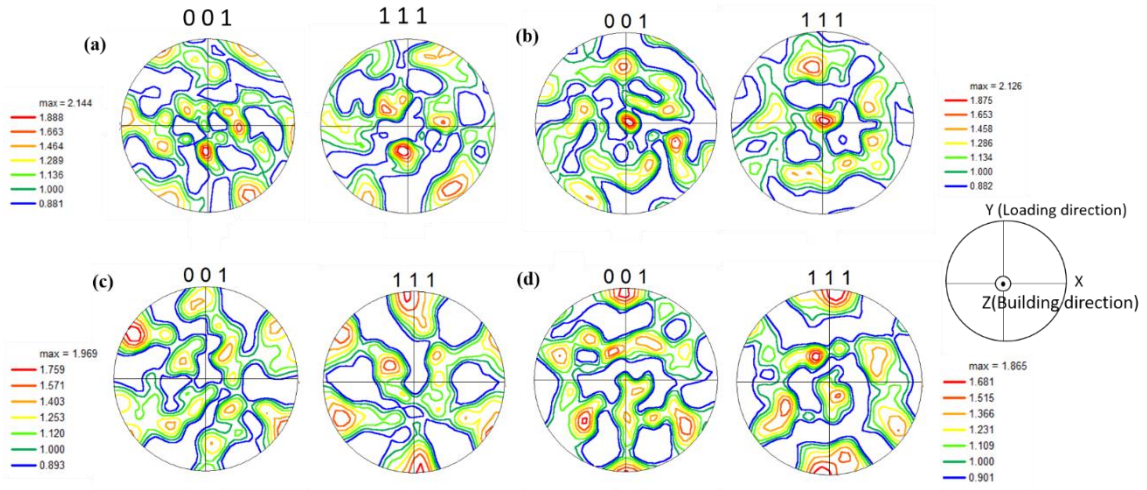


Fig 5. 7 The (001) and (111) pole figures of heat-treated maraging steel samples during high strain rate test  
 (a) undeformed and deformed in strain rates of (b) 650, (c) 680, (d) 950 s<sup>-1</sup>.

To obtain more detailed information about the crystallographic orientations, the orientation distribution function (ODF) was calculated, and the  $\phi_2 = 0$  and  $\phi_2 = 45^\circ$  sections of the ODFs in the as-built and heat-treated conditions are presented in Figs 5.8. and 5.9. An orthonormal coordinate system based on Z (or BD), X, and Y (or LD) was used for the ODF calculations. The reference ideal texture components used to interpret all the orientation distribution functions (ODF) are presented in these figures. It should be noted that no sample symmetry was imposed and that the same key is valid for intervals of 90-180°, 180-270° and 270-360° due to crystal symmetry. As can be seen in the ODF sections of the as-built samples, the texture intensity increased with the increase in strain rate. At the strain rate of 3200 s<sup>-1</sup>, strong  $\gamma$ -fibre ( $\{111\}||LD$ ) and cube fibre ( $\{100\}||LD$ ) developed, which is in agreement with IPF and pole figure results. Table 5.3. shows the volume fraction of fibres in as-built and heat treated samples before and after deformation. As can be seen, the volume fraction of gamma and cube fibres was increased with the increase of strain rate. This enhancement of fibres is more significant in as-built samples. With the

increase in strain rate, grains rotate towards the shear direction to accommodate localized stress, and this is the reason for texture evolution. However, in heat-treated samples, no preferred orientation was observed with the increase in strain rate, and texture intensity did not change.

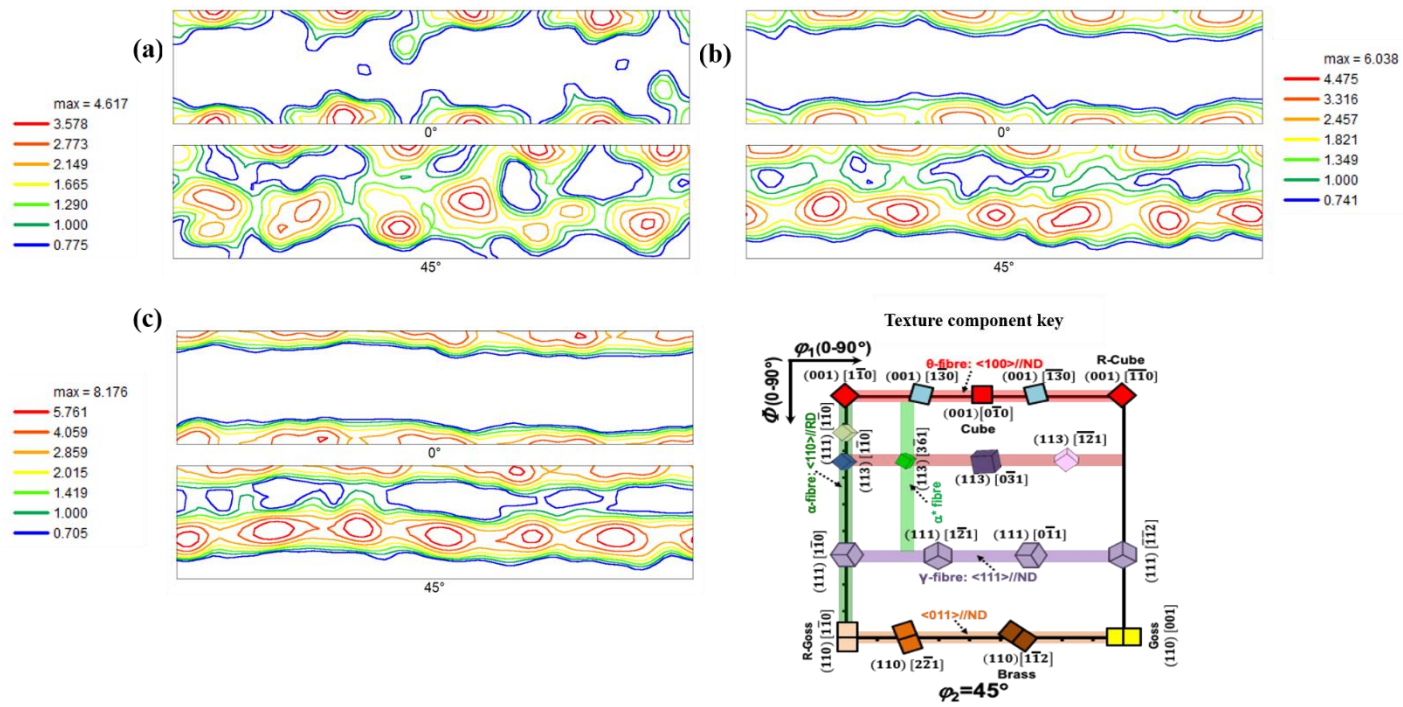


Fig 5. 8 The  $\phi_2=0^\circ$  and  $45^\circ$  sections of the ODF of as-built maraging steel samples during high strain rate test in strain rates of (a) 2000, (b) 2300, (c) 3200 s<sup>-1</sup>.

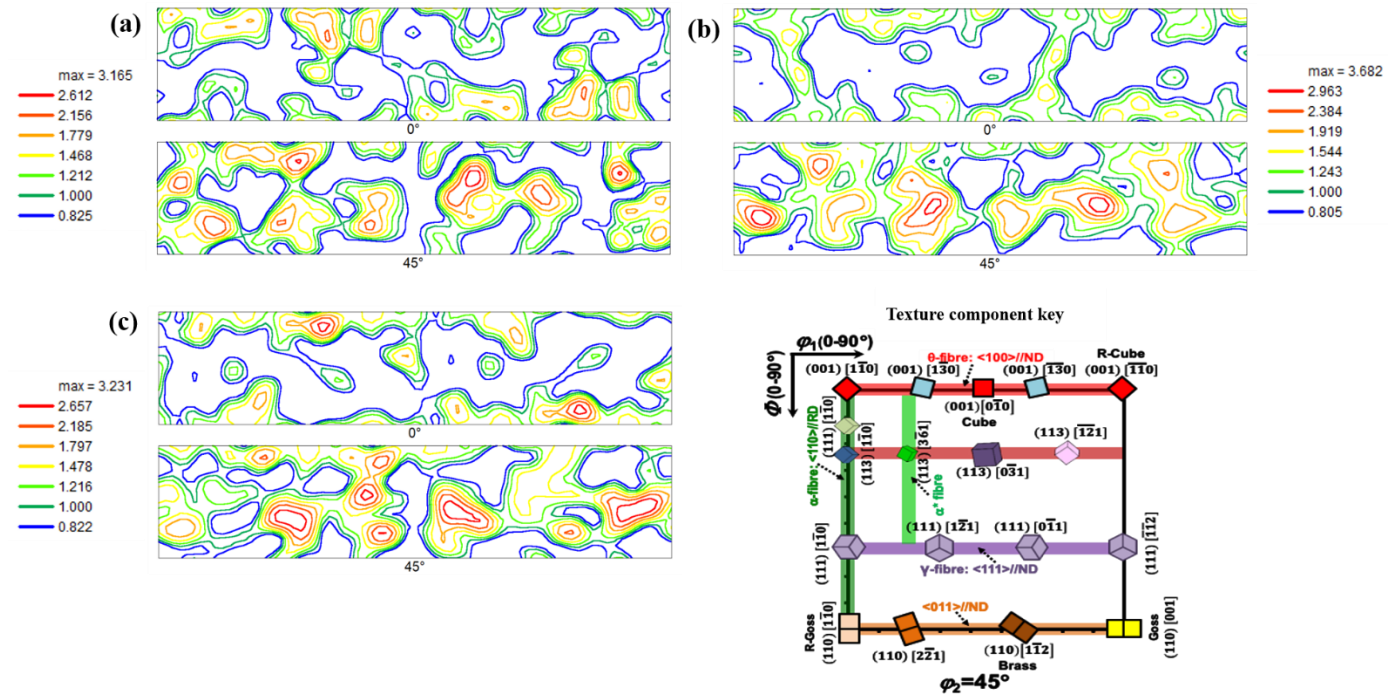


Fig 5. 9. The  $\phi_2=0^\circ$  and  $45^\circ$  sections of the ODF of heat-treated maraging steel samples during high strain rate test in strain rates of (a) 650, (b) 680, (c) 950 s<sup>-1</sup>.

Table 5. 3. The volume fraction of fibres in different strain rates in as-built and heat treat maraging steel samples before and after deformation.

Sample	<100>   LD	<110>   LD	<111>   LD
<b>As-built-undeformed</b>	<b>18.2</b>	<b>33</b>	<b>14.3</b>
<b>2000 (s<sup>-1</sup>)</b>	<b>20.7</b>	<b>19.1</b>	<b>30.6</b>
<b>2300 (s<sup>-1</sup>)</b>	<b>24.8</b>	<b>11.8</b>	<b>38.5</b>
<b>3200 (s<sup>-1</sup>)</b>	<b>28.5</b>	<b>6.7</b>	<b>45.4</b>
<b>Heat treat-undeformed</b>	<b>17</b>	<b>22.5</b>	<b>14.9</b>
<b>650 (s<sup>-1</sup>)</b>	<b>14.3</b>	<b>36.2</b>	<b>15</b>
<b>680 (s<sup>-1</sup>)</b>	<b>18.8</b>	<b>24.7</b>	<b>25.2</b>
<b>950 (s<sup>-1</sup>)</b>	<b>19.2</b>	<b>28.2</b>	<b>23.8</b>

During compression, the crystal lattice rotates such that the normal to the active slip plane aligns with the direction of the compression load. The compression axis rotates towards both <100> and <111> crystallographic directions. However, the initially orientated grains are realigned into preferred orientations, and the net rotation is toward <111> direction [28]. The {111}||LD and {100}||LD, which were observed in IPF maps and pole figures of as-built samples, are related to crystal lattice rotations as a result of compression loading. Indeed, the crystal lattice rotates to the point where {111} and {100} slip planes become parallel to the maximum shear direction and lead to ASB formation.

The  $\{111\}$ ||LD and  $\{100\}$ ||LD fibres were observed before for BCC structures subjected to dynamic compression loading [29][30].

As seen from ODFs, IPF maps, and pole figures, a strong  $\gamma$ -fibre and cube fibre are developed with the increase of strain rate of as-built samples, which is related to the activation of preferred slip systems during compression loading. To better understand the mechanism of texture evolution during high strain rate deformation of LPBF-maraging steels, activation of possible slip systems should be considered. Activated deformation mechanism (i.e., slip) and associated critical resolved shear stress is important to understand how plastic deformation is accommodated in a material. In BCC metals, slip planes are  $\{110\}$ ,  $\{112\}$  and  $\{123\}$  and the slip direction is always  $\langle 111 \rangle$  (the direction of close packing). In total, there are 48 slip systems based on these plane-direction pairs for maraging steels. During plastic deformation, a slip system with the highest Schmid's factor is activated first. However, except primary slip planes  $\{110\}$ , the other two slip planes  $\{112\}$  and  $\{123\}$  can be activated during deformation of Fe based alloys [31][32].

As can be seen in the (112) pole figure of the as-built samples deformed in strain rates of 2300 and 3200  $\text{s}^{-1}$  (cf. Fig 5.10.), (112) planes show a high intensity at  $\sim 45^\circ$  to the loading direction, which is the direction of maximum shear stress. It is expected that shear bands form in the direction of  $45^\circ$  to the impact direction. This intensive localized shear region (ASB region) leads to the fracture of the specimen at  $45^\circ$  to the loading direction. In other words, the increase of strain rate leads to the increase of Schmid factor, which has been reported before [33]. Zhu *et al.* [34] investigated the deformation localization and temperature evolution of the adiabatic shear band by high-speed photography and high-speed IR temperature measurement. They concluded that temperature does not play a role

in the initiation of ASB, and with the initiation and propagation of ASB after peak stress, the temperature increased significantly. Therefore, it can be postulated that the formation of adiabatic shear bands is triggered by activation of slip system as a result of severe shear localization and then, softening starts and temperature increased in shear bands. Localized shear band is proposed to start with slip in favored crystallographic orientation in an individual grain and then it propagates into adjacent grains leading to form macroscopic shear bands [35] [17].

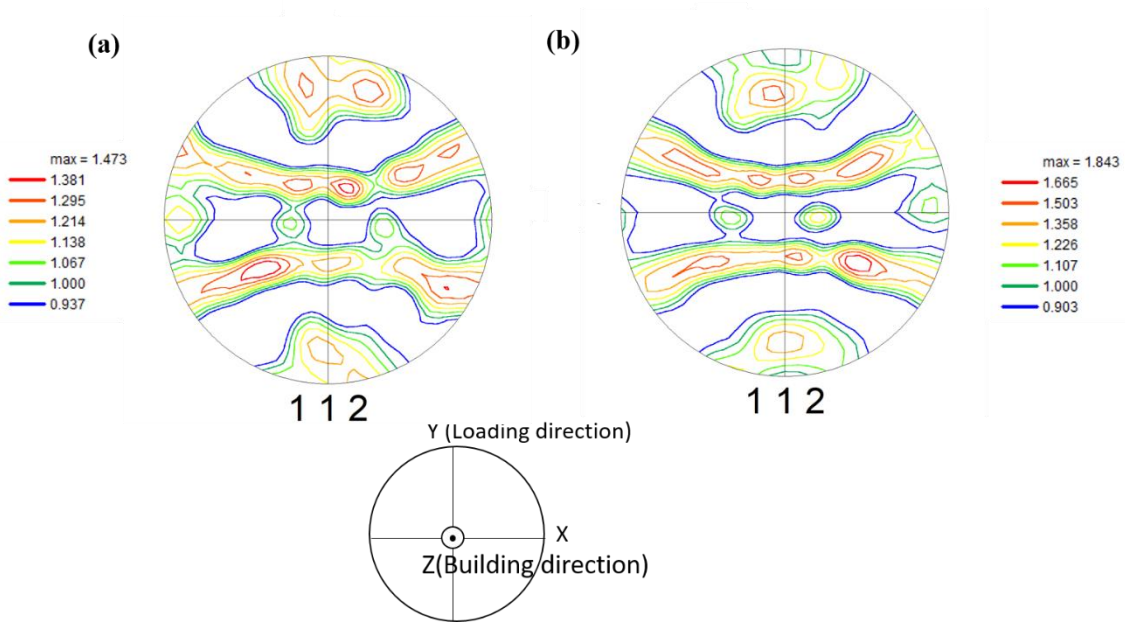


Fig 5. 10 The (112) pole figure of as-built maraging steel samples during high strain rate test in strains of (a) 2300, (b) 3200 s<sup>-1</sup>.

Fig 5.11. shows the initial and deformed as-built sample at the strain rate of 3200 s<sup>-1</sup>. Meltpool boundaries are displayed in the as-built maraging steel sample, which consists of cellular, columnar and equiaxed grains. However, after deformation due to the fragmentation of grains, melt pool boundaries can not be detected. As can be seen in Fig

5.11., in strain rate of  $3200 \text{ s}^{-1}$ , where the temperature rise was significant (Table 5.1.), adiabatic shear bands are formed in the microstructure as a result of activation of slip systems. Indeed, deformation banding is accompanied by large lattice rotations of crystals, and the strong texture observed in highly deformed samples is due to adiabatic shear band formation. Deformation bandings are zones where crystal orientation differs from surroundings and is a result of crystal rotation as deformation proceeds [36][37].

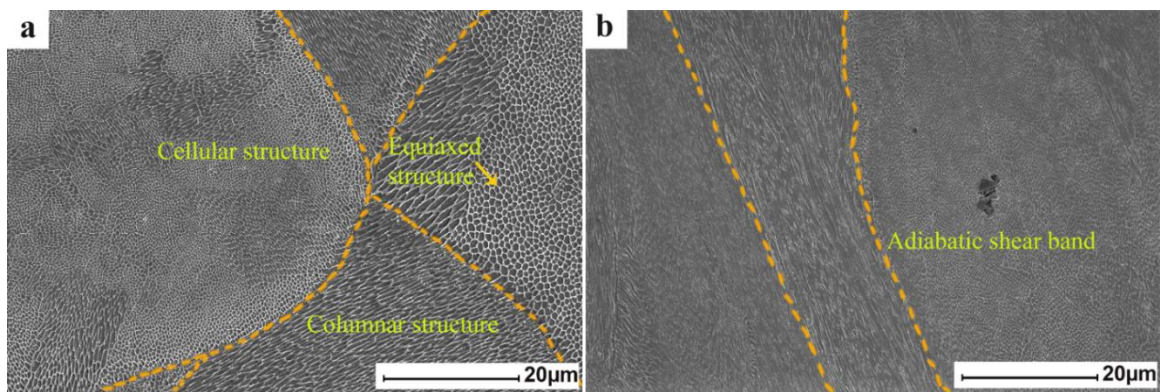


Fig 5. 11 Microstructures of the a) as-built initial sample, b) deformed sample at the strain rate of  $3200 \text{ s}^{-1}$ .

Canova *et al.* [38] investigated lattice rotation during high strain-rate deformation, and they concluded that the total number of active slip systems increased in high strain rate due to lattice rotation. At the strain rate of  $3200 \text{ s}^{-1}$ , texture evolution is significant, which shows that maximum shear localization and heat accumulation happened along the slip planes. This change in orientation at high strain rates leads to the formation of ASBs. This implies that the sample at the strain rate of  $3200 \text{ s}^{-1}$  and strain of 25% is more susceptible to ASB formation. It should be noted that ASBs develop within a very short time, and the formation of the shear band is one way to accommodate intense stress and to dissipate shock energy. Indeed during dynamic deformation, heat and stress accumulate in grains with a close orientation to the slip system, which results in the formation of ASBs [35] [17]. As can be

seen from Tables 5.1. and 5.2., the ductility of heat-treated samples is lower than that of the as-built samples indicating the limited number of active slip systems involved during deformation [39]. The random texture in heat treated samples might be an indication that the formation of ASBs in heat-treated samples is limited. In other words, in heat-treated samples, heat dissipates due to the lower number of activated slip systems, and the probability of formation of adiabatic shear bands is low.

It can be speculated that in the as-built maraging steel plastic deformation is controlled by the motion of dislocations. Dynamic stress-strain curves of as-built samples (Fig 5.2.) show a steady steady-state region resulting from activation of slip after the elastic region (high work hardening ability due to the high number of activated slip systems [39]). However, in the heat-treated condition, dislocations and slip systems contribute less in deformation [39] (lower ductility of heat treated samples), and as it was seen in Fig 5.5., a drop in stress after maximum flow stress can be observed (low work hardening ability due to low activated slip systems). In other words, in the heat-treated condition, due to limited sources of dislocations and restricting effect of precipitates, slip activity is limited (i.e., dislocation annihilation happened due to heat treatment) [39]. As clearly shown, activated slip systems have a paramount influence on the onset of shear band formation in maraging steels. Furthermore, it is evident that plastic deformation causes grain rotation and the evolution of strong texture components to accommodate imposed strain.

This study indicated that the formation of adiabatic shear bands at high strain rates correspond to the strain rate and texture evolution of LPBF maraging steels. This means that after a certain amount of strain rate and change in texture, deformation banding is preferred to homogenous deformation. This study showed that adiabatic shear bands are

formed along the direction to activate slip systems and relax stress concentration. It should be noted that materials under high strain rate do not always show banding structure and the possible existence of band structure is related to slip activity as well.

From the previous discussion, it is evident that in as-built samples that have a higher number of activated slip systems, ductility is higher, so the shear bands are more likely to form (as a path to accommodate imposed shear strain). However, in heat-treated samples, which have a lower number of activated slip systems, ductility is lower, and the probability of shear band formation is lower.

### 5.3.3. Grain analysis

Fig 5.12. shows the kernel average misorientation (KAM) distribution of undeformed and deformed as-built samples in strain rates of  $2000 \text{ s}^{-1}$ ,  $2300 \text{ s}^{-1}$ , and  $3200 \text{ s}^{-1}$  and heat-treated maraging steel samples in strain rates of  $650 \text{ s}^{-1}$ ,  $680 \text{ s}^{-1}$ , and  $950 \text{ s}^{-1}$ . The high KAM values represent strain accumulation (high stored energy), while the low KAM values represent recrystallized grains [40]. In other words, a high KAM value is an indication of slip deformation mechanism and considerable stored energy. As can be seen, with the increase of strain rate, KAM value increases (dislocation density increased), which has also been reported previously [41]. Indeed, high KAM values and dislocation pile-ups with the increase of strain rate confirm slip activities. In addition, the fraction of grains with  $\text{KAM} < 1$  has significantly increased for strain rate of  $3200 \text{ s}^{-1}$ , confirming the occurrence of recrystallization process. Li *et al.* [42] suggested that  $\text{KAM} > 1$  represents deformed grains while  $\text{KAM} < 1$  represents DRX grains. High KAM values at the strain rate of  $2300 \text{ s}^{-1}$  suggest that dislocation density is higher for this strain rate, which means that the driving

force for recrystallization is higher. This is the reason that more recrystallized grains evolved at the strain rate of  $3200 \text{ s}^{-1}$ . The low KAM values of heat-treated samples imply low dislocation density and less slip activity in the heat-treated condition. Due to the annihilation of dislocations during heat treatment, a large network of dislocations cannot be detected in these samples. With the increase of strain rate to  $680 \text{ s}^{-1}$  and  $950 \text{ s}^{-1}$ , KAM value increased slightly. With the increase of strain rate to  $680 \text{ s}^{-1}$  and  $950 \text{ s}^{-1}$ , dislocation density increased and precipitates act as a barrier for dislocation movement. This results in the accumulation of dislocations, as evident in the KAM values. With the increase of strain rate, the volume fraction of precipitates is fixed; however, dislocation density increases, which results in the accumulation of dislocations.

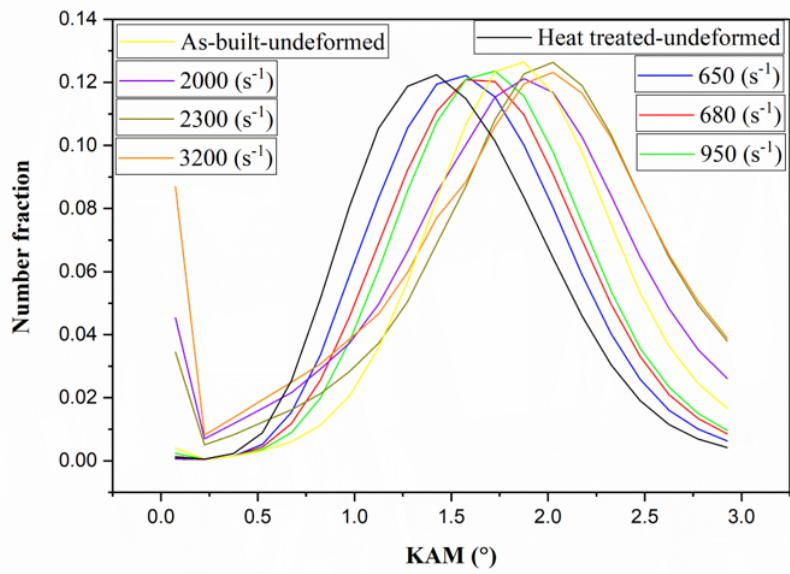
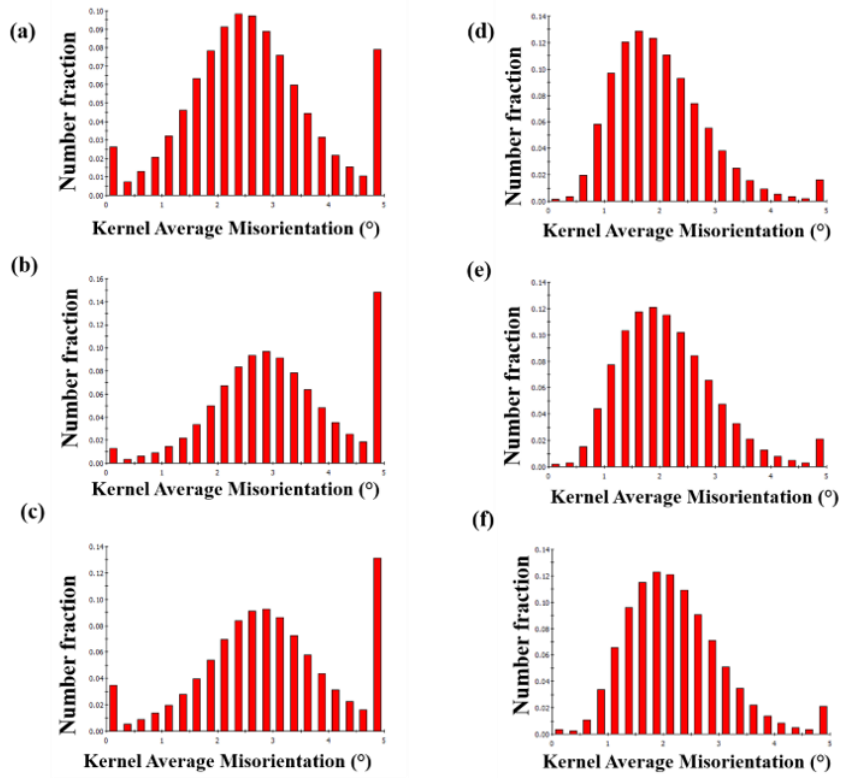


Fig 5. 12 The KAM distribution of as-built and heat treated maraging steel samples during high strain rate test in strain rates of (a) 2000, (b) 2300, (c) 3200 s<sup>-1</sup> for as-built samples (d) 650, (e) 680, (f) 950 s<sup>-1</sup> for heat treated samples.

Fig 5.13. shows grain size distribution and misorientation angle distribution for samples deformed at strain rates of (a)  $2000 \text{ s}^{-1}$ , (b)  $2300 \text{ s}^{-1}$ , and (c)  $3200 \text{ s}^{-1}$ . The maximum flow stress increased with an increase of strain rate, which can be attributed to dislocation multiplication and grain size refinement [15]. Grain refinement contributes to strengthening through the Hall-Petch equation. It can also be observed that with the increase in strain rate from  $2000 \text{ s}^{-1}$  to  $2300 \text{ s}^{-1}$  and  $3200 \text{ s}^{-1}$  (due to severe plastic deformation), the area fraction of grains with diameter  $< 2 \mu\text{m}$  increased from 30% to 50%. Besides, with the increase in strain rate from  $2000 \text{ s}^{-1}$  to  $2300 \text{ s}^{-1}$  and  $3200 \text{ s}^{-1}$ , the number fraction of low angle grain boundaries (misorientation angle of less than  $15^\circ$ ) increased (from 47% LAGB to 49% LAGB), which suggests dominations of dynamic recovery and recrystallization [40].

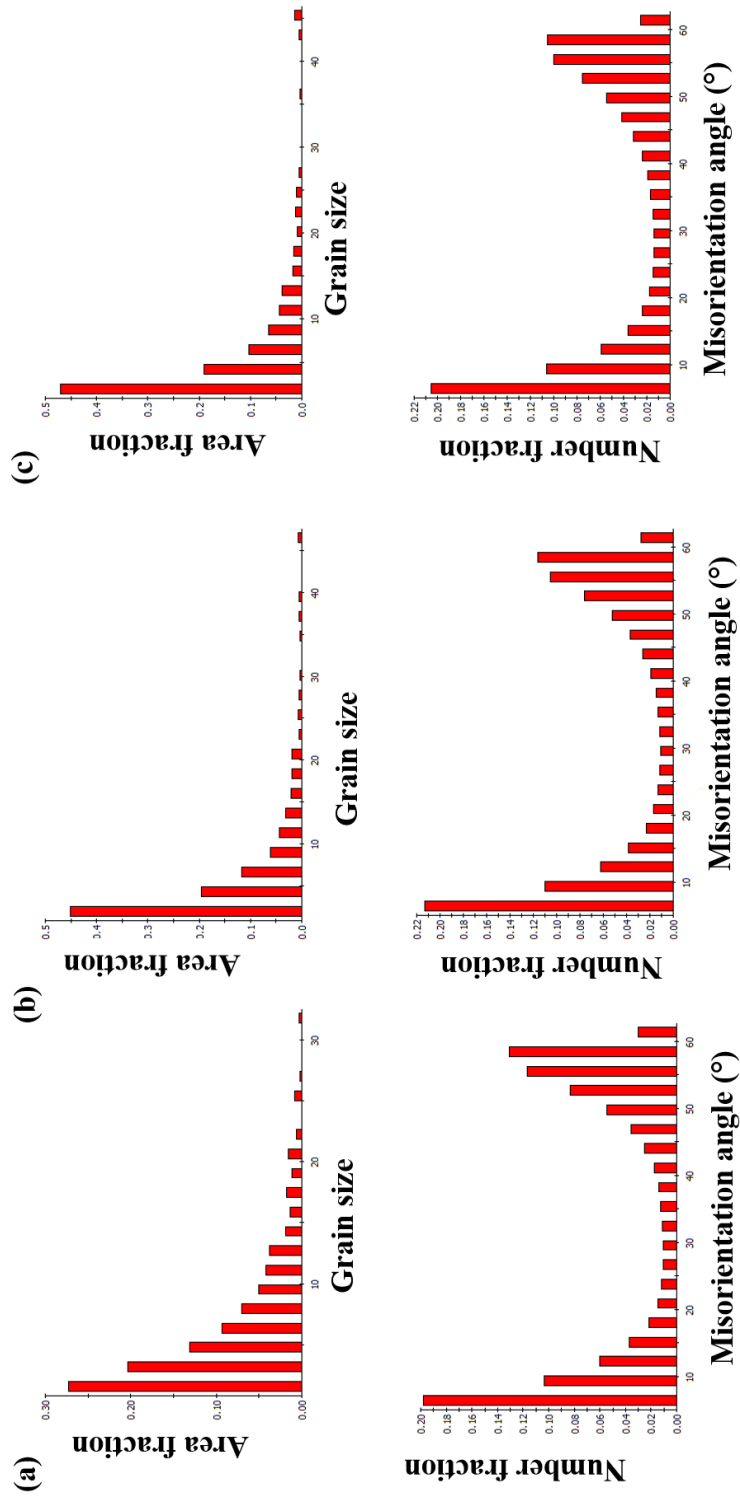


Fig 5. 13 Grain size distribution, misorientation angle distribution of as-built maraging steel samples during high strain rate test in strain rates of (a) 2000, (b) 2300, (c) 3200 s<sup>-1</sup>.

## 5.4. Conclusion

As-built and heat-treated LPBF maraging steel samples were subjected to high strain rate compressive loads using Split Hopkinson pressure bar apparatus. As-built samples were tested at strain rates of  $2000 \text{ s}^{-1}$ ,  $2300 \text{ s}^{-1}$ ,  $3200 \text{ s}^{-1}$  and heat-treated samples were tested at strain rates of  $650 \text{ s}^{-1}$ ,  $680 \text{ s}^{-1}$ , and  $950 \text{ s}^{-1}$ . Microstructural evolution and texture development were investigated with respect to the strain rate in both sets of samples. Results showed that the crystallographic texture changed significantly in as-built samples due to the high strain-rate deformation. To accommodate the imposed shear stress during the dynamic compression test, different slip systems will be activated. In these slip planes, heat and stress accumulate, which results in the formation of shear bands. As a result of the activation of slip systems in as-built samples, a strong texture change was seen in these samples. However, in heat-treated samples, no significant texture change was observed, which could be related to the limited number of activated slip systems in the heat treated condition.

## 5.5. References

- [1] D. Herzog, V. Seyda, E. Wycisk, C. Emmelmann, Additive manufacturing of metals, *Acta Mater.* 117 (2016) 371–392.
- [2] W.E. King, A.T. Anderson, R.M. Ferencz, N.E. Hodge, C. Kamath, S.A. Khairallah, A.M. Rubenchik, Laser powder bed fusion additive manufacturing of metals; physics, computational, and materials challenges, *Appl. Phys. Rev.* 2 (2015) 41304.

- [3] S. Dehgahi, M.H. Ghoncheh, A. Hadadzadeh, M. Sanjari, B.S. Amirkhiz, M. Mohammadi, The role of titanium on the microstructure and mechanical properties of additively manufactured C300 maraging steels, *Mater. Des.* (2020) 108965.
- [4] C. Tan, K. Zhou, W. Ma, P. Zhang, M. Liu, T. Kuang, Microstructural evolution, nanoprecipitation behavior and mechanical properties of selective laser melted high-performance grade 300 maraging steel, *Mater. Des.* 134 (2017) 23–34. <https://doi.org/10.1016/j.matdes.2017.08.026>.
- [5] S. Shamsdini, S. Shakerin, A. Hadadzadeh, B.S. Amirkhiz, M. Mohammadi, A trade-off between powder layer thickness and mechanical properties in additively manufactured maraging steels, *Mater. Sci. Eng. A.* 776 (2020) 139041. <https://doi.org/10.1016/j.msea.2020.139041>.
- [6] J. Mutua, S. Nakata, T. Onda, Z.C. Chen, Optimization of selective laser melting parameters and influence of post heat treatment on microstructure and mechanical properties of maraging steel, *Mater. Des.* 139 (2018) 486–497. <https://doi.org/10.1016/j.matdes.2017.11.042>.
- [7] S. Loewy, L. Hjortd, B. Rheingans, E.J. Mittemeijer, Modulated formation of lath martensite: Influence of uniaxial compressive load and transformation-induced plasticity, *Acta Mater.* 109 (2016) 46–54.
- [8] B. Song, B. Sanborn, P.E. Wakeland, M.D. Furnish, Dynamic Characterization and Stress-Strain Symmetry of Vascomax® C250 Maraging Steel in Compression and Tension, *Procedia Eng.* 197 (2017) 42–51.
- [9] R. Schnitzer, G.A. Zickler, E. Lach, H. Clemens, S. Zinner, T. Lippmann, H.

- Leitner, Influence of reverted austenite on static and dynamic mechanical properties of a PH 13-8 Mo maraging steel, *Mater. Sci. Eng. A.* 527 (2010) 2065–2070.
- [10] Y.M. Wang, T. Voisin, J.T. McKeown, J. Ye, N.P. Calta, Z. Li, Z. Zeng, Y. Zhang, W. Chen, T.T. Roehling, Additively manufactured hierarchical stainless steels with high strength and ductility, *Nat. Mater.* 17 (2018) 63–71.
- [11] A. Hadadzadeh, B.S. Amirkhiz, A. Odeshi, J. Li, M. Mohammadi, Role of hierarchical microstructure of additively manufactured AlSi10Mg on dynamic loading behavior, *Addit. Manuf.* 28 (2019) 1–13.
- [12] P. Bajaj, A. Hariharan, A. Kini, P. Kürnsteiner, D. Raabe, E.A. Jäggle, Steels in additive manufacturing: A review of their microstructure and properties, *Mater. Sci. Eng. A.* 772 (2020) 138633. <https://doi.org/10.1016/j.msea.2019.138633>.
- [13] C. Baxter, E. Cyr, A. Odeshi, M. Mohammadi, Constitutive models for the dynamic behaviour of direct metal laser sintered AlSi10Mg\_200C under high strain rate shock loading, *Mater. Sci. Eng. A.* 731 (2018) 296–308.
- [14] A. Hadadzadeh, B.S. Amirkhiz, A. Odeshi, M. Mohammadi, Dynamic loading of direct metal laser sintered AlSi10Mg alloy: Strengthening behavior in different building directions, *Mater. Des.* 159 (2018) 201–211. <https://doi.org/10.1016/j.matdes.2018.08.045>.
- [15] A. Hadadzadeh, C. Baxter, B.S. Amirkhiz, M. Mohammadi, Strengthening mechanisms in direct metal laser sintered AlSi10Mg: Comparison between virgin and recycled powders, *Addit. Manuf.* 23 (2018) 108–120.

- [16] R. Alaghmandfard, C. Dharmendra, A.G. Odeshi, M. Mohammadi, Dynamic mechanical properties and failure characteristics of electron beam melted Ti-6Al-4V under high strain rate impact loadings, *Mater. Sci. Eng. A.* 793 (2020) 139794.
- [17] Y. Xu, J. Zhang, Y. Bai, M.A. Meyers, Shear localization in dynamic deformation: microstructural evolution, *Metall. Mater. Trans. A.* 39 (2008) 811–843.
- [18] E.A. Jäggle, Z. Sheng, P. Kürnsteiner, S. Ocylok, A. Weisheit, D. Raabe, Comparison of maraging steel micro- and nanostructure produced conventionally and by laser additive manufacturing, *Materials (Basel)*. 10 (2017) 2–15. <https://doi.org/10.3390/ma10010008>.
- [19] T. Gladman, Precipitation hardening in metals, *Mater. Sci. Technol.* 15 (1999) 30–36.
- [20] P.C. Brand, R.B. Helmholtz, B. Pathiraj, B.H. Kolster, Dynamic recovery and recrystallization in a cold rolled ultra low carbon steel plate: a neutron and X-ray diffraction study, *J. Mater. Sci.* 30 (1995) 1307–1312.
- [21] V.F. Nesterenko, M.A. Meyers, J.C. LaSalvia, M.P. Bondar, Y.J. Chen, Y.L. Lukyanov, Shear localization and recrystallization in high-strain, high-strain-rate deformation of tantalum, *Mater. Sci. Eng. A.* 229 (1997) 23–41.
- [22] A.A. Tihamiyu, M. Eskandari, M. Nezakat, X. Wang, J.A. Szpunar, A.G. Odeshi, A comparative study of the compressive behaviour of AISI 321 austenitic stainless steel under quasi-static and dynamic shock loading, *Mater. Des.* 112 (2016) 309–319.

- [23] H. Asgari, A. Odeshi, K. Hosseinkhani, M. Mohammadi, On dynamic mechanical behavior of additively manufactured AISi10Mg\_200C, *Mater. Lett.* 211 (2018) 187–190.
- [24] R. Sonkusare, R. Jain, K. Biswas, V. Parameswaran, N.P. Gurao, High strain rate compression behaviour of single phase CoCuFeMnNi high entropy alloy, *J. Alloys Compd.* 823 (2020) 153763.
- [25] A. Bhattacharyya, D. Rittel, G. Ravichandran, Effect of strain rate on deformation texture in OFHC copper, *Scr. Mater.* 52 (2005) 657–661.
- [26] M. Saleh, M.M. Kariem, V. Luzin, K. Toppler, H. Li, D. Ruan, High strain rate deformation of ARMOX 500T and effects on texture development using neutron diffraction techniques and SHPB testing, *Mater. Sci. Eng. A.* 709 (2018) 30–39.
- [27] S. Dehgahi, R. Alaghmandfard, J. Tallon, A. Odeshi, M. Mohammadi, Microstructural evolution and high strain rate compressive behavior of as-built and heat-treated additively manufactured maraging steels, *Mater. Sci. Eng. A.* 815 (2021) 141183.
- [28] W.F. Hosford, *Mechanical behavior of materials*, Cambridge university press, 2010.
- [29] A.A. Tihamiyu, A.G. Odeshi, J.A. Szpunar, Multiple strengthening sources and adiabatic shear banding during high strain-rate deformation of AISI 321 austenitic stainless steel: Effects of grain size and strain rate, *Mater. Sci. Eng. A.* 711 (2018) 233–249.
- [30] A.A. Tihamiyu, V. Tari, J.A. Szpunar, A.G. Odeshi, A.K. Khan, Effects of grain

refinement on the quasi-static compressive behavior of AISI 321 austenitic stainless steel: EBSD, TEM, and XRD studies, *Int. J. Plast.* 107 (2018) 79–99.

- [31] C. Tian, D. Ponge, L. Christiansen, C. Kirchlechner, On the mechanical heterogeneity in dual phase steel grades: Activation of slip systems and deformation of martensite in DP800, *Acta Mater.* 183 (2020) 274–284.
- [32] C. Du, F. Maresca, M.G.D. Geers, J.P.M. Hoefnagels, Ferrite slip system activation investigated by uniaxial micro-tensile tests and simulations, *Acta Mater.* 146 (2018) 314–327.
- [33] H.-W. Son, C.-H. Cho, J.-C. Lee, K.-H. Yeon, J.-W. Lee, H.S. Park, S.-K. Hyun, Deformation banding and static recrystallization in high-strain-rate-torsioned Al-Mg alloy, *J. Alloys Compd.* 814 (2020) 152311.
- [34] S. Zhu, Y. Guo, Q. Ruan, H. Chen, Y. Li, D. Fang, Formation of adiabatic shear band within Ti-6Al-4V: An in-situ study with high-speed photography and temperature measurement, *Int. J. Mech. Sci.* 171 (2020) 105401.
- [35] Y.B. Xu, Y.L. Bai, Q. Xue, L.T. Shen, Formation, microstructure and development of the localized shear deformation in low-carbon steels, *Acta Mater.* 44 (1996) 1917–1926.
- [36] F. Basson, J.H. Driver, Deformation banding mechanisms during plane strain compression of cube-oriented fcc crystals, *Acta Mater.* 48 (2000) 2101–2115.
- [37] C.S. Lee, B.J. Duggan, R.E. Smallman, A theory of deformation banding in cold rolling, *Acta Metall. Mater.* 41 (1993) 2265–2270.

- [38] G.R. Canova, C. Fressengeas, A. Molinari, U.F. Kocks, Effect of rate sensitivity on slip system activity and lattice rotation, *Acta Metall.* 36 (1988) 1961–1970.
- [39] S. Dehgahi, M. Sanjari, M.H. Ghoncheh, B.S. Amirkhiz, M. Mohammadi, Concurrent improvement of strength and ductility in heat-treated C300 maraging steels produced by laser powder bed fusion technique, *Addit. Manuf.* (2021) 101847.
- [40] A. Hadadzadeh, B.S. Amirkhiz, J. Li, A. Odeshi, M. Mohammadi, Deformation mechanism during dynamic loading of an additively manufactured AlSi10Mg\_200C, *Mater. Sci. Eng. A.* 722 (2018) 263–268.
- [41] N.P. Gurao, R. Kapoor, S. Suwas, Texture evolution in high strain rate deformed Cu–10Zn alloy, *Mater. Sci. Eng. A.* 558 (2012) 761–765.
- [42] H. Li, E. Hsu, J. Szpunar, H. Utsunomiya, T. Sakai, Deformation mechanism and texture and microstructure evolution during high-speed rolling of AZ31B Mg sheets, *J. Mater. Sci.* 43 (2008) 7148–7156.

# **Chapter 6: Effect of building direction on high strain rate compressive behavior of heat-treated LPBF-maraging steel using Split Hopkinson pressure bar apparatus**

## **6.1. Introduction**

Additive manufacturing (AM) is a modern process of creating an object which uses 3D computer-aided design to create bulk metal parts. Powder bed fusion and direct energy deposition are two major AM techniques. Laser powder bed fusion (LPBF) is one of the AM processes, in which powders on top of a substrate are fused by a laser source [1]. LPBF process is appealing for the production of metallic components ascribed to its ability to produce parts in less time and with relatively complex geometries. The sophistication and the interest in the industrial application of AM have continued to grow, and AM parts are currently being built for aerospace, marine, and automotive applications [2]. Laser powder bed fusion has been applied to produce low carbon steels such as maraging steels to exploit their superior mechanical properties [3].

The 18Ni-300 maraging steel is known for possessing superior strength and toughness, widely implemented in aerospace and other applications which require high strength steels [4]. These applications usually need parts with excellent mechanical properties, and maraging steel is a good candidate ascribed to its superior strength and toughness. Properties of maraging steel stem from the fine-scale complex microstructure that contains precipitates such as  $\text{Ni}_3(\text{Ti}, \text{Mo})$  and  $\text{Ni}_3\text{Al}$  [3]. Through the aging in the temperature range of 480-510 °C, these precipitates are embedded in a martensitic matrix tempered [3]. These precipitates block dislocations motion and decrease dislocations mean

free paths, which results in the reduction of elongation and enhancement of strength for maraging steel heat treated samples [5].

Several studies have been conducted on maraging steel 300 produced by LPBF to investigate microstructure [6], quasi-static mechanical properties [7] and post heat treatment routes [8]. However, the effect of dynamic loading on the mechanical performance of maraging steel samples produced by LPBF remains to be explored.

Aircraft components made of maraging steels are susceptible to dynamic impact loading in service in which their capability to keep toughness and high strength at raised strain rates can be of crucial importance. With the aim of study, the high strain rate performance of materials, the widespread Split-Hopkinson bar equipment has become the standard method. The Split Hopkinson bar techniques (SHB) can be used for various loading modes such as torsion, compression, shear and tension. Split Hopkinson pressure bar (SHPB) has been used for AM materials to predict high strain rate compression performance [9].

The effect of building direction on the quasi-static mechanical performance of maraging steel samples produced by LPBF has been investigated in previous studies [4][6]. Directional growth during during additive manufacturing process leads to maraging steel parts anisotropy [4][6]. Mutua *et al.* [7] described the dependency of uniaxial tensile properties of maraging steel samples fabricated by LPBF on the build direction. They observed that the strength of horizontal specimens with building direction perpendicular to loading direction is higher. In other words, horizontal samples offer more load-bearing capacity than vertical samples. Mooney *et al.* [10] studied plastic anisotropy of maraging

steel samples produced by LPBF, and they concluded that after a 6h heat treatment at 490°C, elongation is increased in vertically built samples.

There are some research gaps regarding the dynamic performance of maraging steels manufactured by LPBF. In addition, investigations that consider the effect of factors such as building direction and heat treatment with detailed microstructural analysis are very few. In our previous studies [11], we studied the high strain rate compression performance of maraging steels produced by LPBF process in heat-treat and as-built conditions, and we found out that fracture took place at the strain rate of 3500 s<sup>-1</sup> for as-built maraging steel samples. However, heat-treated samples begin to fragment at strain rate of 1930 s<sup>-1</sup>, which is ascribed to the lower ductility of maraging steel samples in heat treat condition.

This investigation provides an insight into the effect of build orientation on the dynamic performance of maraging steel processed by LPBF. An aging temperature of 6h at 490°C approved by the LPBF system manufacturer was chosen for the present study. Vertical and horizontal samples with respect to scanning direction were produced using the similar process parameters. High strain rate test was done on vertical and horizontal samples using the SHPB apparatus. Microstructure evolution during deformation under dynamic impact loading was investigated utilizing electron microscopy characterization techniques. It is well known that numerical simulation reduces experiments' costs and is considered an economical method. To obtain a highly accurate description of plastic performance of horizontal and vertical specimens, the Johnson–Cook [12] and Voyiadjis and Abed [13] models were used for the prediction of temperature-dependent viscoplastic response of vertically and horizontally built maraging steels.

## 6.2. Experimental procedure

### 6.2.1. LPBF process

Cylindrical maraging steel specimens (12 mm diameter and 120 mm length) were fabricated using the LPBF technique. For this purpose, an EOS M290 machine was utilized. The chemical composition of the feedstock maraging steel powder is presented in Table 6.1. Besides, the manufacturing process parameters are shown in Table 6.2. The specimen's longitudinal direction was set at an orientation of 0° and of 90° with respect to building orientation to study the effect of building orientation on dynamic compression performance (the geometry of vertical and horizontal specimens is provided in Fig 6.1.). In the horizontal samples, the loading direction is perpendicular to the build orientation, and in vertical samples, the loading direction is parallel to the build orientation. The same process parameters and scan strategy (strip scanning strategy) were employed for the fabrication of horizontal and vertical specimens. After manufacturing, aging at 490 °C for 6 hours was performed on samples.

Table.6. 1. Chemical composition of maraging steel 300 based on EOS datasheet [14].

Element	Fe	Ni	Co	Mo	Ti	Al	C
Composition (wt. %)	Balance	17-19	8.5-9.5	1.5-5.2	0.6-0.8	0.05-0.15	<0.03

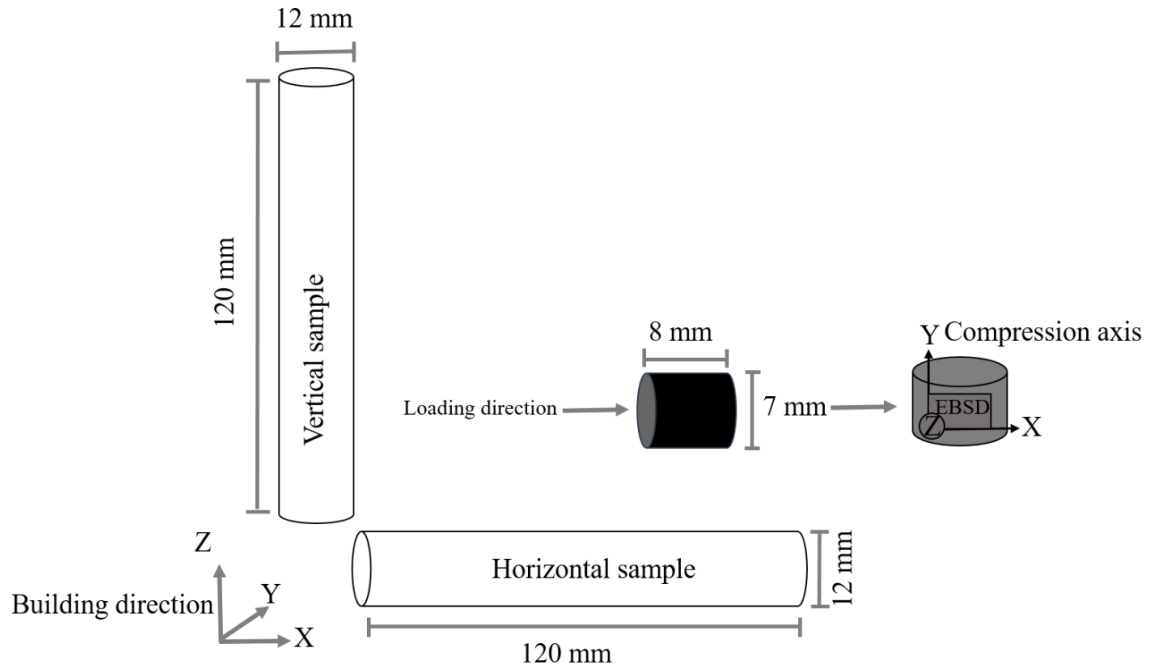


Fig 6. 1 Schematic of specimen geometry used for Split Hopkinson pressure bar (SHPB) apparatus.

Table.6. 2. Process parameter of the LPBF process.

Laser power (W)	Scanning speed (mm/s)	Layer thickness ( $\mu\text{m}$ )	Hatch distance ( $\mu\text{m}$ )
285	960	40	110

### 6.2.2. Dynamic compression testing

The dynamic compression tests were accomplished utilizing the SHPB apparatus. In this apparatus, stress and strain values that material experienced during high loading rates are calculated by the theory of elastic stress wave propagation. The SHPB schematic is shown in Fig 6.2. A projectile strikes the incident bar and some part of the generated wave passes across the specimen and some part of that reflected to the incident bar. The

approaching wave and the reflected wave are computed with the strain gauge adhered to the incident bar. The transferred wave across the specimen is captured by a strain gauge adhered to the transmitted bar. High strain rate tests were conducted on both vertical and horizontal samples. Firing pressures of 60, 70, 80, 90, 100 kPa were employed for vertical samples, generating strain rates of 190, 460, 810, 1100, 1300 s<sup>-1</sup>, respectively. Furthermore, firing pressures of 50, 60, 70, 80, 90 kPa were applied to the horizontal samples, which results in strain rates of 120, 615, 745, 890, 2200 s<sup>-1</sup>, respectively. The following equations has been used for calculating the nominal strain, strain rate and stress during the SHPB tests [9].

$$\sigma(t) = \left(\frac{A_B}{A_S}\right) \cdot E_B \cdot \varepsilon_T \quad (6-1)$$

$$\varepsilon(t) = \left(-2 \frac{C_B}{L_S}\right) \cdot \int_0^t \varepsilon_R \cdot dt \quad (6-2)$$

$$\varepsilon'(t) = \left(-2 \frac{C_B}{L_S}\right) \cdot \varepsilon_R \quad (6-3)$$

In these equations,  $A_S$  and  $A_B$  are the initial cross-sectional area of the specimen and bars, respectively.  $C_B$  is the velocity of the elastic wave in the bars and  $E_B$  is Young's modulus of the bar material. Furthermore,  $\varepsilon_T$  is transmitted signal and  $\varepsilon_R$  is reflected signal.  $L_S$  is the initial length of the sample. Besides, following equations has been used to calculate true strain, strain rate and stress [9].

$$\sigma = \sigma(t)(1 - \varepsilon(t)) \quad (6-4)$$

$$\varepsilon = -\ln(1 - \varepsilon(t)) \quad (6-5)$$

$$\dot{\varepsilon} = \varepsilon'(t)/(1 - \varepsilon(t)) \quad (6-6)$$

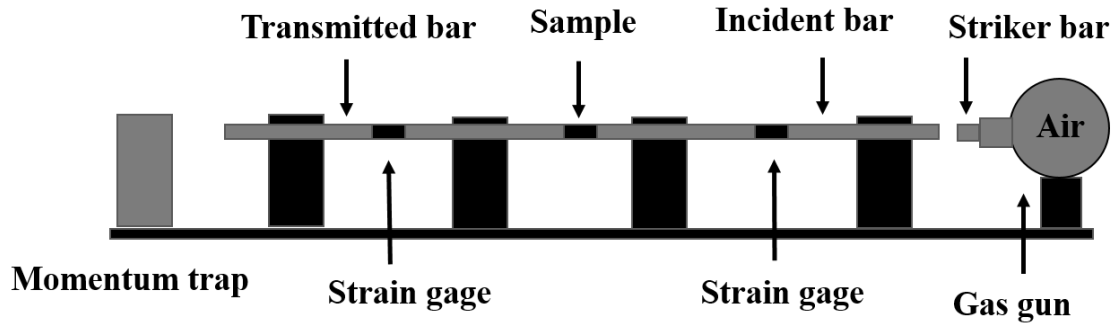


Fig 6. 2 Schematic of Split-Hopkinson pressure bar (SHPB) apparatus

### 6.2.3. Microstructural studies

The microstructure of the impacted samples was examined with a Hitachi SU-70 Field Emission Gun (FEG) ultra-high-resolution SEM. Samples were sectioned along the compression direction for SEM studies. Texture measurement was conducted using a FEI Quanta™ 450 FEG-SEM microscope on the sectioned part, as shown in Fig 6.1. With the TSL® OIM data collection software, the diffraction patterns were collected and OIM data analysis software (version 7.3) were used for refining. EBSD scans were performed on an area of  $500 \times 500 \mu\text{m}^2$  with a step size of 500 nm for both horizontal and vertical samples. The EBSD samples were prepared through a standard metallography procedure. For the vertical samples, loading and building directions are parallel while for horizontal samples, loading and building directions are perpendicular to each other. Precipitates were characterized using EDX attached to a transmission electron microscopy (of type JEOL

JEM-2200FS) operated in bright field imaging mode at an operating voltage of 200 kV. These samples were prepared by usual ion milling procedure.

### **6.3. Results and discussion**

#### **6.3.1. Dynamic compressive behavior of horizontal and vertically oriented maraging steel**

Different firing pressures result in different strain rates, as shown in Fig 6.3. for vertical samples. Firing pressures of 60, 70, 80, 90, 100 KPa were employed on vertical samples, which generated strain rates of 190, 460, 810, 1100, 1300 s<sup>-1</sup>, respectively. Considering strain rate variation, the strain rate raised until it gained a maximum value and subsequently, it decreased gradually and at the end, it experienced sharp drop. In this study, the maximum value of the strain rate is considered as nominal strain rate.

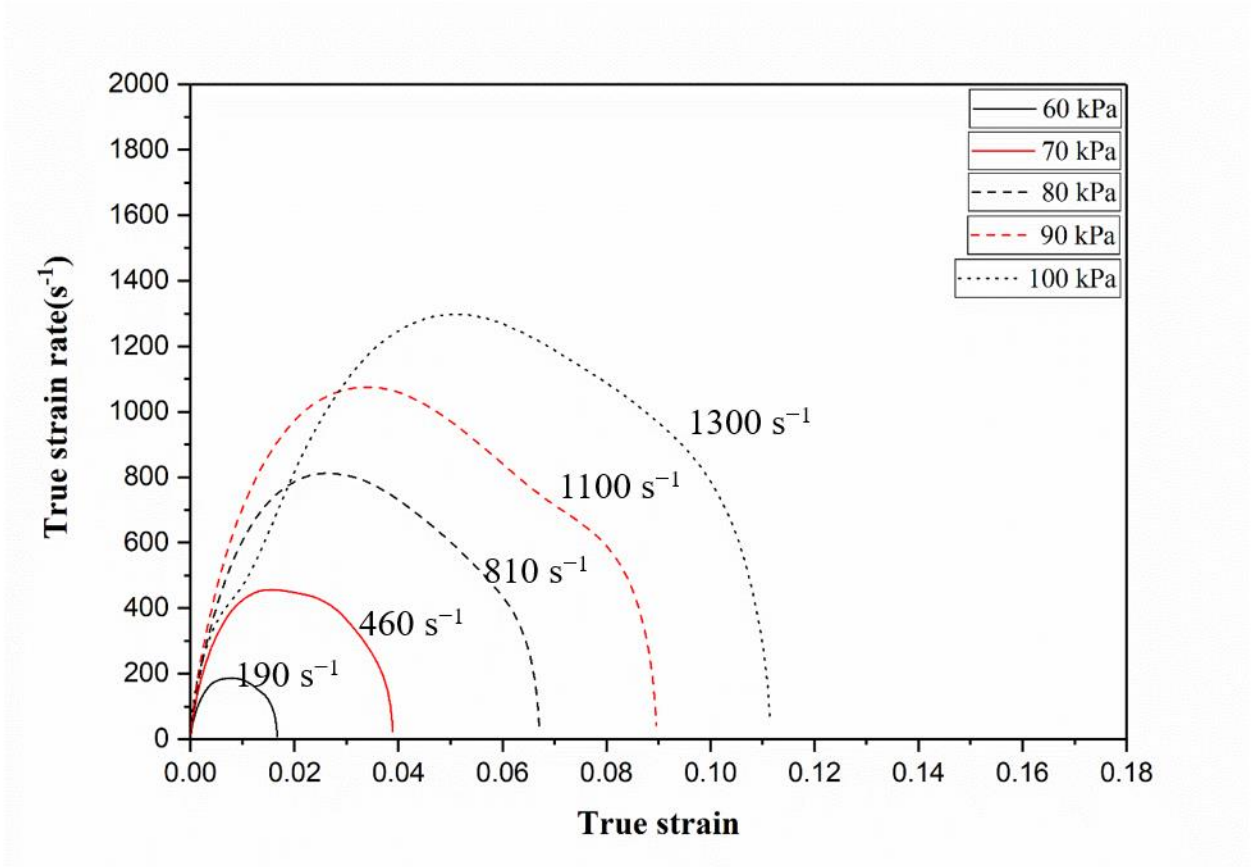


Fig 6. 3 True strain rate-strain curves of vertical heat-treated maraging steel samples in different firing pressure bars (KPa).

The true stress-true strain curves for vertical samples are shown in Fig 6.4. The inset shows the consistency of the data obtained in the high strain rate compression tests. For the vertical sample, fracture was detected at strain rate of  $1300 \text{ s}^{-1}$ . Table 6.3. shows total strain, yield and maximum flow stress values obtained from the dynamic compression test for vertical samples. With the enhancement of the strain rate, strain and maximum flow stress increased in vertical samples. The increase of dynamic strength is related to dislocation generation and multiplication and grain refinement leading to strain hardening with increased strain rate [11]. Two phenomena are involved during dynamic deformation, work softening (i.e. drop in stress, which can be attributed to the occurrence of thermally

activated phenomena such as dynamic recover, dynamic recrystallization and thermal softening (as a consequence of dynamic loading with plastic straining) and work hardening (increase in stress as plastic strain increases). With focus on stress-strain curves (Fig 6.4.), it is noted that, with straining, vertical specimens are subjected to minor work hardening. After maximum stress, specimens lose their load-carrying capacity ascribed to thermal softening and stress drops which ultimately results in shear strain localization.

The formation of adiabatic shear bands (ASBs) is an important phenomenon during dynamic loading. As deformation proceeds, shear localization occurs once critical strain rate and strains are reached. The formation of ASBs is a consequence of localized adiabatic heating and thermal softening [11]. Thermo-mechanical instability during dynamic loading leads to the shear localization along the ASBs. The intense strain localization occurred over a short time ascribed to a substantial momentary local rise in temperature [15]. During high strain rate dynamic deformation, conversion of kinetic energy into heat results in temperature rise. The energy absorbed by the specimen up to fracture defines the toughness of the materials and is given by the area under the stress-strain curves up to failure. The temperature rise in the specimen can be calculated based on the following equation [9]:

$$\Delta T = \left( \frac{\beta}{\rho C_P} \right) \cdot \int \sigma \cdot d\varepsilon \quad (6-7)$$

where  $\rho$  is the density (8 g/cm<sup>3</sup> for maraging steel),  $C_p$  is specific heat (450 ± 20 J/Kg°C for maraging steel),  $\varepsilon$  is effective strain and  $\sigma$  is effective stress.  $\beta$  is considered as the amount of plastic work that is transformed into heat and they supposed to be 90 % [16]. As seen in Table 6.3., with strain rate increment, the temperature in vertical samples increases.

However, the temperature rise in these samples is not significant, and the maximum temperature is 55°C. The temperature in the ASBs is usually significantly higher than the overall temperature of the impacted specimen.

During high strain-rate deformation, imposed strain rate, strain and temperature determine the operative deformation mechanisms. Plastic work can be dissipated in different ways during deformation. The major part of this power is converted to heat, while the minor part of that results in microstructural changes [11]. It should be noted that, during the heat treatment process, ascribed to precipitation hardening the ductility decreased, which can be inferred from total strain values. The maximum fracture strain is about 11%, showing limited plastic deformation.

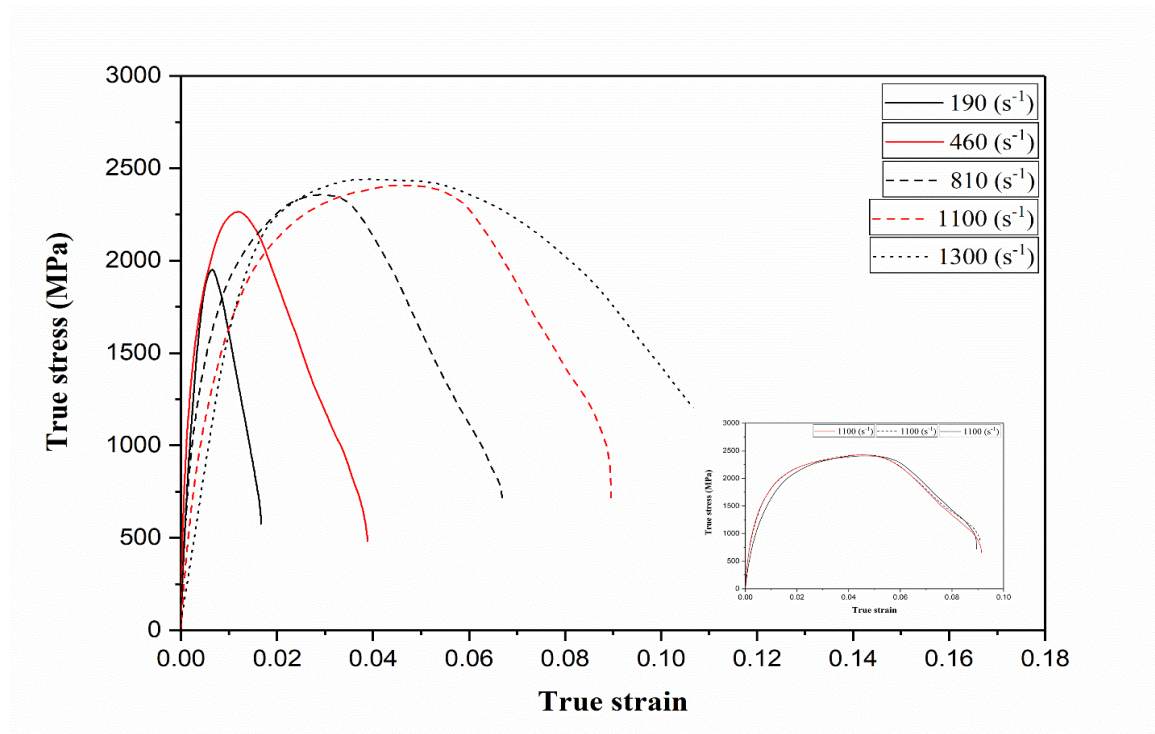


Fig 6. 4 Dynamic true stress-strain curves of vertical heat-treated maraging steel samples deformed at strain rates of 190 to 1300  $s^{-1}$ . The specimens' flow curves deformed at the strain rate of 1100  $s^{-1}$  in the inset show repeatability.

Table.6. 3. Dynamic mechanical properties of the compressed vertical heat-treated maraging steel specimens

Pressure (KPa)	Strain rate (s <sup>-1</sup> )	Yield stress (MPa)	Maximum flow stress (MPa)	Total strain (%)	Toughness (MJ/m <sup>3</sup> )	Temperature rise (°C)
60	190	1700±12.3	1952±11.2	1.6±0.05	22.5±2.3	5.6±1.1
70	460	2015±20.5	2265±23.3	3.8±1.2	61.8±6.8	15.4±2.3
80	810	2114±15.6	2357±12.7	6.7±1.8	119.5±23.3	29.8±6.5
90	1100	2161±23.2	2411±17.1	8.9±1.3	172.1±23.4	43.1±5.4
100	1300	2171±11.7	2441±12.3	11.1±2.1	217.9±12.6	54.4±5.5

Fig 6.5 shows the variation of strain hardening rate ( $d\sigma/d\varepsilon$ ) with true strain for vertical heat-treated samples. Three distinct stages of hardening during high strain rate loading. Vertical samples deformed with quick strain hardening (stage I), accompanied by gradual hardening (stage II), and finally fall in strain hardening [9]. Stage I is a region marked by a fall in strain hardening rate. This region is attributed to the elastic-plastic transition of the material during compression loading [17]. As strain increases, a steady state condition can be observed ascribed to the competition between thermal softening and strain hardening (stage II). As plastic deformation continues, shear localization and thermal softening become dominant. At stage III, stress decreases with the strain increment, which shows thermal softening is dominant [18].

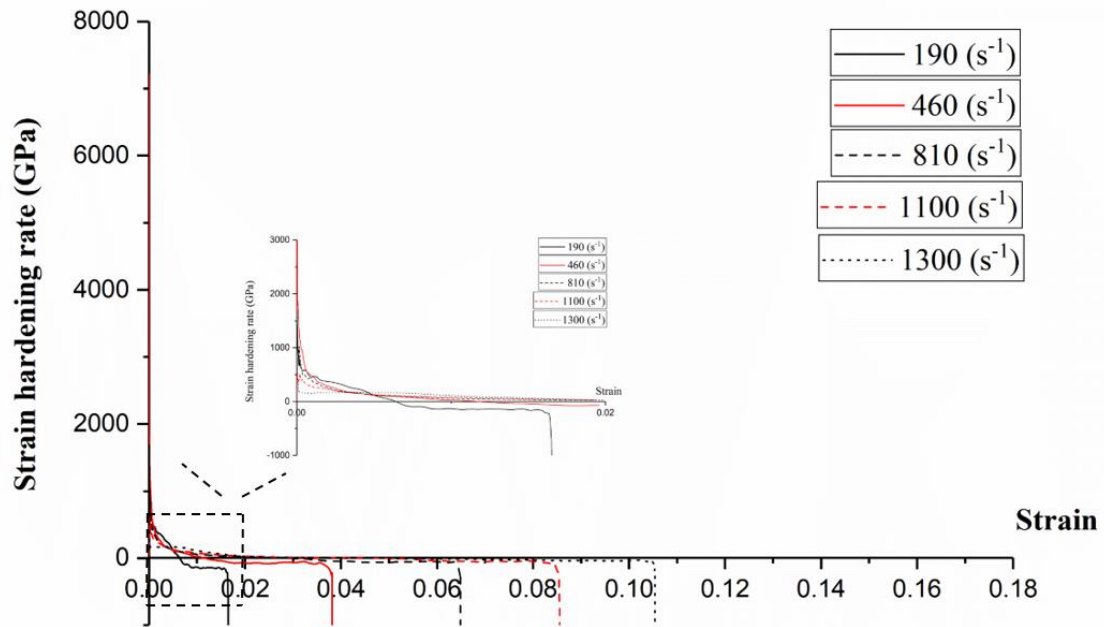


Fig 6. 5 Strain hardening rate vs. strain curves of vertical heat-treated maraging steel dynamically compressed at the strain rates of  $190 \text{ s}^{-1}$ ,  $460 \text{ s}^{-1}$ ,  $810 \text{ s}^{-1}$ ,  $1100 \text{ s}^{-1}$ , and  $1300 \text{ s}^{-1}$ .

Fig 6.6. shows the strain rates in high speed deformation of horizontal samples. Firing pressures of 50, 60, 70, 80, 90 KPa were applied on horizontal samples, which results in strain rates of 120, 615, 745, 890, 2200  $s^{-1}$ . Generally, the same firing pressure generated higher strain rates in horizontal samples than those in the vertical samples, which is related to the higher strength of horizontally built maraging steels. By comparing Fig 6.3. and Fig 6.6., it can be concluded that despite the vertical samples, plateau region in horizontal samples can be noticed.

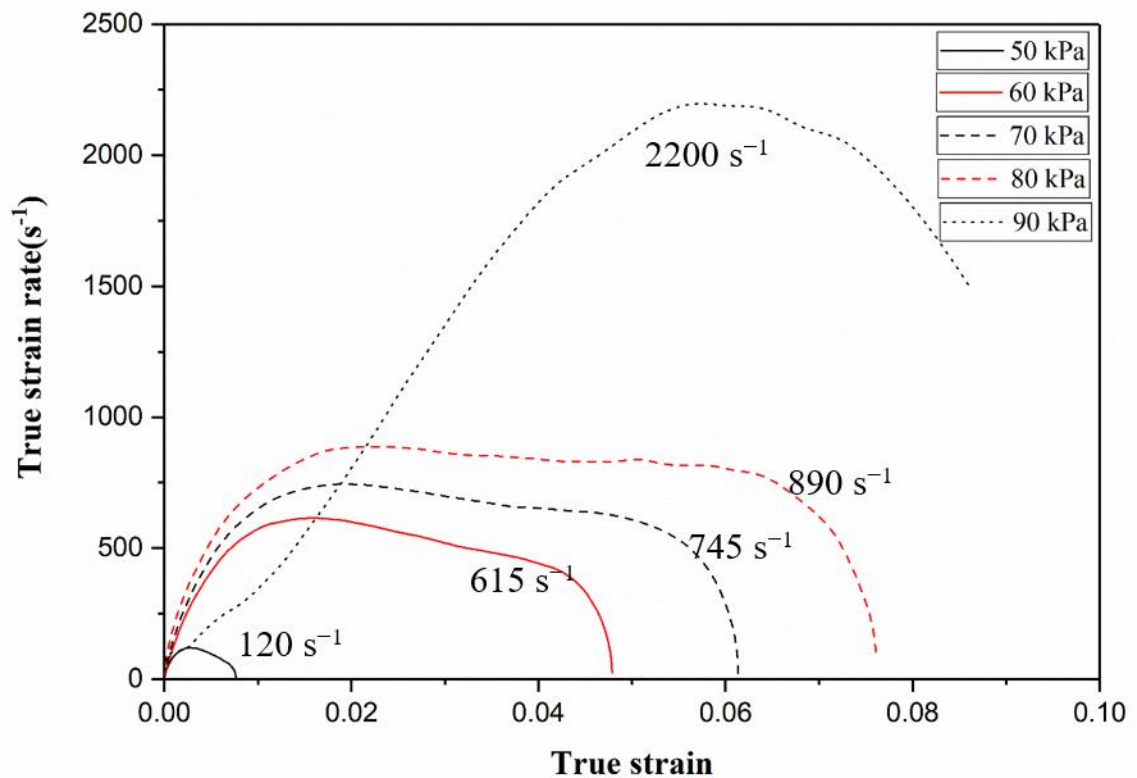


Fig 6. 6 True strain rate-strain curves of horizontal heat-treated maraging steel samples in different firing pressure bars (KPa).

The corresponding true stress-strain curves for horizontal samples are shown in Fig 6.7. and Table 6.4. lists the corresponding values of strain, yield stress, maximum flow

stress. For the horizontal samples, failure occurred at a strain rate of  $2200 \text{ s}^{-1}$ . In these samples, with strain rate increment, stress did not change significantly. Higher dynamic strength can be observed in horizontal samples (2300 MPa for vertical samples versus 3400 MPa for horizontal samples), while higher elongation is readily apparent in vertical samples (11% for vertical samples versus 8% for horizontal samples). Mutua *et al.* [7] observed an enhancement in dynamic strength for horizontal maraging steel specimens in quasi-static condition. In addition, Mooney *et al.* [10] reported an increase in ductility for vertically built maraging steels in quasi-static condition. Table 4 also shows the amount of temperature rise in horizontal samples caused by deformation at different strain rates; similar to the vertical samples the maximum temperature in the horizontal samples is  $55^\circ \text{C}$ .

In vertical samples, building orientation and loading are parallel, while in horizontal samples, loading and building orientation are perpendicular. In the vertical samples, cracks and voids perform as stress propagation sites, and these samples exhibit lower strength [19].

Flow behavior of horizontal and vertical samples followed the same trend where no sign of pronounced thermal softening (decrease in flow stress with plastic straining) can be observed in these two sets of samples. As noted in true stress-true strain curves, a limited plastic zone is evident for the vertical samples. However, in the horizontal samples, the plateau region (stage II) is more pronounced (flat trend in the stress-strain curve shows balance between thermal softening and strain hardening). In other words, horizontally printed samples showed better work hardening ability than vertical samples. This means that horizontally printed samples show an almost flat trend at peak stress over a certain

percentage of strain. However, in vertical samples, the stress-strain curves show peak stress at a single point (not over a range). The similar behavior was seen in quasi-static conditions too [6]. This difference is related to grain morphology in vertical and horizontal samples. It has been reported that in vertical samples, the volume fraction of columnar grains is higher, while horizontal samples contain more cellular and equiaxed grains [20]. In vertical samples, the cooling rate is slower and the thermal gradient is higher along the building direction, resulting in the formation of elongated grains. The fast cooling rate of horizontal samples suppresses grain growth, resulting in more equiaxed grains [21].

Different grain morphologies in vertically and horizontally built samples explain higher strength in horizontal samples and higher elongation to failure in vertical samples. In vertical samples, which contain mostly columnar grains, higher thermal gradient allows more time for precipitates to grow. These coarse precipitates lose precipitate-lattice coherency and effectiveness of dislocation hindrance, resulting in lower strength (will be discussed in the section 3.2).

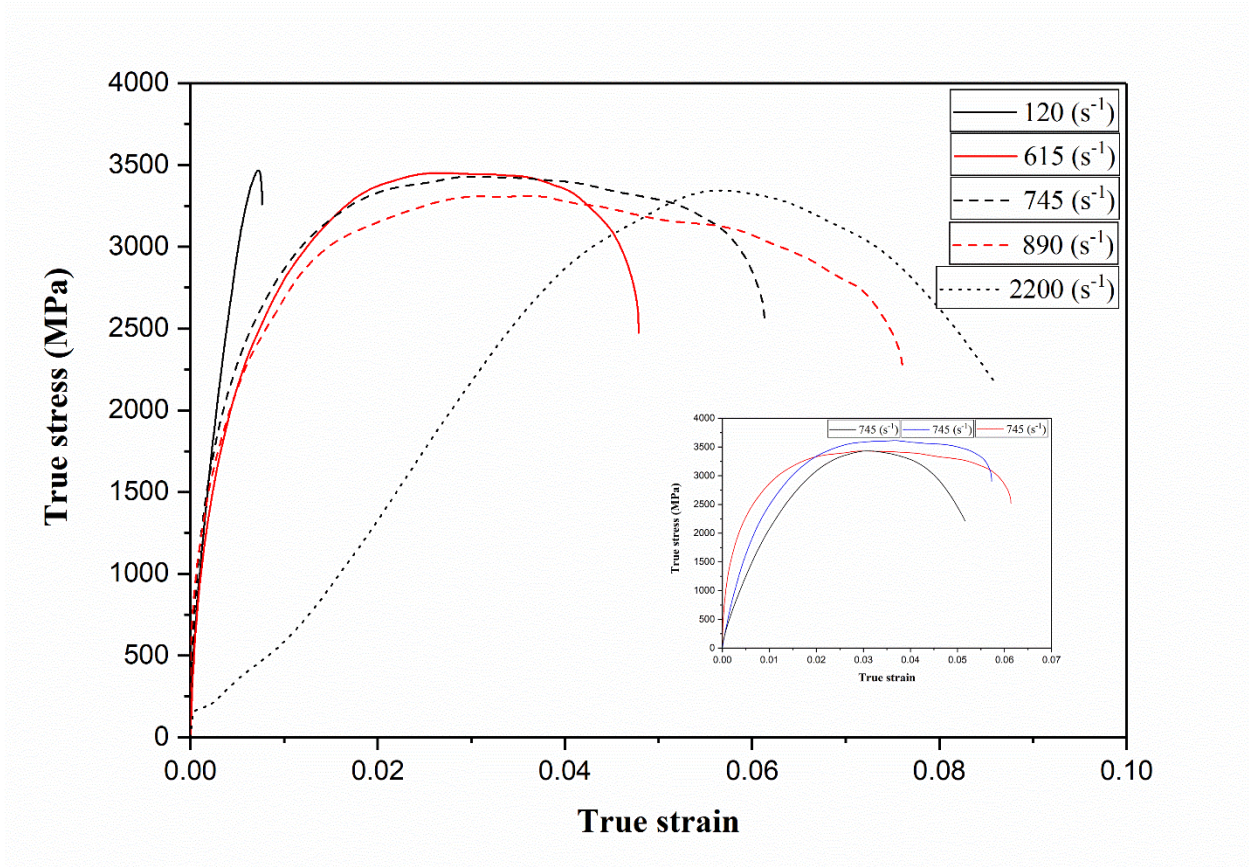


Fig 6. 7 Dynamic true stress-strain curves of horizontal heat-treated maraging steel samples at strain rates of 120 to 2200  $s^{-1}$ . The specimens' flow curves deformed at the strain rate of 745  $s^{-1}$  in the inset ensure repeatability.

Table.6. 4. Dynamic mechanical properties of the compressed horizontal heat-treated maraging steel specimens

Pressure (KPa)	Strain rate (s <sup>-1</sup> )	Yield stress (MPa)	Maximum flow stress (MPa)	Total strain (%)	Toughness (MJ/m <sup>3</sup> )	Temperature rise °C
50	120	3111±11.3	3467±9.7	0.8±0.1	17.6±4.2	4.4±0.2
60	615	3130±23.5	3452±13.8	4.7±1.2	144.1±21.3	36.1±3.6
70	745	3011±26.7	3429±19.2	6.1±1.3	189.3±19.3	47.3±1.3
80	890	2536±35.9	3311±12.1	7.6±2.3	224.1±15.6	56.1±2.2
90	2200	2443±31.4	3344±12.6	8.6±2.1	195.3±11.7	48.8±2.6

The hardening diagrams of horizontal samples are presented in Fig 6.8. These diagrams are divided into three stages. A sharp fall in strain hardening rate can be observed which is stage I. With strain increment, the hardening rate remains constant (stage II). Afterwards, it drops again which indicate stage III. The beginning of stage II is an indication of phenomena related to high-speed deformation such as thermal softening and stage III is an indication of the complete dominance of thermal softening where  $d\sigma/d\varepsilon$  is negative [18]. By comparing Fig 6.5. and Fig 6.8., particularly by considering the strain rate of  $120 \text{ s}^{-1}$  of horizontal samples and the strain rate of  $190 \text{ s}^{-1}$  of vertical samples, it can be noted that stage II is more pronounced in the vertical samples, which demonstrate the dominance of thermal softening at lower strain rates in the vertical samples.

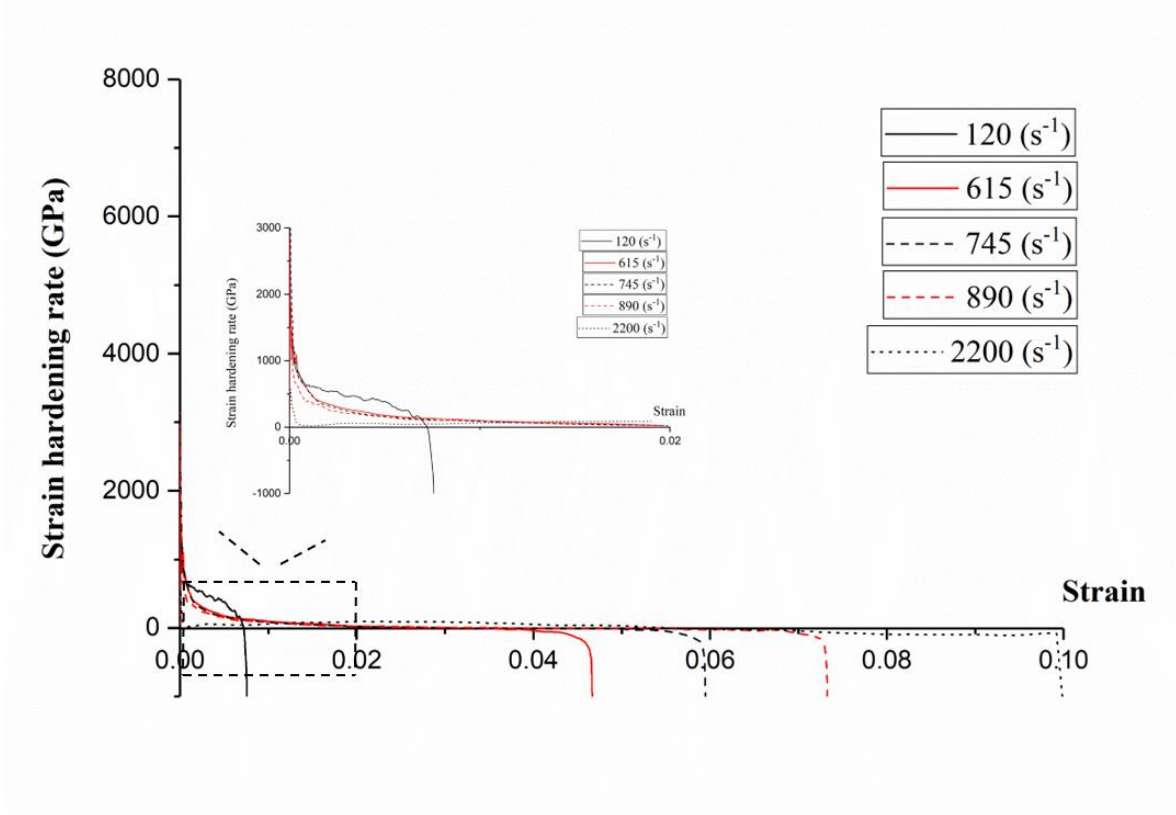


Fig 6. 8 Strain hardening rate vs. strain curves of horizontal heat-treated maraging steel dynamically compressed at the strain rates of  $120 \text{ s}^{-1}$ ,  $615 \text{ s}^{-1}$ ,  $745 \text{ s}^{-1}$ ,  $890 \text{ s}^{-1}$ , and  $2200 \text{ s}^{-1}$ .

### 6.3.2. Microstructural evolution during dynamic loading of horizontal and vertically printed maraging steel (TEM studies)

To investigate the effect of high-speed deformation on precipitates, TEM studies were conducted on horizontal and vertical heat-treated samples. TEM bright-field images of horizontal and vertical samples along with elemental distribution are illustrated in Fig 6.9. and Table 6.5. Fig 6.9. (a) shows the microstructure of the heat-treated horizontal samples after compression at a strain rate of  $890 \text{ s}^{-1}$  (before fracture) and Fig 6.9. (b) shows TEM image of vertical sample compressed at a strain rate of  $1100 \text{ s}^{-1}$  (before fracture).

After heat treatment at 490 °C for 6h, Ni<sub>3</sub>Ti and Ni<sub>3</sub>Mo precipitates form in maraging steel [22]. Precipitates containing nickel, titanium, and molybdenum are depicted in these figures and presented in Table 5. As it is evident, two types of precipitates formed in horizontal and vertical samples. Ni-Ti based precipitates are associated with the areas enriched in Ti, Ni, and only hardly noticeable in Mo. In addition, Mo-based precipitates are related to regions enriched with Mo. Ni<sub>3</sub>Ti precipitates formed during the first stages of heat treatment because of their low lattice misfit and act as a nucleation site for Ni<sub>3</sub>Mo precipitates [3]. These precipitates inhibit the dislocation motion, which results in the strengthening in heat-treated maraging steel samples. However, in different building directions, the volume fraction and size of precipitates are different. On the one hand, in vertical samples containing columnar grains, precipitates tend to grow, and coarse precipitates can be observed. On the other hand, in horizontal samples, the volume fraction of precipitates is higher and precipitates are finer, bringing on an increase of strength. The lower strength of vertical samples allows thermal softening to easily become dominant and consequently the susceptibility formation of ABSs increases. ABSs susceptibility is a standard that indicates the ability of ASB formation during dynamic deformation. Generally, the difference in precipitates morphology, size, and volume fraction cause different behaviors in dynamic deformation.

Using image-J software, the size of precipitates was calculated in both horizontal and vertical samples. The average precipitates' length was  $61.7 \pm 15.4$  nm and  $25.9 \pm 3.5$  nm for vertical and horizontal samples, respectively. Growth and elongation of precipitates are significant in vertical samples, which triggers lower strength during dynamic loading.

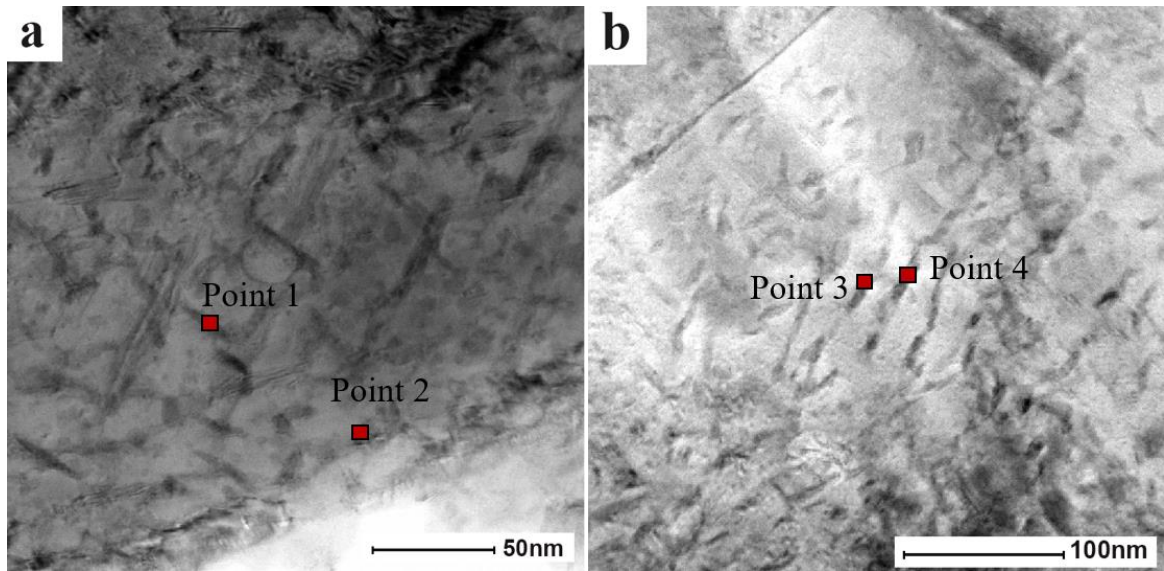


Fig 6. 9 TEM bright-field images of (a) horizontally built maraging steel deformed at the strain rate of  $890 \text{ s}^{-1}$  and (b) vertically built maraging steel deformed at the strain rate of  $1100 \text{ s}^{-1}$ .

Table.6. 5. Chemical composition (wt. %) by EDS/TEM of vertical and horizontal samples.

Precipitates/Elements	Fe	Ni	Mo	Ti
1	69.53	22.52	6.43	1.52
2	58.89	24.23	14.59	2.28
3	57.54	31.72	8.48	2.27
4	53.68	29.85	15	1.47

### **6.3.3. Microstructural evolution during dynamic loading of horizontal and vertically printed maraging steel (SEM studies)**

SEM images presented in Figs 6.10. and 6.11. show the microstructures of maraging steel samples in two building directions. The microstructure of deformed samples after high strain-rate deformation is characterized by ASBs. The fracture mechanism of dynamically deformed samples was investigated before and it was described that ASBs are regions of intense shear stress localization, which are susceptible to void formation[9]. These voids merge and form cracks which lead to fracture of the specimen [9]. Fracture of dynamically impacted specimens has been noticed to initiate and propagate in ASBs [9]. There is a strain rate above which, heat dissipation from specific deformation regions does not readily occur, leading to formation of ASBs [11]. Localized deformation is a progressive process and shear deformation becomes concentrated step by step [15].

Fig 6.10. shows that in vertical samples ASBs are formed at strain rates of  $460\text{s}^{-1}$  and above, whereas ASBs are only observed with a strain rate of minimum  $745\text{ s}^{-1}$  in horizontal heat-treated samples, cf. Fig 6.11. At specific strain rate and strain, the shear localization occurs in maraging steel produced by LPBF with different building directions. It is evident that, vertical samples have more tendency to show ASBs. Severe localization is followed by a drop in the load-carrying ability or drop in flow stress, and as can be observed in Fig. 4, vertical samples lost load-carrying capacity suddenly, which agrees well with the microstructure analysis. A material is more prone to ASB formation if it has low strain hardening [15]. Vertical samples, which showed low work hardening ability, are more prone to ASB formation (Fig 6.4).

These ASBs are paths, which accommodate imposed shear strain. In other words, these ASBs, help to accommodate intense shear strain [11]. From SEM analysis, it can be inferred that vertical samples are more prone to ASB formation, which is in agreement with the dominance of thermal softening in the hardening curves in Fig 6.5. This feature of vertical samples is compatible with the lower dynamic strength of vertical samples compared to the horizontal ones. It is worth mentioning that development of shear bands is attributed to the strength of the material as well. In other words, as vertical samples have lower strain hardening capacity are more prone to ASBs formation. Indeed, the maximum strain rate before fracture that vertical samples can tolerate is  $1300 \text{ s}^{-1}$ , while for horizontal samples, the maximum strain rate is  $2200 \text{ s}^{-1}$ .

It should be noted that temperature rise inside ASBs is more than the calculated values presented in Tables 6.3. and 6.4. Temperature rise calculations were done based on the simplifying assumption of uniform strain in the entire gauge section of the specimens, which obviously is not valid for a localized regions of deformation like ASBs [23]. Indeed, inside the ASBs, strain localization happens, and real temperature is much more than what is measured and presented in Tables 6.3. and 6.4.

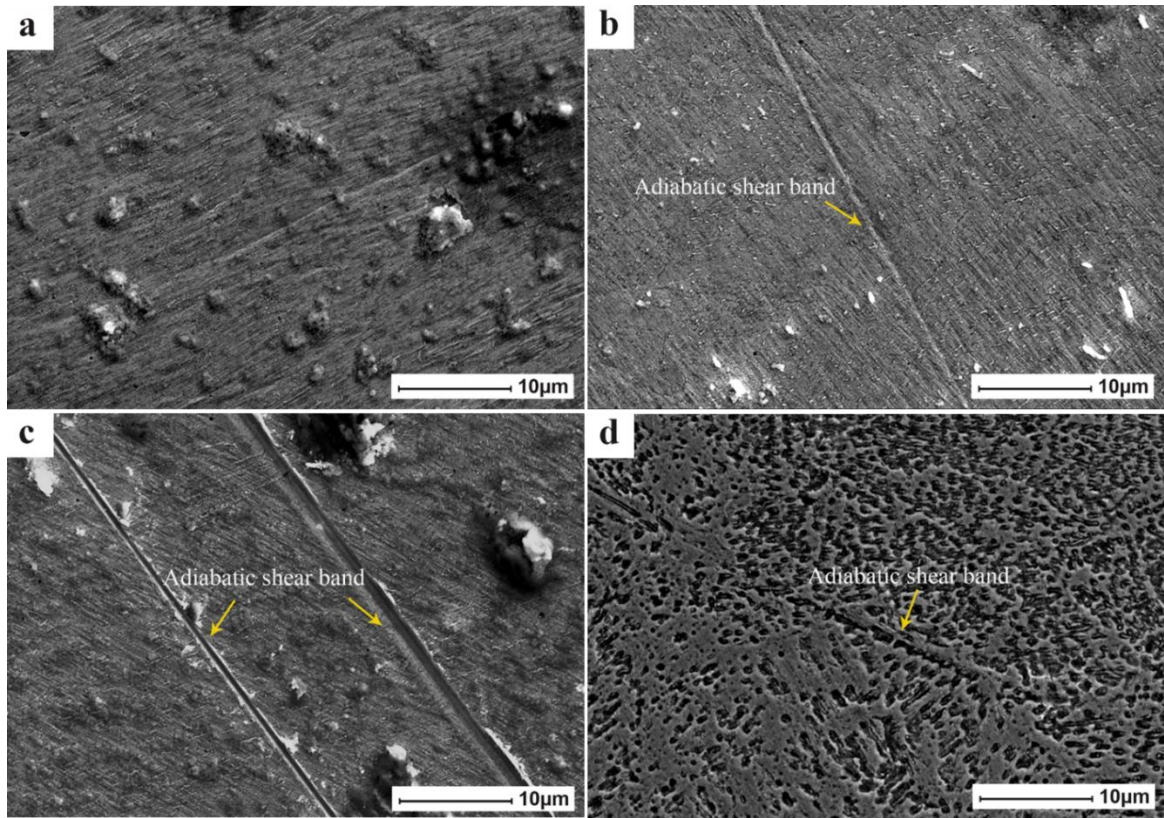


Fig 6. 10 Microstructures of the vertical heat-treated specimens at strain rates of a) 190 of b) 460, c) 810, and d) 1100 s<sup>-1</sup>.

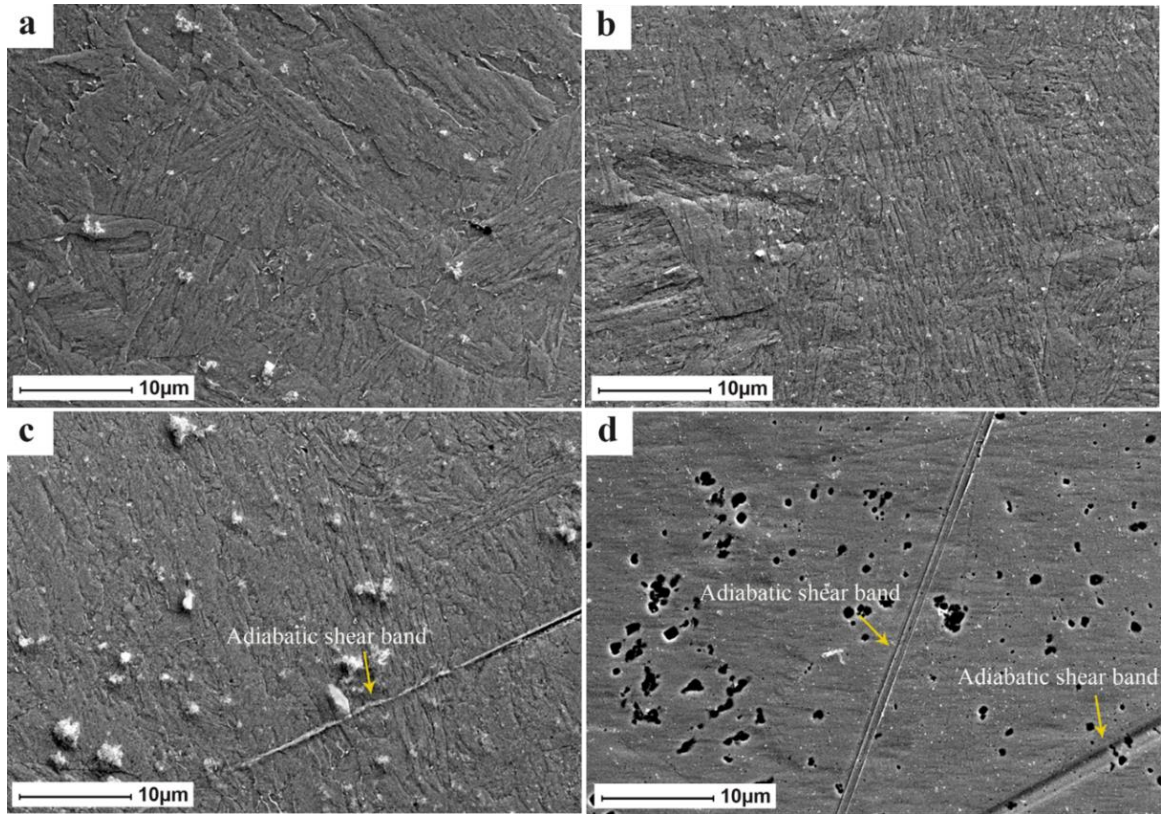


Fig 6. 11 Microstructures of the horizontal heat-treated specimens at strain rates a) 120, b) 615, c) 745, and d) 890  $s^{-1}$ .

Fig 6.12. shows the results of SEM fractography of heat treated vertical samples. For vertical samples, fracture happened at the strain rate of  $1300 s^{-1}$ . As noted in Fig 6.12. (a), fracture occurred at  $45^\circ$  to the impact direction. This direction is the maximum shear stress direction. Localized shear deformation during high-speed deformation promotes nucleation of voids [9]. Growth, and merging of microcrack and voids triggers crack formation and, therefore, accelerates failure along the ASBs. Due to the tension inside ASBs, voids widen until they reach the border of ASBs. Voids do not develop inside the adjacent material because of lower strength of ASBs compared to adjacent material [15]. Dimples which are characteristics of ductile fracture along with cleavage planes can be observed in vertically printed samples. However, the dominant fracture mode for vertical

heat-treated samples is a brittle fracture. Ductility of heat-treated maraging steels is not comparable with as-built samples which results in brittle fracture of heat treated samples [11]. In fracture surface, elongated dimples lie along the shear direction (Fig 6.12 (a). As shown in Fig 6.12. (c), dimples in vertical samples are more elongated, which agrees with the higher plastic strain that these samples accommodated during dynamic loading (around 11 %). Indeed, the stretching of dimples in the load direction is remarkable in vertical samples due to the merging of neighboring voids and this behavior was observed this behaviour in maraging steel produced by LPBF in quasi-static conditions too [24].

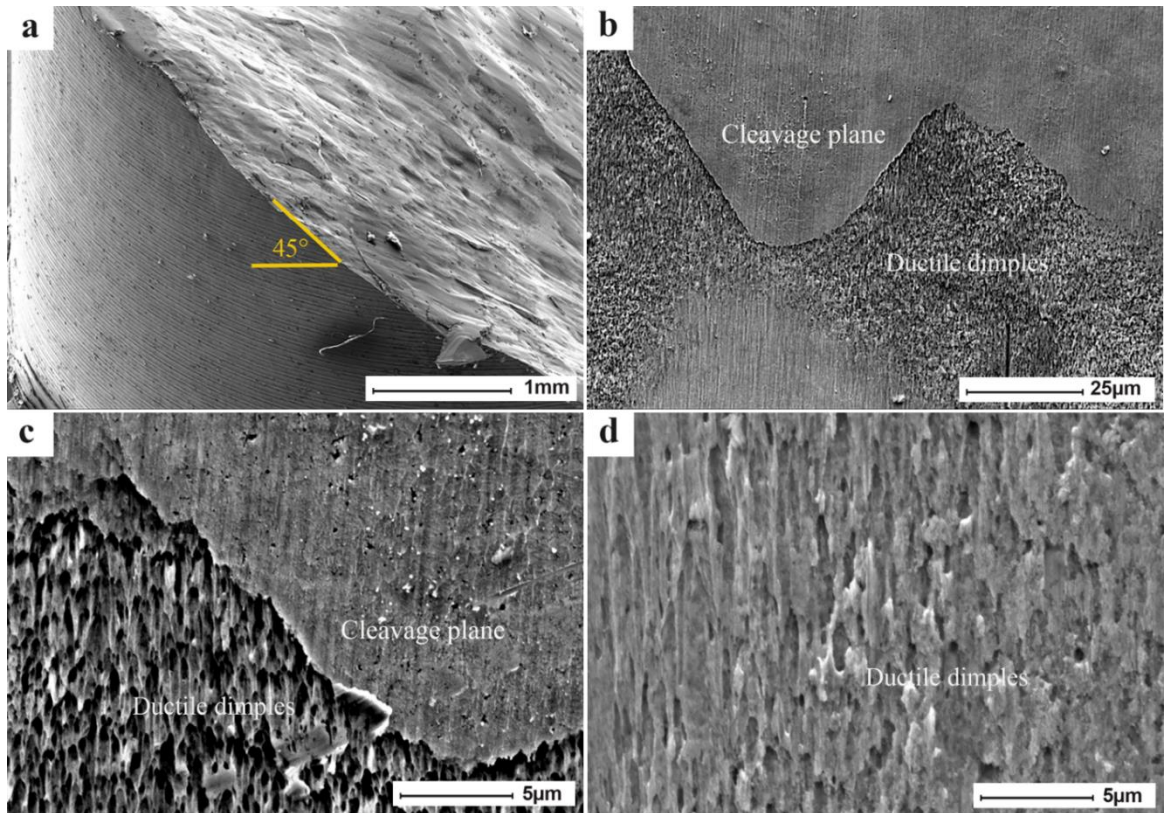


Fig 6. 12 SEM fractography of the fracture surfaces of vertical heat-treated specimen deformed at the strain rates of  $1300 \text{ s}^{-1}$ .

SEM fractographs of heat-treated horizontal samples are presented in Fig 6.13. Failure of horizontal samples occurred at a strain rate of  $2200 \text{ s}^{-1}$ . The fractured sample features shear at an angle of  $45^\circ$  to the loading direction. Similar to the vertical samples, a combination of dimples and cleavage planes exist and the dominant fracture mode is brittle fracture. However, compared to vertical samples, horizontal samples feature more spherical dimples generated during plastic deformation. In horizontal samples, the probability of joining of defects is lower (than that in the vertical samples), leading to higher resistance to failure, higher strength and lower elongation and this behavior was reported before for maraging steel produced by LPBF in quasi-static condition [24].

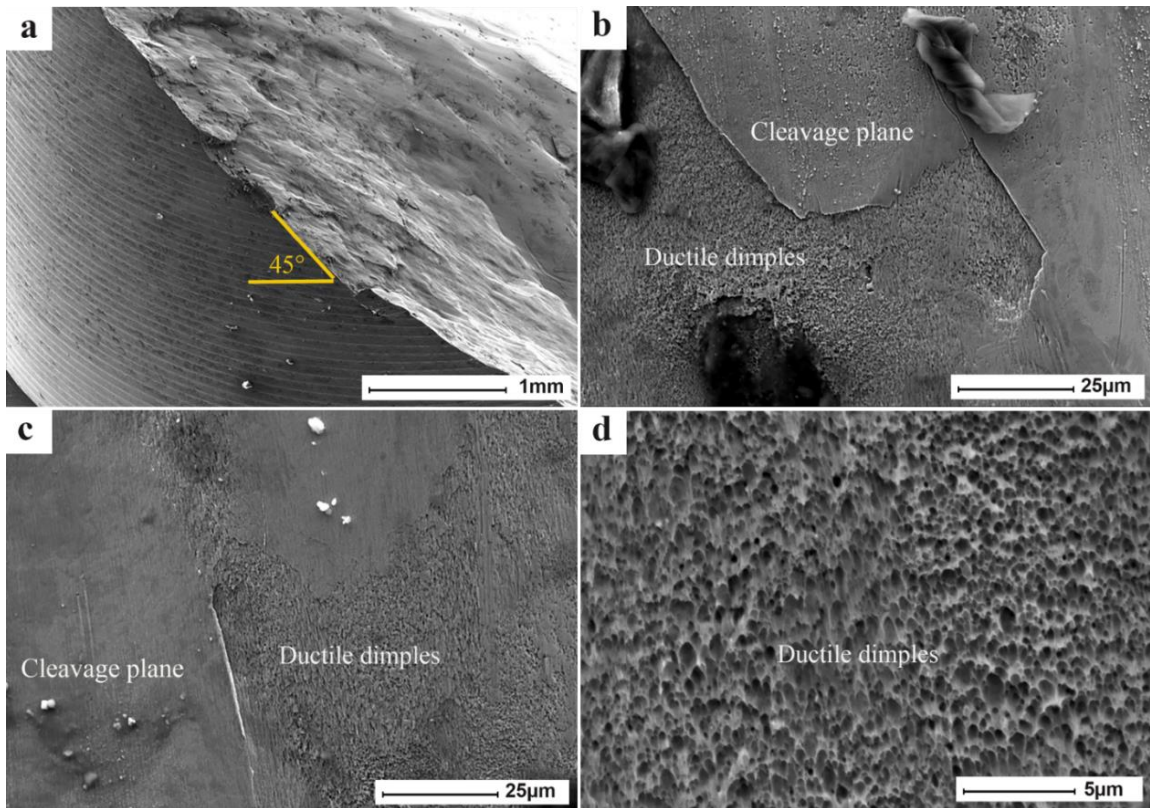


Fig 6. 13 SEM fractography of the fracture surfaces of horizontal heat-treated specimen deformed at the strain rates of  $2200 \text{ s}^{-1}$ .

#### **6.3.4. Texture evolution during dynamic loading of horizontal and vertically printed maraging steel:**

EBSD technique was used for crystallographic texture analysis of the maraging steels manufactured by the LPBF with different building directions and different strain rates. After high strain-rate compressive loading, different textures are developed in horizontal and vertical samples (Fig 6.14.). Grain morphology and texture evolution are also responsible for the different dynamic mechanical performance of the horizontal and vertical samples. Fig 6.14. shows the inverse pole figure (IPF-Y) maps of horizontal and vertical samples deformed at different strain rates over a large scan area. Y is the direction of compressive loading. Figs 6.14. (a), (b) and (c) shows the microstructure of vertical samples compressed at strain rates of  $460 \text{ s}^{-1}$ ,  $810 \text{ s}^{-1}$  and  $1100 \text{ s}^{-1}$  and (d), (e) and (f) shows horizontal samples deformed at strain rates of  $615 \text{ s}^{-1}$ ,  $745 \text{ s}^{-1}$ , and  $890 \text{ s}^{-1}$ . In vertical samples, which consist mostly of columnar grains, clear alignment of the  $\langle 001 \rangle$  crystal direction with the building direction occurred (represented by red grains), which is parallel to loading direction (Y-axis). Columnar grains predominantly possess a  $\langle 001 \rangle // \text{BD}$  texture, which is an easy growth direction [25]. Shamsdini *et al.* [4] observed  $\langle 001 \rangle // \text{BD}$  fibre for vertical maraging steel samples before deformation, and they reported strong  $\langle 110 \rangle // \text{LD}$  fibres after uniaxial tensile testing for maraging steel produced by LPBF. It should be noted that the reason for the lower load-carrying capacity of vertical samples is the presence of these columnar grains with  $\langle 001 \rangle$  orientation. However, based on Fig6.14 (a-c), with strain rate enhancement, and as plastic straining continue, most of the red grains (grains with  $\langle 001 \rangle // \text{LD}$  orientation) have been substituted with blue (grains with  $\langle 111 \rangle$

// LD).  $\langle 111 \rangle // LD$  texture evolution is attributed to compression loading in a BCC crystal structure [26].

In BCC structures, the probability of crack propagation and cleavage fracture in (001) planes is higher, and this could be the reason for the less dynamic strength of vertical samples [27]. In vertical samples that showed the  $\langle 001 \rangle // LD$  texture, fracture occurred at lower strain rates than the horizontal samples, and maximum dynamic strength was much lower. However, as it is evident in the IPF maps (Fig 6.14 (a-c)), the length of columnar grains decreased with strain rate increment. This is associated with the fact that columnar grains, which are lined up along the building direction (Y-axis), are subjected to compressive loading in the same direction (Y-axis). This compression results in the reduction in the length of columnar grains.

Horizontal samples consist mostly of equiaxed grains and do not show preferred orientation at low strain rates (Fig 6.14. (d)). However, compared to vertical samples, horizontal samples contain finer grains which are responsible for higher strength (~3500 MPa) of these samples during compressive loading. The average grain size of the horizontal and vertical samples was calculated using EBSD analysis, which confirms finer grains in horizontal samples. Average grain size diameter in the vertical sample at the strain rate of  $460 \text{ s}^{-1}$ , and in the horizontal sample at the strain rate of  $615 \text{ s}^{-1}$  was  $30.64 \pm 10.02 \mu\text{m}$  and  $9.71 \pm 6.27 \mu\text{m}$ , respectively. In addition, grain refinement leads to strength increase based on the Hall-Petch relationship [11]. It is noted that, with strain rate increase in horizontal samples, blue grain  $\{111\}$  have become dominant as a result of grain rotation during plastic straining. Therefore, texturing of grains around  $\langle 111 \rangle // LD$  (LD: loading direction) in both vertical and horizontal samples can be observed.

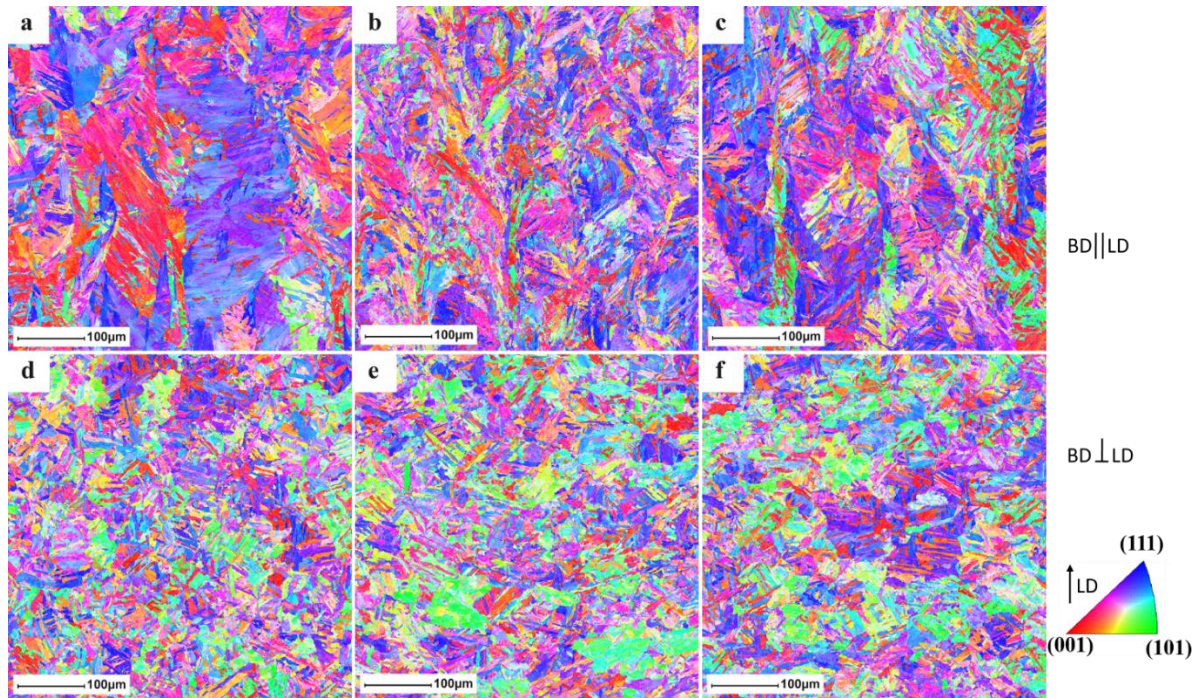


Fig 6. 14 IPF-Y map of vertical and horizontal samples after dynamic compressive loading at different strain rates (a) Vertical-  $460 \text{ s}^{-1}$ , b) Vertical-  $810 \text{ s}^{-1}$ , c) Vertical- $1100 \text{ s}^{-1}$ , d) Horizontal- $615 \text{ s}^{-1}$ , e) Horizontal-  $745 \text{ s}^{-1}$ , f) Horizontal-  $890 \text{ s}^{-1}$ .

Fig 6.15. shows (001) and (111) pole figures of vertical samples compressed at different strain rates and Fig 6.16. represent the pole figures of horizontal samples at different strain rates. As can be noted, no significant texture sharpening with strain rate increment can be observed in vertical and horizontal samples. Alignment of (111) poles along the loading direction (Y-axis) can be detected in both samples compressed at high strain rates ( $1100 \text{ s}^{-1}$  for vertical and  $890$  for horizontal  $\text{s}^{-1}$ ). {111} planes are aligned as a result of grain rotation to accommodate intense stresses during compression loading. To accommodate the intensive plastic deformation imposed during high strain rate compression, a  $\langle 111 \rangle // \text{LD}$  texture evolution occur [26]. Furthermore, in vertical samples,

due to the dominance of columnar grains, (100) poles with high intensity can be noted at the low strain rate of  $460 \text{ s}^{-1}$ .

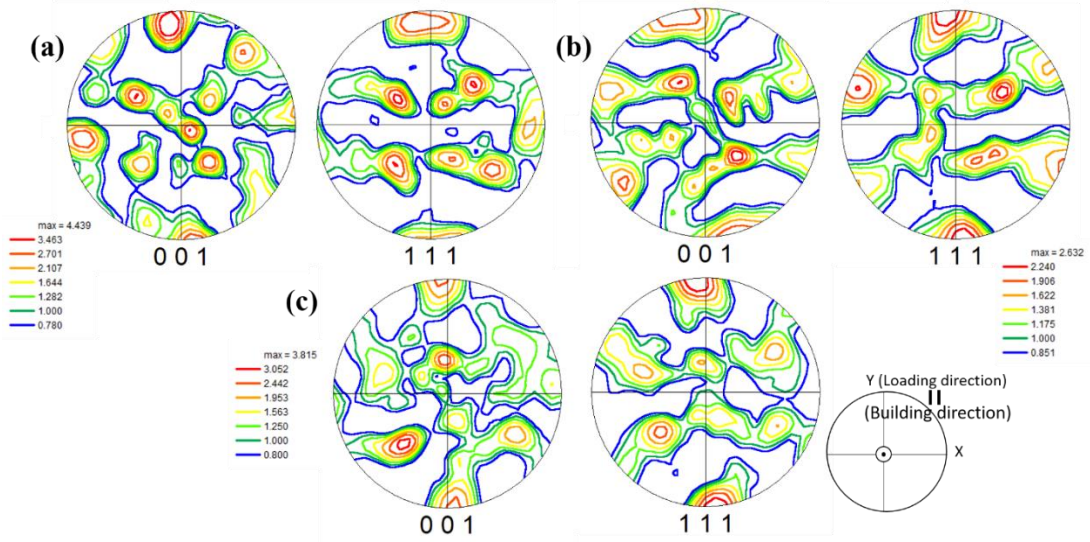


Fig 6. 15 (001) and (111) pole figures of vertical samples after dynamic compressive loading. a) Vertical-  $460 \text{ s}^{-1}$ , b) Vertical-  $810 \text{ s}^{-1}$ , c) Vertical-  $1100 \text{ s}^{-1}$ .

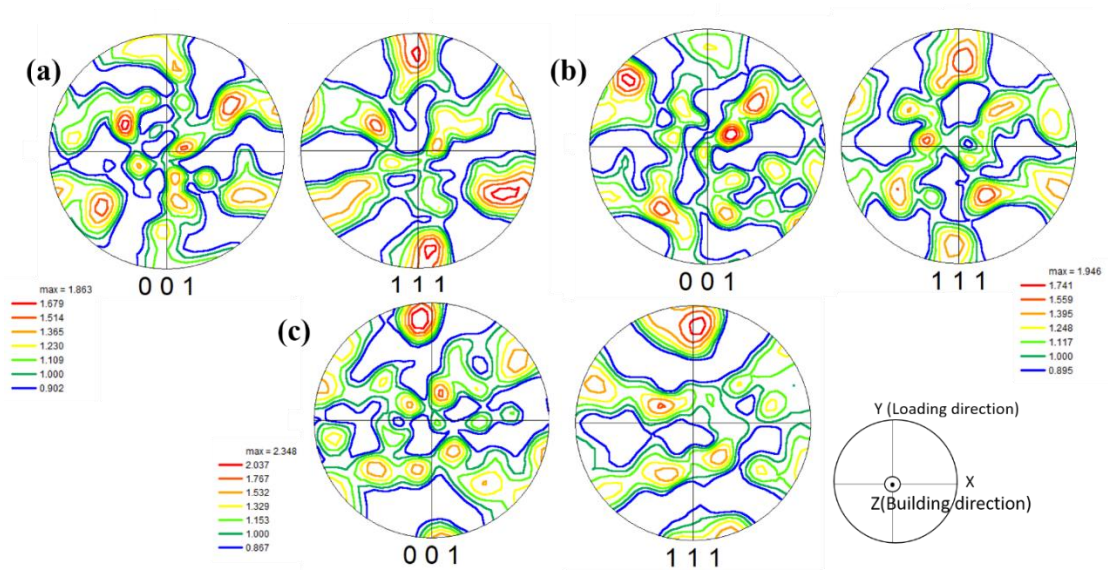


Fig 6. 16 (001) and (111) pole figures of horizontal samples after dynamic compressive loading. a) Horizontal-  $615 \text{ s}^{-1}$ , b) Horizontal-  $745 \text{ s}^{-1}$ , c) Horizontal-  $890 \text{ s}^{-1}$ .

To obtain a more complete picture of the texture, orientation distribution functions (ODFs) were calculated. Fig 6.17. represents the ODF in the  $\phi_2 = 0$  and  $45^\circ$  sections for the vertical and Fig 6.18. shows ODF maps of horizontal samples. Fig 6.17. shows the ODF map of vertical samples deformed at strain rates of 460, 810, and  $1100 \text{ s}^{-1}$ . As can be noted, for lower strain rates in vertical samples, cube component ( $\{100\}\langle 100\rangle$ ) can be observed, which is a result of the presence of columnar grains along the building directions (for vertical samples BD // LD). However, with strain rate increment, this cube texture becomes weak and  $\{100\}$  grains rotated towards  $\{111\}$  grains. This effect is confirmed with the presence of the E texture component ( $\{111\}\langle 110\rangle$ ).

Fig 6.18. shows the ODF maps of horizontal samples compressed at strain rates of 615, 745, and  $890 \text{ s}^{-1}$ . Significant texture sharpening with strain rate increment, can not be noted from these figures. However, the evolution of E texture is noted with strain rate increment. This texture evolution is a consequence of activation of slip system and grain rotation to accommodate imposed strains during compression loading.

For high strain-rate deformation of maraging steel samples in different building direction, texture weakening can be noted. According to the Canova *et al.* [28] model, texture weakening is expected to occur under high strain-rate compressive loading, that is in agreement with the current study. They suggested that the number of active slip systems increases when deformed at high strain rates and consequently, lattice rotation is reduced, which results in texture weakening at high strain rates.

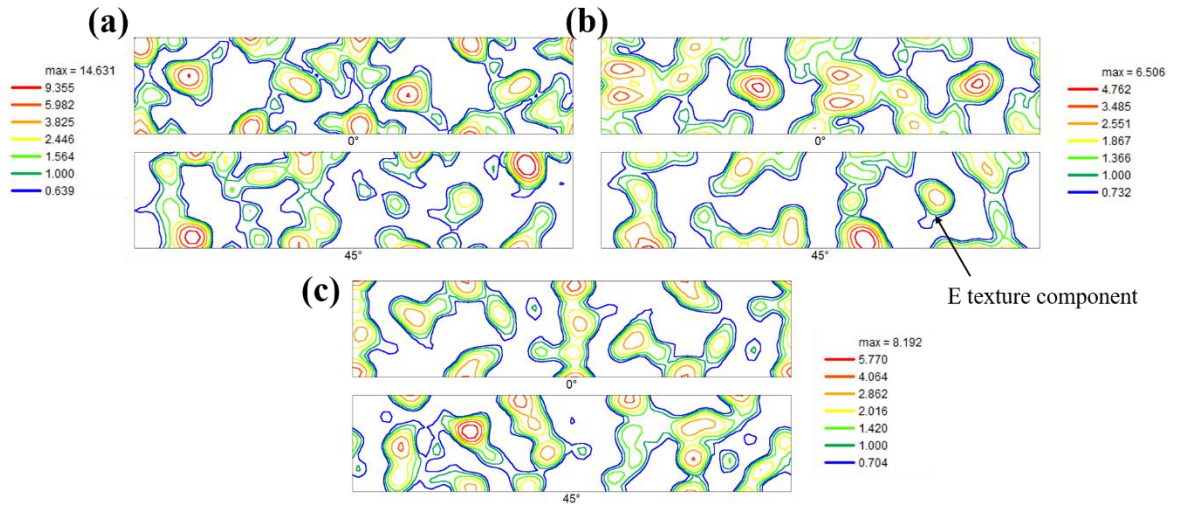


Fig 6. 17 The  $\phi_2=0^\circ$  and  $45^\circ$  sections of the ODF maps of vertical samples after dynamic compressive loading. (a) Vertical- 460 s<sup>-1</sup>, b) Vertical- 810 s<sup>-1</sup>, c) Vertical-1100 s<sup>-1</sup>.

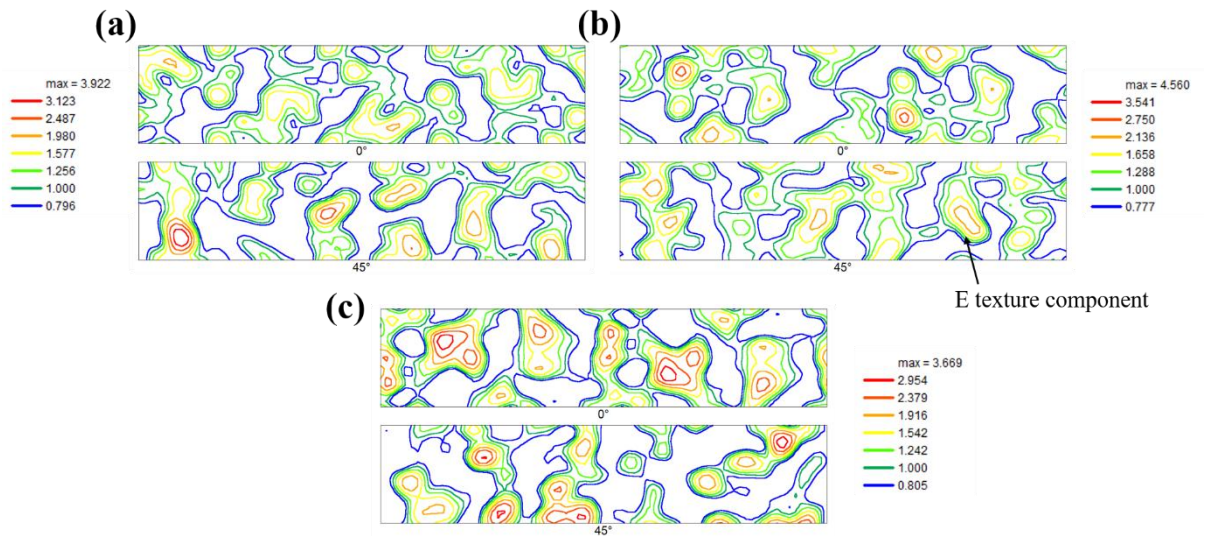


Fig 6. 18 The  $\phi_2=0^\circ$  and  $45^\circ$  sections of the ODF maps of horizontal samples after dynamic compressive loading. a) Horizontal-615 s<sup>-1</sup>, b) Horizontal- 745 s<sup>-1</sup>, c) Horizontal- 890 s<sup>-1</sup>.

To study recrystallization process during high strain rate compression, kernel average misorientation (KAM) values were used. Fig 6.19 shows the KAM values for

vertical and horizontal samples after deformation at different strain rates. It is inferred from Fig 6.19. that with strain rate increment, the fraction of grains with high KAM values increased. The KAM value bears a connection to the plastically stored energy and dislocation density in crystal grains [29]. They believed that with increasing strain rate, dislocation density increased, which was reported previously. KAM value  $<1$  shows recrystallized grains and KAM $>1$  shows deformed grains with have more dislocations [30]. The driving force for recrystallization process increased with strain rate increment, leading to a rise in the fraction of DRX grains with KAM values  $<1$ .

It is noted that, in vertical samples, the fraction of grains with high KAM values (KAM value  $>1$ ) is lower, and the fraction of grains with KAM $<1$  is higher compared with horizontal samples. This indicates the dominancy of thermal softening in vertical samples. Due to temperature rise and annihilation of dislocations in vertical samples, the recovery process becomes activated, followed by formation of recrystallized grains and reduction of dislocations.

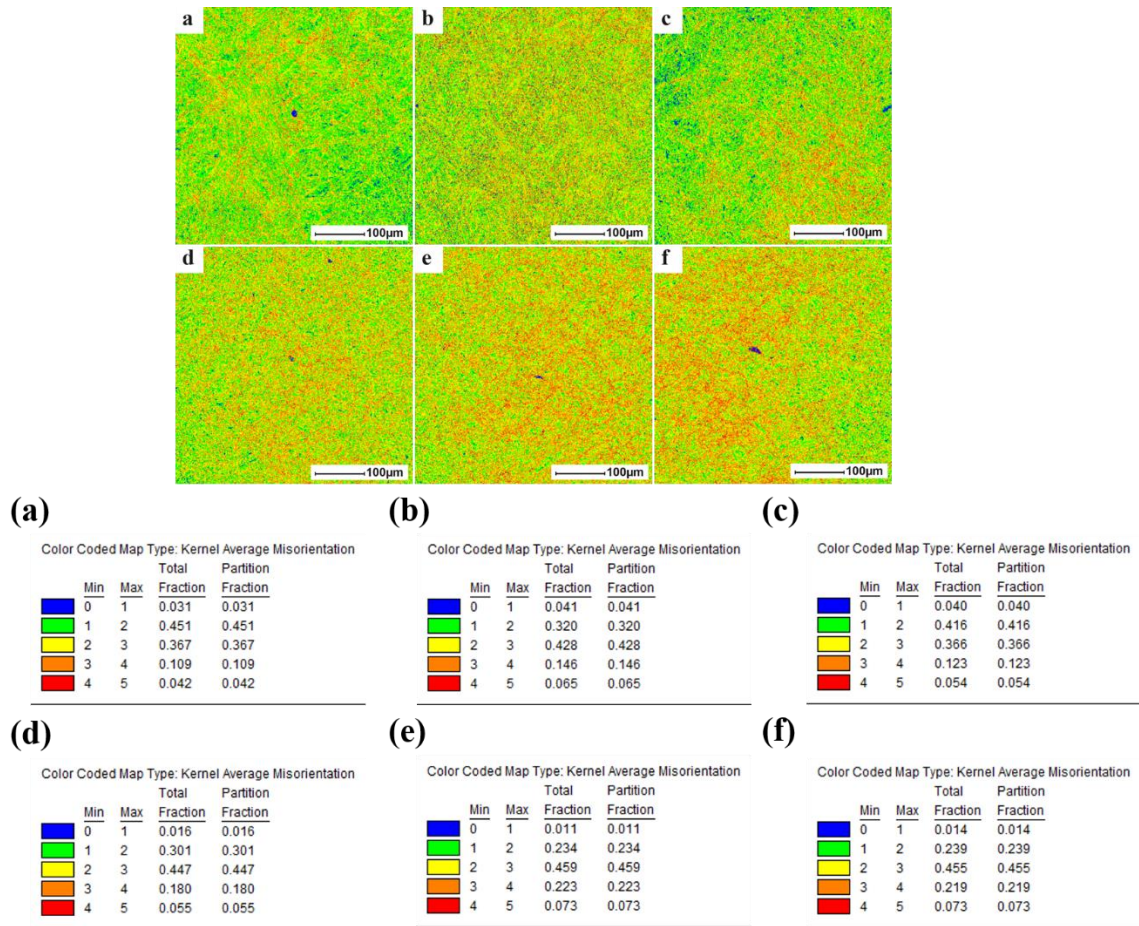


Fig 6. 19 KAM values of vertical and horizontal samples after dynamic compressive loading in different strain rates (a) Vertical- 460 s<sup>-1</sup>, b) Vertical- 810 s<sup>-1</sup>, c) Vertical-1100 s<sup>-1</sup>, d) Horizontal-615 s<sup>-1</sup>, e) Horizontal- 745 s<sup>-1</sup>, f) Horizontal- 890 s<sup>-1</sup>.

#### 6.4. Mathematical modeling

Two constitutive models were used to predict dynamic compressive performance of maraging steels produced by LPBF. The phenomenological Johnson-Cook [12] model and the micromechanically based Voyiadjis and Abed [13] model have been used for the illustration of the dynamic reaction of materials previously. Voyiadjis and Abed's model is a kind of constitutive relation derived from thermal activation analysis, which is similar

to the Zerilli-Armstrong [31], Nemat-Nasser [32] and Meyers [33] models. In these models, dislocation interaction mechanisms for different crystal structures are related to material performance under dynamic loading. Voyiadjis and Abed's model was chosen for this study because unlike other dislocation-based models, the Voyiadjis and Abed model considers the effect of dislocation density rate.

#### 6.4.1. Johnson-Cook model

Johnson-Cook was used in this study to predict the performance of vertically and horizontally built maraging steels during the dynamic compression test. The well established Johnson-Cook equation relates flow stress with competition between temperature, strain and strain rate. The model was used for vertical samples deformed at strain rates of  $1100 \text{ s}^{-1}$  and  $1300 \text{ s}^{-1}$ . For horizontal samples, strain rates of  $890 \text{ s}^{-1}$  and  $2200 \text{ s}^{-1}$  were used for the analysis. In the J-C model, von Mises flow stress is expressed as [12]:

$$\sigma = (A + B\varepsilon^n)(1 + C \ln \varepsilon'^*)(1 - T^{*m}) \quad (6-8)$$

where  $\varepsilon'^* = \varepsilon'/\varepsilon_0'$  is plastic strain rate and  $\varepsilon_0'$  is the reference strain rate, which for vertical samples was considered  $1000 \text{ s}^{-1}$  and for horizontal samples, was considered  $800 \text{ s}^{-1}$ . The first part of the equation  $(A + B\varepsilon^n)$  represents the strain hardening effect of the true plastic curve and the second part of the equation  $(1 + C \ln \varepsilon'^*)$  describes the strain rate hardening behaviour, and third part is related to thermal softening in the material as it is plastically deformed. B is the hardening modulus (MPa), n is work hardening coefficient,

C is the strain rate sensitivity coefficient, A is the yield strength (MPa), and m is the temperature index [12].

$T^* = (T - T_r)/(T_m - T_r)$  is the equivalent temperature in which  $T_r$  is the reference temperature which was considered to be 273K, and  $T_m$  is the melting point of maraging steel, which is 1723K. As discussed before, for the dynamic compression test, temperature enhancement in the material can be determined using equation 7.

The model constants for each sample were determined and shown in Table 6.5. As listed in Table 6.6., as the strain rate increases, work hardening coefficient (n) and hardening modulus (B) decreases for both vertical and horizontal samples. Work hardening is an indication of dislocation multiplication. Xu *et al.* [34] described that work hardenability decreased with the strain rate increment ascribed to the dominant effect of thermal softening at high strain rates. Indeed, as Tihamiyu [18] stated the strain hardening rates dropped as a consequence of excessive thermal softening leading to thermomechanical instability.

It should be noted that the work hardening coefficient in the vertical samples is lower than that for horizontal samples, which is consistent with the dominance of thermal softening, as observed in Fig 6.4. and Fig 6.5., and also the increased probability of ASBs formation in vertical samples. Indeed, the sharp fall in flow stress after peak (Fig. 6.4.) in vertical samples occurs as a consequence of dropping in load-carrying capacity in consequence of the accumulation of heat and thermal softening. Furthermore, horizontal samples showed less tendency to develop ASBs, which is consistent with their higher work hardening coefficients. The higher susceptibility of vertical samples to thermal softening and formation of ASB leads to fracture at lower strain rates as compared to horizontal samples.

Table.6. 6. Determined values of J-C model parameters.

Sample	A (MPa)	B(MPa)	n	C	m
<b>Vertical-1100 s<sup>-1</sup></b>	500	3600	0.2	0.25	1
<b>Vertical 1300 s<sup>-1</sup></b>	700	2855	0.089	0.268	0.38
<b>Horizontal-890 s<sup>-1</sup></b>	1820	4070	0.3	0.245	1.7
<b>Horizontal-2200 s<sup>-1</sup></b>	300	2950	0.25	0.97	1

Comparison between model prediction and experimental data of vertical and horizontal samples are shown in Fig 6.20. A good match between the presented model and experimental data is noticeable.

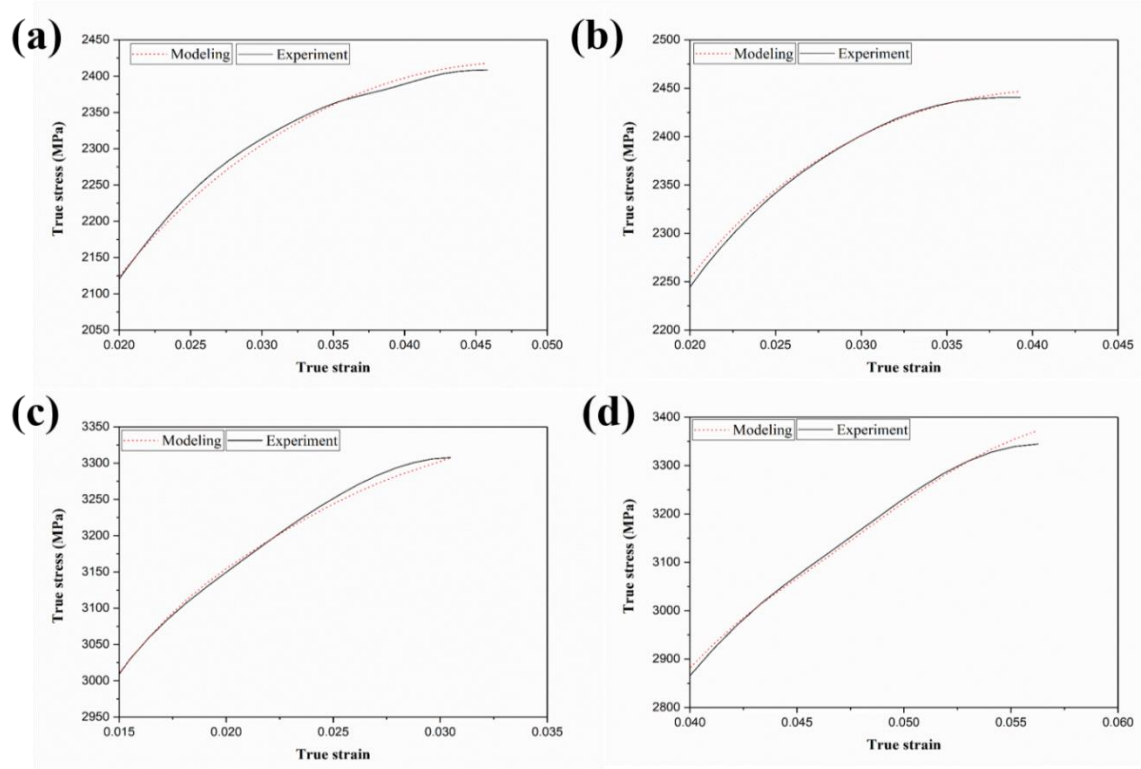


Fig 6. 20 Comparison between the tested flow stress curves and the J-C model description for (a) Vertical-1100 s<sup>-1</sup>, (b) Vertical-1300 s<sup>-1</sup>, (c) Horizontal-890 s<sup>-1</sup>, (d) Horizontal-2200 s<sup>-1</sup>.

### 6.4.2. Voyiadjis-Abed model

In maraging steel with BCC structure, obstacles to dislocation motion can be divided into long-range and short-range barriers. Long-range barriers include grain boundaries, twin boundaries which can not be controlled by thermal activation (athermal) [13]. Short-range barriers are such as alloy elements, defects, impurities which can be controlled by thermal activation (thermal). It should be noted that the deformation mechanism of BCC metals is inferred from the dislocations disobedient to Peierls barriers (short-range barriers) [13]. The constitutive relation of Voyiadjis-Abed is obtained through the following equation [13]:

$$\sigma = Y^{\wedge} \left( 1 - \left( 1 - (B_1 T - B_2 T \ln \epsilon')^{\frac{1}{q}} \right)^{\frac{1}{p}} + B \epsilon^n + Y_a \right) \quad (6-9)$$

where  $p$  and  $q$  are the constants describing the shape of short-range barriers and can be obtained from the Kocks study [35]. When material is deformed beyond the elastic limit, dislocations start proceeding along the crystal.  $B_1$  and  $B_2$  are related to dislocation density and dislocation velocity. Furthermore,  $Y^{\wedge}$  is the yield stress of the Peierls barrier to dislocation motion.  $Y_a$  represents the athermal constituent of the initial yield stress, which is considered to be 1000. The temperature ( $T$ ) in high speed deformation can be calculated by equation 7.

$B \epsilon^n + Y_a$  illustrate the athermal constituent of the flow stress, and the first part illustrate the thermal constituent of the flow stress. In BCC metals, hardening is independent of both strain rate and temperature [13]. It can be observed in Table 6.7. that hardening parameters

changed significantly from test to test, and parameters related to the thermal constituent of flow stress remain approximately constant.

Table.6. 7. Determined values of V-A model parameters.

Sample	$Y^{\wedge}$	B1	B2	q	p	B	n
<b>Vertical-1100 s<sup>-1</sup></b>	2000	0.0020	0.000090	2	0.55	3800	0.4
<b>Vertical 1300 s<sup>-1</sup></b>	2150	0.0020	0.000090	1	0.4	3100	0.4
<b>Horizontal-890 s<sup>-1</sup></b>	1500	0.0020	0.000090	2	0.15	4350	0.18
<b>Horizontal-2200 s<sup>-1</sup></b>	3000	0.0020	0.000090	1	0.1	20800	0.75

The comparisons illustrated in Fig. 21 express high compatibility acceptance with the theoretical model and the experimental data.

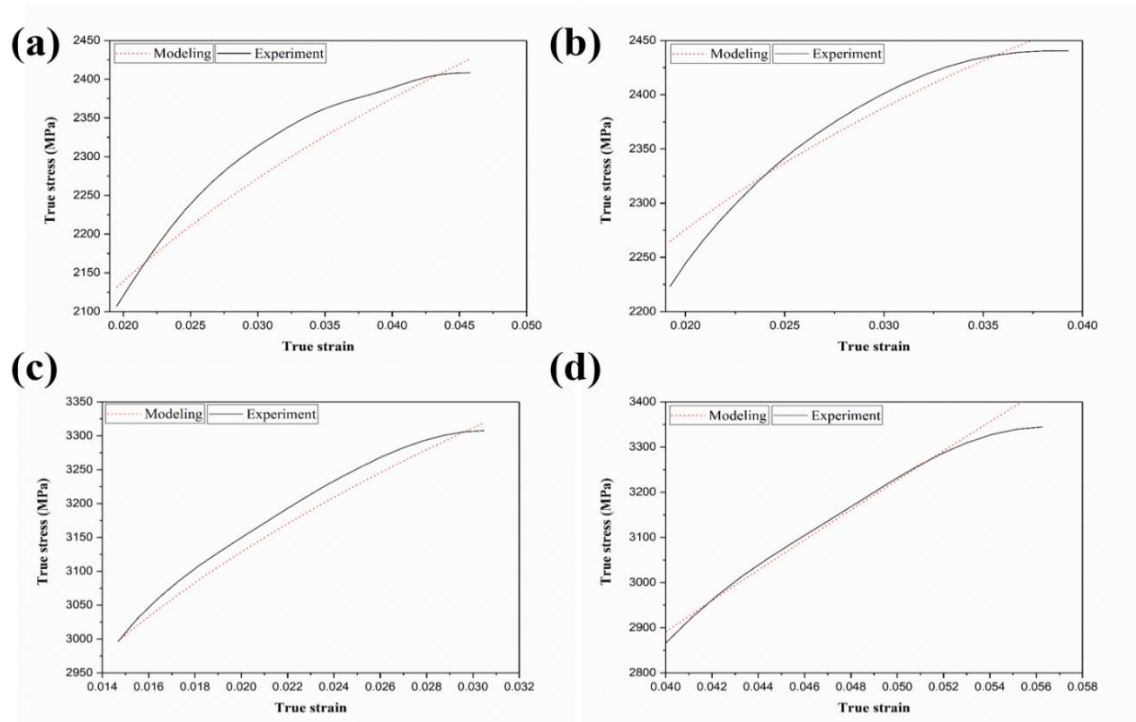


Fig 6. 21 Comparison between the tested flow stress curves and the V-A model description for (a) Vertical-1100 s<sup>-1</sup>, (b) Vertical-1300 s<sup>-1</sup>, (c) Horizontal-890 s<sup>-1</sup>, (d) Horizontal-2200 s<sup>-1</sup>.

Considering Fig 6.21, it is inferred that the physically based model (Voyiadjis-Abed model) is more suitable for higher strain rates compared to low strain rates as a better fit can be observed in those strain rate regimes.

## 6.5. Conclusion

The effect of building orientation on high strain rate compressive performance of maraging steel samples produced by LPBF was investigated using Split Hopkinson pressure bar (SHPB) apparatus. Heat-treated vertical and horizontally built maraging steel samples were subjected to dynamic compressive loading at different strain rates. The followings are some of the main findings of the current study:

- When deformed at high speed loading, the materials exhibit a behavior showing the possibility of unstable plastic flow leading to intense shear strain localization followed by fracture.
- Horizontal samples fragmented at strain rate of  $2200 \text{ s}^{-1}$ . However, in the case of the vertical samples, failure happened at strain rate of  $1300 \text{ s}^{-1}$ .
- Correlation between microstructural characteristics and mechanical performance showed that vertical samples, which consist mainly of columnar grains, are more susceptible to adiabatic shear band (ASBs) and crack formation, and they showed lower dynamic strength.
- Texture studies proved that Cube texture component evolved in vertical samples due to the presence of columnar grains, which was substituted with the E texture component after high strain-rate loading.

- In horizontal samples, which consist of equiaxed grains, no preferred orientation was detected at low strain rates. However, the evolution of the E texture component at high strain rates is attributed to compression loading was observed.
- Cube texture in vertical samples led to lower strength of these samples. Besides, the TEM studies showed that in vertical samples, growth and elongation of precipitates occurred, which is another cause for the lower strength of the vertical samples.
- Mathematical modeling of the vertical and horizontal samples' high strain-rate dynamic performance was carried out. Johnson-Cook and Voyiadjis and Abed models were utilized to predict the flow stress of this alloy. Fair simulation of plastic behavior under dynamic compressive loading was noted for both horizontal and vertical samples.

## 6.5. References

- [1] J.P. Oliveira, A.D. LaLonde, J. Ma, Processing parameters in laser powder bed fusion metal additive manufacturing, *Materials & Design*. 193 (2020) 108762.
- [2] S.L. Sing, W.Y. Yeong, Laser powder bed fusion for metal additive manufacturing: perspectives on recent developments, *Virtual and Physical Prototyping*. 15 (2020) 359–370.
- [3] C. Tan, K. Zhou, W. Ma, P. Zhang, M. Liu, T. Kuang, Microstructural evolution, nanoprecipitation behavior and mechanical properties of selective laser melted high-

performance grade 300 maraging steel, *Materials and Design*. 134 (2017) 23–34.  
<https://doi.org/10.1016/j.matdes.2017.08.026>.

- [4] S. Shamsdini, H. Pirgazi, M.H. Ghoncheh, M. Sanjari, B.S. Amirkhiz, L. Kestens, M. Mohammadi, A relationship between the build and texture orientation in tensile loading of the additively manufactured maraging steels, *Additive Manufacturing*. 41 (2021) 101954.
- [5] S. Dehgahi, M. Sanjari, M.H. Ghoncheh, B.S. Amirkhiz, M. Mohammadi, Concurrent improvement of strength and ductility in heat-treated C300 maraging steels produced by laser powder bed fusion technique, *Additive Manufacturing*. (2021) 101847.
- [6] S. Dehgahi, M.H. Ghoncheh, A. Hadadzadeh, M. Sanjari, B.S. Amirkhiz, M. Mohammadi, The role of titanium on the microstructure and mechanical properties of additively manufactured C300 maraging steels, *Materials & Design*. (2020) 108965.
- [7] J. Mutua, S. Nakata, T. Onda, Z.C. Chen, Optimization of selective laser melting parameters and influence of post heat treatment on microstructure and mechanical properties of maraging steel, *Materials and Design*. 139 (2018) 486–497.  
<https://doi.org/10.1016/j.matdes.2017.11.042>.
- [8] Y. Bai, D. Wang, Y. Yang, H. Wang, Effect of heat treatment on the microstructure and mechanical properties of maraging steel by selective laser melting, *Materials Science and Engineering A*. 760 (2019) 105–117. <https://doi.org/10.1016/j.msea.2019.05.115>.
- [9] R. Alaghmandfard, C. Dharmendra, A.G. Odeshi, M. Mohammadi, Dynamic mechanical properties and failure characteristics of electron beam melted Ti-6Al-4V under high strain rate impact loadings, *Materials Science and Engineering: A*. 793 (2020) 139794.

- [10] B. Mooney, K.I. Kourousis, R. Raghavendra, Plastic anisotropy of additively manufactured maraging steel: Influence of the build orientation and heat treatments, *Additive Manufacturing*. 25 (2019) 19–31. <https://doi.org/10.1016/j.addma.2018.10.032>.
- [11] S. Dehgahi, R. Alaghmandfard, J. Tallon, A. Odeshi, M. Mohammadi, Microstructural evolution and high strain rate compressive behavior of as-built and heat-treated additively manufactured maraging steels, *Materials Science and Engineering: A*. 815 (2021) 141183.
- [12] G.R. Johnson, A constitutive model and data for materials subjected to large strains, high strain rates, and high temperatures, *Proc. 7th Int. Sympo. Ballistics*. (1983) 541–547.
- [13] G.Z. Voyiadjis, F.H. Abed, Microstructural based models for bcc and fcc metals with temperature and strain rate dependency, *Mechanics of Materials*. 37 (2005) 355–378.
- [14] E.O.S.N.I.D. Sheet, EOS GmbH-Electro Optical Systems, (2014).
- [15] Y. Xu, J. Zhang, Y. Bai, M.A. Meyers, Shear localization in dynamic deformation: microstructural evolution, *Metallurgical and Materials Transactions A*. 39 (2008) 811–843.
- [16] A.A. Tihamiyu, A.G. Odeshi, J.A. Szpunar, Multiple strengthening sources and adiabatic shear banding during high strain-rate deformation of AISI 321 austenitic stainless steel: Effects of grain size and strain rate, *Materials Science and Engineering: A*. 711 (2018) 233–249.
- [17] H. Beladi, I.B. Timokhina, Y. Estrin, J. Kim, B.C. De Cooman, S.K. Kim, Orientation dependence of twinning and strain hardening behaviour of a high manganese twinning

induced plasticity steel with polycrystalline structure, *Acta Materialia*. 59 (2011) 7787–7799.

- [18] A.A. Tihamiyu, A.Y. Badmos, A.G. Odeshi, J.A. Szpunar, The influence of temper condition on adiabatic shear failure of AA 2024 aluminum alloy, *Materials Science and Engineering: A*. 708 (2017) 492–502.
- [19] A. Pineau, A.A. Benzerga, T. Pardoen, Failure of metals I: Brittle and ductile fracture, *Acta Materialia*. 107 (2016) 424–483. <https://doi.org/10.1016/j.actamat.2015.12.034>.
- [20] P. Bajaj, A. Hariharan, A. Kini, P. Kürnsteiner, D. Raabe, E.A. Jäggle, Steels in additive manufacturing: A review of their microstructure and properties, *Materials Science and Engineering A*. 772 (2020) 138633. <https://doi.org/10.1016/j.msea.2019.138633>.
- [21] T. Bhardwaj, M. Shukla, Effect of laser scanning strategies on texture, physical and mechanical properties of laser sintered maraging steel, *Materials Science and Engineering A*. 734 (2018) 102–109. <https://doi.org/10.1016/j.msea.2018.07.089>.
- [22] T. Allam, K.G. Pradeep, P. Köhnen, A. Marshal, J.H. Schleifenbaum, C. Haase, Tailoring the nanostructure of laser powder bed fusion additively manufactured maraging steel, *Additive Manufacturing*. 36 (2020) 101561.
- [23] M.C. Jo, S. Kim, D.W. Kim, H.K. Park, S.S. Hong, H.K. Kim, H.S. Kim, S.S. Sohn, S. Lee, Understanding of adiabatic shear band evolution during high-strain-rate deformation in high-strength armor steel, *Journal of Alloys and Compounds*. 845 (2020) 155540.
- [24] A.R. Oliveira, J.A.A. Diaz, A.D.C. Nizes, A.L. Jardini, E.G. Del Conte, Investigation of Building Orientation and Aging on Strength–Stiffness Performance of Additively

- Manufactured Maraging Steel, *Journal of Materials Engineering and Performance*. (n.d.) 1–11.
- [25] M. Garibaldi, I. Ashcroft, M. Simonelli, R. Hague, Metallurgy of high-silicon steel parts produced using Selective Laser Melting, *Acta Materialia*. 110 (2016) 207–216.
- [26] W.F. Hosford, *Mechanical behavior of materials*, Cambridge university press, 2010.
- [27] M. Masoumi, I.F. de Barros, L.F.G. Herculano, H.L.F. Coelho, H.F.G. de Abreu, Effect of microstructure and crystallographic texture on the Charpy impact test for maraging 300 steel, *Materials Characterization*. 120 (2016) 203–209.
- [28] G.R. Canova, C. Fressengeas, A. Molinari, U.F. Kocks, Effect of rate sensitivity on slip system activity and lattice rotation, *Acta Metallurgica*. 36 (1988) 1961–1970.
- [29] N.P. Gurao, R. Kapoor, S. Suwas, Texture evolution in high strain rate deformed Cu–10Zn alloy, *Materials Science and Engineering: A*. 558 (2012) 761–765.
- [30] H. Li, E. Hsu, J. Szpunar, H. Utsunomiya, T. Sakai, Deformation mechanism and texture and microstructure evolution during high-speed rolling of AZ31B Mg sheets, *Journal of Materials Science*. 43 (2008) 7148–7156.
- [31] F.J. Zerilli, R.W. Armstrong, Dislocation-mechanics-based constitutive relations for material dynamics calculations, *Journal of Applied Physics*. 61 (1987) 1816–1825.
- [32] S. Nemat-Nasser, J.B. Isaacs, Direct measurement of isothermal flow stress of metals at elevated temperatures and high strain rates with application to Ta and TaW alloys, *Acta Materialia*. 45 (1997) 907–919.

- [33] M.A. Meyers, D.J. Benson, O. Vöhringer, B.K. Kad, Q. Xue, H.-H. Fu, Constitutive description of dynamic deformation: physically-based mechanisms, *Materials Science and Engineering: A*. 322 (2002) 194–216.
- [34] Z. Xu, F. Huang, Plastic behavior and constitutive modeling of armor steel over wide temperature and strain rate ranges, *Acta Mechanica Solida Sinica*. 25 (2012) 598–608.
- [35] U.F. Kocks, Realistic constitutive relations for metal plasticity, *Materials Science and Engineering: A*. 317 (2001) 181–187.

## **Chapter 7: Influence of composition on mechanical and corrosion behavior of L-PBF maraging steel**

### **7.1. Introduction**

Maraging steel C300 (yield strength of 300 ksi) is a member of low carbon precipitation hardening martensitic steel, which is primarily alloyed with Ni, Mo, and Co. Due to a combination of high strength and ductility, C300 has been considered to be an excellent material for aircraft, aerospace, military, and tooling applications[1].

Additive manufacturing (AM) is one of the fast-developing technologies that involves layer-by-layer buildup of parts. It allows for the fabrication of complex geometries without elaborate tooling to produce near net-shaped components. Numerous innovative AM methods are available today, and the laser powder bed fusion (LPBF) technique is one of the best-known AM methods to fabricate parts through laser melting [2]. In addition, the lack of carbon in C300 leads to good weldability and therefore makes this material a preferred candidate for the LPBF process resulting in a widespread application of LPBF maraging steel parts in the industry[1][3][4]. Nevertheless, the high cooling and rapid solidification process that occur during the LPBF process results in a microstructure that is usually different from conventional counterparts [3]. Most of the variation in the microstructure of the LPBF maraging steel induced during the process could significantly influence their mechanical and corrosion performance.

A few research studies have been conducted on the dynamic mechanical behavior of LPBF fabricated maraging steel parts [4][5]. The evaluation of mechanical performance in dynamic compressive conditions similar to those that occurred in car crashes and bird

strikes in airplanes, where applied strain rates can be of the order of  $10^2$  to  $10^4$   $s^{-1}$ , needs to be investigated [6] [7]. The study of the dynamic compressive behavior of metals at high strain rates commonly involves the use of the Split Hopkinson Pressure Bar technique (SHPB) developed by Kolsky [8]. There are many studies on AM parts in which the dynamic mechanical properties were tested using a SHPB apparatus [9][10]. In our previous study, the high strain rate compressive behavior of LPBF-maraging steel in as-built and heat-treated conditions was investigated using SHPB [10]. It was observed that as-built samples fragmented at strain rate of  $3500$   $s^{-1}$ , while the heat-treated samples fractured at the strain rate of  $1930$   $s^{-1}$  due to lower ductility corresponding to the evolution of precipitates with the heat-treatment condition. The role of titanium, one of the main alloying elements, has been studied on the quasi-static mechanical properties of C300 in our previous work [11]. Recently, our team produced C300 parts with excellent mechanical properties with the increase of titanium content [12]. However, the effect of titanium on mechanical performance of C300 parts fabricated by LPBF process under high strain rate dynamic compressive loading has not been studied.

Depending upon the actual service environment, LPBF maraging steel parts may be subjected to a corrosive environment in the presence of external loading, which may shorten its service life in various industrial applications. Accordingly, investigation on corrosion resistance of maraging steel has received a considerable amount of attention. Only a few studies on electrochemical corrosion behavior of maraging steels fabricated by AM process and their correlation with microstructures have been reported. Bouzakis *et al.* [13] conducted research on corrosion fatigue of AM maraging steels. They observed that AM parts showed lower corrosion fatigue performance due to cellular-dendritic structure

and multiple melt pools. The effect of reverted austenite on corrosion behavior of 18Ni 300 maraging steel fabricated by AM process was also studied by Avelino *et al.* [14]. Their findings indicated reverted austenite formed during heat treatment has a detrimental impact on corrosion resistance of the alloy. A similar corrosion behavior was also observed in hydrofluoric acid (HF) medium for 300 and 350 grade of maraging steels [15]. Their results showed that solution annealing improved the corrosion performance. In addition, researchers postulated that higher amount of cobalt and titanium in grade 350 maraging steel leads to the formation of precipitates resulting in the formation of micro-galvanic cell, which deteriorate corrosion resistance of the maraging parts [15]. The combination of dynamic loading condition and corrosive environment could induce environmentally induced crack propagation known as stress corrosion cracking (SCC). The SCC behavior of maraging steels was attributed to the role of hydrogen in relationship with the presence of precipitates, dislocations, and austenite grains [16].

The present study correlates the dynamic mechanical and corrosion properties of LPBF C300 maraging steels in relation to titanium content (an important alloying element) for the first time. In order to understand the role of titanium content on dynamic mechanical performance as well as corrosion behavior, samples with two different contents of titanium were fabricated through LPBF. The LPBF C300 components were exposed to external dynamic compressive loading using SHPB apparatus. The aim is also to determine the way different contents of titanium affect the dynamic compressive and corrosion performance of the LPBF C300 maraging steel parts.

## 7.2. Material and methods

### 7.2.1. Material and process parameters

Two gas atomized maraging steel powders with two different titanium contents (0.72 and 1.17 wt. % Ti) were used for the L-PBF process. The chemical composition of the powders with different titanium contents are abbreviated as High-Ti and Low-Ti and presented in Table 7.1. An EOS M290 machine, was used in this study to manufacture the C300 maraging steel samples. The process parameters of the LPBF system are provided in Table 7.2. The same process parameters and scan strategy (strip scanning pattern *i.e.*, the laser beam was rotated  $67^\circ$  after each step layer deposition) were used to fabricate High-Ti and Low-Ti samples. Cylindrical rods having dimensions of  $\Phi$  12 mm  $\times$  120 mm were deposited vertically (perpendicular to the laser scan path) for this study. Test samples were cut into cylinders of  $\Phi$  7mm  $\times$  8mm to carry out the high strain-rate compression tests.

Table 7. 1. Chemical composition of two C300 powders used for this study.

Elements (wt.%)											
	Ni	Co	Mo	Ti	Si	Mn	C	Al	S	P	Cr
Low-Ti	17.98	8.85	4.85	0.72	0.09	0.06	0.016	0.09	0.008	-	0.15
High-Ti	17.68	9.26	4.82	1.17	0.06	0.03	0.012	0.11	0.011	-	0.11

Table 7. 2. Process parameters of the L-PBF process.

Laser power (W)	Scanning speed (mm/s)	Layer thickness ( $\mu$ m)	Hatch distance ( $\mu$ m)
285	960	40	110

### 7.2.2. Dynamic compression loading on Split Hopkinson pressure bar

A Split Hopkinson Pressure Bar (SHPB) apparatus was used to investigate the high strain-rate compressive behavior of the LPBF-managing steel samples as described in our previous paper [17]. The conventional SHPB system consists of five major elements namely: (1) incident and transmitted steel bars, (2) a fixture system to allow free axial movement of the bars, (3) a projectile bar, which is fired by a compressed gas gun and generates elastic waves on striking the incident bar, (4) axial strain gauges connected to the input and out bars to capture the elastic waves propagating through the bars, (5) a data acquisition system to condition and amplify the elastic wave signals capture by the strain gages as incident and reflected waves (through the input bar), and the transmission waves (through the output bar). The elastic wave signals are used for calculating of nominal strain rate ( $\epsilon'(t)$ ), strain( $\epsilon(t)$ ), and stress ( $\sigma(t)$ ) values using equations (1) to (3), respectively [9]:

$$\sigma(t) = \left(\frac{A_B}{A_S}\right) \cdot E_B \cdot \epsilon_T \quad (7-1)$$

$$\epsilon(t) = \left(-2 \frac{C_B}{L_S}\right) \cdot \int_0^t \epsilon_R \cdot dt \quad (7-2)$$

$$\epsilon'(t) = \left(-2 \frac{C_B}{L_S}\right) \cdot \epsilon_R \quad (7-3)$$

where  $A_B$  and  $A_S$  are the initial cross-sectional area of the bars and specimen, respectively  $L_S$  is the initial length of the test specimen and  $C_B$  is the elastic wave velocity in the bars.  $E_B$  is Young's modulus of the bar material.  $\epsilon_T$  is transmitted signal and  $\epsilon_R$  is reflected signal. Each experiment at each strain rate was conducted three times to ensure repeatability. True stress ( $\sigma_t$ ), strain ( $\epsilon_t$ ) and strain rate ( $\epsilon'_t$ ) values were calculated with the following equations C[10].

$$\sigma_t = \sigma(t)(1 - \varepsilon(t)) \quad (7-4)$$

$$\varepsilon_t = -\ln(1 - \varepsilon(t)) \quad (7-5)$$

$$\dot{\varepsilon}_t = \varepsilon'(t)/(1 - \varepsilon(t)) \quad (7-6)$$

### 7.2.3. Electrochemical measurements

The corrosion behavior of both deformed (under high strain-rate compressive loading) and undeformed LPBF C300 samples was evaluated using the electrochemical tests. The Low- and High-Ti samples were used for the electrochemical tests and were mounted in epoxy resin, with the exposed area of the electrodes being about 0.4 to 1cm<sup>2</sup>. The sample surfaces were mechanically grounded using silicon carbide (SiC) paper down to 4000 grades, then polished with diamond paste down to 1 μm. After polishing, specimens were rinsed using distilled water and absolute ethanol. The Gamry potentiostat/galvanostat model reference 600+ was used to conduct the electrochemical measurements using the conventional three-electrode cell at room temperature in 3.5 wt. % NaCl solution. A saturated Ag/AgCl electrode served as the reference electrode and a graphite rod as the counter electrode in this study. Electrochemical tests were carried out using electrochemical impedance spectroscopy (EIS) and potentiodynamic polarization measurements. Before the electrochemical tests, the open circuit potential (OCP) trend was measured to achieve a stable value, indicating the system's stability. The EIS tests were conducted by applying 10 mV /AC sinusoidal perturbation potential with the frequency ranging from 100 kHz to 0.01 Hz after an immersion time of 24 h, 10 points per decade at OCP. The EIS results were analyzed using Z-view software.

The potentiodynamic tests were carried out at a scanning rate of 0.167 mV/s from 500 mV below the OCP to an anodic potential of 1500 mV above the OCP. All the electrochemical results obtained in this study are reproducible and are representative of the multiple measurements.

#### 7.2.4. Microstructure analysis

A Hitachi SU-70 Field Emission Gun (FEG) ultra-high-resolution scanning electron microscope (FE - SEM) was used for microstructural studies. Impacted samples were cut along the compression direction and were used for the SEM studies, as shown in Fig 7.1. All the selected areas were ground, mechanically polished, and then etched by Nital 3% (3 ml HNO<sub>3</sub> + 97 ml ethanol) as the etchant. Post corrosion observations were carried with the same scanning electron microscope and parameters.

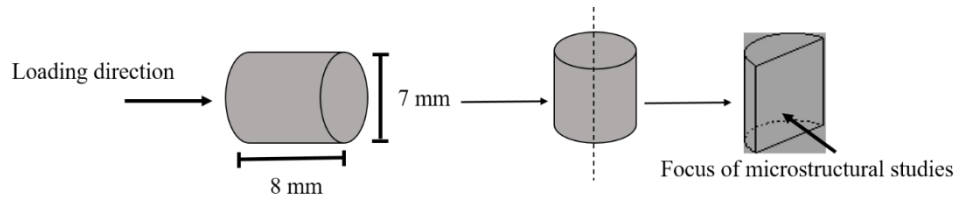


Fig 7. 1 Schematic of compression samples used for SEM studies.

### 7.3. Results and discussion

#### 7.3.1. Dynamic impact behavior of Low-Ti C300 maraging steel

The dynamic behavior of Low-Ti maraging steel samples tested in SHPB at different strain rates are presented in Figs 7.2-4. Firing pressures of 100 kPa, 120 kPa, 140 kPa, 170 kPa, and 200 kPa generated strain rates of 1500 s<sup>-1</sup>, 1950 s<sup>-1</sup>, 2770 s<sup>-1</sup>, 3150 s<sup>-1</sup>, and 3670 s<sup>-1</sup> in the specimens respectively (Fig 7.2.). Moreover, the maximum value of strain rate is

considered as nominal strain rate in this study. At the start, strain rate increased rapidly and it reached a plateau followed by a constant strain rate at the second part of the curves (Fig 7.2.). This behavior could be attributed to a competition between strain hardening and strain softening [9]. Also, the sudden drop in the strain rate-strain curves towards the end of the curves is due to the exhaust of the impact energy [18].

The true strain–stress curves of the LPBF Low-Ti maraging steel samples are presented in Fig 7.3. Table 7.3. shows the results of dynamic impact tests on Low-Ti samples at different strain rates. It is noted that, the loading pulses up to the strain rate of  $3150 \text{ s}^{-1}$  were not sufficient to cause failure of Low-Ti samples. It can be observed that, the dynamic strength increases with an increase in strain rate. This trend could be attributed to the massive multiplication of dislocations and mutual interaction between dislocations and grain refinement during dynamic loading [10]. At the beginning of the plastic region, the true stress rises to the maximum flow stress. This behavior indicates that a significant strain hardening occurred at the start of deformation. After the maximum peak flow stress, the dynamic curve falls and then rise again. This flow behavior suggests an intensive competition between strain hardening and thermal softening. Thermal softening occurs due to the conversion of impact energy into thermal energy, which leads to an increase in the sample temperature resulting in thermomechanical instability and loss of load-carrying capacity. Also, the dynamic curves of the samples impacted at strain rates of 2770, 3150 and  $3670 \text{ s}^{-1}$  show two distinct peaks of flow stress as evidence of thermal softening. Furthermore, it was found that strain increases with an increase in strain rate, which can be related to thermal softening, which becomes more intense at higher strain rates. Eq. (7) is used to calculate the temperature rise in the specimen during plastic deformation [9]:

$$\Delta T = \left( \frac{\beta}{\rho C_P} \right) \cdot \int \sigma \cdot d\epsilon \quad (7-7)$$

where  $\beta$  is the amount of plastic deformation energy that converts to heat, and it is assumed to be 90% [9].  $\sigma$  and  $\epsilon$  are effective stress and strain, respectively.  $\rho$  is the density of maraging steel, which is  $8 \text{ g/cm}^3$ , and  $C_p$  is the specific heat, which is  $450 \pm 20 \text{ J/kg}^\circ\text{C}$  for maraging steel. The integral term is toughness or the area under the true stress- true strain curve. The temperature rise in the samples (Table 7.3.) calculated by Eq. (7) indicates an increasing temperature rise with an increasing strain rate. Therefore, the thermal softening as a result of increased specimens' temperature becomes dominated in the dynamic curves. Besides, the domination of thermal softening during, localized adiabatic heating can occur in the specimen during dynamic loading results leading to thermomechanical instability and strain localization in narrow regions resulting in the formation of adiabatic shear bands (ASBs) [9]. Adiabatic shear bands are regions on intense strain localization in the deformed specimens. The rapid drop in flow stress observed in the stress-strain curves could be associated with the onset of ASBs. Many studies have been carried to understand the mechanism of formation of the adiabatic shear bands [19][20]. Hwang *et al.* [21] reported the occurrence of dynamic recrystallization in ultra-fine-grained low-carbon steels due to the rise in the adiabatic temperature during high strain rate deformation. They also concluded that the microstructure is prone to relaxation by thermally activated processes. Accordingly, the adiabatic temperature rises within the localized ASB impel the dynamic recrystallization, which results in the formation of some fine equiaxed grains. Furthermore, they stated that some elongated grains were formed near ASB which are subjected to

dynamic recovery (annihilation of dislocations). In addition, these grains can subsequently experience dynamic recrystallization at high strain rates.

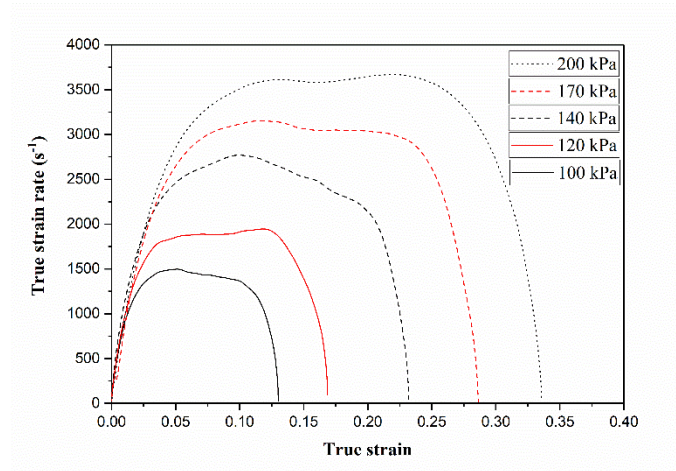


Fig 7. 2 Strain rate-strain curves of Low-Ti- maraging steel samples deformed using different firing pressures (kPa).

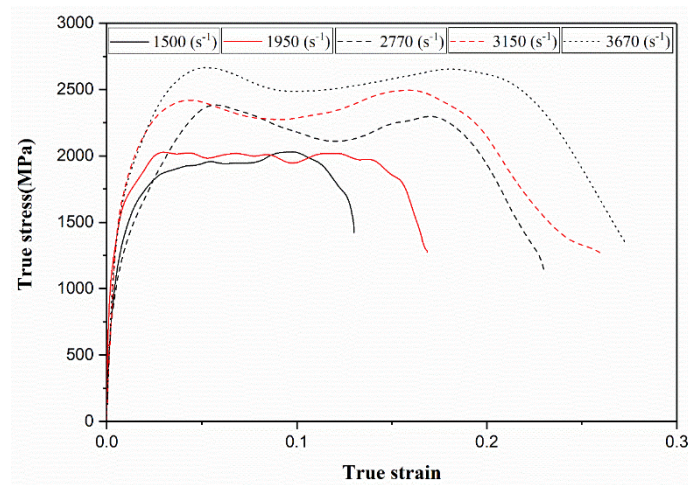


Fig 7. 3 Dynamic stress-strain curves of Low-Ti maraging steel samples in strain rates of 1500 to 3670 s<sup>-1</sup>.

Table 7. 3. Observations from the dynamic impact responses of Low-Ti maraging steel specimens

Pressure (KPa)	Strain rate (s <sup>-1</sup> )	Yield stress (MPa)	Maximum flow stress (MPa)	Total strain (%)	Toughness (MJ/m <sup>3</sup> )	Temperature rise (°C)
100	1500	1677.7	2030.5	13.1	237.4	59.3
120	1950	1869.9	2027.9	16.8	320.1	80.1
140	2770	2101.9	2384.8	23.1	466.5	116.6
170	3150	2197.3	2496.1	26.1	554.2	138.5
200	3670	2418.8	2665.2	27.3	648.4	162.1

Fig 7.4. shows the variation of strain hardening rate obtained from the true stress-strain curves of Low-Ti maraging steel. The strain hardening rate curves exhibits three distinct stages. At the first stage, strain hardening rate decreases and constant strain hardening rate occurred at the second stage. Then decrease of strain hardening rate is dominant at the third stage. The second stage shows balance between strain hardening and strain softening effects, and the third stage indicates the dominance of softening, which is related to temperature rise in the specimen [10].

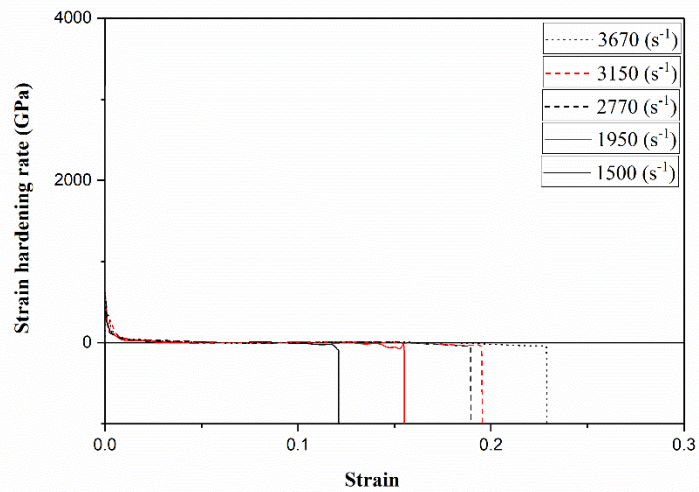


Fig 7. 4 Strain hardening rate vs. strain curves of Low-Ti maraging steel dynamically compressed at the strain rates of  $1500 \text{ s}^{-1}$ ,  $1950 \text{ s}^{-1}$ ,  $2770 \text{ s}^{-1}$ ,  $3150 \text{ s}^{-1}$ , and  $3670 \text{ s}^{-1}$ .

### 7.3.2. Dynamic impact behavior of High-Ti C300 maraging steel

Fig 7.5. shows the strain rates generated in the High-Ti maraging steel specimens for various firing pressures of the striker. Firing pressures of 100 kPa, 120 kPa, 160 kPa, 170 kPa, 180 kPa, and 200 kPa generated strain rates of  $1500 \text{ s}^{-1}$ ,  $2000 \text{ s}^{-1}$ ,  $2900 \text{ s}^{-1}$ ,  $3000 \text{ s}^{-1}$ ,  $3600 \text{ s}^{-1}$ , and  $5000 \text{ s}^{-1}$  in the High-Ti alloy. It is noted that, firing pressure of 200 kPa can create a strain rate of  $3670 \text{ s}^{-1}$  for the dynamic loading on the Low-Ti samples, while the same firing pressure generated a strain rate of  $5000 \text{ s}^{-1}$  in the High-Ti specimens. Fig 7.6. shows the true stress-strain curves of dynamically loaded High-Ti samples. High-Ti dynamically loaded at the strain rate of  $5000 \text{ s}^{-1}$  did fracture. Table 7.4. shows the mechanical data for the High-Ti sample under dynamic impact loading. At the beginning of the stress-strain curves, samples exhibited rapid strain hardening followed by more gradual hardening to reach the maximum flow stress. Finally, the drop in stress-strain

curves towards the end of the curves was observed. The rising and falling of stress-strain curves are related to the competition between strain hardening and thermal softening [9]. Strain hardening corresponds to the generation of dislocations, and thermal softening is associated with the annihilation of dislocations [9]. From these observations (Fig 7.6. and Table 7.4.), it is noticeable that the maximum flow stress does not change significantly with an increase in strain rate, which is related to the presence of CoNi precipitates in High-Ti samples [12]. In our previous study on the effect of Ti addition on the microstructure of C300, it was shown that CoNi precipitates exist in High-Ti samples [12]. It is stated that, the dislocation density increases with an increase in strain rate [9], and CoNi precipitates are suitable areas for the accumulation of dislocations. With the increase of dislocations density, dislocations accumulate at precipitates. Accumulation of dislocations and temperature increase can promote dislocation annihilation at a higher strain rate and as a result, maximum flow stress does not change. The effect of dislocations and precipitates, the temperature rise during the high strain rate leads to partial annihilation of dislocations leading softening. Therefore, a competition between the generation of dislocations and their annihilation at higher strain rates, accounts for the dynamic strength of High-Ti samples becoming constant [10][17]. Furthermore, it is noticeable that, with an increase in the strain rate, the total strain increases to a maximum value of 43% at the strain rate of  $5000 \text{ s}^{-1}$ .

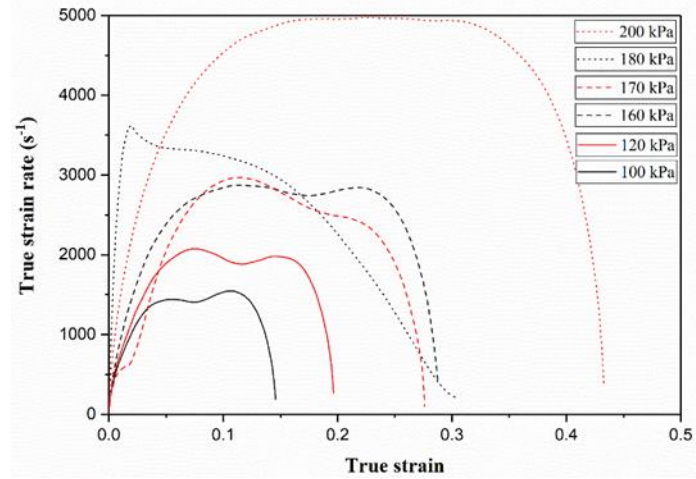


Fig 7. 5 Strain rate-strain curves of High-Ti maraging steel samples deformed using different firing pressures (kPa).

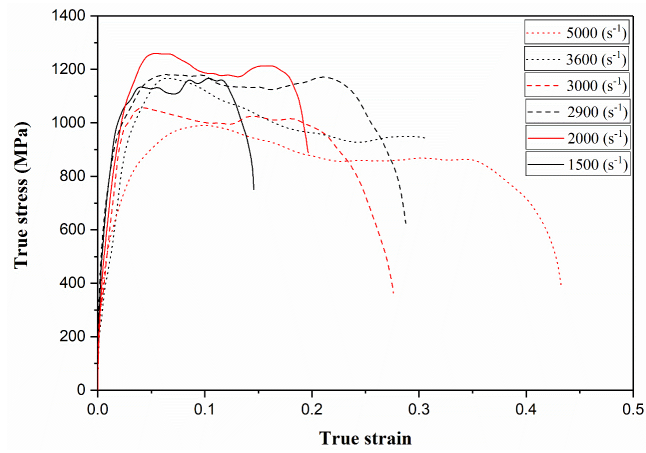


Fig 7. 6 Dynamic stress-strain curves of High-Ti maraging steel samples at strain rates of 1500 to 5000  $s^{-1}$ .

Table 7. 4. Observations from the dynamic impact responses of High-Ti maraging steel specimens.

Pressure (KPa)	Strain rate (s <sup>-1</sup> )	Yield stress (MPa)	Maximum flow stress (MPa)	Total strain (%)	Toughness (MJ/m <sup>3</sup> )	Temperature rise (°C)
100	1500	968.7	1166.6	14.5	153.2	38.3
120	2000	1156.4	1259.6	19.6	221.5	55.4
160	2900	1106.4	1180.1	28.7	310.1	77.5
170	3000	1003.1	1056.5	27.6	253.1	63.2
180	3600	1076.7	1167.1	30.6	299.4	74.8
200	5000	887.8	990.2	43.3	365.3	91.3

Fig 7.7. shows strain hardening vs. strain curves of the High-Ti maraging steel. As observed in the Low-Ti samples, three stages can be distinguished in the strain hardening plots of the High-Ti samples. At the beginning of the curves, the strain hardening drops, which is followed by a steady-state region related to the balance between thermal softening and strain hardening. Also, the sudden drop in the strain hardening curves towards the end of the curves is detected [10]. The steady-state regime revealed in the strain hardening curve of the strain rate of 5000 s<sup>-1</sup> extends to the higher strain level than those obtained at lower strain rates. This trend is consistent with the stress-strain curve of the sample at the strain rate of 5000 s<sup>-1</sup> as an indication of the dominance of thermal softening.

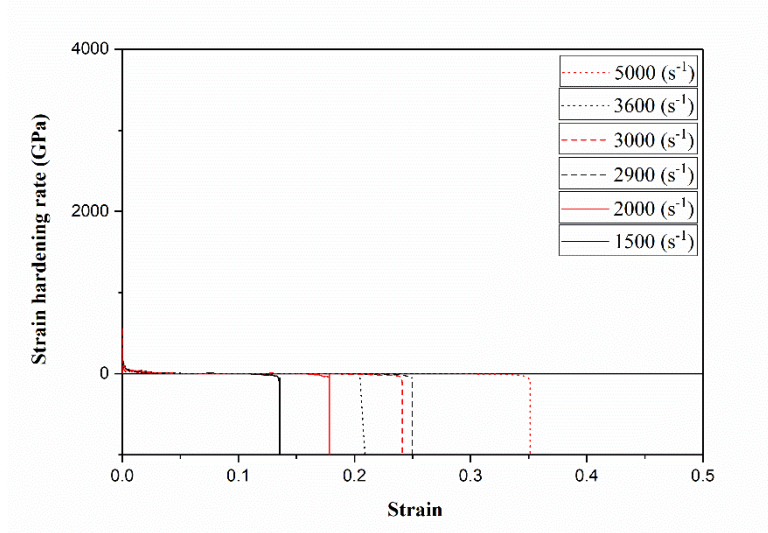


Fig 7. 7 Strain hardening rate vs. strain curves of High-Ti maraging steel dynamically compressed at the strain rates of  $1500 \text{ s}^{-1}$ ,  $2000 \text{ s}^{-1}$ ,  $2900 \text{ s}^{-1}$ ,  $3000 \text{ s}^{-1}$ ,  $3600 \text{ s}^{-1}$ , and  $5000 \text{ s}^{-1}$ .

### 7.3.3. Comparison of dynamic behavior of Low and High-Ti tested samples

Comparison of the flow behavior of the Low and High-Ti samples under different strain rates provides an insight into the role of titanium as the important variable on dynamic behavior of the LPBF maraging steel samples. By comparing the dynamic curves of Low and High-Ti samples at the strain rates of about  $3150 \text{ s}^{-1}$  and  $3000 \text{ s}^{-1}$ , respectively, the conclusion is higher stress toleration of Low-Ti than those of the High-Ti. The role of titanium on microstructural changes was investigated in our previous study [12]. It was shown that High-Ti maraging steel contains a higher volume fraction of austenite compared to that of Low-Ti maraging steel. Therefore, the increased volume fraction of austenite was a possible cause of the reduction in maximum flow stress of High-Ti samples. On the one hand it is pointed that the dynamic strength of the Low-Ti samples tested at different strain rates is significantly higher than that of High-Ti samples. Similar results were also obtained

by Schnitzer *et al.* [22], who investigated the effect of austenite fraction on the dynamic behavior of the maraging steel using SHPB. They observed that with increase in the phase fraction of austenite (soft part), strain-hardening sensitivity increases and strength decreases. On the other hand, the total strain of High-Ti samples is clearly higher than that of the Low-Ti samples. Wang *et al.* [23] also obtained the similar trend with increase of austenite phase. They noted that the ductility of the samples with a higher volume fraction of austenite is more affected by the austenite to martensite transformation under transformation-induced plasticity (TRIP) effect. It is well-known that TRIP plays a critical role in improving ductility of the steel. They also observed that at the early stage of deformation, austenite accommodates most applied strains. Subsequently, the martensite plasticity contributes to deformation by the slip (motion of dislocations) in the martensite matrix to accommodate the induced strain. Furthermore, another reason for the higher strain level of the High-Ti sample can also be related to its higher number of activated slip systems due to the evolution of  $\langle 111 \rangle \gamma$  fiber texture. Our previous study [24] showed that the dominant texture of the L-PBF-maraging steel samples changed with the increase in titanium content. It was found that adding titanium led to developing the  $\langle 111 \rangle \gamma$  fiber texture in the High-Ti sample. It is also well-known that slip in body-centered cubic (bcc) crystals occurred along the  $\{110\}$ ,  $\{112\}$  and  $\{123\}$  planes and the  $\langle 111 \rangle$  direction (direction of close packing) [25]. Accordingly, the formation of  $\langle 111 \rangle \gamma$  fiber texture induces the favorite slip directions leading to easily plastic deformation and increase of strains during dynamic loading in High- Ti samples.

Nevertheless, at the same level of firing pressure during the dynamic loadings of both samples, the loadings of High- Ti samples were at higher generated strain rates in

comparison with those of the Low-Ti specimens. The evolution of more activated slip systems in the High- Ti samples is the reason for this difference. Moreover, the temperature rise of Low-Ti samples was higher than that of High- Ti samples (Tables 7.3. and 7.4.), which causes a higher susceptibility of the ASB formation in the Low- Ti sample than that of samples containing a higher value of titanium.

As shown in the comparison of the strain hardening rate plots of both samples (Figs 7.5. and 7.8.), the third stage of strain hardening of High- Ti samples begins at higher strain compared to that of Low-Ti samples. Besides, the third stage of the strain hardening rate implies the dominance of thermal softening associated with temperature rise during the dynamic compression. Accordingly, the beginning of the third stage of strain hardening for the Low- Ti samples shifted to lower strains, which shows thermal softening was more dominant in Low- Ti samples. Furthermore, it can be concluded that High-Ti samples with higher volume fraction of austenite exhibits higher strain hardening rate during deformation. The similar results were also obtained by Wang et al. [23].

#### **7.3.4. Microstructural studies after dynamic loading**

The SEM micrographs in Fig 7.8. show the microstructure of the cross-section plane of the dynamically tested Low-Ti samples at different strain rates. Microstructure of the LPBF-maraging steel consists of columnar, cellular and equiaxed grains [12]. Under high strain rate loading, the plastic deformation is accompanied by a significant temperature rise. Also, severe plastic deformation is restricted to a narrow region in which the heat and strain are localized due to thermomechanical instability and loss of load-carrying capacity. Generally, this narrow region is referred to as adiabatic shear bands (ASBs) [9].

Furthermore, ASBs are susceptible regions to the formation of internal cracks and become preferential sites of eventual failure of material. Fig 7.8. (a and b) show the micrograph of the Low-Ti sample tested at strain rate of 1500 and 1950  $s^{-1}$ , respectively, in which ASBs can be observed. These observations are in agreement with the results obtained from the stress-strain curves of Low-Ti sample. Accordingly, the results of the dynamic curves indicate the occurrence of thermal softening and the temperature rise at the strain rates of 1500 and 1950  $s^{-1}$ . Figs 7.8. (c and d) show the microstructure of the Low-Ti samples tested at strain rate of 2770  $s^{-1}$  where the ASB and crack in ASB can be observed in Fig 7.8. (c) and (d) respectively. It was previously noted that the thermal softening become more dominated with increase in strain rate. The domination of the thermal softening could result in the formation of more ASB. Moreover, microstructural observations of the Low- Ti sample deformed at the strain rate of 2770  $s^{-1}$  confirmed the evolution of more ASBs with some internal micro cracks. Also, it is postulated that the growth of internal cracks along the ASBs continued within the dynamic loading at a higher strain rate (3150  $s^{-1}$ ). Consequently, at the strain rate of 3150  $s^{-1}$ , the further growth and coalescence of cracks led to the eventual failure of the Low-Ti sample. Wider ASB observed from micrographs related to the strain rate of 2770  $s^{-1}$  are consistent with the thermal softening detected from the stress-strain curves (Fig 7.3.).

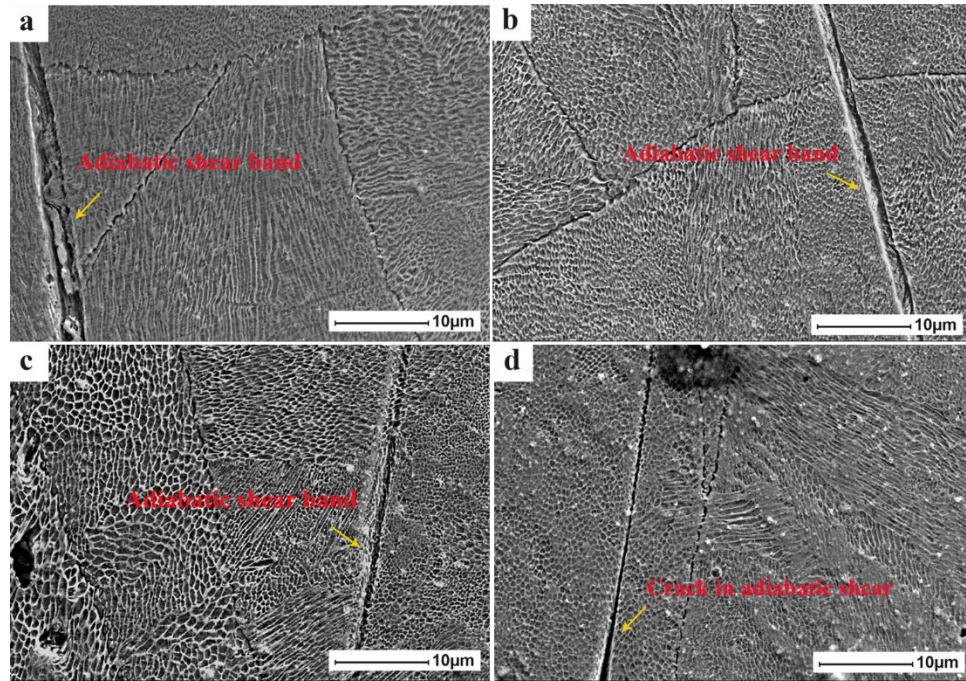


Fig 7. 8 Microstructures of the deformed Low-Ti specimens at strain rates of (a) 1500, (b) 1950, (c) 2770, and (d) 2770  $s^{-1}$ .

The microstructure of the High-Ti deformed samples is also shown in Fig 7.9. As expected, the ASBs were also observed from the micrograph of the High-Ti sample deformed at the strain rate of 2000  $s^{-1}$ . The ASBs observed in the High-Ti samples seem to be narrower and formed at higher strain rates compared to the ASBs developed in the Low-Ti samples. Such behavior of the High- Ti sample could be due to having a higher volume fraction of austenite, which accommodates imposed strains. Wang *et al.* [23] also reported that a higher volume fraction of austenite could delay strain localization and subsequent failure.

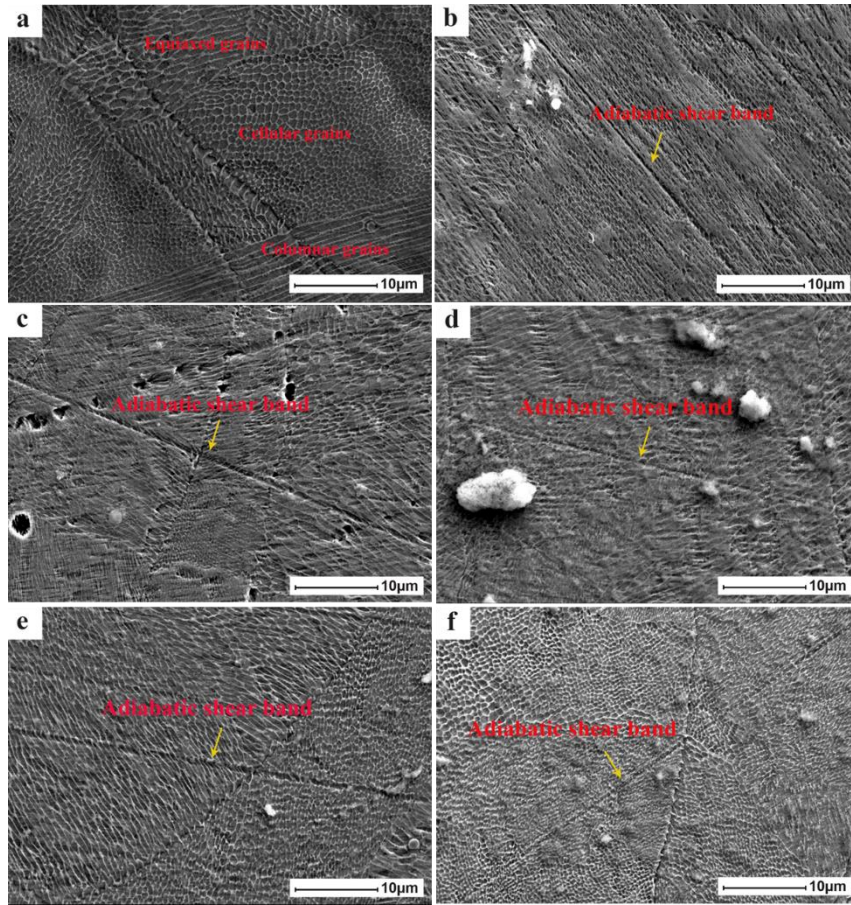


Fig 7. 9 Microstructures of the deformed High-Ti specimens at strain rates of (a) 1500 (b) 2000, (c) 2900, (d) 3000, (e) 3600, and (f) 5000  $s^{-1}$

In addition to plastic flow, the observation of fracture features is important for understanding the dynamic deformation mechanism. Dynamic compression loading at the strain rates of 3150  $s^{-1}$  and 3670  $s^{-1}$  led to the fracture of Low-Ti samples. Therefore, the fracture surfaces of the Low-Ti samples compressed at strain rates of 3150 and 3670  $s^{-1}$  were evaluated. SEM fractographs of the Low-Ti samples at the mentioned strain rates<sup>1</sup> are presented in Figs 7.10. and 7.11. at different magnifications. The fracture surface of the Low-Ti sample consists of elongated dimples (Fig 7.10.), indicating ductile shear fracture

mode. Fracture of the Low-Ti sample is a result of intensive localized shearing force oriented at  $45^\circ$  to the impact direction (along the plane of the maximum shear stress). Results of the current investigation show that dynamic failure of the Low-Ti sample involves a number of metallurgical events such as the formation of ASB, nucleation, growth and coalescence of micro-voids inside the ASB. Micro-voids coalescence occurred due to the differential deformation and stress concentration in ASB compared to neighborhood. Such coalescence of micro-voids results in a progressive reduction of the strength, reaching a critical stage where the void coalescence forms cracks and eventual failure happened [9] [10]. The fracture surface of the Low-Ti specimen deformed at the strain rate of  $3670 \text{ s}^{-1}$  (Fig 7.11.) shows a high density of smaller dimples compared with the dimples formed at the strain rate of  $3150 \text{ s}^{-1}$  (Fig 7.10.). It seems that with an increase in strain rate, the number fraction of dimples has increased. The variation in dimples features is consistent with the results of stress-strain curves presented in Table 7.3., in which total strain to failure increased with increasing strain rate.

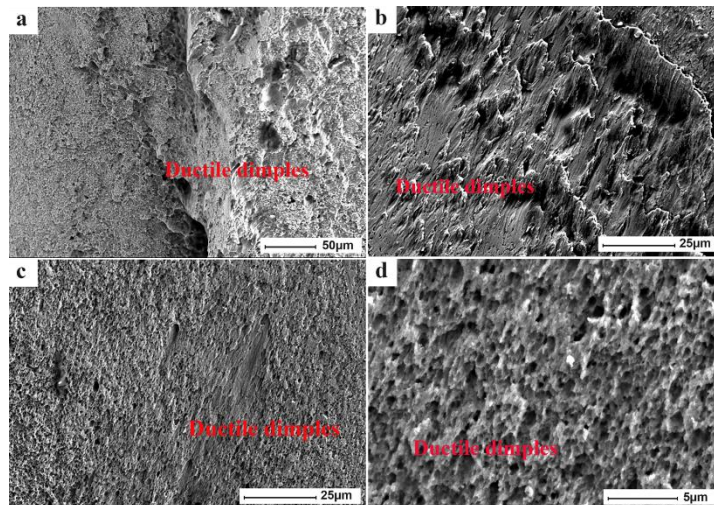


Fig 7. 10 SEM fractography of the fracture surfaces of Low-Ti samples deformed at the strain rates of 3150  $\text{s}^{-1}$ .

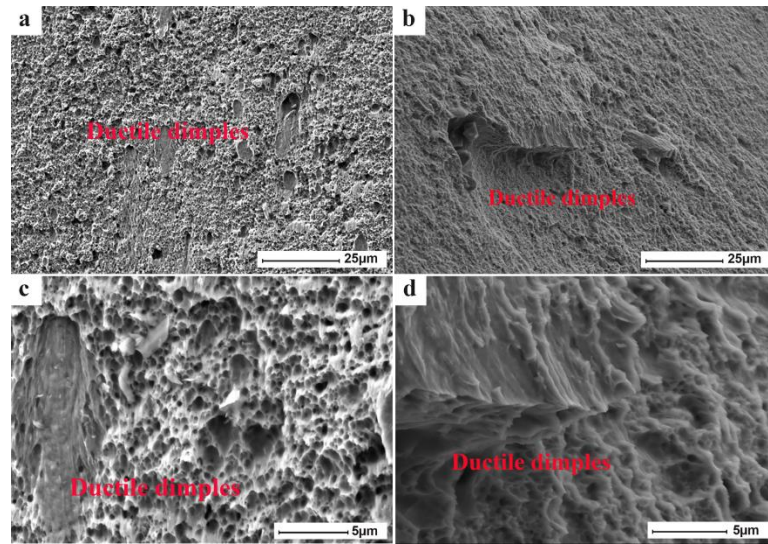


Fig 7. 11 SEM fractography of the fracture surfaces of Low-Ti sample deformed at the strain rate of 3670 s<sup>-1</sup>.

It is noted that, fragmentation did not occur for the High- Ti samples even at the high strain rate of 5000 s<sup>-1</sup>, which could be related to the higher ductility of High- Ti samples compared to specimens of low titanium contents. In previous work of our group, it was found that the ductility of the High-Ti samples was higher than that of the Low-Ti samples, which were subjected to uniaxial tensile tests. Also, it was observed that the increase in volume fraction of austenite influences the corresponding increase in ductility of samples [12][24]. Therefore, in our current study, it is found that the resistance to imposed shear stress and subsequent failure is higher for High-Ti samples than the Low-Ti specimens. Such behavior can be attributed to the changes in microstructure, as a higher amount of austenite formed in High-Ti maraging steel samples. Wang *et al.* [23] also reported the improvement of the crack arresting ability of microstructure consisting of a higher volume fraction of austenite. In the High-Ti samples containing a higher amount of austenite, nanolaminate morphology formed between the newly martensite grains transformed from austenite and

the previous martensite grains prevents further growth of cracks and failure under dynamic compression loading. The larger elongation estimated from the stress-strain curves of the High-Ti samples (shown in Table 7.4.) also confirms their higher resistance to fracture.

### 7.3.5. Electrochemical tests

The corrosion behavior of both undeformed and deformed samples under dynamical loading at the strain rates of about  $2000 \text{ s}^{-1}$  and  $3000 \text{ s}^{-1}$  with the two different contents of titanium (Low-Ti and High-Ti) were studied using electrochemical tests and surface characterization after exposure to 3.5 wt.% NaCl solution. The role of titanium and the mechanical deformation process are discussed in this section. Also, samples are named based on prior mechanical processes and the value of titanium. The details of samples' nomenclature are shown in Table 7.5.

Table 7. 5. Nomination of samples, titanium content, and prior mechanical treatments.

Sample	Titanium content (wt.%)	Prior mechanical process	Strain rate ( $\text{s}^{-1}$ )
Low-Ti	0.72	undeformed	---
Low-Ti-1950	0.72	dynamical loading	1950
Low-Ti-2770	0.72	dynamical loading	2770
High-Ti	1.17	undeformed	---
High-Ti-2000	1.17	dynamical loading	2000
High-Ti-2900	1.17	dynamical loading	2900

### 7.3.5.1. Potentiodynamic polarization measurement

Before electrochemical tests, it took enough time to achieve a relatively stable open circuit potential (OCP) trend for the samples. Samples were immersed in NaCl solution for about 24 hours prior to corrosion tests.

Fig 7.12. shows potentiodynamic curves of the undeformed and deformed L-PBF maraging steel parts with two different values of titanium. As shown in Fig 7.12., the anodic current densities increase with an increase in anodic potential relating to the active corrosion behavior of all samples without passivation. Also, there was no significant difference in the cathodic processes of the LPBF maraging steel samples. The oxygen reduction occurred as the cathodic reaction for all samples in the NaCl solution. The electrochemical parameters acquired from the potentiodynamic polarization curves are listed in Table 7.6. It can be observed that there are less differences in the corrosion potentials compared to corrosion currents after the deformation under dynamical compression tests. The  $I_{\text{corr}}$  of Low-Ti, Low-Ti-1950, and Low-Ti-2770 are lower than that of samples containing a higher amount of titanium (High-Ti samples). This trend indicated that the reactivity of the chlorine ion is the cause for the breakdown of the formed surface films, allowing more dissolution of the deformed and undeformed High-Ti samples than the Low-Ti samples. The changes in corrosion behavior could be attributed to differences in the microstructural features developed before and after dynamic deformation. As shown in Table 6, the  $I_{\text{corr}}$  of deformed samples is slightly lower than those of undeformed samples, indicating improvement in corrosion resistance after deformation. The improvement in corrosion resistance after deformation could also be related to recovery/recrystallization processes

accompanied by the partial transformation of the austenite to martensite under the TRIP mechanism.

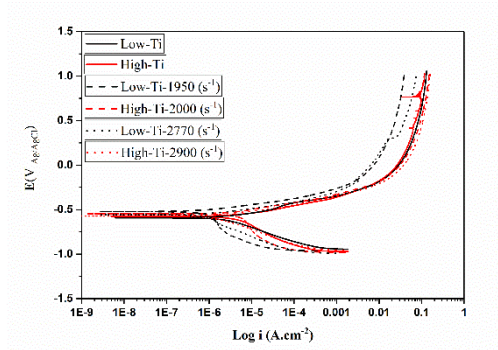


Fig 7. 12 Potentiodynamic polarization curves of Low-Ti and High-Ti, Low-Ti-1950 and High-Ti-2000, and Low-Ti-2770 and High-Ti 2900 specimens in 3.5 wt.% NaCl solution at room temperature.

Table 7. 6. Open circuit potential and Tafel fitted parameters after potentiodynamic test.

	Low-Ti	High-Ti-	Low-Ti- 1950-	Low-Ti- - 2770 -	High-Ti- 2000	High-Ti- 2900
$E_{\text{corr}}$ (V <sub>Ag/AgCl</sub> )	-0.60	-0.58	-0.52	-0.56	-0.54	-0.57
$I_{\text{corr}}$ ( $\mu\text{A}/\text{cm}^2$ )	3.95	5.38	1.04	1.38	1.9	3.3

### 7.3.5.2. Electrochemical impedance spectrum measurement

To further, study the electrochemical performance of the samples, EIS measurements in 3.5% wt.% NaCl solution were carried out. Fig 7.13. shows Nyquist and Bode plots of the experimental samples under OCP. It can be seen that, the spectra of all samples exhibited a capacitive loop characteristic, which could be related to the domination of the charge-

transfer control mechanism of the electrochemical reactions. From the Nyquist plot, it is noted that the diameters of the loop/arcs of the undeformed and deformed Low-Ti samples are higher than those of the High-Ti samples, which suggests improvement in the film and charge transfer resistance with decreasing in titanium contents.

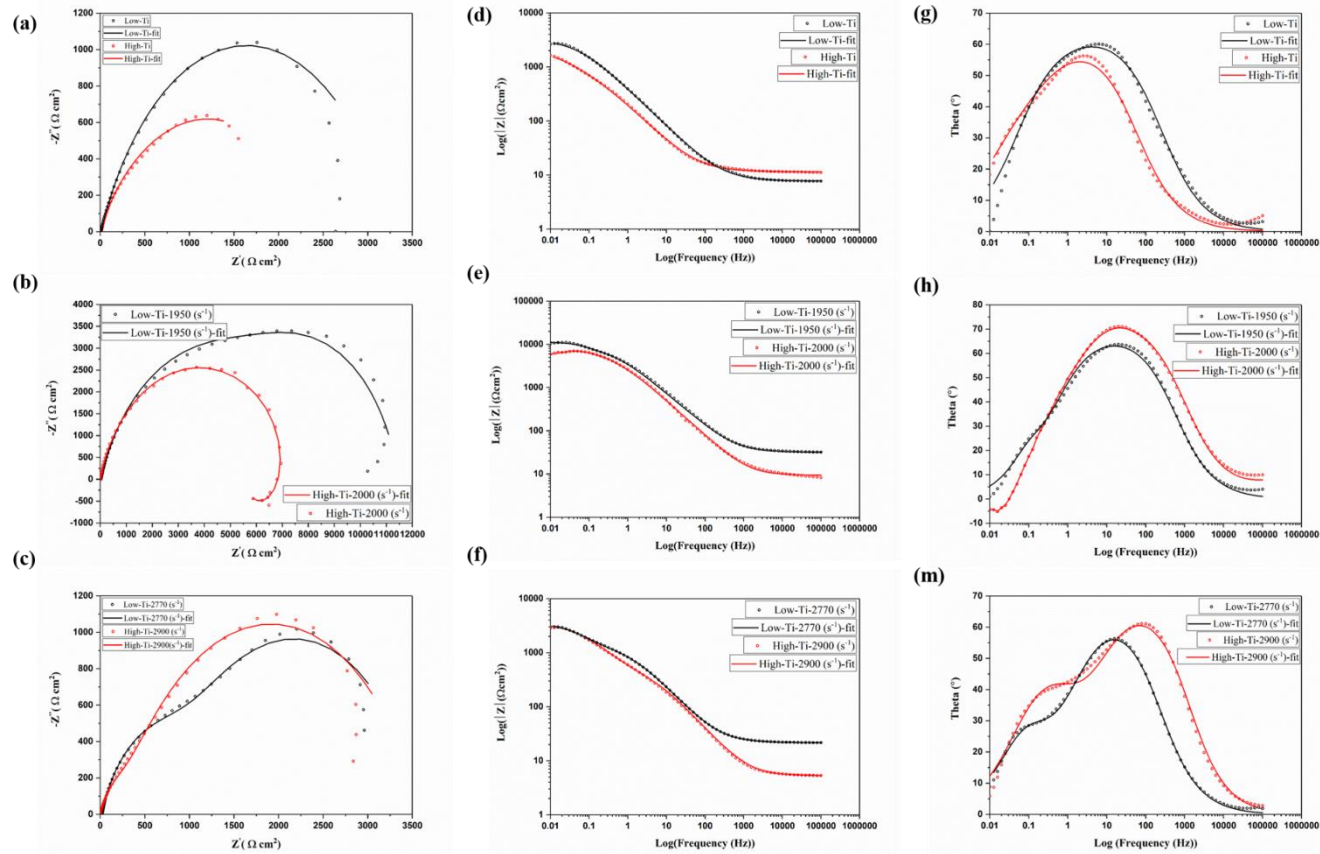


Fig 7. 13 EIS spectrum of the LPBF maraging steel samples before and after deformation. (a)-(g) plots before deformation, (b)-(h) Nyquist and bode plots of Low-Ti-1990 and High-Ti-2000, and (c)-(m) EIS plots of Low-Ti-2770 and High-Ti-3000. (a)-(c): Nyquist diagrams, (d)-(f): Bode, and (g)-(m): Bode phase plots.

Fig 7.13. also illustrates the EIS results in the forms of Bode plots (modulus of impedance and phase angle vs. frequency). The Bode plots provide the necessary information about the electrochemical frequency-dependent behavior than do the Nyquist plots, where the frequency values are implicit. As shown in Figs 7.13. (d)-(f), a linear relationship between the  $\log |Z|$  and  $\log f$  with a slope of approximately  $\sim -1$  over a wide range of frequencies indicates the presence of time-constant systems. The maximum phase angles for all specimens are far away from  $90^\circ$ , which is required in the case of pure capacitive behavior [26]. This is due to non-homogeneity and the effect of porosities in surface films (corrosion products) formed on the specimens' surfaces [27][28]. In addition, the bode phase plots show a wide peak, which could be better characterized by two-time constants linked to the surface films and double layer capacitances. By comparison with the bode phase plots presented in Figs 7.13. (g)-(m), it is seen that two-time constants are better separated for the Low-Ti-2770 and High-Ti-2900 samples (Fig 7.13.(m)). In the low frequency area (frequency of  $10^{-1}$  and lower), the impedance moduli of both types of samples dynamically loaded at higher strain rates of about  $3000 \text{ s}^{-1}$ , were of order of  $10^3 \text{ } \Omega \cdot \text{cm}^2$  which is lower than those values measured for the samples deformed at lower strain rates of about  $2000 \text{ s}^{-1}$  (of order of about  $10^4 \text{ } \Omega \cdot \text{cm}^2$ ), indicating a decline in the corrosion resistance of the Low-Ti and High-Ti samples after deformation at higher strain rates. Moreover, the EIS spectra of the High-Ti exhibited a capacitance loop characteristic at medium and high frequency followed by an obscured inductance behavior at lower frequencies, which could be related to an incomplete localized electro-dissolution or repassivation of the surface film [28][29]. To quantitatively confirm the experimental EIS data, EIS plots were analyzed using equivalent electrical circuit models shown in Fig 7.14. In this circuit models,  $R_s$  represents

the solution resistance,  $R_f$  and  $CPE_f$ , respectively, denote the resistance and capacitance of the space charge of the surface film.  $R_{ct}$  and  $CPE_{dl}$ , respectively, represent the charge transfer resistance and double layer constant phase element formed at the interface of the sample surface and solution. In the circuit models, constant phase element (CPE) was used instead of pure capacitance due to a non-linear surface impedance distribution and the inhomogeneity of surface reaction [27, 31]. To account for the obscured spectrum observed at low frequencies of the EIS plots of the High-Ti-2000 sample, a  $R_L$  in series with  $L$  is added into the model (Fig 7.14. (b)), of which  $R_L$  is the resistance and  $L$  represents the pseudo inductance attributed to the relaxation processes obtained from the adsorption/desorption of some species [14] [29] [30].

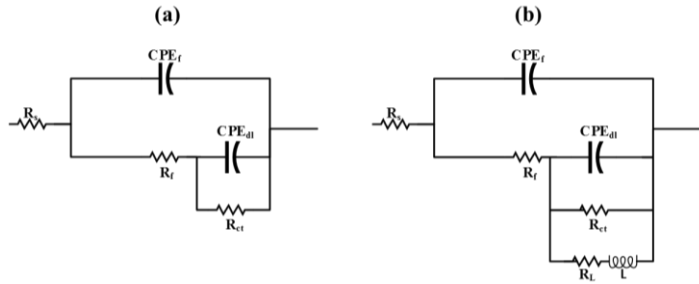


Fig 7. 14 Equivalent circuits used to fit the experimental impedance data obtained from (a) all samples expect High-Ti-2000 sample and (b) High-Ti-2000 sample.

Using the equivalent circuit shown in Fig 7.14., the AC impedance spectrum was fitted, and the parameters of each component are shown in Table 7. The calculated chi-square ( $\chi^2$ ) values of all plots were found to be of the order of  $1 \times 10^{-3}$  and lower, which represents the goodness of fit of experimental data for the representative electrical equivalent circuits.

Table 7. 7. Fitting parameters obtained from EIS spectra.

Sample	$R_s$ ( $\Omega.cm^2$ )	$CPE_r$ ( $F cm^{-2} S^{n-1}$ )	$N_1$	$R_f$ ( $k\Omega.cm^2$ )	$CPE_{dl}$ ( $F cm^{-2} S^{n-1}$ )	$N_2$	$R_{ct}$ ( $k\Omega.cm^2$ )	$R_L$ ( $k\Omega.cm^2$ )	$L$ ( $kH.cm^{-2}$ )	$\chi^2$
Low-Ti	7.7	$6.4*10^{-3}$	0.7	2.6	$6.3*10^{-3}$	0.7	0.6	-	-	0.004
High-Ti	11.4	$1.3 *10^{-3}$	0.7	1.1	$2.1*10^{-3}$	0.6	1.3	-	-	0.004
Low-Ti-1950	29.5	$0.96*10^{-4}$	0.7	8.7	$4.6*10^{-4}$	1	2.8	-	-	0.008
High-Ti-2000	9.4	$0.65*10^{-4}$	0.8	3.1	$1.3*10^{-4}$	0.3	7.3	4.4	5.0	0.009
Low-Ti-2770	20.3	$1.7 *10^{-4}$	0.8	1.4	$1.1*10^{-3}$	0.8	2.2		-	0.0006
High-Ti-2900	5.3	$1.5*10^{-4}$	0.8	0.5	$5.5*10^{-4}$	0.7	3.1		-	0.003

According to Table 7.7., both values of  $R_f$  and  $CPE_f$  values for Low-Ti samples are higher than those of the High-Ti samples, which could be related to the improvement of the effectiveness of the deposited surface films corrosion barriers [31]. This behavior is consistent with the results obtained from the potentiodynamic polarization measurements. Also, Low-Ti and High-Ti samples deformed at the strain rate of about  $2000 \text{ s}^{-1}$ , displayed higher values of  $R_f$  and  $R_{ct}$  in comparison with the corresponding values obtained for the undeformed samples. Therefore, the impedance data suggest that the film deposited on samples deformed at the strain rate of about  $2000 \text{ s}^{-1}$  is more protective than those deposited on undeformed samples. This observation could be traced to partial recovery/recrystallization and austenite to martensite transformation during high strain-rate deformation. Moreover, a comparison between the total values of  $R_{ct}$  and  $R_f$  ( $R_{total} = R_{ct} + R_f$ ) obtained for the Low-Ti-1950 and High-Ti-2000 samples showed that the barriers properties of the surface slightly decreased after deformation by adding the titanium. Accordingly, Low-Ti-1950 samples showed a slightly higher value of  $R_{total}$  ( $1.15 \text{ k}\Omega \cdot \text{cm}^2$ ) in comparison with that of the High-Ti-2000 sample ( $1.04 \text{ k}\Omega \cdot \text{cm}^2$ ). Furthermore, the double-layer capacitance ( $CPE_{dl}$ ) for the Low-Ti-1950 sample is higher than that of the High-Ti-2000 specimen. The growth of the surface film could increase the surface roughness and the area at which the double layer has formed, leading to the increase in capacitance [32]. Finally, when the samples were deformed at a higher strain rate of about  $3000 \text{ s}^{-1}$ , the  $R_f$  values decrease by order of six orders of magnitude than the samples deformed at lower strain rate of about  $2000 \text{ s}^{-1}$ . Also, there is a reduction in  $R_{ct}$  values for the samples dynamically loaded at the strain rate of about  $3000 \text{ s}^{-1}$  in comparison with those of the samples deformed at about  $2000 \text{ s}^{-1}$ . However, the  $CPE_f$  and  $CPE_{dl}$  values of the Low-Ti-2770 and High-Ti-2900

samples did not show a significant change in comparison with those of the Low-Ti-1950 and High-Ti-2000 samples, indicating that the formation of surface films could play an important role as corrosion barriers on the specimen surface and affect the charge transfers. It also reveals that the higher strain rate deformation hampers the formation of the more protective surface layers compared with deformation at a lower strain rate.

It is well-recognized that microstructural changes caused by different methods such as mechanical processing or loading affect the corrosion behavior of the material. In making sense of microstructural effects that are related to chemical composition and mechanical processes, it is important to recognize that the electrochemical behavior of LPBF C300 maraging steel samples can be influenced by a wide variety of microstructural entities, including precipitates, different phase structures, residual stress, etc. As in our previous study [12] the formation of NiCo precipitates in the martensitic matrix of LPBF High-Ti samples was found. It is important to highlight the way the chemical composition and the presence of intermetallic precipitates affect the material's corrosion resistance. The inferior corrosion resistance of High-Ti samples could be related to the precipitation of NiCo as an intermetallic compound. This precipitation could lead to the depletion from the metallic matrix of elements such as nickel, and cobalt, which provides corrosion resistance to the steel. As a result, small micro-galvanic piles could be formed, deteriorating the corrosion resistance of the material [15][28][33]. In addition, the poorer corrosion performance of High-Ti samples could result from the formation of a higher amount of austenite inside the material [12][24]. Regions at the interface of martensite-austenite phase boundary contain higher elastic energy, which could create more active sites for electrochemical reactions triggering micro galvanic corrosion along the interface [32]. In addition, the austenite is

rich in nickel and molybdenum, which promotes the formation of areas more reactive to corrosion through increasing the differences in electrochemical potentials between interphases of austenite and martensite [15].

Furthermore, the annihilation and rearrangement of dislocations could take place through recovery/recrystallization, resulting in the formation of new equiaxed strain-free grains that affect the electrochemical behavior of the alloys [10][34][35][36]. With prior deformation, recrystallization and grain refinement has been increased leading to corrosion improvement [37][36]. The effect of thermomechanical instability during the dynamic loading is the formation of ASB in which the strain and heat are localized, leading to recrystallization. The dynamic recrystallized areas could provide the perfect sites for the nucleation of the surface films [36]. For samples deformed at strain rates of about  $2000 \text{ s}^{-1}$  and  $3000 \text{ s}^{-1}$ , significant ASB were observed and these ASB are suitable sites for nucleation of surface layers which acts as the barriers to transfer of ions. Moreover, the development of some closed-packed orientations and austenite to martensite transformation induced by the TRIP mechanism during the deformation could be considered as other reasons for the improvement of corrosion behavior after the high strain-rate compressive deformation [35][38]. The higher corrosion resistance of the deformed samples at a lower strain rate (about  $2000 \text{ s}^{-1}$ ) than those deformed at a strain rate of about  $3000 \text{ s}^{-1}$  could be attributed to a competition between the recovery/recrystallization, austenite to martensite transformation and also residual stresses developed in the microstructure. Accordingly, it could be assumed that the higher level of residual stresses in the microstructure of the sample deformed at a high strain rate in comparison with that deformed at a lower strain rate could lead to the deterioration of corrosion resistance [39][40]. However, for samples

deformed at high strain rates ( $3000 \text{ s}^{-1}$ ), the diameter of capacitive arc decreased due to dominant thermal softening as Tiamiyu *et al.* suggested [35].

### **7.3.6. Surface observation after immersion**

Figs 7.15. and 7.16. show SEM images of surface morphology of the Low-Ti and High-Ti samples deformed at the strain rate of about  $3000 \text{ s}^{-1}$  after the potentiodynamic polarization tests. As observed, micro-pits are more frequently formed adjacent to ASB. ASBs are the most probable sites for both nucleation and growth of pits. This could confirm the proposition that deterioration in corrosion resistance of the samples is due to microstructural inhomogeneity, which developed inside and adjacent to the ASB. The microstructural inhomogeneities and defects such as residual stresses formed inside the ASB represent micro-chemical discontinuities and are responsible for enhanced corrosion attacks along the ASB. Although the impact of ASB on corrosion performance of additively manufactured materials has not been studied, Ly *et al.* [41] [42] also stated the localized corrosion susceptibility of severely deformed aluminum alloys occurred at ASB as preferred regions for the formation of pits due to microstructural inhomogeneities developed between ASB and matrix. Similar results were also obtained by Nie *et al.* [43], who investigated the effect of ASB in cold-rolled Zr based metallic glass on pitting corrosion attacks. They reported shear band as the preferential site for corrosion attacks due to its different microstructural features from the matrix.

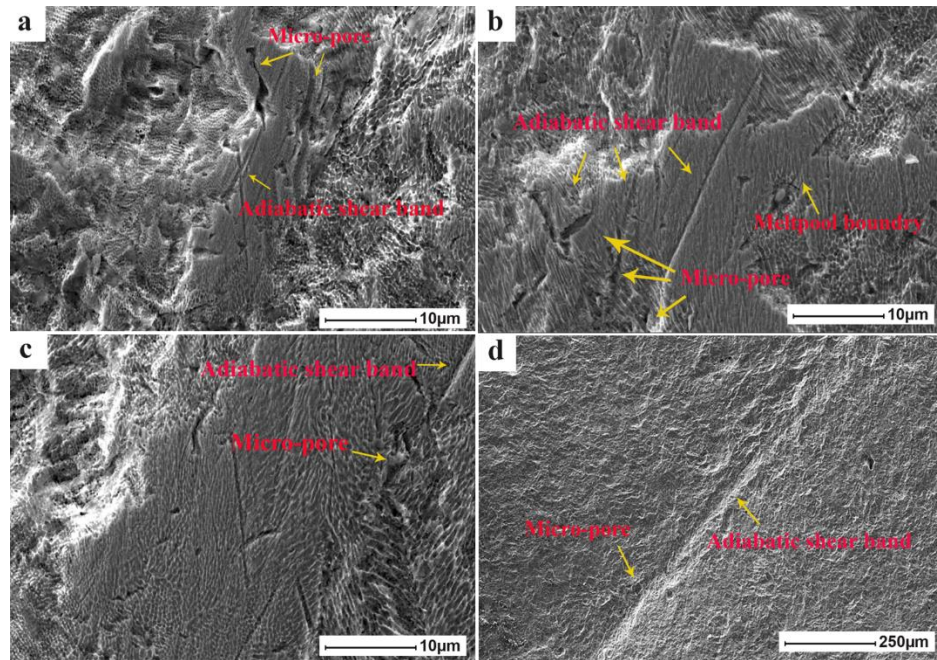


Fig 7. 15 SEM images showing the surface morphologies of Low-Ti-2770 sample after polarization test in 3.5% NaCl solution.

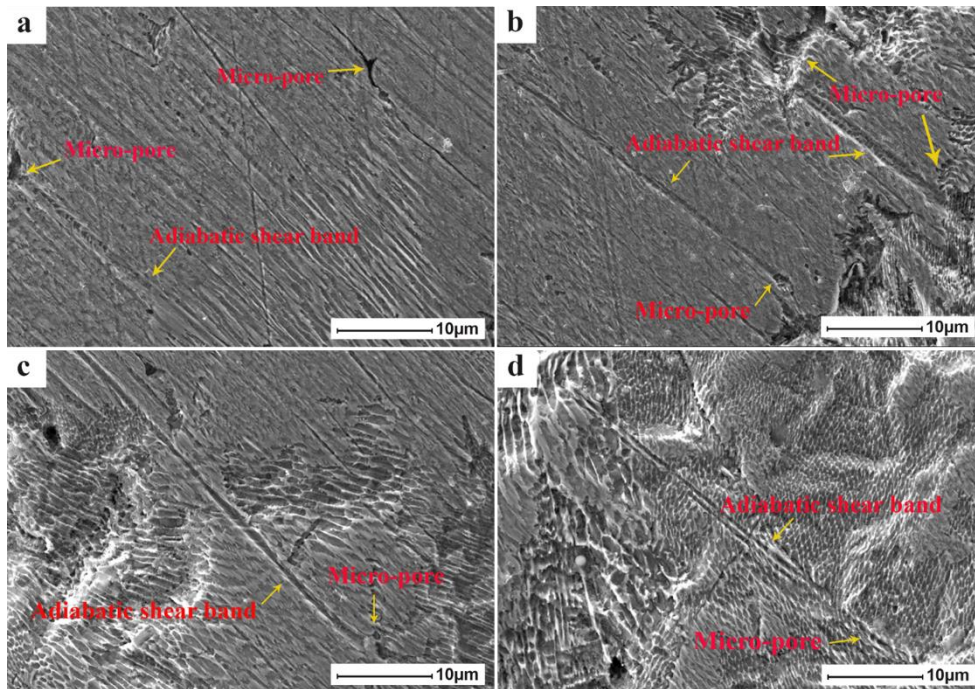


Fig 7. 16 SEM images of the surface degradation of High-Ti-2900 sample after polarization test in 3.5% NaCl solution.

## 7.4. Conclusions

In this study, the effects of titanium content on the high-strain rate response and corrosion behavior of C300 maraging steels printed using the LPBF technique were investigated. The high strain rate compressive behavior of Low-Ti (Titanium content of 0.72wt.%) and High-Ti (Titanium content of 1.17 wt.%) maraging steel samples has been studied using SHPB. The main conclusions are as follows:

- High-Ti samples showed a better dynamic deformation behavior in terms of ductility than Low-Ti samples. High-Ti samples did fracture up to the strain rate of  $5000 \text{ s}^{-1}$ . Addition of 1.7 wt. % Ti to the maraging steel increased the volume fraction of austenite in the martensitic matrix of alloy, improving the ductility of High-Ti samples and resulting in higher plasticity in comparison with Low-Ti samples at high strain rates.
- During dynamic deformation, strain localization occurs along narrow bands called adiabatic shear bands (ASB). During high strain rate deformation, plastic work converted to heat, which resulted in thermal softening. Low-Ti sample was more susceptible to thermal softening and ASB formation than High-Ti sample. Higher austenite fraction in High-Ti sample delayed strain localization and formation of ASBs.
- Potentiodynamic and EIS curves electrochemical corrosion testing showed that the corrosion resistance of both types of samples improved after the dynamic loading. This behavior could be associated with partial recovery/recrystallization accompanied by austenite to martensite transformation induced by TRIP mechanism during the high strain-rate deformation.

- Increasing the titanium content of the alloy from 0.72 to 1.7 wt. % led to further reduction in corrosion resistance. The presence of NiCo precipitates has a detrimental impact on corrosion resistance of High-Ti samples, which triggers the formation of galvanic couples between the NiCo particles and their surrounding matrix.
- The evolution of ASB during the high strain rate deformation has a negative effect on the corrosion performance of the deformed samples. The presence of different microstructural features developed within the ASB could promote the formation micro-galvanic pairs between the ASB and their surrounding area. Therefore, it is possible to observe the localized corrosion attacks in the form of pores adjacent to the ASB.
- An increase in residual stresses and microstructural inhomogeneities and dominance of thermal softening as strain rate was increased from  $2000 \text{ s}^{-1}$  to about  $3000 \text{ s}^{-1}$  resulted in a slight decrease in the corrosion resistance of both Low and High-Ti samples.

## 7.5. References

- [1] S. Shamsdini, M.H. Ghoncheh, M. Sanjari, H. Pirgazi, B.S. Amirkhiz, L. Kestens, M. Mohammadi, Plastic deformation throughout strain-induced phase transformation in additively manufactured maraging steels, *Mater. Des.* 198 (2020) 109289.
- [2] J.P. Oliveira, A.D. LaLonde, J. Ma, Processing parameters in laser powder bed

- fusion metal additive manufacturing, *Mater. Des.* 193 (2020) 108762.
- [3] C. Tan, K. Zhou, W. Ma, P. Zhang, M. Liu, T. Kuang, Microstructural evolution, nanoprecipitation behavior and mechanical properties of selective laser melted high-performance grade 300 maraging steel, *Mater. Des.* 134 (2017) 23–34. <https://doi.org/10.1016/j.matdes.2017.08.026>.
- [4] Y. Bai, D. Wang, Y. Yang, H. Wang, Effect of heat treatment on the microstructure and mechanical properties of maraging steel by selective laser melting, *Mater. Sci. Eng. A.* 760 (2019) 105–117. <https://doi.org/10.1016/j.msea.2019.05.115>.
- [5] J. Song, Q. Tang, Q. Feng, S. Ma, R. Setchi, Y. Liu, Q. Han, X. Fan, M. Zhang, Effect of heat treatment on microstructure and mechanical behaviours of 18Ni-300 maraging steel manufactured by selective laser melting, *Opt. Laser Technol.* 120 (2019) 105725.
- [6] P.F. Hao, X.B. Hou, J.Z. Gao, Y. Liu, X.F. Shu, The dynamic response of Q345 steel at high strain rates and high temperature, in: *Appl. Mech. Mater.*, Trans Tech Publ, 2012: pp. 483–487.
- [7] E. El-Magd, M. Abouridouane, Characterization, modelling and simulation of deformation and fracture behaviour of the light-weight wrought alloys under high strain rate loading, *Int. J. Impact Eng.* 32 (2006) 741–758.
- [8] M.M. Al-Mousawi, S.R. Reid, W.F. Deans, The use of the split Hopkinson pressure bar techniques in high strain rate materials testing, *Proc. Inst. Mech. Eng. Part C J. Mech. Eng. Sci.* 211 (1997) 273–292.

- [9] R. Alaghmandfard, C. Dharmendra, A.G. Odeshi, M. Mohammadi, Dynamic mechanical properties and failure characteristics of electron beam melted Ti-6Al-4V under high strain rate impact loadings, *Mater. Sci. Eng. A.* 793 (2020) 139794.
- [10] S. Dehgahi, R. Alaghmandfard, J. Tallon, A. Odeshi, M. Mohammadi, Microstructural evolution and high strain rate compressive behavior of as-built and heat-treated additively manufactured maraging steels, *Mater. Sci. Eng. A.* 815 (2021) 141183.
- [11] P. Kürnsteiner, M.B. Wilms, A. Weisheit, P. Barriobero-Vila, E.A. Jäggle, D. Raabe, Massive nanoprecipitation in an Fe-19Ni-xAl maraging steel triggered by the intrinsic heat treatment during laser metal deposition, *Acta Mater.* 129 (2017) 52–60. <https://doi.org/10.1016/j.actamat.2017.02.069>.
- [12] S. Dehgahi, M.H. Ghoncheh, A. Hadadzadeh, M. Sanjari, B.S. Amirkhiz, M. Mohammadi, The role of titanium on the microstructure and mechanical properties of additively manufactured C300 maraging steels, *Mater. Des.* (2020) 108965.
- [13] E. Bouzakis, A. Arvanitidis, F. Kazelis, G. Maliaris, N. Michailidis, Comparison of Additively Manufactured vs. Conventional Maraging Steel in Corrosion-Fatigue Performance after various surface treatments, *Procedia CIRP.* 87 (2020) 469–473.
- [14] A.F. Avelino, W.S. Araújo, D.F. Dias, L.P.M. dos Santos, A.N. Correia, P. de Lima-Neto, Corrosion investigation of the 18Ni 300 grade maraging steel in aqueous chloride medium containing H<sub>2</sub>S and CO<sub>2</sub>, *Electrochim. Acta.* 286 (2018) 339–349.
- [15] M.A.C. Florez, Ú.C. Pereira, J.L. Cardoso, F.J. dos Santos Oliveira, W.S. Araújo, G.F. Ribas, H.F.G. de Abreu, M.J.G. da Silva, Microstructural characterization of

- grade 300 and grade 350 maraging steels and electrochemical study in hydrofluoric solution, *J. Fluor. Chem.* 243 (2021) 109738.
- [16] T. Zhao, S. Wang, Z. Liu, C. Du, X. Li, Effect of cathodic polarisation on stress corrosion cracking behaviour of a Ni (Fe, Al)-maraging steel in artificial seawater, *Corros. Sci.* 179 (2021) 109176.
- [17] S. Dehgahi, H. Pirgazi, M. Sanjari, R. Alaghmandfard, J. Tallon, A. Odeshi, L. Kestens, M. Mohammadi, Texture evolution during high strain-rate compressive loading of maraging steels produced by laser powder bed fusion, *Mater. Charact.* (2021) 111266.
- [18] X.-M. Zhang, H. LI, H. Li, G.A.O. Hui, Z. GAO, L.I.U. Ying, L.I.U. Bo, Dynamic property evaluation of aluminum alloy 2519A by split Hopkinson pressure bar, *Trans. Nonferrous Met. Soc. China.* 18 (2008) 1–5.
- [19] Y.B. Xu, Y.L. Bai, Q. Xue, L.T. Shen, Formation, microstructure and development of the localized shear deformation in low-carbon steels, *Acta Mater.* 44 (1996) 1917–1926.
- [20] Y. Xu, J. Zhang, Y. Bai, M.A. Meyers, Shear localization in dynamic deformation: microstructural evolution, *Metall. Mater. Trans. A.* 39 (2008) 811–843.
- [21] B. Hwang, S. Lee, Y.C. Kim, N.J. Kim, D.H. Shin, Microstructural development of adiabatic shear bands in ultra-fine-grained low-carbon steels fabricated by equal channel angular pressing, *Mater. Sci. Eng. A.* 441 (2006) 308–320.
- [22] R. Schnitzer, G.A. Zickler, E. Lach, H. Clemens, S. Zinner, T. Lippmann, H.

- Leitner, Influence of reverted austenite on static and dynamic mechanical properties of a PH 13-8 Mo maraging steel, *Mater. Sci. Eng. A.* 527 (2010) 2065–2070.
- [23] M.-M. Wang, C.C. Tasan, D. Ponge, A.-C. Dippel, D. Raabe, Nanolaminate transformation-induced plasticity–twinning-induced plasticity steel with dynamic strain partitioning and enhanced damage resistance, *Acta Mater.* 85 (2015) 216–228.
- [24] S. Dehgahi, M. Sanjari, M.H. Ghoncheh, B.S. Amirkhiz, M. Mohammadi, Concurrent improvement of strength and ductility in heat-treated C300 maraging steels produced by laser powder bed fusion technique, *Addit. Manuf.* (2021) 101847.
- [25] C. Tian, D. Ponge, L. Christiansen, C. Kirchlechner, On the mechanical heterogeneity in dual phase steel grades: Activation of slip systems and deformation of martensite in DP800, *Acta Mater.* 183 (2020) 274–284.
- [26] A. Lasia, Electrochemical impedance spectroscopy and its applications, in: *Mod. Asp. Electrochem.*, Springer, 2002: pp. 143–248.
- [27] G. Moretti, F. Guidi, G. Grion, Tryptamine as a green iron corrosion inhibitor in 0.5 M deaerated sulphuric acid, *Corros. Sci.* 46 (2004) 387–403.
- [28] K.H. Kim, S.H. Lee, N.D. Nam, J.G. Kim, Effect of cobalt on the corrosion resistance of low alloy steel in sulfuric acid solution, *Corros. Sci.* 53 (2011) 3576–3587.
- [29] H. Torbati-Sarraf, M. Shabani, P.D. Jablonski, G.J. Pataky, A. Poursaee, The influence of incorporation of Mn on the pitting corrosion performance of CrFeCoNi High Entropy Alloy at different temperatures, *Mater. Des.* 184 (2019) 108170.

- [30] M. Kissi, M. Bouklah, B. Hammouti, M. Benkaddour, Establishment of equivalent circuits from electrochemical impedance spectroscopy study of corrosion inhibition of steel by pyrazine in sulphuric acidic solution, *Appl. Surf. Sci.* 252 (2006) 4190–4197.
- [31] Y. Xiao, J. Gu, J. Zhang, Semiconductor property and corrosion behavior of passive film formed on steel with zinc coating in 5% NaCl solution, *Arab. J. Sci. Eng.* 42 (2017) 4273–4280.
- [32] A. Shahriari, M. Ghaffari, L. Khaksar, A. Nasiri, A. Hadadzadeh, B.S. Amirkhiz, M. Mohammadi, Corrosion resistance of 13wt.% Cr martensitic stainless steels: Additively manufactured CX versus wrought Ni-containing AISI 420, *Corros. Sci.* 184 (2021) 109362.
- [33] A.H. Seikh, H. Halfa, M. Baig, S.M.A. Khan, Microstructure characterization and corrosion resistance behavior of new cobalt-free maraging steel produced through ESR techniques, *J. Mater. Eng. Perform.* 26 (2017) 1589–1597.
- [34] H.-W. Son, C.-H. Cho, J.-C. Lee, K.-H. Yeon, J.-W. Lee, H.S. Park, S.-K. Hyun, Deformation banding and static recrystallization in high-strain-rate-torsioned Al-Mg alloy, *J. Alloys Compd.* 814 (2020) 152311.
- [35] A.A. Tiamiyu, U. Eduok, J.A. Szpunar, A.G. Odeshi, Corrosion behavior of metastable AISI 321 austenitic stainless steel: Investigating the effect of grain size and prior plastic deformation on its degradation pattern in saline media, *Sci. Rep.* 9 (2019) 1–18.
- [36] A.G. Rao, V.A. Katkar, G. Gunasekaran, V.P. Deshmukh, N. Prabhu, B.P. Kashyap,

Effect of multipass friction stir processing on corrosion resistance of hypereutectic Al–30Si alloy, *Corros. Sci.* 83 (2014) 198–208.

- [37] M. Rafieezad, M. Mohammadi, A. Gerlich, A. Nasiri, Enhancing the corrosion properties of additively manufactured AlSi10Mg using friction stir processing, *Corros. Sci.* 178 (2021) 109073.
- [38] A. Shahriari, L. Khaksar, A. Nasiri, A. Hadadzadeh, B.S. Amirkhiz, M. Mohammadi, Microstructure and corrosion behavior of a novel additively manufactured maraging stainless steel, *Electrochim. Acta.* 339 (2020) 135925.
- [39] W. Chen, G. Van Boven, R. Rogge, The role of residual stress in neutral pH stress corrosion cracking of pipeline steels–Part II: Crack dormancy, *Acta Mater.* 55 (2007) 43–53.
- [40] G. Van Boven, W. Chen, R. Rogge, R. Sutherby, The Effect of Residual Stress on Pitting and Stress Corrosion Cracking of High Pressure Natural Gas Pipelines, *Acta Mater.* 55 (2007) 29–43.
- [41] R. Ly, K.T. Hartwig, H. Castaneda, Influence of dynamic recrystallization and shear banding on the localized corrosion of severely deformed Al–Mg–Si alloy, *Materialia.* 4 (2018) 457–465.
- [42] R. Ly, K.T. Hartwig, H. Castaneda, Effects of strain localization on the corrosion behavior of ultra-fine grained aluminum alloy AA6061, *Corros. Sci.* 139 (2018) 47–57.
- [43] X.P. Nie, Q.P. Cao, Z.F. Wu, Y. Ma, X.D. Wang, S.Q. Ding, J.Z. Jiang, The pitting

corrosion behavior of shear bands in a Zr-based bulk metallic glass, *Scr. Mater.* 67 (2012) 376–379.

# **Chapter 8: High strain rate torsional response of maraging steel parts produced by laser powder bed fusion techniques: deformation behavior and constitutive model**

## **8.1. Introduction**

Laser powder bed fusion (LPBF) is one of the powder-based additive manufacturing techniques that allows the fabrication of three-dimensional parts with intricate designs from a computer-aided design (CAD) model [1]. During the LPBF process, powder metal particles are melted by a scanning laser beam and are consolidated on top of each other. Laser energy melts powders and creates solid metal upon cooling [2]. Additive manufacturing processes offer several prominent advantages over conventional manufacturing methods, such as reducing manufacturing time and costs, freedom of design, and capacity for fabricating complex parts [2].

Progress in laser additive manufacturing has led to the development of metal parts, including maraging steel parts with remarkable mechanical properties as opposed to the conventional counterparts [3]. Special attention has been paid to maraging steels ascribable to their promising properties in different applications. Maraging steel C300 (M.S) is a special class of Fe-Ni alloys containing a relatively low carbon content and a martensitic phase that is reinforced with intermetallic precipitates. The high strength and high ductility of M.S makes it an attractive candidate for aircraft, aerospace, tool, and die-making industries [4].

Recent research studies on the properties of LPBF-M.S under quasi-static loading conditions have been the center of interest. The emphasis has been on laser process optimization and annealing exploration. Regarding the effect of process parameters, Souza

*et al.* [5] looked into the effect of part position, layer thickness, and laser speed on the mechanical performance of LPBF-M.S. They reported that layer thickness plays a significant role on manufacturing time, concluding that increasing the layer thickness led to reduced manufacturing time. Regarding the effect of the annealing procedure, Conde *et al.* [6] focused on suitability of different annealing procedures on the mechanical properties of LPBF-M.S. They observed that martensite-to-austenite transformation during the aging process increases the fraction of austenite. However, the presence of austenite phase in the matrix improves the ductility of M.S parts at the expense of strength [6].

As M.S parts in industries experienced high strain-rate loadings such as collision, deformation performance during high speed is important. Despite comprehensive studies on annealing procedures, process parameters and plastic deformation during quasi-static loading condition of LPBF-M.S, mechanical performance during dynamic loading has not been studied thoroughly. However, not many research works are available on the high strain-rate compressive performance of M.S produced by the LPBF technique [7][8].

The high strain-rate performance of materials attracted much attention over the last years. The modified split Hopkinson bar technique designed by Kolsky in 1949, has been employed to study materials' dynamic deformation over the years [9]. The Hopkinson bar can be used for various loading modes such as torsion, compression, and tension. Baker *et al.* [10] introduced split Hopkinson torsion bar (SHTB) for research on the dynamic torsion performance of materials. During the past years, SHTB was implemented in numerous studies to explore the dynamic torsional properties of materials [11].

In practice, M.S parts tend to be employed in complex loading environments, involving a torsional mode of mechanical loading. As far as the authors can tell, there are

no available reports on the high-speed torsion performance of M.S in the open literature. The main purpose of the research is to examine the change of the twist angle on the deformation performance of the alloy under pure shear loading. A series of tests have been carried out on each specimen with the modified SHTB to investigate the relationship between macroscopic stress-strain reaction of the materials with the microstructure evolution during deformation. Needless to say, that numerical simulation offers an effective approach to predicting deformation performance and helps to reduce the cost and time of experimental investigations. In this study, two constitutive equations (Kobayashi-Odd and Nemat-Nasser models) were implemented with success to describe the flow performance of LPBF-M.S under dynamic mechanical loading in torsion.

## 8.2. Materials and methods

### 8.2.1. Material and process parameters

Gas atomized M.S powder was used for manufacturing the investigated specimens. Table 8.1 shows the chemical composition of the M.S powder.

Table 8. 1. Chemical composition of M.S based on EOS datasheet.

Element	Fe	Ni	Co	Mo	Ti	Al	C
Composition (wt. %)	balance	17-19	8.5-9.5	1.5-5.2	0.6-0.8	0.05-0.15	<0.03

The LPBF technique was utilized for the fabrication of M.S specimens in this study. Using an EOS M290 additive machine, hexagonal samples were produced. The process parameters of LPBF are given in Table 8.2. These parameters having been selected so that maximum density and the lowest fraction of defects could be achieved [4]. The strip scan

strategy (rotation of laser beam about  $67^\circ$  after each layer deposition) was employed in this process. The LPBF process was carried out under a 99.99% argon gas atmosphere, and the bed temperature was held at  $40^\circ\text{C}$ .

Table 8. 2. Process framework of the LPBF process.

Laser power (W)	Scanning speed (mm/s)	Layer thickness ( $\mu\text{m}$ )	Hatch distance ( $\mu\text{m}$ )
285	960	40	110

### 8.2.2. High strain rate torsion test

The schematic representation of the SHTB apparatus implemented in this study is shown in Fig 8.1. This apparatus made up of a transmission bar, an incident bar, a loading wheel to twist the incident bar and a clamp with a abrupt release mechanism. Fig 8.2 shows the geometry of the test specimens, a thin-wall tube with hexagonal flanges subjected to pure shear during the rapid torsional loading. Thin-wall specimens were tested at room temperature using the angles of twist of 3, 6, 9, and 12 degrees. In order to obtain reliable data, at least three specimens were tested for each angle of twist.

The thin-wall test specimens were placed between two elastic bars. Torque is remained in the incident bar in the middle of the loading wheel and clamp by twisting the loading wheel up to a certain angle, which is called the angle twist. The gathered torque is released by releasing the clamp instantaneously and propagates in the form of elastic waves along the incident bar. This wave (called incident wave) is arrested by the strain gauge adhered to the incident bar. Some of the elastic waves are returned on reaching the specimen. The reflected waves are gained by the strain gauge adhered to the incident bar. Some of the incident waves transmitted across the specimen rapidly twisted before propagating onto the

transmitter bar as transmitted waves. The strain gauge attached to the transmitter bar captured the transmitted waves. The strain gauges are located at appropriate distances from the specimen to avoid overlaying of the transmitted and incident waves. Shear strain, strain rate, and shear stress are computed from the elastic waves gained by the strain gauges adhered to the bars [12]. As the incident bar should remain in the elastic region, twist angle must be lower than  $27^\circ$  [13].

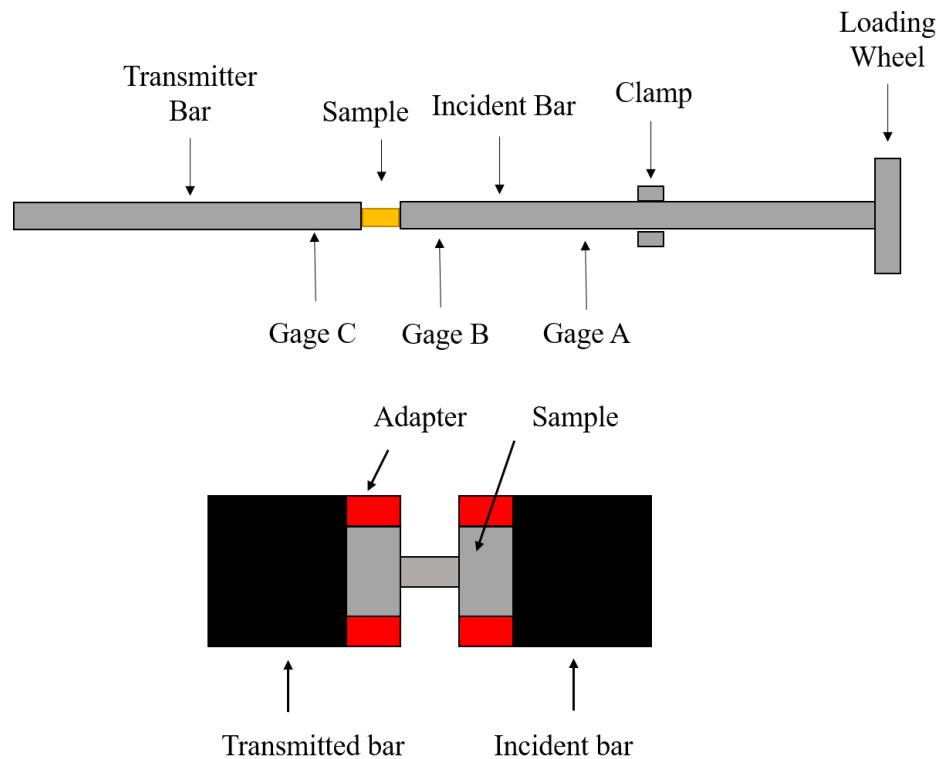


Fig 8. 1 Schematic of the torsional SHTB apparatus.

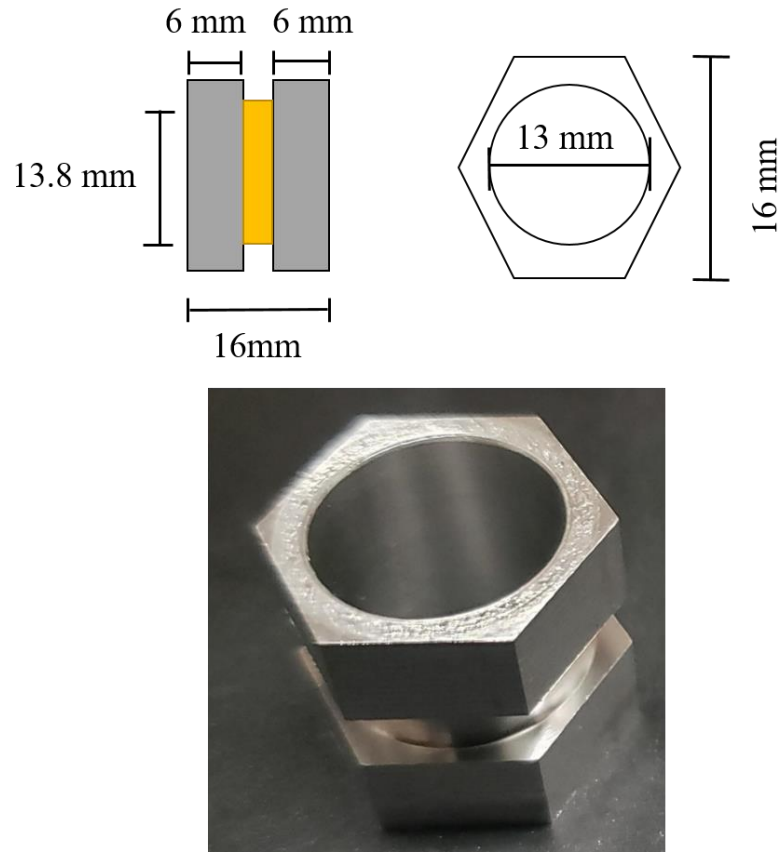


Fig 8. 2 The geometry of specimens in the SHTB test.

During torsional deformation, shear stress ( $\tau$ ) from the measured torque ( $M$ ) for any radial position and thickness can be computed through equation (1), where  $t$  is the wall thickness and  $r$  is the mean radius.

$$\tau = \frac{M}{2\pi t r^2} \quad (8-1)$$

The shear strain ( $\gamma$ ) can be determined from the angle of rotation using the following equation, where  $L$  is specimen's gage length and  $\phi$  is the angle of rotation.

$$\gamma = \frac{\phi r}{L} \quad (8-2)$$

Since shear strain varies linearly with distance from the center to the surface of a torsion specimen, the circumferential edge, where shear strain is maximum, this study focuses on. This basic knowledge of torsion performance is employed in SHTB system for the purpose of estimating the strain-stress response of the test material at high speeds. Needless to say, that in this test, the specimen experienced uniform and pure shear stress. Equations for calculating shear stress and shear strain rates from the transmitted, reflected, and incident waves are provided as follows [14][15]:

$$\dot{\gamma} = \frac{2CD_s}{L_s D} \gamma_R \quad (8-3)$$

$$\gamma = \frac{2CD_s}{L_s D} \int_0^t \gamma_R dt \quad (8-4)$$

$$\tau = \frac{GD^3}{8D_s^2 t_s} \gamma_T \quad (8-5)$$

where  $D_s$  is the average diameter of the thin wall of the specimen and  $C$  is the speed of the sound in the bar,  $D$  is the diameter of the input/output bar,  $L_s$  is specimen's gage length,  $t_s$  is the wall thickness of the specimen and  $G$  is the shear modulus of the bar material.  $\gamma$  (T) is transmitted strains and  $\gamma$  (R) is reflected strains. By using the angles of twist from 3, 6, 9 and 12 degrees, strain rates of  $260 \text{ s}^{-1}$ ,  $650 \text{ s}^{-1}$ ,  $720 \text{ s}^{-1}$ ,  $650 \text{ s}^{-1}$  were achieved in the specimens, respectively.

### 8.2.3. Microstructural studies

The focus of microstructural studies was on the thin wall as shown in Fig 8.3. To this purpose, samples were sectioned parallel to the axis of the specimen. Sample preparation for microscopy included polishing with SiC papers and electrochemical etching with 3% Nital solution. The microstructural inspection of twisted samples was performed using a Hitachi SU-70 Field Emission Gun (FEG) ultra-high-resolution SEM. A FEI Quanta™ 450 FEG-SEM microscope was utilized for texture measurement. With the TSL® OIM data collection software, the diffraction patterns were gathered and the OIM data analysis software was utilized for post processing of data. Electron backscattering diffraction (EBSD) scans were performed on an area of  $500 \times 500 \mu\text{m}^2$  with a step size of 500 nm to cover detailed microstructural features of the torsion samples.

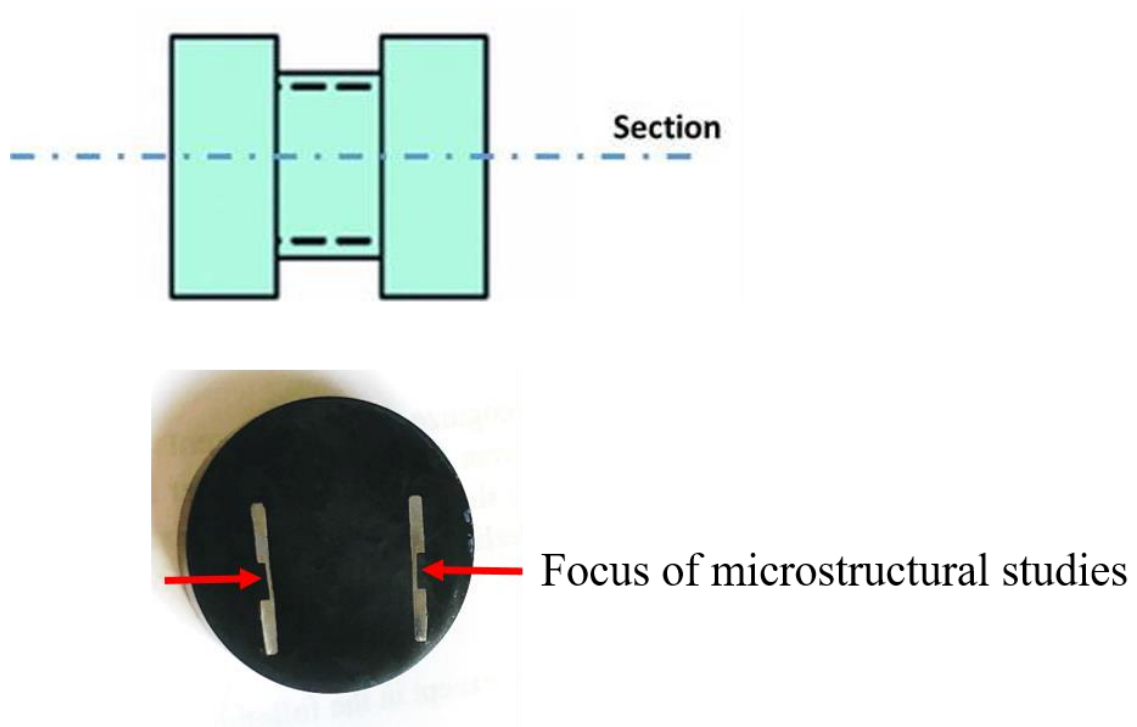


Fig 8. 3 Schematic and real samples used for microstructural studies.

### **8.3. Results and discussion**

#### **8.3.1. Dynamic torsion test of LPBF-maraging steel samples**

Fig 8.4 shows the typical shear strain-shear strain rate curves for the specimens at different twist angles. In this study, the maximum strain rate is defined as official strain rate. It may be noted from Fig 8.4 that strain rates first increase with strain and then decreases. In dynamic compression, it was observed that strain rates increased until they reached a plateau and then decreased [7]. However, in dynamic torsion, a significant second stage (plateau) has not been observed. This shows that dynamic performance is closely attributed to the stress state. The second stage was associated with competition between thermal softening (associated with work to heat transformation) and the rate of strengthening (ascribable to strain hardening and/or strain-rate hardening). The lack of the second stage can be ascribable to the dominance of strain hardening over softening. In dynamic loading, at a specific strain, plastic deformation becomes inhomogeneous. This often leads to intense strain localization, which occurs when the heat generated by plastic work cannot dissipate at sufficient speed, leading to increase in temperature locally and thermal softening [16].

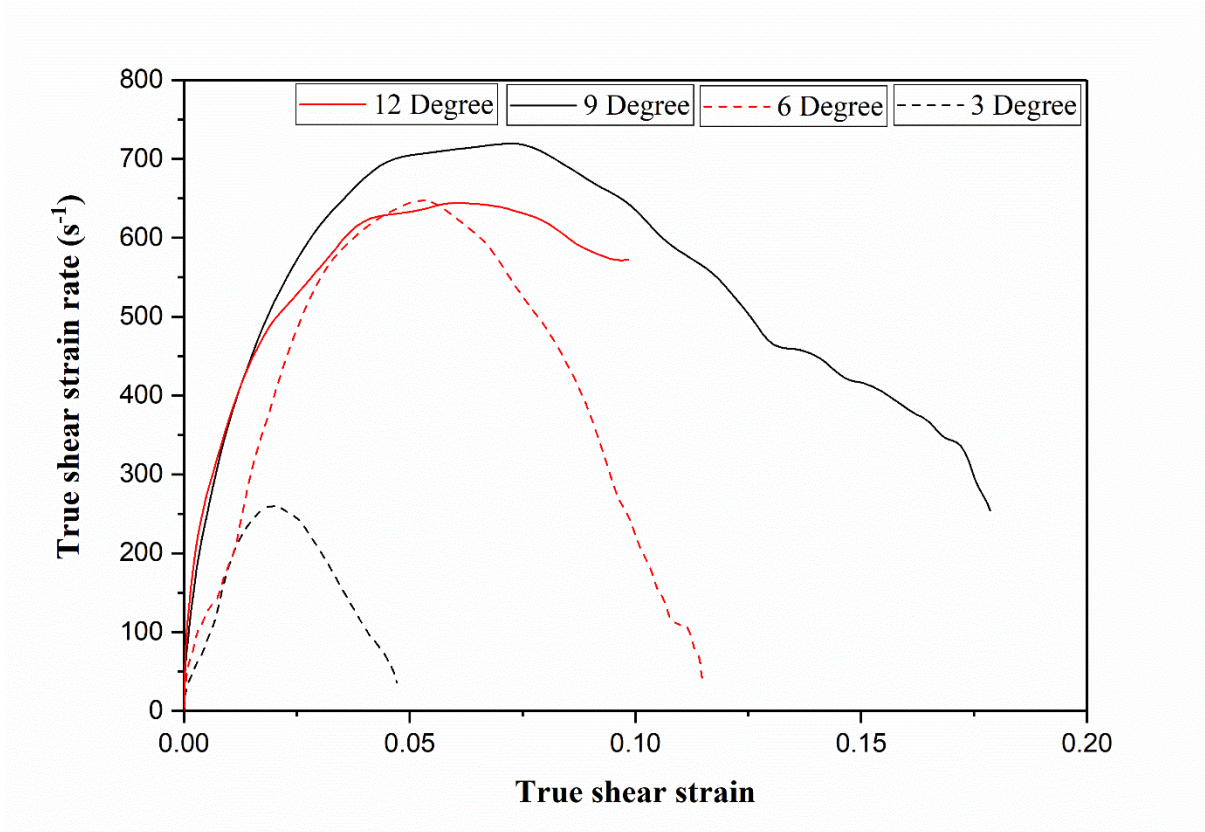


Fig 8. 4 True strain- strain rate curves of M.S samples at different angles of twist.

Fig 8.5 shows the shear strain-shear stress curves of the M.S when deformed at angles of twists of 3, 6, 9 and 12°, which generate strain rates of 260 s<sup>-1</sup>, 650 s<sup>-1</sup>, 720 s<sup>-1</sup>, and 650 s<sup>-1</sup> in the specimens, respectively. The 0.2% offset yield shear strength, toughness, ultimate shear strength, strain, temperature rise, and strain rate sensitivity are summarized in Table 8.3. The inset shows the repeatability and reliability of the data extracted in the high-speed torsion tests. The angle of twist determines the applied torsional load resulting in shear stress generated in the specimens. It is possible to see from Fig 8.5 that strain rate has a pronounced influence on ultimate stress and yield stress. The maximum shear stress with increment in the angle of twist and strain rate enhanced, which is related to strain hardening ascribable to dislocation multiplication. Maximum shear stress of 855 MPa and

strain rate of  $650 \text{ s}^{-1}$  were achieved for the 12-degree angle of twist. The strain increment with an intensifying in strain rate is associated with the thermal softening phenomenon. With strain rate enhancement, more heat is generated in the sample, increasing strain. In this study, the maximum strain of 18% was achieved for the 9-degree angle of twist and strain rate of  $720 \text{ s}^{-1}$ . As the strain rate increased, high dense dislocation cells and dislocation walls formed in microstructure to accommodate the excess strain, which results in strength increase [11]. With strain rate enhancement, the total shear strain intensified. For specimen deformed at the 12-degree angle of twist, the shear strain decreased ascribable to excessive stress concentration. Increment of shear stress, shear strain to failure with strain rate enhancement has been previously recorded for dynamic shearing of steels [17]. Another interesting feature of the strain-stress curves is that all strain-stress curves have a very similar shape. As can be noted in shear stress-strain curves, shear stress increases with strain enhancement, indicating that the material is experiencing work hardening. The work-hardening rate (i.e., the slopes of the shear strain- shear stress curves in the plastic area) increases with strain rate enhancement. Indeed, work hardening is attributed to the generation of dislocations during plastic deformation [17]. Flow curves show the same parabolic shape, and near the end of the test, sudden drop in stress occurred ascribable to thermal softening. In other words, during first stage of deformation process, plastic strain distribution is homogenous. With continued deformation, strain distribution becomes inhomogeneous, and localized deformation likely occurred leading to fracture of specimen. When loaded at an angle of twist of 12 degree, producing a strain rate of  $650 \text{ s}^{-1}$ , failure occurred in the M.S samples during the dynamic torsion test.

With the angle of twist of 6 °and 12° (Fig 8.5), a small plateau region can be observed, which is related to the opposition of thermal softening and strain hardening. With the increase in the angle of twist to 12, thermal softening became dominant, which resulted in the failure of the specimen.

Strain rate sensitivity ( SRS) is described as the dependency of strain rate hardening on strain rate, where the increment of the flow stress ascribable to strain rate enhancement can be estimated via the strain rate sensitivity parameter ( $\alpha$ ) [18]. Enhancement of strain rate sensitivity with an increase in strain rate has been discussed before [17]. The strain rate sensitivity of samples at different strain rates can be computed through equation (6) where  $\tau$  is the shear stress and  $\dot{\gamma}$  is the shear strain rate [18].

$$\alpha = \frac{\partial \tau}{\partial (\ln \dot{\gamma})} = \frac{\tau_2 - \tau_1}{\ln \left( \frac{\dot{\gamma}_2}{\dot{\gamma}_1} \right)} \quad (8-6)$$

At a given strain, strength increased by increasing strain rates, which means SRS improves with the enhancement of strain and strain rate. Results of strain rate sensitivity are listed in Table 8.3. It is possible to see that, with strain rate increment, strain rate sensitivity increased which is ascribable to increment of dislocation density [17]. However, at an angle of twist of 12 degrees, strain rate sensitivity decreases under the circumstances of intensive shear localization, which results in the dominancy of thermal softening and fracture of the sample. Shen *et al.* [19] attributed negative values of strain rate sensitivity to stress concentration. With the localization of strain and thermal softening, dislocation mobility and consequently the SRS decreased. These strain rate sensitivity changes show that the

changes in flow stress result from the occurrence of work hardening and thermal softening phenomena.

During dynamic deformation, ascribable to localized strain, thermomechanical instability occurred, whereby heat cannot dissipate from some regions and thermal softening occurred. The deformation temperature rise during the dynamic test can be computed through equation (8.7) [20][21]:

$$T - T_0 = \Delta T = \frac{\beta W}{\rho \cdot C_v} \quad (8-7)$$

where  $T_0$  is the temperature of the sample before the test, which is the 25°C, and  $T$  is sample's temperature after the test.  $\beta$  is the Taylor-Quinney parameter and can be calculated with this equation [20][21]:

$$\beta = \frac{Q_p}{W_p} \quad (8-8)$$

$$W_p = \int \tau \cdot d\gamma \quad (8-9)$$

where  $Q$  is the generated heat stemmed from plastic work ( $W_p$ ) during high speed deformation.  $\gamma$  and  $\tau$  are the shear strain and shear stress, respectively. M.S specific heat capacity ( $C_v$ ) is  $450 \pm 20$  J/kg°C and the density ( $\rho$ ) of M.S is  $8.2$  g/cm<sup>3</sup>. Taylor-Quinney coefficient is the efficiency of the thermomechanical conversion, which is assumed to equal 0.9, which means that 90% of plastic work converts to heat [20][21]. The temperature rise of samples after the dynamic torsion test was estimated and is given in Table 8.3. Although the temperature rise is not significant, with an increase of angle of twist from 3 degree to

9 degree, the temperature increased, and decreased when the angle of twist was increased from 9 to 12 degree.

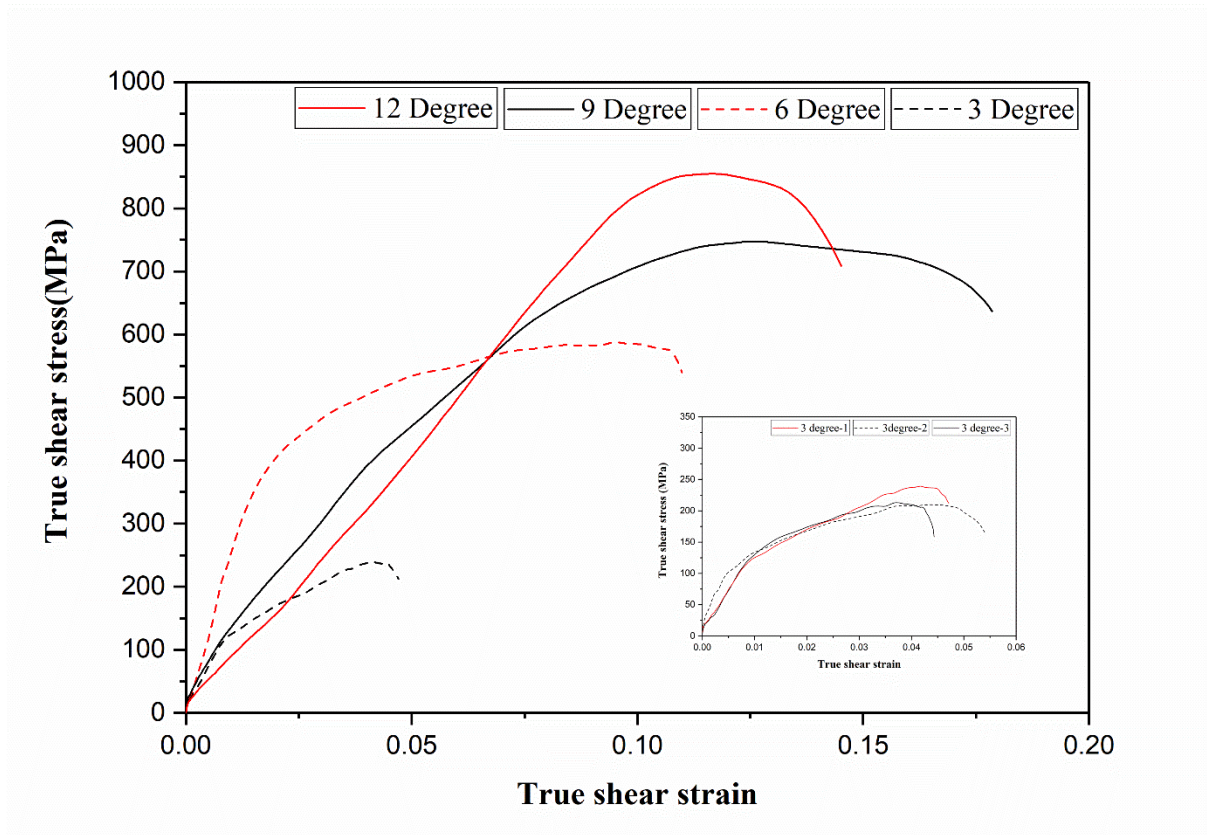


Fig 8. 5 Dynamic true shear strain-true shear stress curves of the M.S samples deformed at the angles of twist 3, 6, 9 and 12. The specimens' flow curves deformed at angle of twist 3 in the inset ensure repeatability.

Table 8. 3. Dynamic mechanical properties of the twisted M.S samples fabricated by LPBF.

The angle of twist (Degree)	Strain rate ( $s^{-1}$ )	Yield stress (MPa)	Maximum shear stress (MPa)	Total strain (%)	Toughness ( $MJ/m^3$ )	Temperature rise $^{\circ}C$	Strain rate sensitivity (MPa)
3	260	189.6	239.1	4.7	7.97	1.99	143.52
6	650	389.5	587.5	10.98	53.26	13.31	198.79
9	720	581.4	747.3	17.85	99.79	24.94	252.30
12	650	767.5	854.8	11.97	58.29	14.57	231.56

### 8.3.2. Microstructural studies of twisted M.S samples

Figs 8.6 (a) and (b) show the initial martensitic microstructure of LPBF-M.S before deformation. The thin wall of the torsion samples was investigated with SEM, as presented in Fig. 8.3. The microstructure of LPBF-M.S in as-built condition consists of columnar, cellular, and equiaxed grains. Different morphologies can be observed in different regions of the melt pools ascribable to changes in thermal gradient and cooling rate. At the bottom of the melt pool boundaries, ascribable to high thermal gradient, the columnar morphology starts to grow and the equiaxed grains start to form in top central zones [4][22]. Furthermore, a cellular structure can be seen between columnar grains [4][22]. Fig.6 (c) and (d) show the microstructure of loaded M.S samples using an angle of twist 3 degree relative to a strain rate of  $260 s^{-1}$ . Opposed to the initial as-built sample, grains undergo grain fragmentation during high speed deformation. Consequently, the unique microstructure of LPBF-M.S with columnar, equiaxed and cellular structure is destroyed.

After dynamic deformation at high speeds, a drastic change in microstructure can be observed. As deformation proceeds during dynamic loading, ascribable to localized adiabatic heating and the correlated thermal softening leading, loss in load carrying

capacity happened and as a result, localized shear deformation developed gradually inside the narrow bands, which are entitled adiabatic shear bands (ASBs) [16]. The advancement of localized deformation is a progressive process that occurs ascribable to localized adiabatic heating and the associated thermomechanical instability and results in ASB formation [16]. To prevent their harmful effect, it is required to understand the mechanism and conditions under which shear banding develop in the material.

It should be noted that ,the geometry of the torsion sample provides inhomogeneous strain and temperature distribution and accelerates ASBs formation in the thinner region of the specimen [23]. Initiation and propagation of ASBs depend on stress mode, sample geometry, defects, etc. Compared to LPBF-M.S deformed in compression mode [7], ASBs were observed at lower strain rates in M.S deformed under dynamic torsional loading. Indeed, geometric discontinuity and stress mode accelerates inhomogeneous plastic deformation resulting in the rapid formation of ASBs. ASBs would initiate when the effective strain rate and strain reach a critical value. This critical strain rate value implies that the stress decreases ascribable to a discontinuous form of the torsion sample.

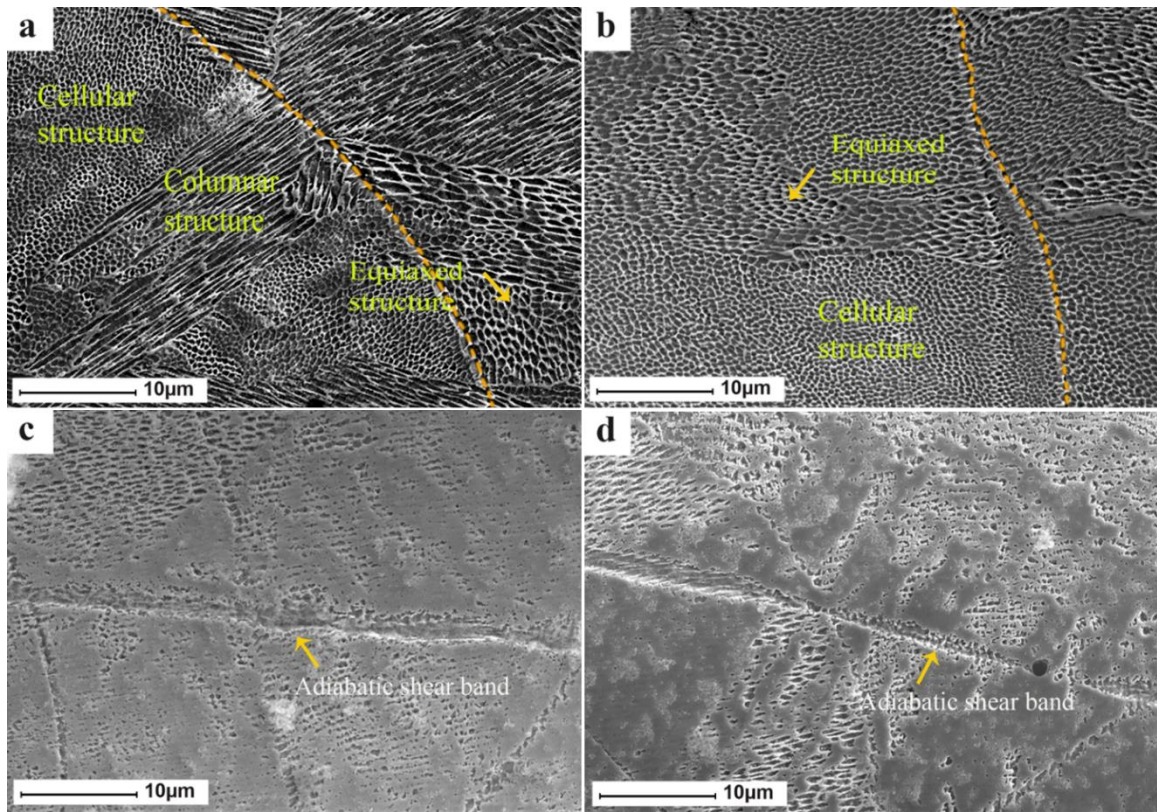


Fig 8. 6 Microstructures of of the a) and b) M.S in as-built condition, c) and d) deformed M.S at strain rates of  $260 \text{ s}^{-1}$ .

In addition, Figs 8.7 (a) and (b) show the microstructure of samples deformed with an angle of twist  $6^\circ$  and strain rate of  $650 \text{ s}^{-1}$  and Figs 8.7 (c) and (d) show the microstructure resulted from an angle of twist of 9 degrees and strain rate of  $720 \text{ s}^{-1}$ . As can be seen, ASBs were detected in the deformed samples at angles of twist 6 and 9 degrees in the middle of the sample (thin wall). It is worth mentioning that these ASBs developed along the shear direction (twist direction). Material inside ASBs is subjected to large strains resulting in a temperature rise, which leads to structural softening, and makes ASBs susceptible to voids and cracks formation [16]. Kobayashi *et al.* [24] proposed a model considering void nucleation and growth at a high speed torsion test. They suggested that

up to the instability strain, deformation is controlled by strain hardening and thermal softening, and at the instability strain, voids form in the gauge section of the torsion specimen. These voids and cracks, which are developed inside the ASBs ascribable to shear instability leads to fracture of material at higher strain rates.

The temperature rise in Table 8.3 is calculated based on the total strains of the specimens. However, it is well known that the strain inside the ASBs is much higher, and as a result, the temperature inside ASBs is much more than what is calculated. Measuring the temperature inside the shear bands is extremely difficult ascribable to the short duration of initiation and propagation of the ASBs. Zhou *et al.* [25] measured the shear band propagation speed of C300 M.S using a high-speed camera, and they figured out that the ASBs propagation speed is about  $1200 \text{ ms}^{-1}$ . Their experiments also showed that the highest temperature of the ASBs in C300 M.S is about  $1400^\circ \text{ C}$  (90% of its melting point). Their investigation revealed that temperature inside the ASBs is dependent on impact speed. Therefore, it can be postulated that at the higher strain rates, evolution of shear bands occurs earlier, and propagation is faster. Besides, Guduru *et al.* [26] studied the beginnings and extension of shear bands in M.S. They found out that temperature distribution inside the ASBs is non-uniform. For torsion samples, the highest temperature happened at the middle of the gage section of tubular thin-walled torsion specimen where ASBs were found [23] [24]. It should be noted that as the martensite-austenite phase conversion is diffusion-based, ascribable to lack of time in dynamic deformation, phase transformation could not occur inside ASBs [23]. Therefore, it can be concluded that microstructural changes ascribable to phase transformation are not involved in the final microstructure of the ASB [23].

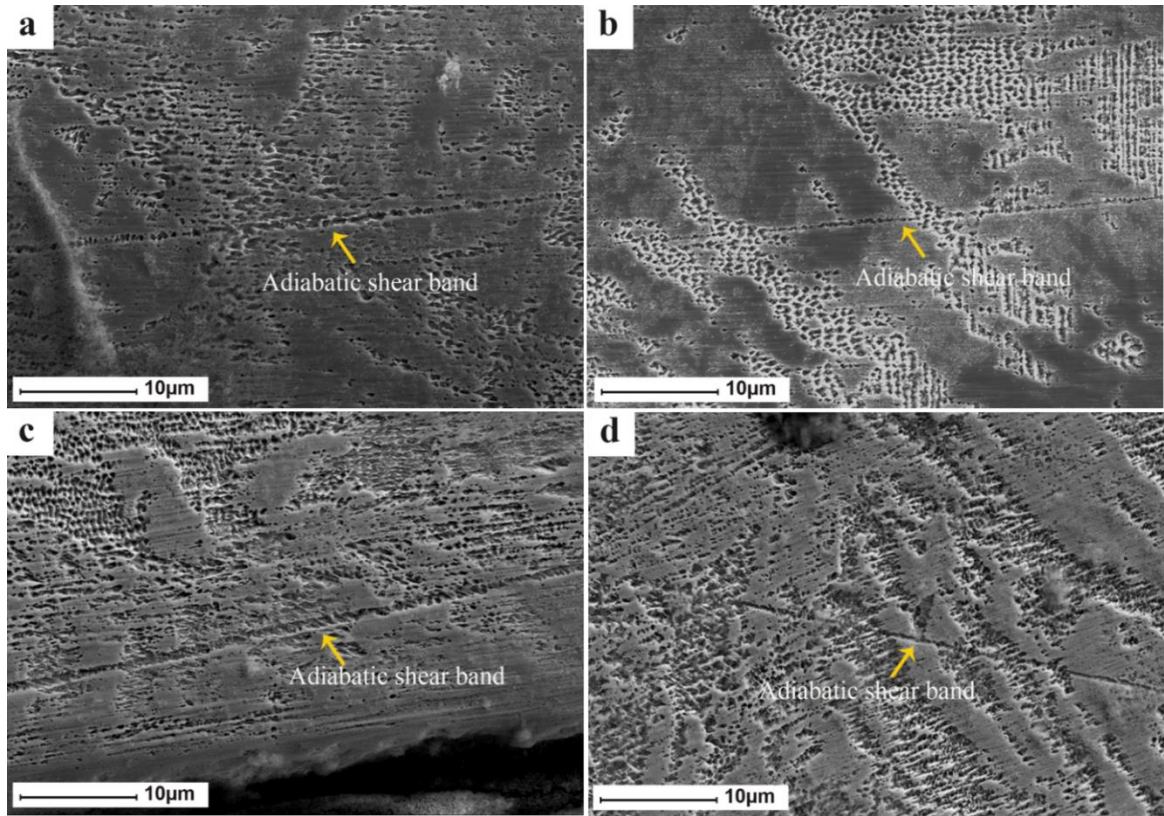


Fig 8. 7 Microstructures of the deformed M.S samples at strain rates of a) and b)  $650 \text{ s}^{-1}$ , c) and d)  $720 \text{ s}^{-1}$ .

Fig 8.8 shows the fracture surfaces of the M.S sample loaded at the angle of twist 12 degrees (strain rate of  $650 \text{ s}^{-1}$ ) where complete separation occurs at the strain value of 12%. When the alloy was loaded at the strain rate of  $650 \text{ s}^{-1}$ , fracture happened in the extensive localized shearing region at the middle of the sample. This type of fracture was observed before in tubular thin-walled specimens during SHTB test [17]. In the thin part of the sample, the shear strain accumulates in the middle of the specimen, which leads to fracture of torsion samples in this region. It can be noted that, the primary failure mechanism in this experiment is localized shearing. Localized shearing is an important mode of deformation, which can lead to the fracture of a sample. Under dynamic loading, ascribable to the dropping of load-carrying capacity in the adiabatically heated region,

ASBs formed in the microstructure, which are susceptible regions for void and crack formation. Nucleation, growth, and coalescence of microvoids inside ASBs occurred, which accelerates the fracture of material along the ASBs [16]. It is postulated that after an increase of temperature inside these ASBs, they cooled rapidly by surrounding bulk material and this leads to residual stress development, which results in failure [16].

The fracture surface shows a tearing type of fracture. As shown in Fig 8.8 (a), in the middle of the sample, localized shear deformation eventually led to the cleavage fracture. It can be proposed that ASBs that formed in the thin wall, encircle the specimen and led to the fracture. Because of the variation in the plasticity of ASBs and that of neighboring area, tensile force is generated inside the ASBs [7]. Ascribable to this tensile force, the opening of cracks inside the ASBs occurs, which results in the tearing of the sample. Mode III fracture (tearing mode), which propagates toward the circle leading to cleavage fracture of the torsion sample can be noted in Fig 8.8 (b), (c), and (d). The detection of failure mode is important as it predicts the failure of materials in actual applications.

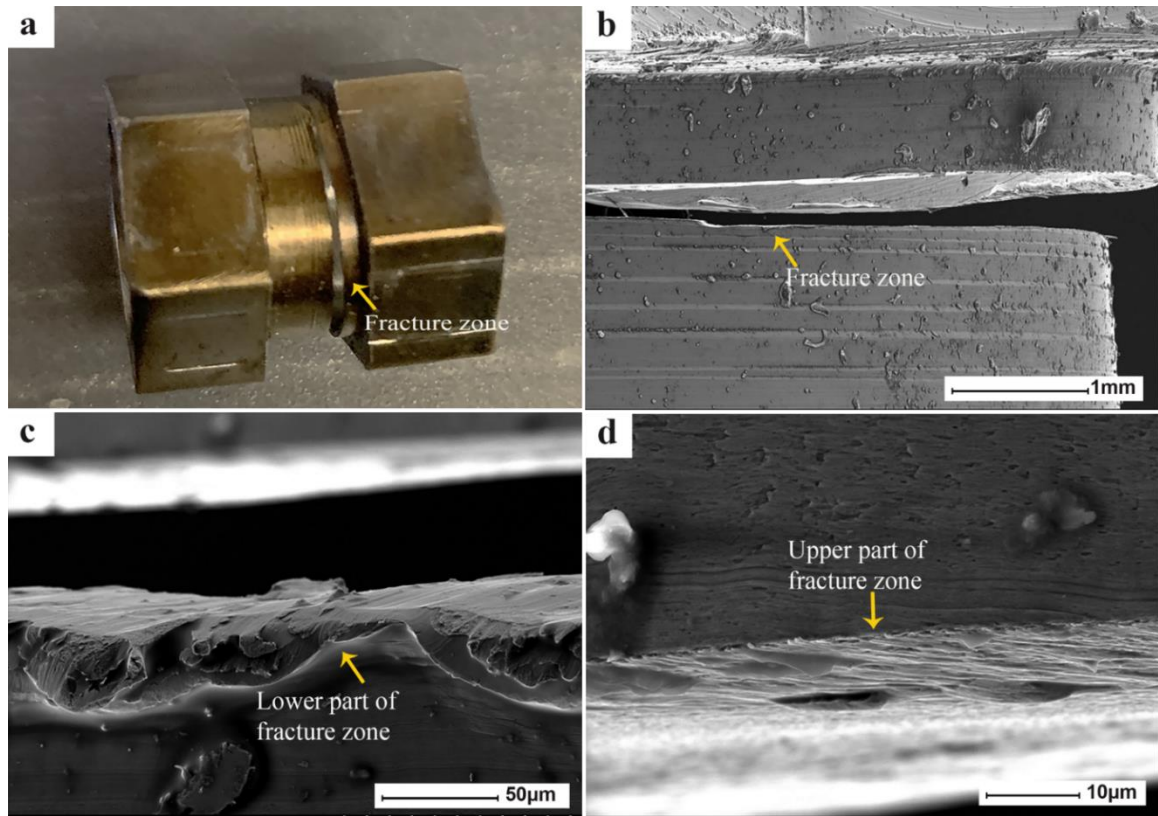


Fig 8. 8 Fractography of the deformed M.S samples at angle of twist of 12 and strain rates of 650 s<sup>-1</sup>.

### 8.3.3. Texture evolution of LPBF-M.S during dynamic torsion

Fig 8.9 shows inverse pole figure (IPF-Z) maps (Z is the direction of twist) of LPBF-M.S after torsion test with the angle of twist of 3, 6, and 9°, which correspond to strain rates of 260, 650, and 720 s<sup>-1</sup> in the specimens, respectively. EBSD scans were conducted on the thin wall of tubular specimens, where the stress concentration of the twisted samples is maximum. Along the Z direction (shear direction), ASBs formed whereby these ASBs encircle the specimen leading to fracture of specimen deformed at the 12-degree angle of twist. It is evident from the IPF maps that crystal orientations are arranged along specific directions with enhancement of angle of twist and strain rate, and severe grain fragmentation and refinement occurred. The IPF maps at high speed show significant grain

size reduction (Fig 8.9 (c)). This grain refinement is also responsible for the higher shear strength of the specimen at higher strain rates based on the Hall-Petch relationship[27]. Grain refinement is not the only mechanism for strength increment with increase of strain rate and dislocation multiplication is also involved [7]. The EBSD results showed that grain size diameter for the angle of twist of 3 degrees is  $25.40 \pm 3.14 \mu\text{m}$ , while that for the angle of twist of 9 degrees is  $16.18 \pm 3.10 \mu\text{m}$ . For specimens deformed at an angle of twist of 9 degrees and strain rate of  $720 \text{ s}^{-1}$ , high shear strength of 750 MPa was achieved ascribable to grain refinement. The corresponding IPF map (cf. Fig. 9(c)) shows clustering of orientations near (110) planes (green color) with the increment in strain rate. To accommodate intense shear in the thin part of the specimen, slips system are activated. In BCC structures such as M.S, slip planes are  $\{112\}$ ,  $\{110\}$ , and  $\{123\}$  and the direction of slip is always  $\langle 111 \rangle$  (close packed direction) [28]. In other words, slip planes such as  $\{110\}$  will be triggered in torsion loading mode to the accommodation of the imposed strain. It may be noted that during high speed deformation, plastic inhomogeneity causes the evolution of elongated grains across the shear direction. In Fig 8.9 (c), elongated grains can be observed in the direction of the twist.

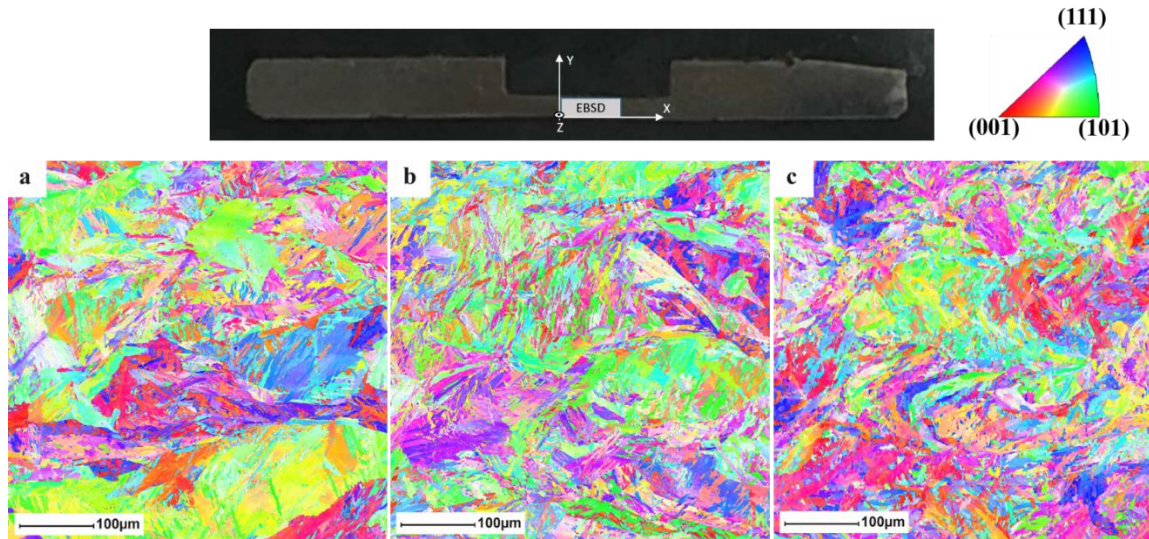


Fig 8. 9 IPF-Z maps of LBPF-M.S samples after torsion test at the angle of twist of (a) 3, (b) 6 and (c) 9 degrees and strain rate of a) 260, b) 650 and c) 720  $s^{-1}$ , respectively.

Fig 8.10 shows (100) and (111) pole figures of LPBF-M.S after torsion test at the angle of twist of 3, 6, and 9 degrees corresponding to of 260, 650, and 720  $s^{-1}$ , strain rates respectively. As can be seen, with an increase of angle of twist and strain rate, (110) planes rotated and place along the direction of shear to accommodate plastic deformation. Torsion loading up to the strain rate of 650  $s^{-1}$  first increases texture intensity, which then decreases with strain rate increment to 720  $s^{-1}$ . Tiwari *et al.* [15] conducted a study focusing on texture formation in an Al-Zn-Mg-Cu alloy during high speed deformation in pure shear (torsion) using SHTB. They concluded that texture weakening occurred with strain rate increment, as observed in the current study.

According to Canova *et al.* [29], texture weakening shall take place for high speed compression and tension, and texture strengthening should be held for high speed shear deformation. Nevertheless, the current study (same as Tiwari's study) does not comply with Canova's.

Guaro *et al.* [30] attributed the texture weakening at high speed to grain fragmentation. From the IPF map of the specimen loaded using the angle of twist of 9 degrees and strain rate of  $720 \text{ s}^{-1}$  (Fig. 9 (c)), significant grain fragmentation occurred, which resulted in texture weakening. Guaro *et al.* believe that grains can not reorient completely at high speed ascribable to lack of time, resulting in grain fragmentation [30]. As deformation proceeds, dislocations are generated, and changes in orientation within grains will occur. However, ascribable to lack of time, entire regions of grain can not orient, resulting in grain fragmentation. The true reason of fragmentation has to do with strain heterogeneities, which result from interaction processes between dislocations. These interaction processes are affected by the state of straining and hence fragmentation is more pronounced at high speeds.

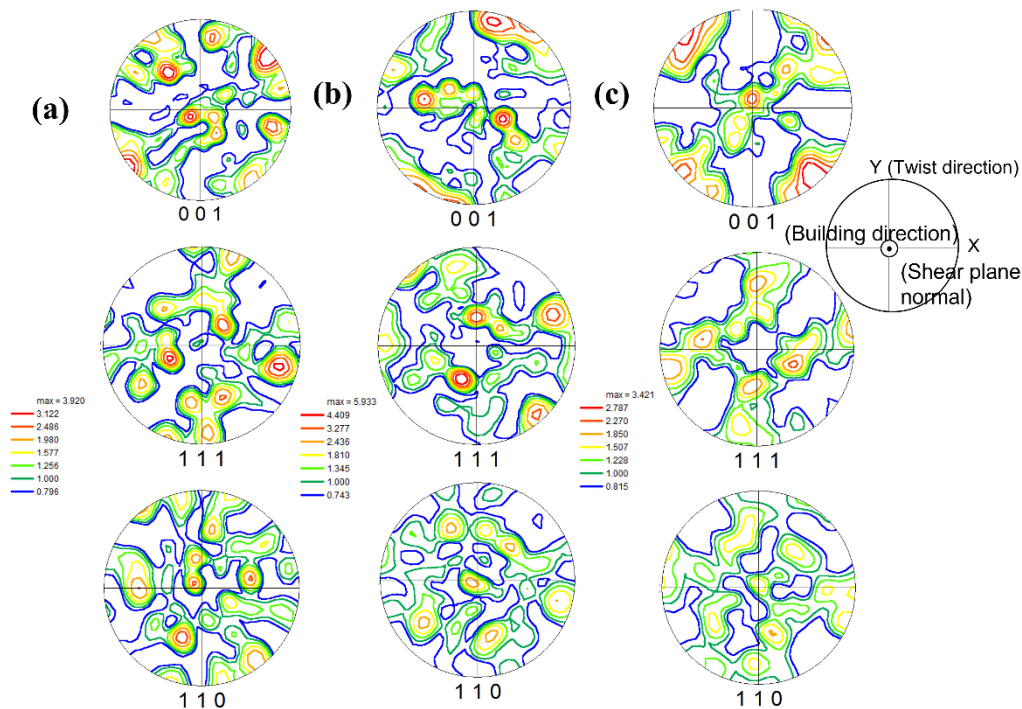


Fig 8. 10 (001), (110) and (111) pole figure of LCPF-M.S samples after torsion test at strain rate of a) 260, b) 650 and c) 720  $\text{s}^{-1}$ .

Orientation distribution function (ODF) maps at  $\phi_2 = 0$  and  $45^\circ$  sections for the M.S samples after torsion test at strain rates of 260, 650 and  $720 \text{ s}^{-1}$  are demonstrated in Fig 8.11. As can be seen, Goss component ( $\{110\}\langle 100\rangle$ ) and Brass component ( $\{110\}\langle 112\rangle$ ) can be seen in material after the high speed torsion test, which agrees well with pole figure and IPF maps. Shen *et al* [19] associated the evolution of Goss and Brass texture to shear banding.  $\{110\}\langle uvw\rangle$  texture was seen before in BCC structures during torsion test [31]. As observed in SEM analysis, at high speed, ascribable to localization of strain and heat, ASBs formed in the thin wall of the twisted sample. The formation of ASBs change the texture of the scanned area to Goss and Brass texture. Moreover, texture weakening in an angle of twist 9 degrees and strain rate of  $720 \text{ s}^{-1}$  can be observed.

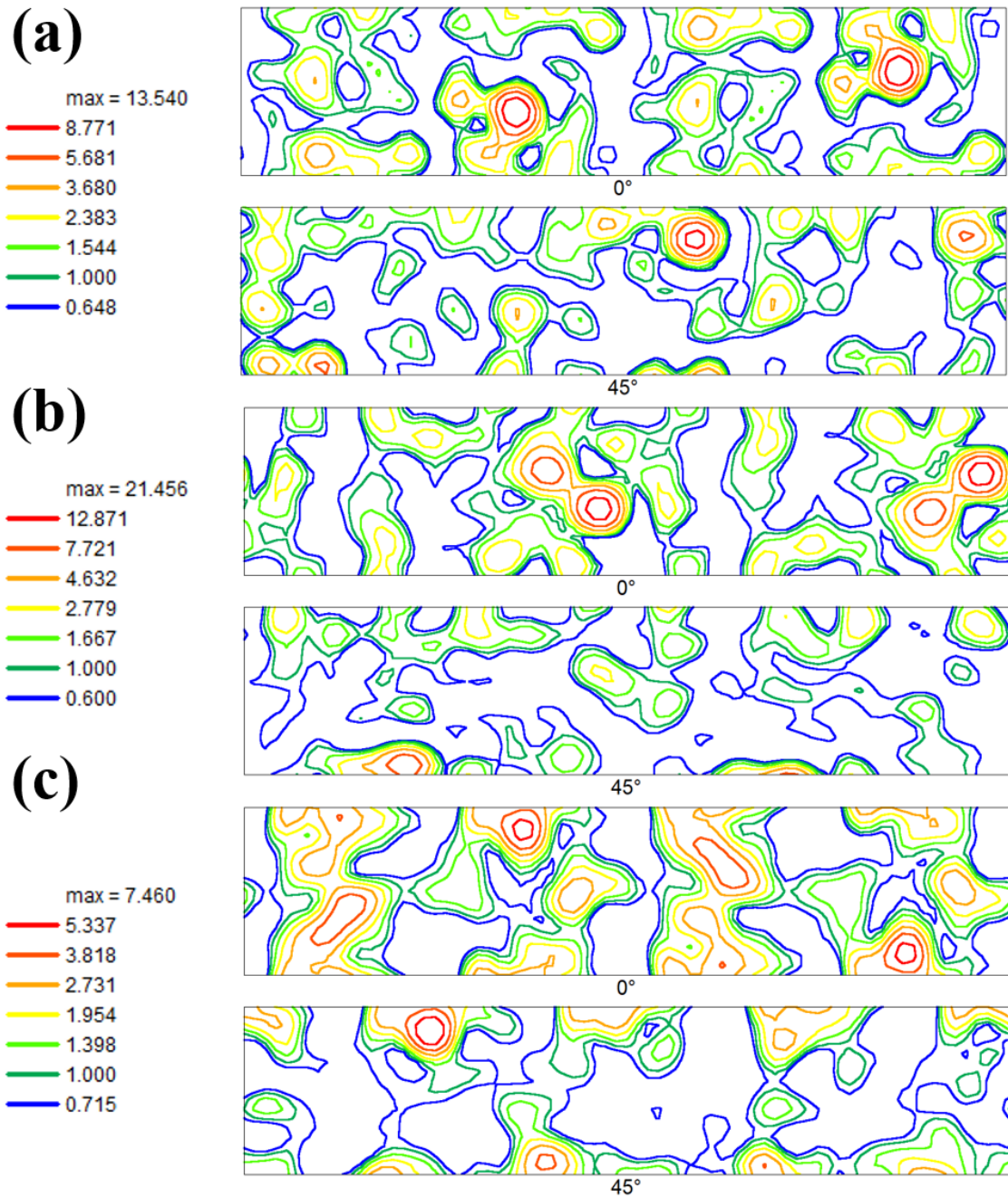


Fig 8. 11 The  $\phi_2=0^\circ$  and  $45^\circ$  sections of the ODF maps of LBPf-M.S samples after torsion test at strain rate of a) 260, b) 650 and c) 720  $s^{-1}$ .

Kernel average misorientation (KAM) map of M.S samples after torsion test are presented in Fig 8.12. Specifically, Fig 8.12 (a), (b), and (c) show the KAM maps for specimens loaded at the angle of twist of 3, 6 and 9 degrees, which correspond to strain

rates of 260, 650 and 720 s<sup>-1</sup>, respectively. In general it can be said that the KAM map is indicative of strain accumulation whereby high KAM values demonstrate deformed grains with high stored energy and high dislocation density [32].

It can be noted that, the KAM value for the samples deformed using 6-degree angle of twist is higher as compared to sample with 3-degree angle of twist, which shows that dislocation density intensifies ascribable to strain hardening. However, with the increase of twist angle to 9 degrees (720 s<sup>-1</sup>), the KAM value decreased, suggesting a reduction in dislocation density. Plastic deformation of LPBF-M.S at high speed torsion test led to the origination of new dislocations. Meanwhile, high speed causes heat generation and temperature rise as well. Temperature rise during high speed results in dislocation, annihilation of dislocation dipoles and formation of dislocation free subgrains [32]. This means that for the angle of twist of 3 to 6 degree, strain hardening has dominated over recovery.

Moreover, increasing the angle of twist to 9 degrees increased the amount of heat generated in the alloy and therefore, the formation of dislocation-free subgrains will occur more readily. In other words, thermal softening becomes more prominent for the angle of twist of 9 degrees resulting in dislocation annihilation. This change in KAM values suggests that restoration processes such as dynamic recovery occurs when the alloy is deformed using the twist angle of 9 degrees. Dynamic recovery consists of dislocations movement, resulting in subgrains and low-angle grain boundaries [15]. Furthermore, for angle of twist 9 degrees, the number fraction of KAM values <1 has increased, which confirms the development of dynamic recrystallization [15] [32]. With the increase of twist angle from 3 to 6 degrees, the dislocation density increased and the driving force for

recovery processes also increased. Activation of dynamic recrystallization processes occurred for deformation 9-degree angle of twist. ASBs are regions of localized deformation, and recrystallized grains in ASBs have been reported by other researchers [33]. Xu *et al.* [33] proposed a mechanism for dynamic recrystallization inside the ASBs based on dislocations dynamics. They suggest that during high speed deformation, grains elongate into substructures, and the elongated substructures break into sub grains, resulting in recrystallized grains. In this study, rotational dynamic recrystallization happened same as Xu's work.

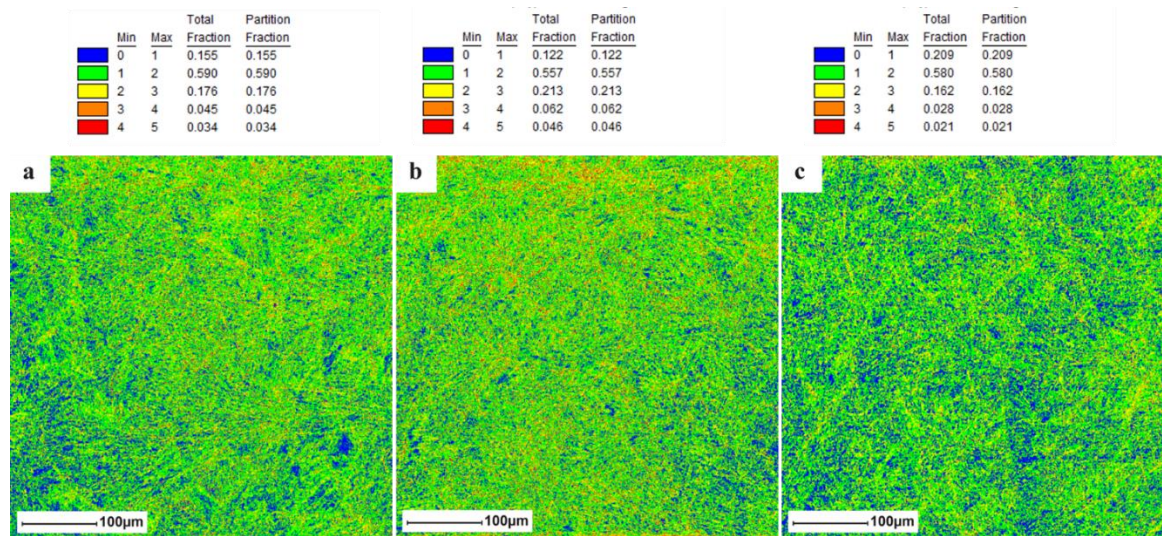


Fig 8. 12 KAM maps of LBPf-M.S samples after torsion test at strain rate of a) 260, b) 650 and c) 720 s<sup>-1</sup>.

#### 8.4. Mathematical modeling

Two constitutive equations were used for describing the response of the investigated M.S to high strain-rate torsional deformation. One of these equations is an empirical model (Kobayashi and Odd [24][17]), and the other one is a physically-based model which incorporates dislocation interaction (Nemat-Nasser and Isaacs model [34]).

#### 8.4.1. Kobayashi-Odd model

Based on the available experimental data, the dependence of true shear stress on true shear strain under dynamic loading of M.S was determined based on the equation suggested by Kobayashi and Odd [24][17]. Plastic region of the shear strain-shear stress curves can be described based on equation 8.10:

$$\tau = B. \gamma^n \dot{\gamma}^m (1 - CT) \quad (8-10)$$

where  $n$ ,  $m$ ,  $B$ , and  $C$  are material unchanging parameters and are listed in table 8.4. The term  $B. \gamma^n \dot{\gamma}^m$  represents a power law of strain rate hardening albeit the term  $(1 - CT)$  represent strain softening. In this equation, the temperature can be calculated based on equation 8.7.

Table 8. 4. Determined parameters values of Kobayashi-Odd model.

Sample	B (MPa.s)	C(K <sup>-1</sup> )	n	m
3 degree	1200	0.00001	0.5	0.002
6 degree	800	0.00001	0.25	0.05
9 degree	630	0.00045	0.45	0.2
12 degree	330	0.0029	0.8	0.7

The correlation between experimental data and model predicting the response of the twisted M.S samples is shown in Fig 8.13. It may be concluded that the model is compatible with the experimental data.

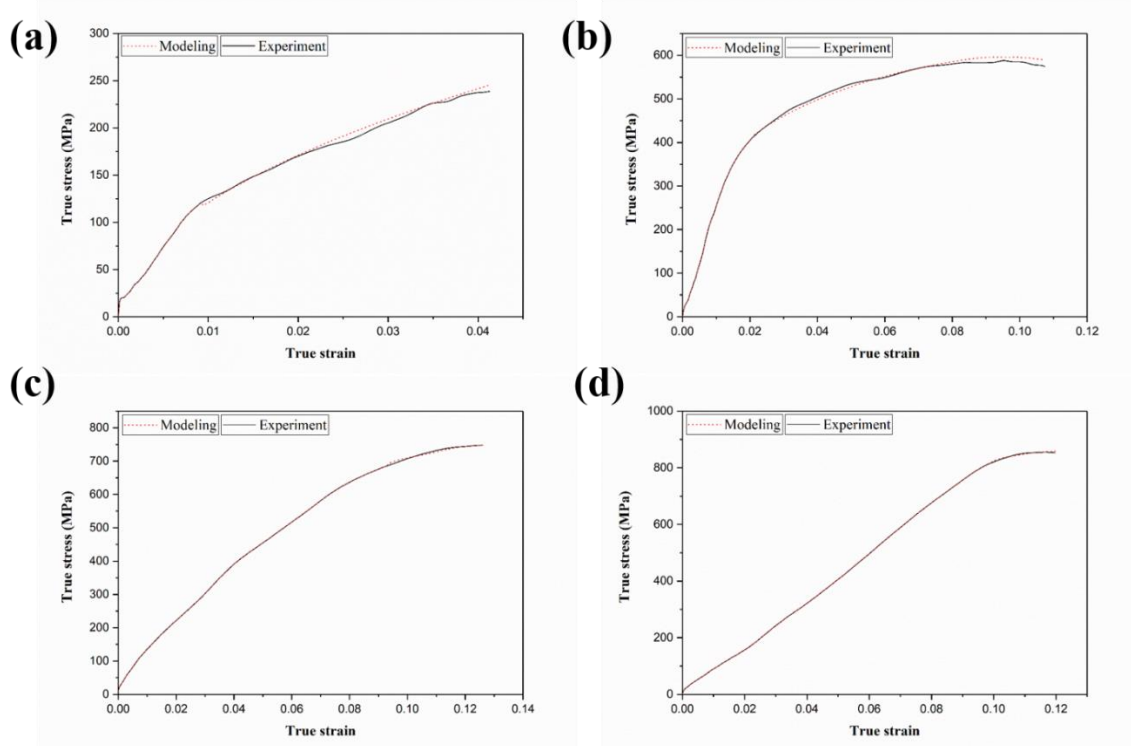


Fig 8. 13 Comparison between the tested flow stress curves and the Kobayashi-Odd model description for (a) 3 degree-260 s<sup>-1</sup>, (b) 6 degree-650 s<sup>-1</sup>, (c) 9 degree-720 s<sup>-1</sup>, (d) 12 degree-650 s<sup>-1</sup>.

#### 8.4.2. Nemat Nasser-Isaacs model

In this model, which is an example of a thermal activation model, stress is decomposed in long-range barriers that cannot be defeated by thermal energy and short-range barriers which can be assisted by thermal energy. In this model, the concept of dislocation motion during plastic deformation is used for describing the flow stress. For M.S with BCC structure, the Peierls barriers (short-range barriers) are the only barriers to dislocation motion. Nemat- Nasser proposed the following equation to estimate dynamic deformation with regard to temperature, strain rate, and strain [34]:

$$\tau = \tau_0 \cdot \dot{\gamma}^n + \tau^* \left( 1 - \left\{ - \left( \frac{k}{G_0} \right) T \left( \ln \left( \frac{\dot{\gamma}}{\dot{\gamma}_r} \right) + \ln \left( \frac{\dot{\gamma}'}{\dot{\gamma}_r'} \right) \right) \right\}^{1/q} \right)^{1/q} \quad (8-11)$$

where  $\tau^{\wedge}$  is the threshold stress of Peierls barrier to dislocation motion,  $G_0$  is the equivalent energy and  $K$  is the Boltzmann constant.  $G_0$  is considered as 1 eV/atom then

$$\frac{k}{G_0} = 8.62 * 10^{-5} K^{-1} \quad (8-12)$$

$\dot{\gamma}^{rr}$  is the reference strain rate, which is calculated by Eq 8.13 with regard to Burgers vector and density of dislocations:

$$\dot{\gamma}^{rr} = \rho b^2 w_0 \quad (8-13)$$

where  $w_0$  is the attempt frequency and Kocks considered it as  $10^{12} \text{ s}^{-1}$  [35]. The burgers vector magnitude for M.S is taken as 0.249 nm [22], and the dislocation density in M.S before plastic deformation is taken as  $10^{15} \text{ m}^{-2}$  [4]. With these assumptions, the reference strain rate is obtained as

$$\dot{\gamma}^{rr} = 6.2 * 10^7 \text{ s}^{-1} \quad (8-14)$$

In equation (8.11), the temperature can be calculated based on equation 8.7 by considering that plastic work is transformed to heat. In this equation,  $q$  and  $p$  are unchanging factors that describe the profile of the energy barrier and are suggested by Kocks [35].

In this equation,  $\tau_0 \dot{\gamma}^n$  is taken as athermal component of the flow stress and the rest of equation is considered thermally activated component of flow stress.

Table 8. 5. Determined parameters values of Nemat-Nasser model.

Sample	$\tau_0$ (MPa)	$\tau^{\wedge}$ (MPa)	n	q	p
3 degree	1200	300	0.5	1.5	0.1
6 degree	1000	350	0.35	1.5	0.5
9 degree	1330	450	0.3	1	0.1
12 degree	905	500	0.17	2	0.66

Fig 8.14 compares the results of the Nemat-Nasser model with experimental data in which the fit is acceptable. As shown in Fig 8.15, with an increase in the angle of twist, the  $\tau^{\wedge}$  values have increased ascribable to dislocation density increment; alternatively, n values, which are indicative of work hardening, have been reduced with angle of twist enhancement ascribable to the superiority of thermal softening over strain-hardening.

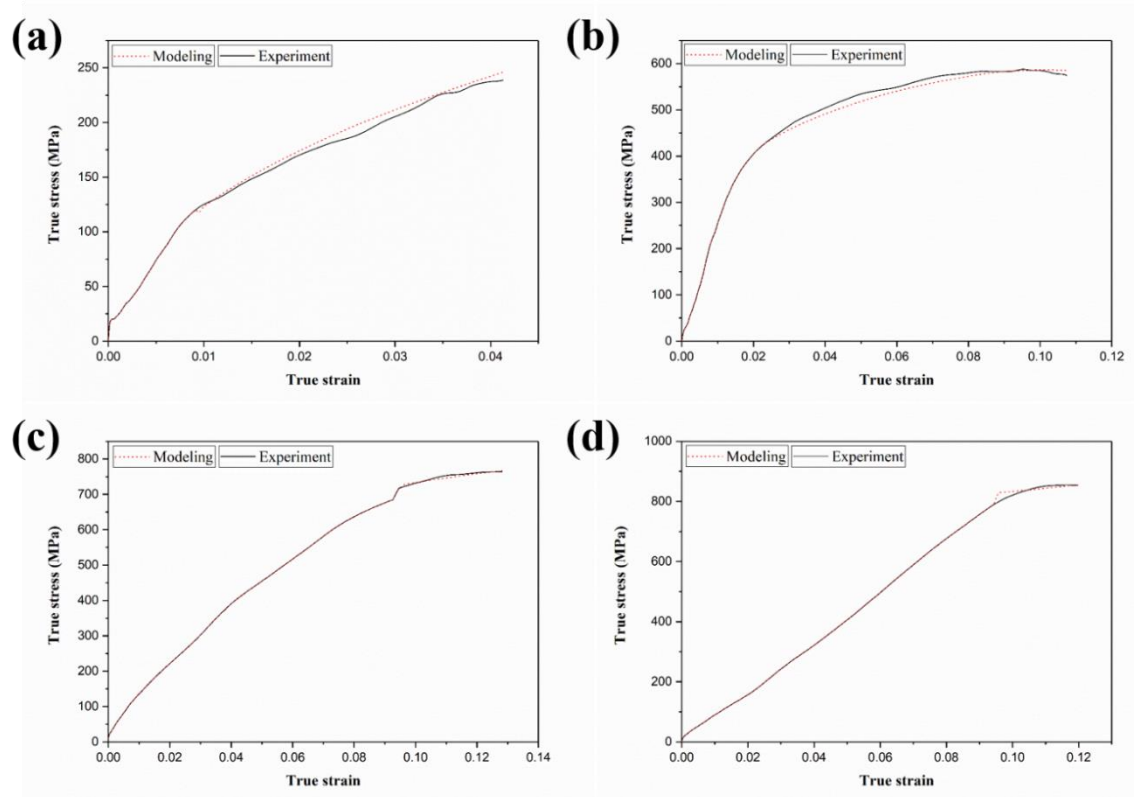


Fig 8. 14 Comparison between the tested flow stress curves and the Nemat-Nasser model description for (a) 3 degree-260 s<sup>-1</sup>, (b) 6 degree-650 s<sup>-1</sup>, (c) 9 degree-720 s<sup>-1</sup>, (d) 12 degree-650 s<sup>-1</sup>.

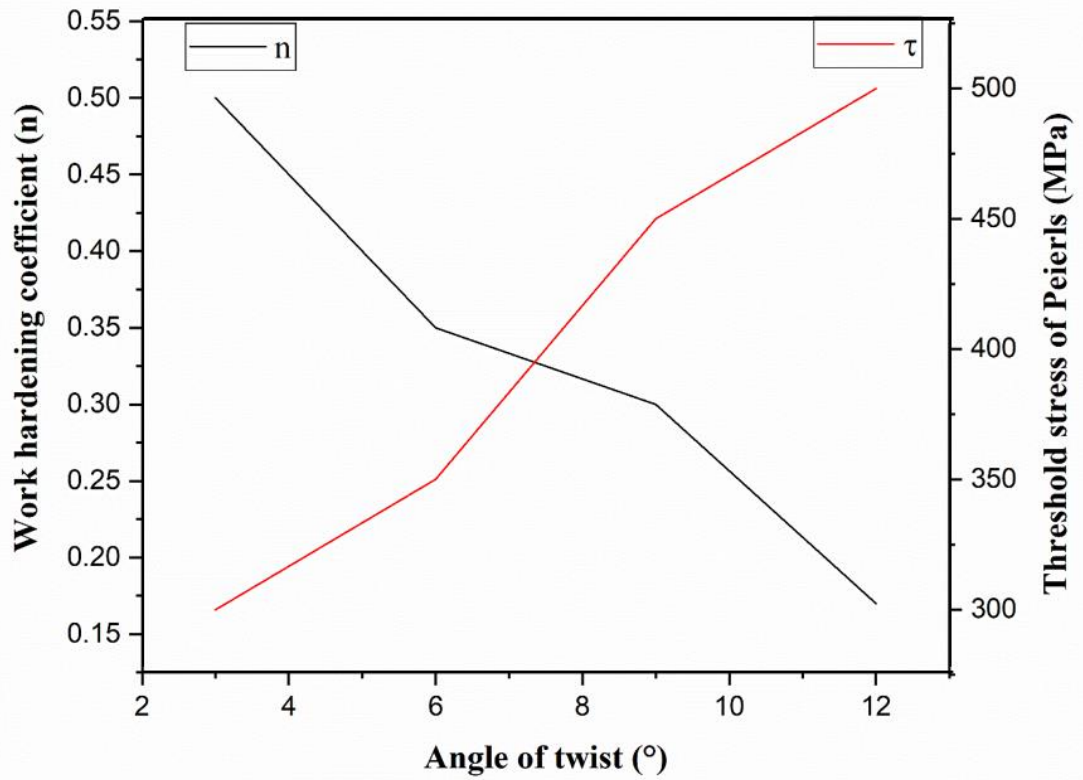


Fig 8. 15 Threshold stress of Peierls stress and work hardening coefficient as function of angle of twist.

### 8.5. Conclusion

The high speed performance of LPBF-M.S in torsion has been studied using SHTB apparatus. With the change of angle of twist in SHTB apparatus, different strain rates were generated in the thin-walled tubular test specimens. In the torsion test specimens, the applied angle of twist of 3, 6, 9, and 12 degrees generated strain rates of 260, 650, 720 and 650 s<sup>-1</sup>, respectively. Due to the small wall thickness of the torsion specimen, the shear strain rate, shear strain, and temperature are suggested to be localized in this part of the specimen. The M.S fractured when the applied twist angle was increased to 12 degrees (strain rates of 650 s<sup>-1</sup>). Microstructural and textural analyses were done on twisted

samples, and results showed that shear localization and ASBs are responsible for fracture of the twisted sample. Texture intensity reduced with increment in strain rate ascribable to grain fragmentation at high speeds. Furthermore, the Kobayashi–Dodd and Nemat-Nasser constitutive models were successfully developed to describe the dynamic shear stress-strain response of LPBF-M.S.

## 8.6. References

- [1] J.P. Oliveira, A.D. LaLonde, J. Ma, Processing parameters in laser powder bed fusion metal additive manufacturing, *Mater. Des.* 193 (2020) 108762.
- [2] S.L. Sing, W.Y. Yeong, Laser powder bed fusion for metal additive manufacturing: perspectives on recent developments, *Virtual Phys. Prototyp.* 15 (2020) 359–370.
- [3] S. Shamsdini, M.H. Ghoncheh, M. Sanjari, H. Pirgazi, B.S. Amirkhiz, L. Kestens, M. Mohammadi, Plastic deformation throughout strain-induced phase transformation in additively manufactured maraging steels, *Mater. Des.* 198 (2020) 109289.
- [4] S. Dehgahi, M.H. Ghoncheh, A. Hadadzadeh, M. Sanjari, B.S. Amirkhiz, M. Mohammadi, The role of titanium on the microstructure and mechanical properties of additively manufactured C300 maraging steels, *Mater. Des.* (2020) 108965.
- [5] A.F. de Souza, K.S. Al-Rubaie, S. Marques, B. Zluhan, E.C. Santos, Effect of laser speed, layer thickness, and part position on the mechanical properties of maraging 300 parts manufactured by selective laser melting, *Mater. Sci. Eng. A.* 767 (2019) 138425.

- [6] F.F. Conde, J.D. Escobar, J.P. Oliveira, M. Béréš, A.L. Jardini, W.W. Bose, J.A. Avila, Effect of thermal cycling and aging stages on the microstructure and bending strength of a selective laser melted 300-grade maraging steel, *Mater. Sci. Eng. A.* 758 (2019) 192–201.
- [7] S. Dehgahi, R. Alaghmandfard, J. Tallon, A. Odeshi, M. Mohammadi, Microstructural evolution and high strain rate compressive behavior of as-built and heat-treated additively manufactured maraging steels, *Mater. Sci. Eng. A.* 815 (2021) 141183.
- [8] S. Dehgahi, H. Pirgazi, M. Sanjari, R. Alaghmandfard, J. Tallon, A. Odeshi, L. Kestens, M. Mohammadi, Texture evolution during high strain-rate compressive loading of maraging steels produced by laser powder bed fusion, *Mater. Charact.* (2021) 111266.
- [9] H. Kolsky, An investigation of the mechanical properties of materials at very high rates of loading, *Proc. Phys. Soc. Sect. B.* 62 (1949) 676.
- [10] W.E. Baker, C.H. Yew, Strain-rate effects in the propagation of torsional plastic waves, (1966).
- [11] G. Chen, L.T. Li, J.W. Qiao, Z.M. Jiao, S.G. Ma, F.L. Ng, Z.G. Zhu, D. Zhao, Z.H. Wang, Gradient hierarchical grain structures of Al<sub>0.1</sub>CoCrFeNi high-entropy alloys through dynamic torsion, *Mater. Lett.* 238 (2019) 163–166.
- [12] A. Gilat, C.-S. Cheng, Torsional split Hopkinson bar tests at strain rates above 10<sup>4</sup> s<sup>-1</sup>, *Exp. Mech.* 40 (2000) 54–59.
- [13] A. Khosravifard, M.M. Moshksar, R. Ebrahimi, High strain rate torsional testing of a high manganese steel: Design and simulation, *Mater. Des.* 52 (2013) 495–503.
- [14] G.H. Majzoobi, K. Rahmani, S. Lahmi, Determination of length to diameter ratio of the bars in torsional Split Hopkinson bar, *Measurement.* 143 (2019) 144–154.

- [15] S. Tiwari, S. Mishra, A. Odeshi, J.A. Szpunar, M. Chopkar, Evolution of texture and microstructure during high strain rate torsion of aluminium zinc magnesium copper alloy, *Mater. Sci. Eng. A.* 683 (2017) 94–102.
- [16] Y. Xu, J. Zhang, Y. Bai, M.A. Meyers, Shear localization in dynamic deformation: microstructural evolution, *Metall. Mater. Trans. A.* 39 (2008) 811–843.
- [17] W.-S. Lee, J.-I. Cheng, C.-F. Lin, Deformation and failure response of 304L stainless steel SMAW joint under dynamic shear loading, *Mater. Sci. Eng. A.* 381 (2004) 206–215.
- [18] Q. Niu, W. Ming, M. Chen, S. Tang, P. Li, Dynamic mechanical behavior of ultra-high strength steel 30CrMnSiNi2A at high strain rates and elevated temperatures, *J. Iron Steel Res. Int.* 24 (2017) 724–729.
- [19] Y.F. Shen, N. Jia, R.D.K. Misra, L. Zuo, Softening behavior by excessive twinning and adiabatic heating at high strain rate in a Fe–20Mn–0.6 C TWIP steel, *Acta Mater.* 103 (2016) 229–242.
- [20] A.A. Tiamiyu, A.G. Odeshi, J.A. Szpunar, Multiple strengthening sources and adiabatic shear banding during high strain-rate deformation of AISI 321 austenitic stainless steel: Effects of grain size and strain rate, *Mater. Sci. Eng. A.* 711 (2018) 233–249.
- [21] R. Alaghmandfard, C. Dharmendra, A.G. Odeshi, M. Mohammadi, Dynamic mechanical properties and failure characteristics of electron beam melted Ti-6Al-4V under high strain rate impact loadings, *Mater. Sci. Eng. A.* 793 (2020) 139794.
- [22] S. Dehgahi, M. Sanjari, M.H. Ghoncheh, B.S. Amirkhiz, M. Mohammadi, Concurrent improvement of strength and ductility in heat-treated C300 maraging steels produced by laser powder bed fusion technique, *Addit. Manuf.* (2021) 101847.

- [23] J. Duffy, Y.C. Chi, On the measurement of local strain and temperature during the formation of adiabatic shear bands, *Mater. Sci. Eng. A.* 157 (1992) 195–210.
- [24] H. Kobayashi, B. Dodd, A numerical analysis for the formation of adiabatic shear bands including void nucleation and growth, *Int. J. Impact Eng.* 8 (1989) 1–13.
- [25] M. Zhou, A.J. Rosakis, G. Ravichandran, Dynamically propagating shear bands in impact-loaded prenotched plates—I. Experimental investigations of temperature signatures and propagation speed, *J. Mech. Phys. Solids.* 44 (1996) 981–1006.
- [26] P.R. Guduru, A.J. Rosakis, G. Ravichandran, Dynamic shear bands: an investigation using high speed optical and infrared diagnostics, *Mech. Mater.* 33 (2001) 371–402.
- [27] A. Hadadzadeh, C. Baxter, B.S. Amirkhiz, M. Mohammadi, Strengthening mechanisms in direct metal laser sintered AlSi10Mg: Comparison between virgin and recycled powders, *Addit. Manuf.* 23 (2018) 108–120.
- [28] C. Tian, D. Ponge, L. Christiansen, C. Kirchlechner, On the mechanical heterogeneity in dual phase steel grades: Activation of slip systems and deformation of martensite in DP800, *Acta Mater.* 183 (2020) 274–284.
- [29] G.R. Canova, C. Fressengeas, A. Molinari, U.F. Kocks, Effect of rate sensitivity on slip system activity and lattice rotation, *Acta Metall.* 36 (1988) 1961–1970.
- [30] N.P. Gurao, R. Kapoor, S. Suwas, Effect of strain rate on evolution of the deformation microstructure and texture in polycrystalline copper and nickel, *Metall. Mater. Trans. A.* 41 (2010) 2794–2804.
- [31] J. Baczynski, J.J. Jonas, Texture development during the torsion testing of  $\alpha$ -iron and two IF steels, *Acta Mater.* 44 (1996) 4273–4288.

[32] A. Hadadzadeh, B.S. Amirkhiz, J. Li, A. Odeshi, M. Mohammadi, Deformation mechanism during dynamic loading of an additively manufactured AlSi10Mg\_200C, *Mater. Sci. Eng. A.* 722 (2018) 263–268.

[33] Y. Xu, H.J. Yang, M.A. Meyers, Dynamic recrystallization in the shear bands of Fe–Cr–Ni monocrystal: Electron backscatter diffraction characterization, *Scr. Mater.* 58 (2008) 691–694.

[34] S. Nemat-Nasser, J.B. Isaacs, Direct measurement of isothermal flow stress of metals at elevated temperatures and high strain rates with application to Ta and TaW alloys, *Acta Mater.* 45 (1997) 907–919.

[35] U.F. Kocks, Realistic constitutive relations for metal plasticity, *Mater. Sci. Eng. A.* 317 (2001) 181–187.

## Chapter 9: Discussion

The performance of maraging steel components has been improved by changing the chemical compositions of the powder. This project introduces a new C300-LPBF material with the same price and better mechanical properties as a result of Ti addition. New maraging steel powder with slightly higher Ti content can be useful for improving the mechanical behavior of manufactured parts. As chemical composition changes do not affect the final price of maraging steel powder, this can be a significant achievement in the manufacturing industry. Researchers and scientists are currently looking for new ways to improve the mechanical behavior of final parts through changing processing parameters of LPBF such as laser power and laser speed or changing building direction or defining post processing heat treatments. Meanwhile, changing chemical composition can be a useful alternative provided that the addition of elements would not affect the powder price.

In this work, the effect of Ti addition on the quasi-static and dynamic behavior of additively manufactured maraging steels was studied and since the improved mechanical behavior was observed, in dynamic torsion test (the main goal of this research), Ti-rich maraging steel was used. Maraging steels are subjected to complex loading conditions including torsion mode in industry and this research was focused on the torsion behavior of maraging steels. At first, the effect of Ti addition on quasi-static and dynamic compression loading was studied. Ti-rich maraging steels showed to have higher strength and ductility in both as-built and heat-treated conditions. In as-built HighTi samples, NiCo precipitates and higher austenite fraction were found that are responsible for better mechanical properties of the HighTi sample. The addition of Ti could benefit maraging

steel properties through introducing new precipitates of NiCo. HighTi samples showed higher hardness and strength due to the presence of these precipitates and higher density of dislocations. Besides, it was shown that more Ti resulted in more fraction of austenite due to segregation of elements in grain boundaries. In addition, it was found that Ti addition could develop gamma-fibre texture in maraging steels. The effect of heat treatment was investigated on LowTi and HighTi maraging steels and it was proved that the addition of Ti leads to the increasing of strength and ductility simultaneously through the development of precipitates and phase transformation of austenite to martensite during deformation. This austenite phase transformed to martensite during deformation, which increased the strength. The addition of Ti not only increased the fraction of austenite but also changed the texture of austenite grains from  $\langle 100 \rangle$  to  $\langle 111 \rangle$  orientation. The microstructural characterization proved that this alloy contains a higher amount of reverted austenite (17.89 wt%), which resulted in higher strength as a result of the transformation-induced plasticity (TRIP) effect. By adding Ti,  $\langle 111 \rangle$   $\gamma$  fibre and Copper texture were developed in as-built and heat-treated maraging steel samples, which resulted in ductility improvement in these samples.

TEM studies showed that a higher fraction of  $\text{Ni}_3\text{Ti}$  precipitates were found in the HighTi sample, which leads to enhanced strength of this sample after heat treatment. Besides, the high strain rate compressive behavior of as-built and heat-treated maraging steels was investigated. It was demonstrated that as-built maraging steels showed better behavior on dynamic compressive loading compared to heat-treated maraging steels due to lower ductility of the heat-treated samples. Lower ductility of heat-treated samples led to their quicker failure compared to as-built samples. As-built samples begin to fracture

around strain rates of  $\sim 3500 \text{ s}^{-1}$ , while for heat-treated samples, failure happened around  $\sim 1930 \text{ s}^{-1}$ . Adiabatic shear bands as a pathway to accommodate imposed shear stresses were observed around  $\sim 1500 \text{ s}^{-1}$  for as-built samples and strain rate of  $890 \text{ s}^{-1}$  for heat-treated ones. Chang-Asaro numerical modeling was used to predict the mechanical response of as-built and heat-treated maraging steels in high strain rate test and good agreements were found between experimental and modeling data. Furthermore, texture evolution during dynamic compressive loading was explored.

As-built maraging steel samples developed significant texture in dynamic compression loading and strong  $\{111\} \parallel \text{LD}$  and  $\{100\} \parallel \text{LD}$  fibres appeared in EBSD analysis. However, heat-treated samples did not show any texture change during high strain rate compressive loading. This was related to a higher number of activated slip systems in as-built samples compared to heat-treated samples. In addition, the effect of interaction between building direction and heat treatment on dynamic compressive behavior of heat-treated maraging steels was discussed and it was concluded that horizontally built samples showed higher strength compared to vertically built samples due to the presence of columnar grains (with  $\{100\} \parallel \text{BD}$  texture) in the vertical samples. Vertically built samples fractured in strain rate of  $1300 \text{ s}^{-1}$ . However, for horizontally built samples, failure occurred in strain rate of  $2200 \text{ s}^{-1}$ . Besides, Johnson-Cook and Voyiadjis and Abed models were used to predict the high strain rate response of horizontally and vertically built samples. Results of modeling were consistent with microstructural analysis and a good fit was observed between modeling and experimental data.

Furthermore, dynamic compressive and corrosion behavior of LowTi and HighTi samples were evaluated. In high strain rate compression loading, LowTi samples fractured

in strain rate of  $3150 \text{ s}^{-1}$ . However, until strain rate of  $5000 \text{ s}^{-1}$ , failure did not happen for HighTi sample. This was related to the presence of more austenite fraction in HighTi sample, which can delay strain localization, and the formation of adiabatic shear bands. However, HighTi sample showed inferior corrosion behavior due to the presence of NiCo precipitates, which trigger galvanic corrosion. The effect of prior deformation on corrosion behavior was investigated and it was concluded that dynamically deformed samples showed better corrosion behavior due to recrystallization process during dynamic deformation, which improves corrosion behavior. Ti-rich maraging steels showed to have superior mechanical properties in quasi-static and dynamic compressive loading, which leads to the investigation of dynamic torsion loading on this newly developed material.

Dynamic torsion response was studied in angles of twist 3, 6, 9 and 12 degrees on hexagonal maraging steel samples. Results showed that in angle of twist 12 degrees, failure happened for LPBF-maraging steel due to localization of shear stress in shear bands. Furthermore, two constitutive models have been employed for describing the torsion behavior of LPBF-maraging steel parts. Kobayashi-Odd and Nemat-Nasser models showed a good fit with the observed experimental data.

Maraging steel components are subjected to complex loadings containing compression and torsion in industry and having a new material with better mechanical properties could help designers and manufacturers to increase the efficiency of the final products. The seven projects conducted in this thesis investigated the effect of chemical composition and dynamic behavior of additively manufactured maraging steels. By implementing this work's outcome, one can use newly developed maraging steels to achieve required properties in the complex loading condition for different industries.

## Chapter 10: Conclusions and future works

### 10.1. Conclusions

In this thesis, a comprehensive study on the dynamic behavior of additively manufactured 18Ni-300 maraging steels was presented. LPBF-maraging steel parts were examined under different loading conditions to examine maraging steel's response under simulated industrial situations.

The first paper published in the journal of "*Materials and Design*", under the title of "*The role of titanium on the microstructure and mechanical properties of additively manufactured C300 maraging steels*". C300 metal powders containing two different Ti contents (0.72 and 1.17 wt.%) were used to additively manufacture maraging steel samples. The powder particle morphology and microstructure were investigated as well as the particle size distribution. The microstructure of both powders was mostly columnar-dendritic, where the area fraction of the equiaxed grains in the HighTi powder was higher. The volume fraction of austenite in both LowTi and HighTi powders was almost the same, while the HighTi AM sample shows higher percentage of austenite compared to the LowTi AM sample. Besides, the HighTi sample showed numerous ultra-fine CoNi precipitates through its TEM micrograph which results in higher hardness of the HighTi sample. The HighTi sample also revealed higher dislocation density providing higher ultimate tensile strength.

The second paper with the title "*Concurrent improvement of strength and ductility in heat-treated C300 maraging steels produced by laser powder bed fusion technique*," published in "*Additive Manufacturing*" journal. In this paper, the effect of aging in 490 °C for 6 hours

on microstructure and mechanical properties of LowTi (Ti content =0.72 wt.%) and HighTi (Ti content=1.17 wt.%) samples were investigated. A pronounced crystallographic orientation was observed after Ti addition where  $\langle 111 \rangle_\gamma$  fiber texture and a copper component ( $\{112\} \langle 111 \rangle$ ) were developed. Both  $\text{Ni}_3\text{Mo}$  and  $\text{Ni}_3\text{Ti}$  precipitates were found in LowTi and HighTi samples, where volume fraction of  $\text{Ni}_3\text{Ti}$  precipitates were higher in the HighTi samples. It was concluded that the HighTi sample showed higher strength due to phase transformation as a result of higher austenite fraction and precipitation hardening as a result of more fraction of  $\text{Ni}_3\text{Ti}$  precipitates.

The third paper “*Microstructural evolution and high strain rate compressive behavior of as-built and heat-treated additively manufactured maraging steels*” was published in the journal of “*Materials Science and Engineering: A*”. In this paper, high strain rate behavior of as-built and heat-treated LPBF-maraging steels were investigated with Split Hopkinson pressure bar apparatus. As-built samples were subjected to strain rates of  $1500 \text{ s}^{-1}$ ,  $2000 \text{ s}^{-1}$ ,  $3200 \text{ s}^{-1}$ ,  $3500 \text{ s}^{-1}$  and  $4000 \text{ s}^{-1}$ , where fracture happened in strain rate of  $3500 \text{ s}^{-1}$ . Heat-treated samples were subjected to strain rates of  $150 \text{ s}^{-1}$ ,  $400 \text{ s}^{-1}$ ,  $670 \text{ s}^{-1}$ ,  $890 \text{ s}^{-1}$  and  $1930 \text{ s}^{-1}$  due to lower ductility of heat-treated samples. For heat-treated samples, fracture happened in strain rate of  $1930 \text{ s}^{-1}$ . During dynamic loading, plastic work converted to heat, which results in thermomechanical instability and formation of adiabatic shear bands. Adiabatic shear bands were seen in strain rates of  $1500 \text{ s}^{-1}$ ,  $2000 \text{ s}^{-1}$  and  $3200 \text{ s}^{-1}$  for as-built samples and in strain rate of  $890 \text{ s}^{-1}$ , adiabatic shear bands were detected for heat-treated samples. Constitutive modeling using Chang-Asaro equation were done on both as-built and heat-treated samples to predict behavior of LPBF-maraging steels on high strain rate compression test.

The fourth paper was published in the journal of “*Materials Characterization*” under the title of “*Texture evolution during high strain-rate compressive loading of maraging steels produced by laser powder bed fusion*”. In this paper, dynamic compressive tests were conducted on as-built and heat-treated maraging steel samples. As-built samples were tested in strain rates of  $2000\text{ s}^{-1}$ ,  $2300\text{ s}^{-1}$  and  $3200\text{ s}^{-1}$ , while heat-treated samples were tested in strain rates of  $650\text{ s}^{-1}$ ,  $680\text{ s}^{-1}$  and  $950\text{ s}^{-1}$ . The texture of the deformed samples was measured using the electron backscattering diffraction (EBSD) technique. Results confirmed that the reason for adiabatic shear band formation in as-built samples is related to texture evolution and activation of slip systems during deformation. Besides, due to compression loading, strong  $\{111\}\|LD$  and  $\{100\}\|LD$  fibres were detected in as-built samples. Due to limited active slip systems in heat-treated samples, possibility of shear band formation has been reduced and also significant texture has not been detected in heat-treated samples.

## **10.2. Recommendations for future work**

### **10.2.1. Tailored mechanical properties**

The current work shows that Ti-rich maraging steel demonstrates exceptional mechanical behavior in quasi-static and dynamic conditions. Maraging steel could have better mechanical properties by changing other elements at lower or the same price. Due to the necessity of industry for high strength parts, maraging steels are used mostly in heat-treated situations. The ductility of heat-treated maraging steels is limited and is a concern for manufacturers. More studies could shed light on new methods to improve the ductility of maraging steel parts.

There is a chance that the amount of austenite governs the ductility of the material. There should be some methods for increasing austenite fraction (soft part) in heat-treated maraging steels. Ti was a good choice as it had two main effects; first, it increased austenite fraction, which leads to improvement of ductility, second, it caused the formation of NiCo precipitates in as-built maraging steels, which act as nucleation sites for Ni<sub>3</sub>Ti precipitates, and in this way, it did not deteriorate the strength of final parts.

In addition, different heat treatment procedures should be conducted on the Ti-rich samples to monitor the fraction of austenite and Ni<sub>3</sub>Ti precipitates. The effect of solution annealing before aging should also be investigated to compare the fraction of austenite/martensite with direct aging.

More studies about the nature of adiabatic shear bands should be conducted. TEM studies on adiabatic shear bands can be done to detect diffraction patterns inside and outside the shear bands. Generally, more studies are essential to understand the formation mechanism of shear bands and to find solutions to prevent their formation, as they are detrimental. In addition, there is no study about the depth of shear bands in the structure. Besides, the corrosion mechanism of shear bands should be investigated to have a better knowledge for designing parts in a corrosive environment. Besides, with the advancement of technology, there are more sophisticated techniques to detect the temperature rise inside the shear bands, which helps to understand their formation mechanism.

Furthermore, the effect of different heat treatment routes on phase transformation and microstructure during dynamic compression tests should be considered. In this study, the effect of the well-known heat treatment of LPBF-maraging steel (490 °C for 6 hours) was evaluated. There is a chance to observe different behaviors in other heat treatment

conditions. In addition, by changing the process parameters, different dynamic behaviors are expected. A comprehensive study based on the necessity of the application in the specific industry is needed.

To have a broad knowledge about the dynamic behavior of LPBF-maraging steels, a comparison of phase transformation on quasi-static and dynamic loading conditions is required to be performed. Ductility is an important factor in materials response under high strain rate loading and improving ductility can be achieved by changing the amount of austenite. More studies are needed on the effect of different fraction of austenite on the dynamic behavior of LPBF-maraging steels.

There are limited works on high strain rate torsion tests and there should be more studies to understand the mechanism of failure in dynamic torsion. The effect of building direction on high strain rate torsion behavior of LPBF-maraging steel is an interesting investigation to gain a better insight about the anisotropy of the parts. The effect of heat treatment (490 °C for 6 hours) has not been evaluated on torsion mode of loading, which is very important as maraging steels are used mostly in heat-treated conditions.

To simulate industrial conditions, temperature and loading should be applied simultaneously. Dynamic compression and torsion tests in high temperatures should be performed to have precise information about the material's response in industry. Furthermore, corrosion tests should be conducted on torsional deformed samples to compare with corrosion results of dynamically deformed samples in compressive loading.

### **10.2.2. Modeling and simulations**

Except for presented physical equations to predict the dynamic behavior in compression and torsion in this study, other constitutive equations can be applied for comparison. In addition to present physical models for describing the material's response in high strain rate compression and torsion, the finite element method can be used for predicting stress distribution and stress concentration zones in the LPBF-maraging steels.

# Appendix A

CCC RightsLink® Home ? Live Chat Sign in Create Account

 **The role of titanium on the microstructure and mechanical properties of additively manufactured C300 maraging steels**  
Author: S. Dehgahi, M.H. Ghoncheh, A. Hadadzadeh, M. Sanjari, B. Shalchi Amirkhiz, M. Mohammadi  
Publication: Materials & Design  
Publisher: Elsevier  
Date: September 2020  
*Crown Copyright © 2020 Published by Elsevier Ltd.*

**Journal Author Rights**  
Please note that, as the author of this Elsevier article, you retain the right to include it in a thesis or dissertation, provided it is not published commercially. Permission is not required, but please ensure that you reference the journal as the original source. For more information on this and on your other retained rights, please visit: <https://www.elsevier.com/about/our-business/policies/copyright#Author-rights>

[BACK](#) [CLOSE WINDOW](#)

© 2021 Copyright - All Rights Reserved | Copyright Clearance Center, Inc. | Privacy statement | Terms and Conditions  
Comments? We would like to hear from you. E-mail us at [customer-care@copyright.com](mailto:customer-care@copyright.com)

CCC RightsLink® Home ? Live Chat Sign in Create Account

 **Concurrent improvement of strength and ductility in heat-treated C300 maraging steels produced by laser powder bed fusion technique**  
Author: S. Dehgahi, M. Sanjari, M.H. Ghoncheh, B. Shalchi Amirkhiz, M. Mohammadi  
Publication: Additive Manufacturing  
Publisher: Elsevier  
Date: March 2021  
*Crown Copyright © 2021 Published by Elsevier B.V. All rights reserved.*

**Journal Author Rights**  
Please note that, as the author of this Elsevier article, you retain the right to include it in a thesis or dissertation, provided it is not published commercially. Permission is not required, but please ensure that you reference the journal as the original source. For more information on this and on your other retained rights, please visit: <https://www.elsevier.com/about/our-business/policies/copyright#Author-rights>

[BACK](#) [CLOSE WINDOW](#)

© 2021 Copyright - All Rights Reserved | Copyright Clearance Center, Inc. | Privacy statement | Terms and Conditions  
Comments? We would like to hear from you. E-mail us at [customer-care@copyright.com](mailto:customer-care@copyright.com)

CCC RightsLink® Home ? Live Chat Sign in Create Account

 **Microstructural evolution and high strain rate compressive behavior of as-built and heat-treated additively manufactured maraging steels**  
Author: S. Dehgahi, R. Alaghmandfard, J. Tallon, A. Odeshi, M. Mohammadi  
Publication: Materials Science and Engineering: A  
Publisher: Elsevier  
Date: 20 May 2021  
*© 2021 Elsevier B.V. All rights reserved.*

**Journal Author Rights**  
Please note that, as the author of this Elsevier article, you retain the right to include it in a thesis or dissertation, provided it is not published commercially. Permission is not required, but please ensure that you reference the journal as the original source. For more information on this and on your other retained rights, please visit: <https://www.elsevier.com/about/our-business/policies/copyright#Author-rights>

[BACK](#) [CLOSE WINDOW](#)

© 2021 Copyright - All Rights Reserved | Copyright Clearance Center, Inc. | Privacy statement | Terms and Conditions  
Comments? We would like to hear from you. E-mail us at [customer-care@copyright.com](mailto:customer-care@copyright.com)



**Texture evolution during high strain-rate compressive loading of maraging steels produced by laser powder bed fusion**

**Author:** S. Dehgahi,H. Pirgazi,M. Sanjari,R. Alaghmandfard,J. Tallon,A. Odeshi,L. Kestens,M. Mohammadi  
**Publication:** Materials Characterization  
**Publisher:** Elsevier  
**Date:** August 2021  
 © 2021 Elsevier Inc. All rights reserved.

**Journal Author Rights**

Please note that, as the author of this Elsevier article, you retain the right to include it in a thesis or dissertation, provided it is not published commercially. Permission is not required, but please ensure that you reference the journal as the original source. For more information on this and on your other retained rights, please visit: <https://www.elsevier.com/about/our-business/policies/copyright#Author-rights>

[BACK](#)

[CLOSE WINDOW](#)



**Effect of building direction on high strain-rate compressive behavior of heat-treated LPBF-maraging steels using Split Hopkinson pressure bar apparatus**

**Author:** S. Dehgahi,H. Pirgazi,M. Sanjari,P. Seraj,A. Odeshi,L.A.I. Kestens,M. Mohammadi  
**Publication:** Materials Science and Engineering: A  
**Publisher:** Elsevier  
**Date:** 17 February 2022  
 © 2022 Elsevier B.V. All rights reserved.

**Journal Author Rights**

Please note that, as the author of this Elsevier article, you retain the right to include it in a thesis or dissertation, provided it is not published commercially. Permission is not required, but please ensure that you reference the journal as the original source. For more information on this and on your other retained rights, please visit: <https://www.elsevier.com/about/our-business/policies/copyright#Author-rights>

[BACK](#)

[CLOSE WINDOW](#)

# Curriculum Vitae

**Candidate's full name:** Shirin Dehgahi

**Universities attended:**

Shiraz University of Technology, Shiraz, Fars, Iran (2012-2014): M.Sc. Materials Engineering

Shahid Chamran University of Ahwaz, Ahwaz, Khozestan, Iran (2008-2012): B.Sc. Materials Engineering

**Awards:**

2018-2021: International Differential Scholarship, University of New Brunswick

2018-2019: New Brunswick Innovation Foundation (NBIF)

2018-2021: MITACS accelerate Award

**Publications and Conference Presentations:**

***Peer-Reviewed Publications:***

*Dehgahi, S., Ghoncheh, M.H., Hadadzadeh, A., Sanjari, M., Amirkhiz, B.S., Mohammadi, M." The role of titanium on the microstructure and mechanical properties of additively manufactured C300 maraging steels" Materials and Design 194 (2020) 108965.*

*Dehgahi, S., Sanjari, M., Ghoncheh, M.H., Amirkhiz, B.S., Mohammadi, M." Concurrent improvement of strength and ductility in heat-treated C300 maraging steels produced by laser powder bed fusion technique" Additive Manufacturing 39 (2021)101847.*

*Dehgahi, S., Alaghmandfard, R., Tallon, J., Odeshi, A., Mohammadi, M." Microstructural evolution and high strain rate compressive behavior of as-built and heat-treated additively manufactured maraging steels" Materials Science & Engineering A 815 (2021) 141183.*

*Dehgahi, S., Pirgazi, H., Sanjari, M., Alaghmandfard, R., Tallon, J., Odeshi, A., Kestens, L., Mohammadi, M. " Texture evolution during high strain-rate compressive loading of maraging steels produced by laser powder bed fusion " Materails Characterization 178 (2021) 111266.*

*Dehgahi, S., Pirgazi, H., Sanjari, Seraj, P., Bliznuk, V., Odeshi, A., Kestens, L., Mohammadi, M. " Effect of building direction on high strain rate compressive behavior of heat-treated LPBF-maraging steel using Split Hopkinson pressure bar apparatus". Materials Science and Engineering: A 835 (2022) 142653.*

***Submitted under review publications:***

*Dehgahi, S., Shahriari, A., Odeshi, A., Mohammadi, M. " Influence of composition on high strain rate mechanical and corrosion behavior of additively manufactured maraging steels". Submitted in Engineering failure analysis.*

*Dehgahi, S., Pirgazi, H., Sanjari, Seraj, P., Odeshi, A., Kestens, L., Mohammadi, M. " High strain rate torsional response of maraging steel parts produced by laser powder bed fusion techniques: deformation behavior and constitutive model". Submitted in Mechanics of Materials.*